

# THE BELL SYSTEM TECHNICAL JOURNAL

VOLUME XXXVIII

MARCH 1959

NUMBER 2

*Copyright 1959, American Telephone and Telegraph Company*

## The Three-Level Solid State Traveling-Wave Maser\*

By R. W. DeGRASSE, E. O. SCHULZ-DuBOIS,  
and H. E. D. SCOVIL

(Manuscript received December 18, 1958)

*Broadband very-low-noise microwave amplification can be obtained from solid state maser action in a propagating microwave structure. Such a traveling-wave maser produces unilateral amplification with a high degree of gain stability. The theory of the traveling-wave maser is developed and used to compare the gain, bandwidth and gain stability of the traveling-wave maser with that of the cavity maser. The general requirements for traveling-wave maser slow-wave structures are discussed. Theoretical analysis and experimental results are presented for the comb-in-waveguide slow-wave structure.*

*A traveling-wave maser consisting of a ruby-loaded comb structure was tested. A gain of 23 db at 6 kmc with a bandwidth of 25 mc was obtained. Further performance characteristics of this amplifier and one using gadolinium ethyl sulfate are given. Experimental verification of the low noise temperature of solid state masers was obtained.*

### I. INTRODUCTION

The three-level solid state maser, as proposed by Bloembergen,<sup>1</sup> employs a microwave pump signal to alter the thermal equilibrium of a

\* This work was supported in part by the U. S. Army Signal Corps under Contract DA-36-039 sc-73224.

paramagnetic salt in such a manner that an otherwise absorptive medium becomes emissive when stimulated by radiation at the signal frequency. Successful application of this principle to produce microwave amplification was reported by Scovil *et al.*,<sup>2,3</sup> who used microwave cavities to couple the microwave radiation to the paramagnetic salt. Several laboratories<sup>4,5</sup> have since operated such cavity-type masers.

Microwave amplification can also be obtained by stimulating radiation from active material in a propagating structure. Effective coupling of the microwave fields to the paramagnetic salt is obtained by slowing the velocity of propagation of the microwave energy through the structure. The active material produces an equivalent negative resistance in the slow-wave structure, and a propagating wave having an exponentially increasing amplitude is obtained.

However, if a slow-wave structure is simply filled with the active material, the device will be reciprocal and have gain in both directions. It would therefore require excellent input and output matches and presumably external isolation to obtain unilateral gain. Unidirectional traveling-wave amplification can be obtained in a slow-wave structure which has definite regions of circular polarization of the magnetic field if a maser material is employed which has circularly polarized signal-frequency transitions. The maser material is then loaded in the structure in such a manner that it is coupled to the structure only for one direction of wave propagation. Then, the maser will have high gain in one direction and little or no gain in the reverse direction.

Unidirectional gain alone is not enough to ensure freedom from regenerative instability. One might add reciprocal loss, as in the case of the traveling-wave tube. However, the traveling-wave tube has an electron beam to carry the microwave energy past the loss region, with very little forward attenuation; in the case of the traveling-wave maser, only the one propagation wave is present and the attenuation subtracts directly from the forward gain. Unidirectional loss may be obtained in the same manner as the unidirectional gain, that is, by excitation of a magnetic material through a circularly polarized magnetic field. For the magnetic material, one may use either an absorptive ferrimagnetic material or an absorptive paramagnetic material whose thermal equilibrium is not disturbed by the microwave pump power.

## II. TRAVELING-WAVE MASER THEORY

The amplification in a traveling-wave maser is obtained from power transferred to the microwave circuit by coherent excitation of the paramagnetic spins due to the magnetic fields of the circuit. This effect can

be represented classically in the constitutive equation of electromagnetic theory†

$$B = \mu_0(H + M_m), \quad (1)$$

where  $\mu_0$  is the permeability of free space and  $M_m$  is the magnetic moment per unit volume of maser material. The magnetic moment,  $M_m$ , is computed from the quantum mechanical treatment of the paramagnetic spin system. From this analysis may be obtained a complex permeability, given by

$$\chi' - j\chi'' = \frac{M_m}{H}. \quad (2)$$

The real part of the permeability,  $\chi'$ , will produce reactive effects in the microwave circuit, while the imaginary part can produce gain or loss. In most cases, the magnetic permeability depends upon the orientation of the magnetic field,  $H$ ; thus, it is in general a tensor quantity.

If we have a microwave structure uniform in the  $z$  direction and partially filled with a maser material, the rate of change of power in the circuit with distance is given by

$$\frac{dP}{dz} = -\frac{1}{2} \omega \mu_0 \int_{A_m} H \cdot \chi'' \cdot H^* dS, \quad (3)$$

where the integration is performed over the cross section of the maser material,  $A_m$ . The power in the waveguide is given by

$$P = \frac{1}{2} v_g \mu_0 \int_{A_s} H^2 dS, \quad (4)$$

where  $v_g$  is the group velocity in the waveguide circuit, and the integration is performed over the entire waveguide cross section,  $A_s$ . The gain in a length of structure,  $l$ , is then given by

$$G = \frac{P(l)}{P(0)} = \exp[-\chi''_{\max} F(\omega/v_g)l], \quad (5)$$

where  $\chi''_{\max}$  is the magnitude of the diagonalized  $\chi''$  tensor, and the filling factor,  $F$ , is defined by

$$F \equiv \frac{\int_{A_m} H \cdot \chi'' \cdot H^* dS}{\chi''_{\max} \int_{A_s} H^2 dS}. \quad (6)$$

† All equations are given in MKS units.

Rather than use the exact tensor representation for  $\chi''$ , it is convenient to obtain a value for  $\chi''$  which reflects the magnetic field orientation. In a cavity maser,  $\chi''$  would be defined for linear polarization. In a traveling-wave maser, however, it is desirable to obtain nonreciprocal effects by using circularly polarized magnetic fields to excite the signal transition in the maser material.

In a maser material with small zero field splitting, such as gadolinium ethyl sulfate, the signal transitions have nearly pure circular polarization. Thus, if the magnetic fields of the circuit are resolved into circular polarized components,  $H_+$  and  $H_-$ , the filling factor and gain (in decibels) are given by

$$F_+ = \frac{\int_{A_m} H_+^2 dS}{\int_{A_s} (H_+^2 + H_-^2) dS}, \quad (7)$$

$$G_{db} = -27.3 \chi_+'' F_+ \frac{fl}{v_g}, \quad (8)$$

where  $f$  is the signal frequency.

The permeability for positive circular polarization,  $\chi_+''$ , can be calculated using the notation of Schulz-DuBois.<sup>6</sup> He obtains for the rate of transition per ion from a state  $\bar{n}$  to a state  $\bar{n}'$ ,

$$w_{\bar{n} \rightarrow \bar{n}'}(S_+) = \frac{1}{2} \left( \frac{\pi g \beta}{\hbar} \right)^2 g(f - f_0) |\langle \bar{n}' | S_+ | \bar{n} \rangle|^2 H_+^2, \quad (9)$$

where positive circular polarization is assumed as indicated by  $S_+$ . The power absorbed per unit volume of material is then

$$P = (\rho_{\bar{n}} - \rho_{\bar{n}'}) \hbar f w_{\bar{n} \rightarrow \bar{n}'}(S_+), \quad (10)$$

where  $\rho_{\bar{n}}$  is the density of ions in energy state  $\bar{n}$  per unit volume.

The power absorbed per unit volume is given classically in terms of  $\chi_+''$  as

$$P = \frac{1}{2} \omega \mu_0 \chi_+'' H_+^2. \quad (11)$$

Thus,  $\chi_+''$  is given by

$$\chi_+'' = \frac{\pi}{2\mu_0 \hbar} (g\beta)^2 (\rho_{\bar{n}} - \rho_{\bar{n}'}) g(f - f_0) |\langle \bar{n}' | S_+ | \bar{n} \rangle|^2. \quad (12)$$

If the equilibrium spin populations are inverted by making  $\rho_{\bar{n}'}$  greater than  $\rho_{\bar{n}}$ ,  $\chi_+''$  will be negative and amplification is obtained. The various conditions for maser population inversion have been discussed by Scovil.<sup>3</sup> A companion paper in this issue<sup>7</sup> discusses this problem in more detail.

For the case of propagation of energy in the reverse direction through the amplifier, the magnetic field sense of polarization will reverse and the filling factor will become

$$F_- = \frac{\int_{A_m} H_-^2 dS}{\int_{A_s} (H_+^2 + H_-^2) dS}. \quad (13)$$

The degree of nonreciprocity of gain is then determined by the ratio,  $R_m$ , given by

$$R_m = \frac{\int_{A_m} H_+^2 dS}{\int_{A_m} H_-^2 dS}. \quad (14)$$

This ratio must be optimized in the selection of a suitable slow-wave structure for use in the amplifier.

As was mentioned before, nonreciprocity in gain is not enough to insure that the amplifier will not have regenerative effects due to mismatched input and output terminations. Thus, it is necessary to also include some nonreciprocal loss for isolation. Both ferrimagnetic and paramagnetic isolators have been used. By increasing the concentration of the active ion in the maser crystal, it is possible to prevent maser action. Such a high-concentration crystal will have energy levels which are identical to the maser material; thus, it will provide nonreciprocal loss at the desired magnetic field and orientation. Ferrimagnetic isolators can be designed to operate at the magnetic field required by the maser material by using shape anisotropy to change the frequency of ferrimagnetic resonance.

The isolator loss is determined by (5). If we retain the convention that  $H_+$  produces excitation of magnetic spins for propagation in the direction of amplification, and  $H_-$  for the reverse direction, then the isolator loss in the reverse direction is given by

$$L = 27.3 \chi_{i+}'' F_{i-} \frac{fl}{v_g}, \quad (15)$$

where

$$F_{i-} = \frac{\int_{A_s} H_-^2 dS}{\int_{A_s} (H_-^2 + H_+^2) dS} \quad (16)$$

and  $\chi''_{i+}$  is the lossy permeability of the isolator. The ratio of reverse loss to forward loss,  $R_i$ , then is the figure of merit of the isolator:

$$R_i = \frac{\int_{A_i} H_-^2 dS}{\int_{A_i} H_+^2 dS}. \quad (17)$$

In general, the figure of merit of a paramagnetic isolator will be about the same as that of the paramagnetic maser material. Since  $\chi''_{i+}$  is usually much greater for a ferrimagnetic than for a paramagnetic, it is possible to locate a ferrimagnetic isolator of small cross section in a region which will optimize  $R_i$ .

Some loss,  $L_0$ , will occur in the TWM structure due to the usual resistive losses in the conductors. This loss is reduced below the usual room temperature value by a factor of 2 to 4 by operation at liquid helium temperatures. In some cases this insertion loss can be quite high, and care must be exercised in the selection of a circuit. Uniform current distribution and the largest possible surface area in the circuit conductors are desirable.

In discussing TWM circuits, it is useful to rewrite the factor  $fl/v_n$  as the product of the slowing factor,  $S$ , and the number of free space wavelengths in the length of the structure,  $N$ , where

$$S = \frac{c}{v_a}, \quad N = \frac{l}{c/f}. \quad (18)$$

Then the over-all maser forward gain and reverse loss equations are

$$G = 27.3SN \left( -\chi''_{+} F_{+} - \chi''_{i+} \frac{F_{i-}}{R_i} \right) - L_0, \quad (19)$$

$$L = 27.3SN \left( \chi''_{+} \frac{F_{+}}{R_m} + \chi''_{i+} F_{i-} \right) + L_0. \quad (20)$$

For short-circuit stability of the amplifier,  $L$  must exceed  $G$ . In some cases, it may even be desirable to have  $L$  as much as 20 db greater than  $G$ , in order to eliminate any regenerative gain effects due to load changes. It is often convenient to refer to the product  $\chi''_{+} F_{+}$  as the inverse of the magnetic  $Q$  of the maser material. The magnetic  $Q$  will be defined for amplification in the forward direction as a positive number,

$$Q_m = \frac{-1}{\chi''_{+} F_{+}}. \quad (21)$$

Thus, the gain of the maser material only is simply

$$G = 27.3 \frac{SN}{Q_m}. \quad (22)$$

The frequency variation of the TWM gain is given primarily by the term  $g(f - f_0)$  in (12). If a Lorentzian line shape is assumed for the maser material, then

$$g(f - f_0) = \frac{2}{\pi B_m} \frac{1}{1 + \left(2 \frac{f - f_0}{B_m}\right)^2}, \quad (23)$$

where  $B_m$  is the bandwidth over which  $\chi''$  is greater than one half its peak value. If we assume that the permeability is an analytic function, then it follows that, for the Lorentzian line shape,

$$\chi'_+ = -2 \frac{f - f_0}{B_m} \chi''_+. \quad (24)$$

This rapid variation of  $\chi'_+$  in the vicinity of the amplifying region will produce some perturbation in the phase velocity characteristics of the slow-wave structure. However, in a broadband maser slow-wave structure this effect will be negligible. Using the frequency variation of (23), we obtain for the 3-db bandwidth of a traveling-wave maser

$$B = B_m \sqrt{\frac{3}{G_{db} - 3}}. \quad (25)$$

This derivation of bandwidth assumes a Lorentzian line shape. The actual emission line shape of a maser material depends upon a number of factors, and, at the present state of the art, is best determined experimentally.

The bandwidth variation given by (25) is quite different from that predicted for the cavity maser and it is apparent that the gain-bandwidth product increases at high gain, rather than reaching a constant as in the case of the cavity maser (CM).

The bandwidth variation with gain has been plotted in Fig. 1 for a traveling-wave and a cavity maser. The cavity maser was assumed to have a magnetic  $Q$  equal to that of the TWM. For a typical case, we may take 0.05 per cent  $\text{Cr}^{+++}$  in  $\text{Al}_2\text{O}_3$ , for which  $B_m$  is 60 mc for operation at 6 kmc with the magnetic field at  $90^\circ$  to the crystal axis. In this operation, a magnetic  $Q$  of 150 is obtainable at 1.5°K. The gain of a cavity maser has been calculated, taking into account the effect of  $\chi'$

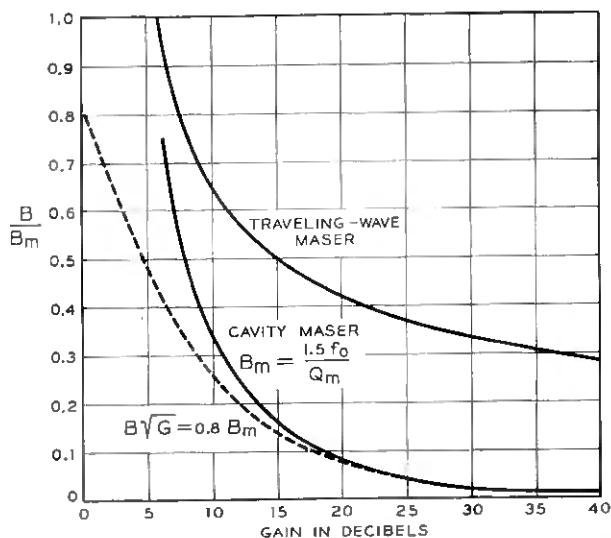


Fig. 1 — Normalized maser bandwidth,  $B/B_m$ , as a function of gain for the cavity maser and the traveling-wave maser.

from (24), as

$$G_{CM}^{1/2} = \frac{(1 - jb_0)(1 + jb_m) - R_0/R_m}{(1 + jb_0)(1 + jb_m) + R_0/R_m}, \quad (26)$$

where

$$b_0 = \left| \frac{R_0}{R_m} \right| \frac{2\Delta f}{f_0} Q_m, \quad (27)$$

$$b_m = 2 \frac{\Delta f}{B_m}, \quad (28)$$

$R_0$  = the effective load impedance of the circulator,

$R_m$  = the effective resistance of the maser material

and

$Q_m$  = the magnetic  $Q$  of the maser material.

In the limit of large gain, the gain-bandwidth product approaches a constant given by (26) as

$$G_{CM}^{1/2} B = \frac{2}{\left( \frac{Q_m}{f_0} + \frac{1}{B_m} \right)}. \quad (29)$$

For the assumed maser operation in ruby,

$$G_{CM}^{1/2} B = 0.8 B_m. \quad (30)$$

The gain-bandwidth curve from (30) is plotted as a dashed line in Fig. 1. It is interesting to note that, for relatively low gains in the cavity maser, the true bandwidth given by (26) is somewhat greater than is estimated from the limiting gain-bandwidth figure of merit.

The required amplifier slowing and length can be determined from (22). Taking the above example for ruby operation at 6 kmc with  $Q_m$  equal to 150 and a structure length of 2 wavelengths (10 cm), we find that a slowing of about 90 is required in the slow-wave structure in order to give a gain of 30 db. An amplifier designed without geometric or resonant slowing, but using the dielectric constant of ruby, would require a length of about 300 cm. The TWM bandwidth for the assumed Lorentzian line shape would be 20 mc. A cavity maser designed using the same material would have a bandwidth of about 1.5 mc. It should also be pointed out that, since a broadband structure is used in the TWM, stagger tuning of the maser material along the maser structure can lead to even greater bandwidths.

The TWM has another important advantage over the cavity maser in that the useful slow-wave structure bandwidth may be an order of magnitude, or more, greater than the maser material bandwidth. Therefore, the center frequency of the maser passband can be tuned electronically over a wide frequency range simply by changing the pump frequency and the dc magnetic field. Thus, a TWM with a 20-mc passband may be tuned over a 200- to 500-mc frequency range at 6 kmc.

An important consideration in maser amplifiers is the sensitivity of the gain to a slight change in the material inversion as measured by  $\chi''$ . We may, therefore, define the ratio of percentage change in gain to the percentage change in  $\chi''$  as a measure of this gain sensitivity,  $s_g$ . The gain sensitivity factors for a cavity maser and a traveling-wave maser are respectively,

$$\text{CM: } s_g = \sqrt{G}, \quad (31)$$

$$\text{TWM: } s_g = \log_e G. \quad (32)$$

These two equations are plotted in Fig. 2. They show that, at a gain of 30 db, the stability of a TWM is better by a factor of 4.6 than that of the cavity maser. Ultimately, gain stability in a maser is obtained by stabilization of the material  $\chi''$  through temperature regulation and regulation of the pump power. It is also advantageous to use sufficient pump power to saturate the pump transition and, hence, make  $\chi''$  rela-

tively insensitive to pump power. These techniques are applicable to both the cavity and the traveling-wave maser, but the stability factor, which is given by  $s_g$ , is always better in the TWM case. Gain stability may be an important factor in system applications as it has been in noise figure measurements, where the gain fluctuations are equivalent to actual system noise.

The gain stability to load changes of a TWM is also much better than that of a cavity maser. This problem is particularly bad in the case of the cavity maser, because of the dependence of the gain upon the iris coupling factor. This leads to gain changes due to thermal expansion and vibration effects.

The power output of a cavity maser, as well as that of a TWM, is limited by the total volume of active maser material present in the structure. In the case of the cavity maser, this volume is quite small, whereas a TWM uses a long interaction region and the volume of material is greater, often by an order of magnitude. As a result, in the case of the TWM a much wider dynamic range is to be expected, with output powers an order of magnitude greater. It is also possible to optimize output power by proper design of the slow-wave structure in order to increase active material volume.

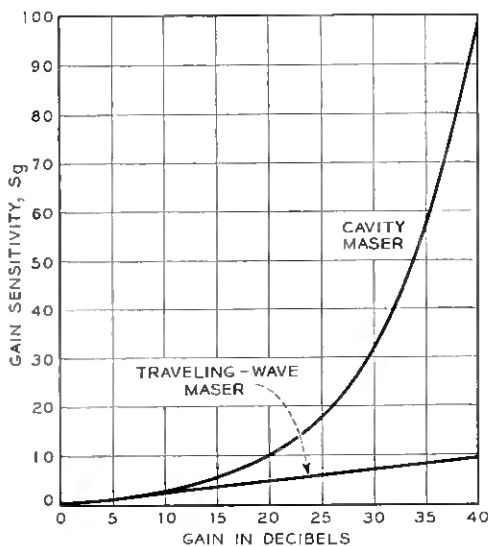


Fig. 2 — Pump saturation gain sensitivity,  $s_g$ , as a function of gain for the cavity maser and the traveling-wave maser.

Just as in the case of the cavity maser, some provision must be made in the propagating structure to allow either a propagating or cavity mode at the pump frequency in order to energize the emissive transition in the material. Finally, ease of fabrication and small size are necessary to the practical realization of the TWM.

### III. SLOW-WAVE MASER STRUCTURES

There are three classes of structures suitable for slowing propagation for use with the TWM. The first class uses geometric slowing, such as one obtains in a helix where the energy is propagated on a long circuitous path. The second class uses resonant slowing, as is obtained in a periodic structure in which the energy is internally reflected in the various periods of the structure. The third class employs dielectric slowing and may be used in combination with either of the first two classes. The simple helix structure has an advantage in that it will produce high slowing over a very wide bandwidth of frequency, whereas periodic structures obtain slowing at the expense of tunable bandwidths. However, the circular polarization present on a helix structure has a plane which rotates around the axis of the helix. As a consequence, one requires a spiraling dc magnetic field in order to have the dc field perpendicular to the circularly polarized RF field.

The flattened helix structure of Fig. 3 is a possible broadband slow-wave structure which does have planar regions of circularly polarized magnetic field. The plane of circular polarization is perpendicular to the flat side of the helix and to the direction of propagation. Changes in the sense of polarization are indicated by the arrows.

The second class of slow-wave structures, the periodic type, has a definite passband with associated upper and lower cutoff frequencies.

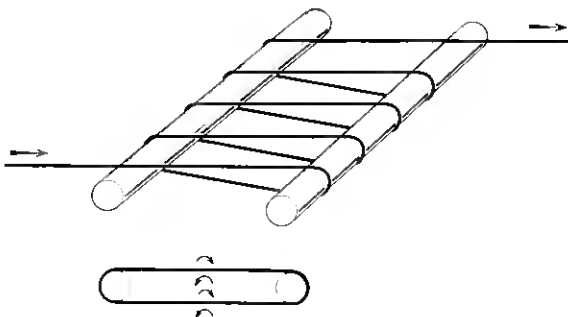


Fig. 3 — Flattened helix structure for broadband nonreciprocal gain.

In general, the narrower the structure passband, the higher is the slowing. It is quite possible to obtain slowing factors of 100 to 1000 in a periodic structure, while 10 to 100 is typical of a helix or other geometrically slowed structure.

It is interesting to note that, while many traveling-wave electron devices require constant phase velocity, the traveling-wave maser requires constant group velocity. As a result, various periodic structures which are very narrowband for tube applications, such as the comb structure, will have wide TWM bandwidths.

Also, it is essential to keep in mind that the structure must propagate at the desired pump frequency. This can be accomplished by propagating the pump power in a waveguide mode and locating the slow-wave structure in the waveguide in such a manner that the two structures are not coupled.

The  $TE_{10}$  mode in rectangular waveguide has an equipotential plane, as indicated by the cross section A-A in Fig. 4(a). Thus a planar arrangement of conductors in this cross section will have a minimum of coupling

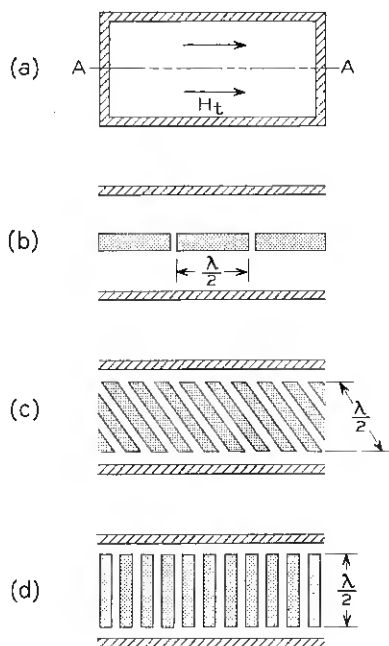


Fig. 4 — (a) The equipotential plane in  $TE_{10}$  waveguide and three parallel plane structures consisting of half-wave strip-line resonators: (b) end-coupled; (c) slant-coupled; (d) side-coupled.

to the waveguide mode. The flattened helix of Fig. 3 could be used in such a waveguide, although some coupling of the two modes would result. Three periodic-type structures consisting of coupled half-wave strip resonators are shown in Figs. 4(b), (c) and (d). The end-coupled arrangement of Fig. 4(b) is least desirable of these structures because the magnetic field is linearly polarized. The structure of Fig. 4(c), suggested by H. Seidel,<sup>8</sup> has mutual magnetic field coupling, which is variable by changing the slant angle. The structures of both Figs. 4(c) and 4(d) have regions of circular polarization of the magnetic field. The plane of circular polarization is perpendicular to the long dimension of the resonators of Fig. 4(d), and the sense of polarization is opposite above and below the plane of the strips.

Another set of slow-wave structures having planar conductors is shown in Fig. 5. Fig. 5(a) consists of an array of half-wave rods shorted to the side walls. Because of its symmetry, it can be shown that there is no component of Poynting's vector,  $E \times H$ , in the direction of the waveguide propagation. Consequently, it is a nonpropagating structure and has been suggested for use in the Easitron.<sup>9</sup> It is interesting because it points out the separate effects of electric and magnetic coupling between adjacent rods. A perturbation of the enclosing waveguide, such

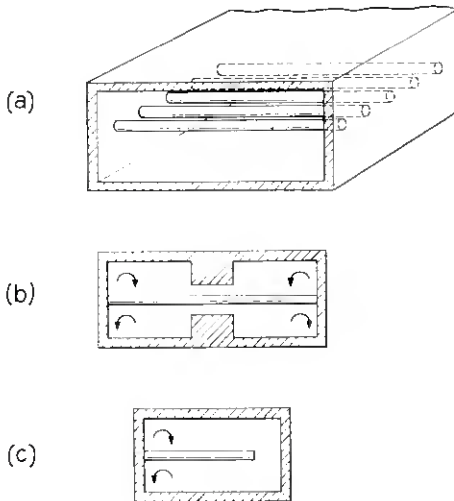


Fig. 5 — Structures consisting of planar arrays of conductors with electrical connection to the waveguide walls; the plane of circular polarization is perpendicular to the fingers and the arrows indicate changes in the sense of polarization: (a) Easitron zero passband structure; (b) Karp propagating structure; (c) comb propagating structure.

as that of the Karp<sup>10</sup> type of structure, in Fig. 5(b), produces a propagating passband in the structure. Thus, the Easitron structure may be called a zero passband structure in which the effect of electric and magnetic coupling between rods just cancels. The general properties of propagating parallel arrays has been discussed by Pierce.<sup>11</sup> Although the structure of Fig. 4(b) is similar to the Easitron, this structure will propagate, due to the fringe capacity at the ends of the resonators. The comb structure of Fig. 5(c) will have characteristics very similar to Fig. 4(d), since it is essentially Fig. 4(d) with a shorting plane along the center line, which is an equipotential plane for the slow-wave structure. A comb-type structure was used by Millman.<sup>12</sup> This structure had rather broad fingers, however, as required for effective electron beam interaction.

A rather extensive study of periodic slow-wave structures is given by Leblond and Mourier.<sup>13, 14</sup> A method for calculating the characteristics of such structures which takes into account coupling between nonadjacent wires was developed by Fletcher<sup>15</sup> and applied to the interdigital line. The interdigital line may be thought of as two comb structures attached to opposite walls of the waveguide with fingers interleaved. The interdigital line does not, in general, produce as much slowing as a comb structure, since, in its passband, the signal wave is propagated at the velocity of light along the circuitous path between adjacent fingers. Thus, the propagation does not depend upon a critical balance of finger to finger coupling and can take place without fringe capacity at the finger tips or a side-wall perturbation. A number of design curves for digital structures have been computed by Walling<sup>16</sup> using the theory of Fletcher. Nonreciprocal attenuation in the interdigital circuit has been analyzed and measured by Haas.<sup>17</sup>

#### IV. THE COMB-TYPE SLOW-WAVE STRUCTURE

As indicated by the arrows in Fig. 5(c), the comb-type slow-wave structure has regions of circularly polarized magnetic field above and below the plane of the fingers. Since the sense of polarization is reversed in the two regions, the structure is particularly suited to the TWM application.<sup>18</sup> The maser material can be placed on one side of the fingers and the isolator material on the opposite side. The magnetic field varies from a maximum at the shorted end of the rod to zero at the end. Since the electric field does just the opposite, it is possible to place a high dielectric material, such as ruby, in a region where effective magnetic interaction is obtained without incurring substantial dielectric loading, which might adversely effect the structure characteristics.

The microwave pump power is propagated through a waveguide enclosing the comb structure, such as in Fig. 6. The  $TE_{10}$  waveguide mode will produce strong longitudinal fields near the waveguide wall and transverse fields in the center of the guide. The dc magnetic field is applied in the direction of the fingers of the structure. Thus, for a maser crystal against the waveguide wall nearest the base of the fingers,  $\Delta S = \pm 1$  pump transitions would be excited, while  $\Delta S = 0$  pump transitions would be most strongly excited for a centrally located crystal. In our operation, both gadolinium ethyl sulfate and ruby maser materials have  $\Delta S = 0$  pump transitions. Thus, it is necessary either to move the crystal away from the waveguide wall slightly, which reduces the gain, or to use a higher pump power, in order to invert the spin population throughout the crystal. The waveguide structure can, of course, be extended beyond the slow-wave structure. A waveguide short and coupling iris can then be used to obtain resonant enhancement of the pumping fields and, hence, better coupling to the pump transition in the crystal.

A perturbation measurement has been made, using a small sphere of ferrimagnetic material to measure the circularly polarized components of the magnetic field in such a comb structure. The absorption of the sphere at ferrimagnetic resonance is a measure of the circularly polarized filling factor per unit volume, which we will call  $F_+^*$ . The result of such a measurement is plotted in Fig. 7. The dashed line in Fig. 7(b), labeled  $F_-^*$ , is obtained either by reversing the direction of propagation through the structure or by reversing the dc magnetic field. The circularly polarized filling factor,  $F_+$ , and the figure of merit,  $R$ , can be obtained by integrating the appropriate curve over the cross section. This one

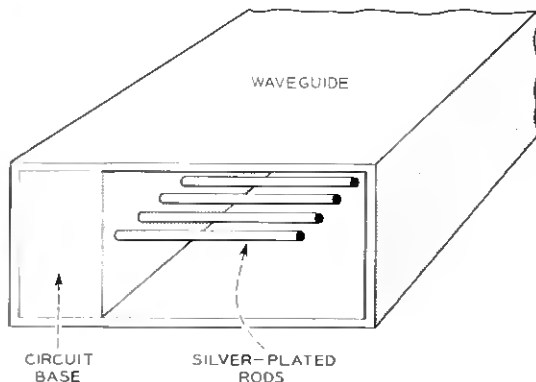


Fig. 6 — The comb-type slow-wave structure.

measurement is not sufficient to get the exact filling factor because the structure is not uniform. The filling factor should be calculated from measurements made over the volume of one period of the structure. The measurement of Fig. 7 predicts a forward-to-reverse gain ratio of about 15 for maser material between one side of the fingers and the wall. In actual tests on gadolinium ethyl sulfate, a value of  $R_m$  of 10 was obtained. Careful placement of ferrimagnetic sphere isolators in the same structure gave a value for  $R_i$  of 30.

The gain and tunable bandwidth of a maser using the comb structure can be computed from the phase-versus-frequency characteristics of the slow-wave structure. A useful equivalent circuit for this calculation is given in Fig. 8(a). The capacity,  $C_1$ , represents the fringe capacity at the ends of the fingers. The transmission line impedances,  $Z_{01}$  and  $Z_{02}$ , can be computed from the TEM characteristic impedance of the finger in waveguide transmission line at the upper and lower cutoff frequencies. When the phase shift between fingers is zero, the electric field pattern,  $Z_{++}$ , is that shown on the left in Fig. 8(b). The electric field pattern at

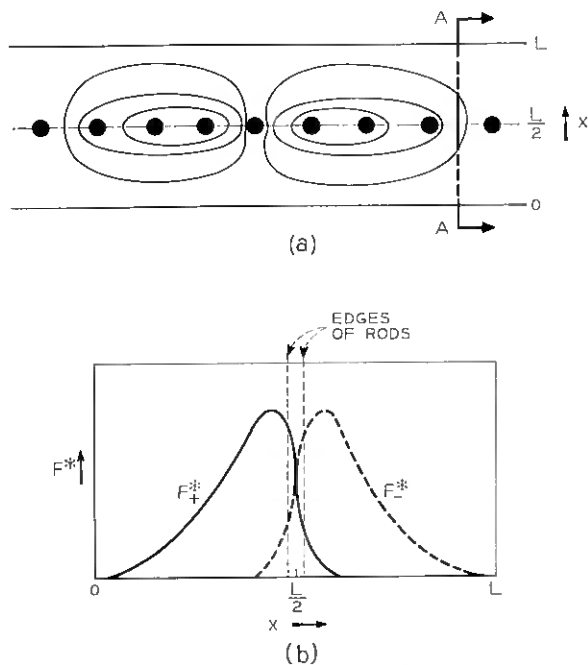


Fig. 7 — The magnetic field pattern (a) and measured amplitudes of circular polarized field components (b) for the comb-type slow-wave structure.

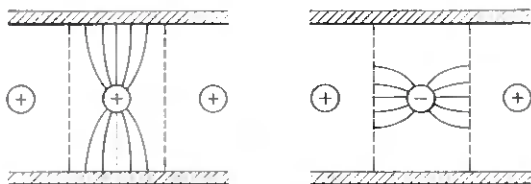
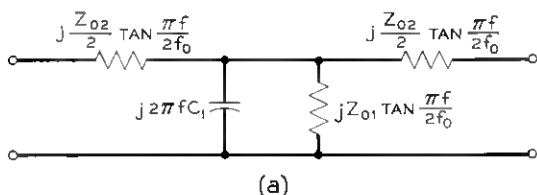


Fig. 8 — (a) Equivalent circuit for the comb structure and (b) the cutoff-frequency TEM mode electric field patterns.

the other cutoff frequency of the structure,  $Z_{+-}$ , is that corresponding to  $\pi$  phase shift, indicated on the right in Fig. 8(b). The impedances  $Z_{++}$  and  $Z_{+-}$  can be obtained analytically or by means of the usual electrolytic tank or resistance card analog computers. These cutoff impedances are related to those in the equivalent circuit by

$$Z_{01} = Z_{++}, \tag{33}$$

$$Z_{02} = \frac{4Z_{+-}}{1 - \frac{Z_{+-}}{Z_{++}}}. \tag{34}$$

The determinantal equation for the circuit of Fig. 8(a) is

$$j2\pi f C_1 + \left( \frac{1}{Z_{01}} + \frac{2}{Z_{02}} \sin^2 \varphi/2 \right) \tan \frac{\pi f}{2f_0} = 0, \tag{35}$$

where  $\varphi$  is the phase shift per section and  $f_0$  is the frequency at which the circuit fingers have an electrical length of one-quarter wavelength. Solution of this transcendental equation is simplified by use of the curve in Fig. 9. The abscissa is the signal frequency normalized to  $f_0$ . The ordinate is  $X_{co}Y(\varphi)$ , which is given by

$$X_{co} = \frac{1}{2\pi f_0 C_1}, \tag{36}$$

$$Y(\varphi) = \frac{1}{Z_{01}} + \frac{4}{Z_{02}} \sin^2 \varphi/2. \tag{37}$$

The signal frequency for a certain phase shift is obtained by computing  $X_{co}Y(\varphi)$ , and then referring to Fig. 9.

The product  $SN$  required in the gain calculation can be obtained from experimental measurement of  $\varphi$  versus frequency from the equation

$$SN = N_s \frac{f_0}{2\pi} \frac{d\varphi}{df}, \quad (38)$$

where  $N_s$  is the total number of sections in the structure. For the equivalent circuit of Fig. 8(a), the  $SN$  product can be obtained from the curve of Fig. 10, which gives the quantity  $s$ , defined by

$$s \equiv \frac{SNX_{co}}{N_s Z_{02}} \sin \varphi. \quad (39)$$

Experimentally measured values of  $\varphi$  versus  $f$  were compared with the values calculated from the equivalent circuit, for a comb structure in which the end capacity,  $C_1$ , could be varied. The resulting calculations are shown in Fig. 11.

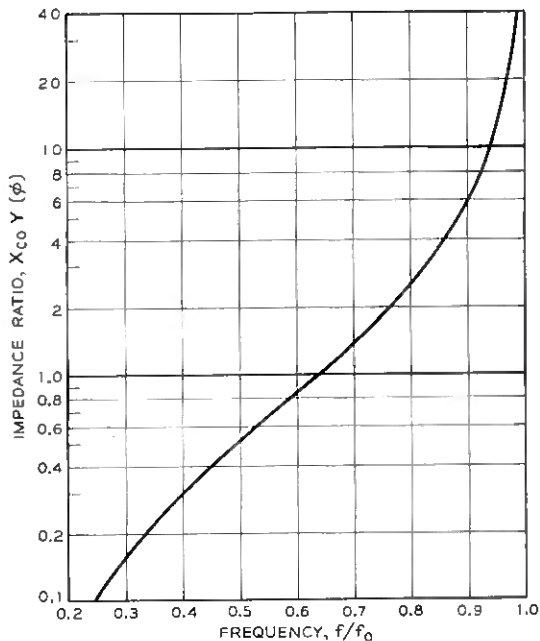


Fig. 9 — The curve,  $X_{co}Y(\varphi)$  vs.  $f$ , used to solve equation (35).

The three curves were computed from the equivalent circuit analysis using the measured values of  $Z_{++}$  and  $Z_{+-}$ . The fringe capacity was determined by using the measured frequency for  $0.2\pi$  phase shift. It should be mentioned that the equivalent circuit does not fully take into account the effect of coupling between nonadjacent fingers, an effect which may be important in this particular circuit.

A rather wide passband was obtained with the particular choice of parameters, even with rather large spacing between the finger ends and the opposite waveguide wall. Also, because of the wide bandwidth, the slowing varies over a wide range. The increase in slowing at the high-frequency end of the band is partially compensated for by the reduction

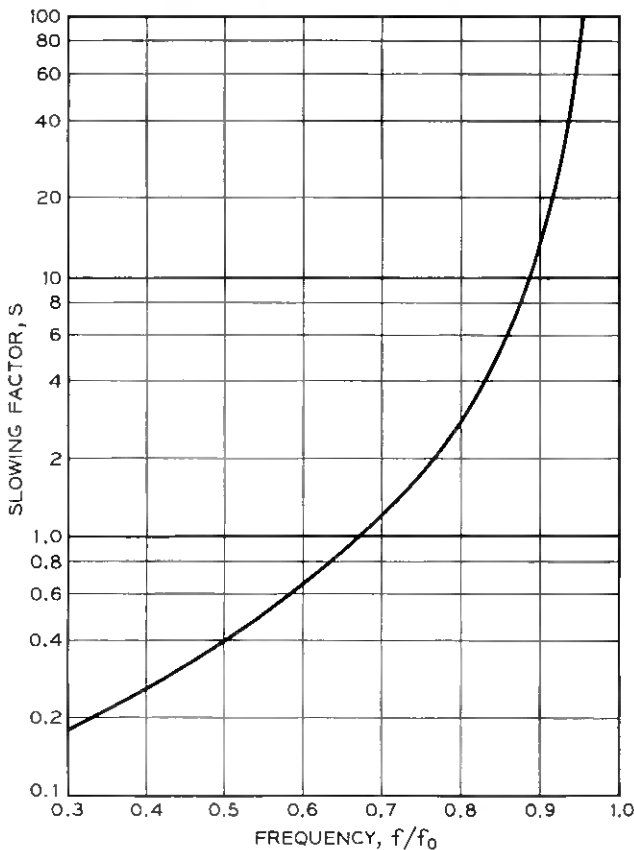


Fig. 10 — The slowing factor,  $s$ , as a function of frequency, used to determine  $SN$  from (39).

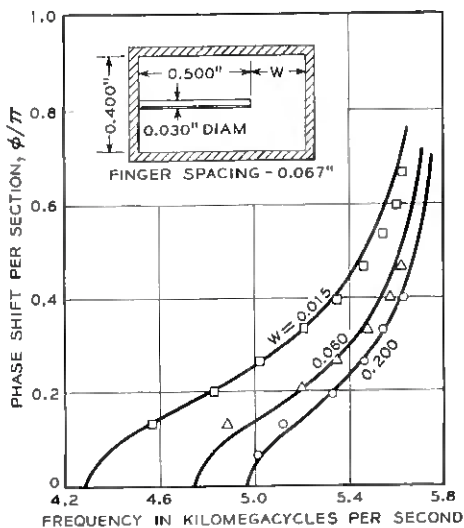


Fig. 11 — Phase shift per section,  $\phi$ , vs. frequency, showing the effect of end wall capacity upon slowing.

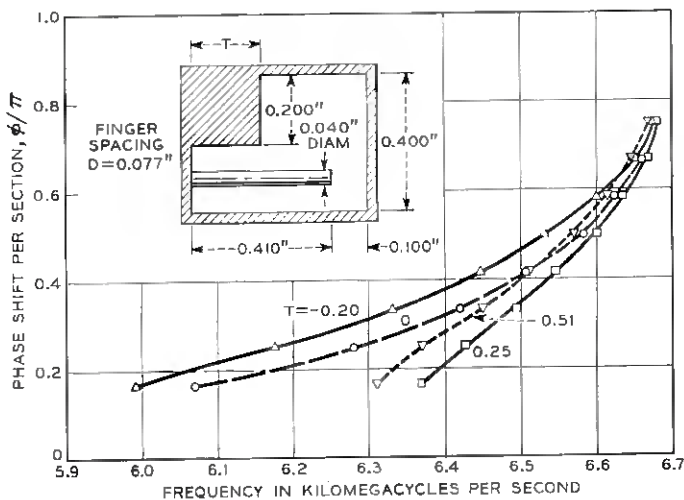


Fig. 12 — Phase shift per section,  $\phi$ , vs. frequency showing the effect of a side wall perturbation upon slowing.

in the filling factor due to an increase in the stored energy between the fingers.

The structure passband can be decreased by reducing the waveguide height and increasing the distance between fingers. Too great a reduction in waveguide height will make the comb fingers a rather serious perturbation of the waveguide pump mode and will degrade the maser gain nonreciprocity factor,  $R_m$ . On the other hand, increasing the distance between fingers increases the over-all length of the amplifier.

Several methods for reducing the bandwidth of the comb structure have been tried. The first consisted of building a structure in which a wall perturbation could be moved across the width of the structure. The cross section of this test structure is shown in Fig. 12, along with the measured results obtained. The curve for  $T = -0.2$  inch is for the case where the sliding side wall perturbation is pulled back from the base of the fingers. In this case, the bandwidth is increased. However, with  $T = 0.25$  the bandwidth is reduced by a factor of 2 and relatively constant slowing is obtained over the band.

A second method for reducing the bandwidth is that shown in Fig. 13. The tips of the structure fingers are dielectrically loaded with a polystyrene strip having holes for the fingers. The dielectric increases the finger-to-finger capacity without greatly increasing the finger-to-wall capacity. Thus, this capacity would be in shunt with  $Z_{02}$  in the equivalent circuit of Fig. 8. It is apparent from the results in Fig. 13 that very narrow bandwidths can be obtained in this manner. However, the varia-

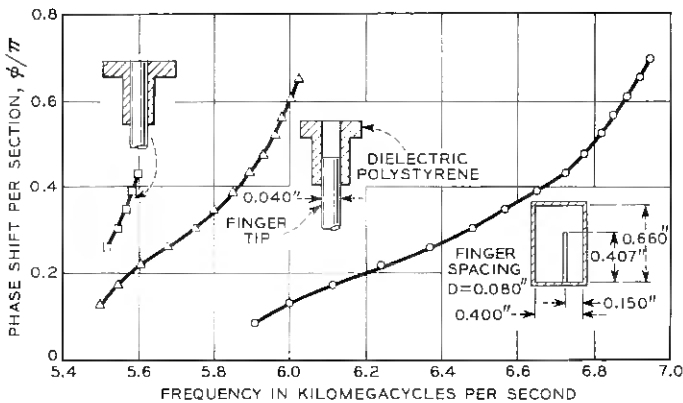


Fig. 13 — Phase shift per section,  $\phi$ , vs. frequency, showing the effect of finger-to-finger capacity upon the slowing.

tions in structure dimensions become rather critical. Thus only a few points on the  $\varphi$ - $f$  curve could be obtained using the structure resonance. This was also due in part to the high losses resulting from the high slowing.

The full-length ruby maser employed a slow-wave structure whose  $\varphi$ - $f$  characteristics are shown in Fig. 14. Notice that the unloaded structure has a wider passband than the final amplifier with dielectric loading of the ruby on both sides of the structure. In this case, the slowing was improved by not loading the ruby to the full height of each side of the waveguide. Thus, in this case, bandwidth narrowing is obtained by selective location of the maser material itself.

A number of different coupling schemes have been employed to match a 50-ohm coaxial cable into the comb structure. The matching arrangement shown in Fig. 15 gives quite broadband results. It has been found that a good impedance match can be obtained only over that frequency range for which the slowing factor is relatively constant. A VSWR less than 1.5 is typical over the useful band of the structure. Rapid variation of measured VSWR is observed which can be attributed to periodic variations in the structure which result in internal resonances. In actual maser operation, these internal resonances should be suppressed by the nonreciprocity of the structure.

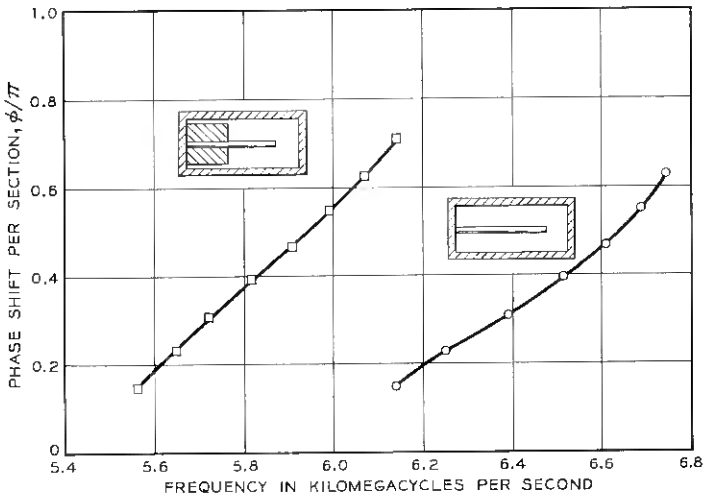


Fig. 14 -- Phase shift per section,  $\varphi$ , vs. frequency for the comb structure used in the full-length ruby maser; the unloaded structure characteristic is compared with that of the ruby loaded structure.

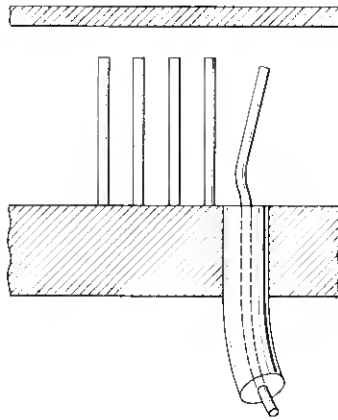


Fig. 15 — Detail of the coaxial-to-comb-structure impedance match.

#### V. GADOLINIUM MASER TEST SECTION RESULTS

The first TWM tests were performed using gadolinium ethyl sulfate as the active maser material and yttrium iron garnet as the isolator material. The cross section of this TWM is shown in Fig. 16. The slow-wave structure was similar to that of Fig. 12, since it employed a perturbation of the side wall to narrow the passband. Of course, the maser material dielectric constant also affected the structure characteristics and a certain optimum loading could be obtained.

Since the maser operation in gadolinium requires the pump magnetic field to be parallel to the applied magnetic field, a slab of dielectric was added against the waveguide wall to enhance the transverse RF waveguide magnetic field.

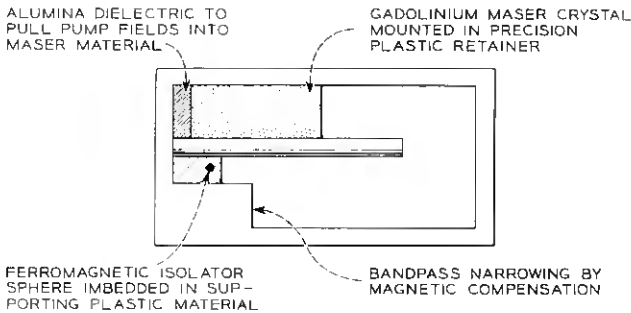


Fig. 16 — Cross section of gadolinium maser, showing location of active material and polycrystalline yttrium iron garnet isolators.

The "impurity dope" maser action in cerium-doped gadolinium ethyl sulfate produced at 1.6°K a magnetic  $Q_m$  of 170 in the structure used. The signal frequency was 6.0 to 6.3 kmc, and the pump frequency was 11.7 to 12.3 kmc. The magnetic field was about 1800 gauss. The non-reciprocity factor,  $R_m$ , was measured as about 10. The maser gain obtained was 12 db with about 1 inch of the slow-wave structure filled with the gadolinium salt. The active material consisted of three separate crystals which had to be accurately cut and aligned. Thus, it became apparent that the physical properties of the gadolinium salt were not too well suited for more than laboratory tests. The gadolinium bandwidth,  $B_m$ , was 30 mc.

It should be mentioned, however, that the maser operation in gadolinium does have the advantage of high saturation power and fast saturation recovery time. A power output of +15 dbm was obtained and the saturation recovery time was measured as about 20 microseconds.

The magnetic field required by the maser material is in the vicinity of that for ferrimagnetic resonance in a sphere. Hence, it was possible to use spheres of a gallium-substituted yttrium iron garnet, which was found to have a relatively high  $\chi''$  at liquid helium temperature. Spheres of yttrium iron garnet were located in the A-A cross section indicated in Fig. 7(a). By careful location of the spheres, approximately one per finger, an isolation ratio of 50 was obtained at room temperature. The isolation ratio at 1.5°K was 30.

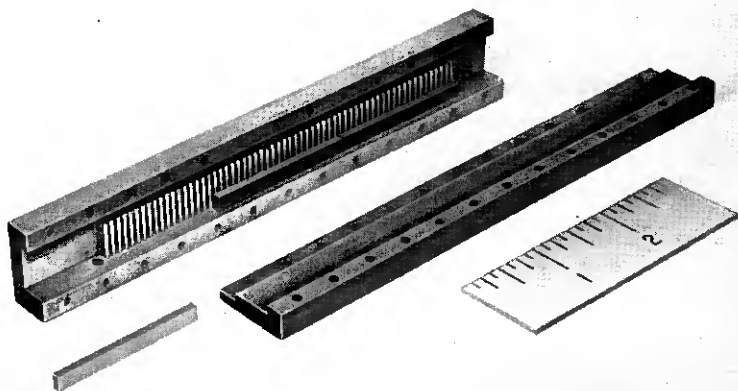


Fig. 17 — View of the disassembled comb structure for the ruby maser, with two pieces of ruby material shown in position.

## VI. RUBY TRAVELING-WAVE MASER PERFORMANCE

The first high-gain full-length TWM was constructed using pink ruby which had approximately 0.05 per cent  $\text{Cr}^{+++}$  in the  $\text{Al}_2\text{O}_3$  parent crystal. The slow-wave structure is shown in Fig. 17 with one side of the waveguide removed. Two pieces of ruby are shown in position, and a third is in the foreground. The comb structure has a length of 5 inches and consists of 62 brass rods approximately 0.4 inch long. The phase-shift characteristics of this structure were given in Fig. 14.

The holes for insertion of the coaxial input and output matches are visible at the ends of comb structure of Fig. 17. Fig. 18 is a cutaway drawing of the complete TWM assembly, showing the waveguide flanges which are added to the ends of the structure for attachment of a movable short and the pump waveguide coupling iris. This drawing also shows the location of the 0.05 per cent ruby amplifying material and the 1 per cent ruby isolator material. Notice that the 1 per cent ruby is spaced away from the circuit fingers by an alumina slab. This reduces the

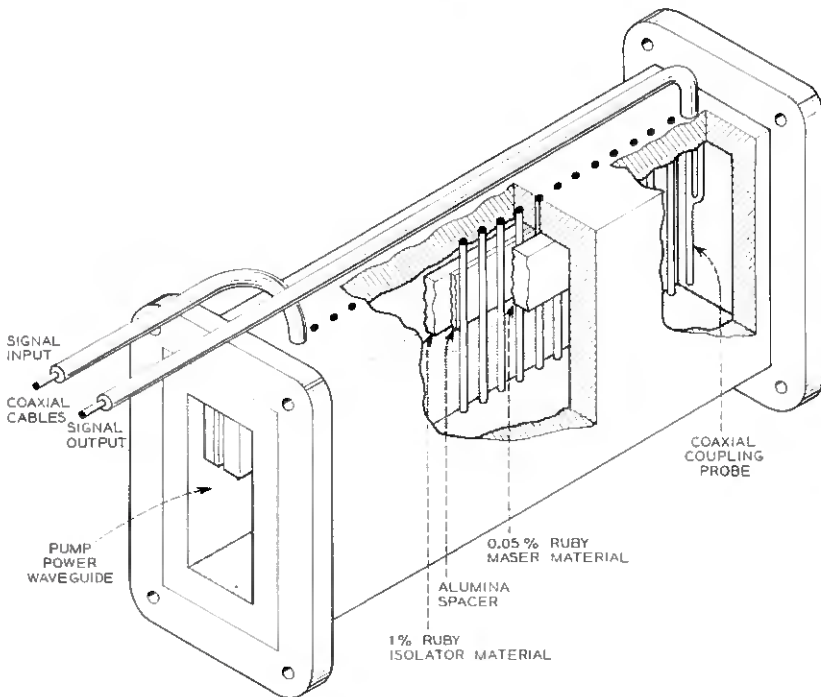


Fig. 18 — Cutaway view of full-length ruby maser assembly.

coupling of the isolator to the forward propagating circuit wave, thus improving the isolation ratio,  $R_i$ .

This TWM gives a net forward gain of 23 db and a net reverse loss of 29 db, including the input and output coaxial cables extending into the 1.5°K helium bath. With the dc magnetic field off, the structure gave a loss,  $L_0$ , of 3 db. The electronic gain of the maser material, the first term in (19), was 30 db, and the loss of the isolator was 35 db. Thus, the ratios  $R_m$  and  $R_i$  are about 3.5 and 8.5 respectively. The improved figure of merit for the isolator is due to the addition of the alumina slab. The high loss of the isolator, in spite of the spacer, is due to the increased Cr concentration.

The 3-db bandwidth of the TWM was measured as 25 mc at a center frequency of 5.8 kmc. This bandwidth is somewhat in excess of that predicted by an assumption of Lorentzian line shape as used in Fig. 1. The passband of the structure allows amplification over a frequency range of 5.75 to 6.1 kmc. The pump frequency must be tuned from 18.9 to 19.5 kmc and the dc magnetic field varied from 3.93 to 4.07 kilogauss to cover this electronic tuning range.

At a power output of -22 dbm, the gain of the amplifier is reduced by 0.5 db. The recovery time of the amplifier after saturation by a large signal is quite long, being on the order of  $10^{-1}$  sec. This is due to the long relaxation time in ruby. It has one compensation, however, in that spin storage is very effective for increasing the pulse saturation power. Thus, with a pulse length of 10 microseconds and a pulse repetition rate of 100 per second, a pulse power output of +8 dbm was measured for the same 0.5-db reduction in gain. The saturation characteristic of a TWM is not abrupt, but is a smooth curve going to lower gain as the power is increased. In the limit of very high power, the TWM is essentially transparent. It will have an insertion loss of about 3 db, since after the maser material saturates, it produces neither gain nor loss.

The pump source had a power output of 100 mw. Recent experiments have been performed which show that satisfactory operation of the ruby TWM can be obtained with no waveguide iris and a short at the end of the amplifier. In this type of operation the pump power absorbed by the amplifier was less than 10 mw. The pump power absorbed by the amplifier determines the refrigeration power input required in a continuously cooled system. Thus a factor-of-10 reduction in maser pump power has a substantial effect upon the size of refrigerator required.

As was mentioned previously, it should be possible to obtain greater bandwidths in a TWM by stagger-tuning of the maser material. This was verified in this amplifier by rotating the maser magnet, which re-

sulted in tuning of the three maser crystals to different frequencies. A bandwidth of 67 mc at a gain of 13 db was measured.

#### VII. TWM NOISE-TEMPERATURE MEASUREMENT

Because of the high gain stability inherent in the TWM it was possible to perform a quite accurate measurement of noise temperature. Also, since the TWM is a unilateral two-port amplifier by itself, no external isolators or circulators are required when it is used, for instance, as a radar preamplifier.

The experimental system for the noise-temperature measurement is shown in Fig. 19. Two noise sources, which are matched loads maintained at different temperatures, are connected alternatively to the TWM input with an electrically operated waveguide switch. Isolators were included at the input and output of the TWM. Although the TWM is short-circuit stable, small gain fluctuations can be produced by changes in the input VSWR. Since gain fluctuations on the order of 0.02 db are significant in this measurement, an input isolator was included to eliminate gain changes when the waveguide switch is operated. An isolator was included on the output of the TWM to insure that no excess noise from the traveling-wave tube (TWT) would be fed back into the TWM

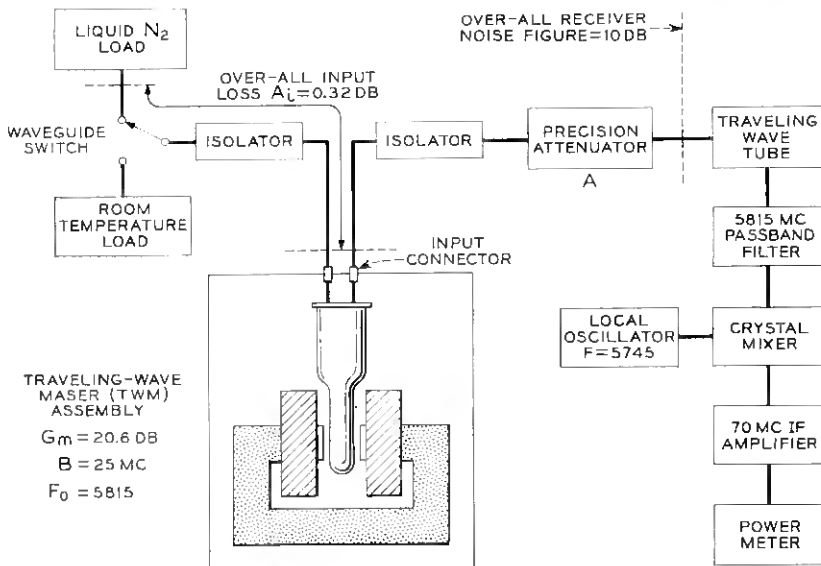


Fig. 19 — Experimental system for TWM noise temperature measurement.

and prevent maser gain changes because of the precision attenuator setting.

The microwave detecting system consisting of the TWT, filter, crystal mixer, etc., had an over-all noise figure of 10 db. The actual noise temperature measurement is made by switching the noise source and adjusting the precision attenuator to maintain constant output power at the power meter.

A total of 37 separate measurements were made over a period of about 30 minutes, and the resulting noise temperature was calculated to be

$$T_m = 10.7 \pm 2.3^\circ\text{K}.$$

Approximately two-thirds of the estimated error was a statistical variation in the observed attenuator reading. About half of this attenuator reading variation can be attributed to gain fluctuations in the system of about  $\pm 0.03$  db during any one measurement and the other half to observational error. The remaining error is principally due to an error of  $\pm 0.02$  db in the determination of the input circuit loss,  $A_i$ .

Since the above-measured noise temperature is referred to an input connector at room temperature, it is a useful system temperature and the noise figure of the resulting preamplifier TWM is

$$F = 1.037 \pm 0.008 (0.16 \pm 0.03 \text{ db}).$$

The TWM employs half-inch diameter 50-ohm coaxial input and output leads of low heat conductivity monel to reduce heat loss from the liquid helium bath which was maintained at a temperature of  $1.6^\circ\text{K}$ . The coaxial cables were silver plated and polished to reduce microwave losses. The input cable, 30 inches long, had a room temperature loss of  $0.28 \pm 0.02$  db. The actual input cable temperature gradient was monitored with 12 thermometers throughout its length. A calculation, using this data and taking into account the known variation of the resistivity of silver with temperature, shows that a noise temperature of  $9 \pm 1^\circ\text{K}$  is produced by the input cable losses.

Another possible type of noise is that fed back into the TWM output from the isolator at room temperature. In the TWM, this produces a negligible contribution at the input because of the reverse isolation.

The noise contributed by the maser proper depends upon the spin temperature and the ratio of spin system gain to the circuit loss. A theoretical noise temperature of  $2.4 \pm 0.2^\circ\text{K}$  is thus calculated from maser noise theory.<sup>19,20,21</sup>

The theoretically calculated over-all TWM noise temperature is then

$$T_m(\text{theory}) = 11.4 \pm 1.2^\circ\text{K}.$$

Since it is apparent that most of the above noise is contributed by the input cable, a second experiment is planned which will exclude the input cable loss and allow a more direct measurement of the actual noise temperature of the maser amplifier proper.

#### VIII. FUTURE STUDIES

An extensive investigation of the ferrimagnetic properties of various ferrite and garnet materials at liquid helium temperatures is being carried out by F. W. Ostermayer of Bell Telephone Laboratories. A number of materials look promising for application as isolators in the ruby TWM. A ferrimagnetic isolator can be expected to have lower forward loss, higher reverse isolation, and low pump-power absorption.

Further reduction of the TWM tunable bandwidth will increase the gain. Thus it should be possible to obtain useful wideband gain at a somewhat higher bath temperature, such as 4.2°K.

It appears that, by using high pump-frequency-to-signal-frequency ratios, it will be possible to build low-frequency traveling-wave masers with about the same percentage tunable bandwidth as the present 6 kmc amplifier. Accordingly, a number of suitable circuits are being investigated.

#### IX. ACKNOWLEDGMENT

The initial slow-wave structure investigation for TWM application was begun by H. Seidel, whose assistance is gratefully acknowledged. We would also like to thank A. Pohly for technical assistance and G. Shimp for computation and plotting of curves.

#### REFERENCES

1. Bloembergen, N., Proposal for a New-Type Solid State Maser, *Phys. Rev.*, **104**, October 1956, p. 324.
2. Scovil, H. E. D., Feher, G. and Seidel, H., Operation of a Solid State Maser, *Phys. Rev.*, **105**, January 1957, p. 762.
3. Scovil, H. E. D., The Three-Level Solid State Maser, *Trans. I.R.E.*, **MTT-6**, January 1958, p. 29.
4. McWhorter, A. L. and Meyer, J. W., Solid State Maser Amplifier, *Phys. Rev.*, **109**, January 15, 1958, p. 312.
5. Makhov, G., Kikuchi, C., Lambe, J. and Terhune, R. W., Maser Action in Ruby, *Phys. Rev.*, **109**, February 15, 1958, p. 1399.
6. Schulz-DuBois, E. O., Paramagnetic Spectra of Substituted Sapphires—Part I: Ruby, *B.S.T.J.*, **38**, January 1959, p. 271.
7. Schulz-DuBois, E. O., Scovil, H. E. D. and DeGrasse, R. W., this issue, p. 335.
8. Seidel, H., private communication.
9. Walker, L. R., unpublished manuscript.

10. Karp, A., Traveling-Wave Tube Experiments at Millimeter Wavelengths with a New, Easily Built Space Harmonic Circuit, Proc. I.R.E., **43**, January 1955, p. 41.
11. Pierce, J. R., Propagation in Linear Arrays of Parallel Wires, Trans. I.R.E., **ED-2**, January 1955.
12. Millman, S., A Spatial Harmonic Amplifier for 6-mm Wavelength, Proc. I.R.E., **39**, September 1951, p. 1035.
13. Leblond and Mourier, Etude des Lignes a Barraux a Structure Périodique pour Tubes Electroniques U.H.F., Ann. de Radioélect. **9**, April 1954, p. 180.
14. Leblond and Mourier, Etude des Lignes a Barraux a Structure Périodique—Deuxieme Partie, Ann. de Radioélect., **9**, October 1954, p. 311.
15. Fletcher, R. C., A Broadband Interdigital Circuit for Use in Traveling-Wave-Type Amplifiers, Proc. I.R.E., **40**, August 1952, p. 951.
16. Walling, J. C., Interdigital and Other Slow-Wave Structures, J. Elect. and Cont., **3**, September 1957, p. 239.
17. Haas, L. K. S., Unilateral Attenuation in the Interdigital Circuit, WADC TR 57-239, Wright-Patterson Air Force Base, Ohio, May 1957.
18. DeGrasse, R. W., Slow-Wave Structures for Unilateral Solid State Maser Amplifiers, I.R.E., WESCON Conv. Record, August 1958.
19. Shimoda, K., Takahasi, H. and Townes, C. H., J. Phys. Soc. Japan, **12**, 1957, p. 686.
20. Pound, R. V., Ann. Phys., **1**, 1957, p. 24.
21. Strandberg, M. W. P., Inherent Noise of Quantum-Mechanical Amplifiers, Phys. Rev., **106**, May 15, 1957, p. 617.

# Use of Active Material in Three-Level Solid State Masers\*

By E. O. SCHULZ-DuBOIS, H. E. D. SCOVIL,  
and R. W. DeGRASSE

(Manuscript received January 2, 1959)

*The three-level excitation method for solid state masers, including some background material on paramagnetic resonance, is reviewed. With respect to the experimental application of the maser material, two cases can be distinguished. In the first, maser action is based mainly on a favorable relaxation time ratio in signal and idler transitions. It is shown that the relaxation time ratio can be changed artificially by a doping technique. Experimental evidence is presented for two such doping techniques, one self-doping, the other impurity doping. In the second case, maser action is based primarily on a favorable frequency ratio of signal and idler transitions. Maser experiments using this approach are described. In addition, excitation of unidirectional gain and attenuation by circular polarization is discussed. Properties of practical isolator materials are surveyed; they include high-concentration paramagnetic and polycrystalline ferrimagnetic materials.*

## I. INTRODUCTION

In 1956, Bloembergen<sup>1</sup> proposed a three-level excitation scheme for obtaining microwave amplification by stimulated emission of radiation in paramagnetic solids, or three-level solid state maser (3LSSM) for short. It is superior to many other microwave amplifiers in that its noise contribution to an amplified signal should be virtually negligible compared to other noise sources in a system. The principal advantage of a solid state maser over a gaseous maser is that the amplified bandwidth should be of the order of megacycles, a magnitude sufficient for many communication applications. In contrast to the two-level solid state masers, its gain factor should be constant in time.

\* This work was supported in part by the U. S. Army Signal Corps under Contract DA-36-039 sc-73224.

Experimental work has confirmed the theoretical predictions. It has been shown that microwave energy can be extracted from paramagnetics by stimulated emission.<sup>2,3,4</sup> If the circuit employed consists of a microwave resonant cavity, the energy extracted can be used to maintain either oscillations or amplification depending on the choice of the coupling parameter. Three paramagnetic salts have been used as active materials. These are gadolinium ethyl sulfate,<sup>2</sup> potassium chromicyanide<sup>3</sup> and ruby.<sup>4</sup> Gain and bandwidth obtained are in agreement with theoretical expectations. Noise measurements have indicated that maser noise is of the magnitude expected.

More recently, traveling wave masers (TWM) have been developed, as described in the accompanying paper.<sup>5</sup> A TWM is a transmission device which can be designed to be nonreciprocal. That is, power traveling from the input to the output is amplified while power traveling the opposite direction is attenuated. A nonreciprocal TWM offers several advantages over a cavity-type maser. Among these are greater gain stability, larger instantaneous bandwidth and the possibility of electronic tuning over a wider frequency range. Gain stability is of great practical importance because in many applications, gain fluctuations deteriorate the system's performance in the same way as noise.

In this paper, the active materials aspect of 3LSSM is treated. Viewpoints are presented on how a given paramagnetic spectrum can be used efficiently in maser applications. Two typical modes of operation are described for active maser materials. Properties of both are evaluated and illustrated by experimental results obtained with gadolinium ethyl sulfate and ruby. Also, those material aspects are discussed which are relevant to nonreciprocal behavior.

## II. PARAMAGNETIC RESONANCE IN CRYSTALS

Consider a dilute concentration of paramagnetic ions placed in a diamagnetic host crystal. Obeying quantum laws, each ion can exist in one of several energy states. The number of such states is  $2S + 1$ , where  $S$  is the effective spin associated with the ion. The energy of any state stems from two contributions. One is Zeeman energy, that is, magnetostatic interaction of an applied magnetic field with the magnetic moment of unpaired electrons within the paramagnetic ion. The other is electrostatic in nature and leads to "zero field splitting", that is, separation of energy levels in the absence of an external magnetic field. This latter interaction takes place between the electrostatic field due to neighbors of the ion considered and the electronic charge present in the orbital states of the ion. It is apparent that this zero field energy will reflect

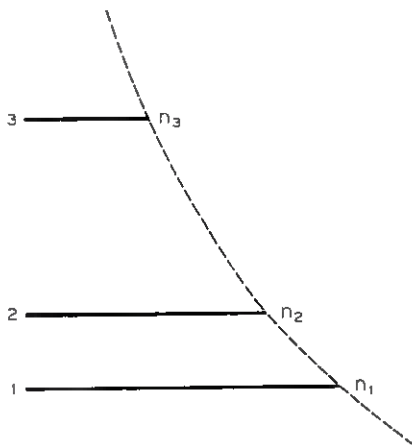


Fig. 1 — Three-level system in thermal equilibrium.

the geometry of the ion environment. As a rule, energy levels are about equally spaced if the magnetic energy outweighs the zero field energy. The spacing is rather unequal in the other extreme.

Fig. 1 shows a three-level scheme which may be part of a scheme of more levels. It is assumed that all three transitions between these are reasonably probable. This can be ascertained by calculations or, preferably, by direct observation of the transitions. A transition from  $E_i$  to  $E_j$  is excited by radiation of frequency  $\nu_{ij} = (E_i - E_j)/h$ , where  $h$  is Planck's constant. Experimentally, absorption of power at this frequency is observed.

If the ions are in thermal equilibrium with the crystal lattice, the average numbers of ions found in each state are related by Boltzmann's distribution law

$$n_i/n_j = e^{-(E_i - E_j)/kT_0}. \quad (1)$$

Here  $k$  is Boltzmann's constant and  $T_0$  the absolute temperature of the lattice. This distribution is indicated in Fig. 1, where the length of each line representing an energy level is made proportional to its population. The thermal contact between ions and lattice occurs through relaxation processes which, to some degree, may be described by a relaxation time  $\tau_{ij}$ . This time may be visualized as the average time of ions in state  $i$  before relaxing to state  $j$ . In thermal equilibrium, as many ions must go from  $i$  to  $j$  as go in the opposite direction. With the help of (1), we thus find

$$\tau_{ij}/\tau_{ji} = n_i/n_j = e^{-(E_i - E_j)/kT_0}. \quad (2)$$

This equation indicates that the relaxation time is shorter for ions in a higher state. For present purposes, this result as based on Boltzmann theory may be sufficient. It might be mentioned, however, that, following Einstein, the situation of (2) can be described by the concept of spontaneous transitions.<sup>6</sup> These occur only in the downward direction and thereby enhance this relaxation rate. In still another, more modern treatment,<sup>7</sup> the inequality of the two relaxation times in (2) follows directly by taking into account the quantum nature of lattice vibrations or radiation field.

With transitions excited by radiation of frequency  $\nu_{ij}$ , the rate of transitions is described by the transition probability  $w_{ij}$ . The transition probability due to applied radiation is the same for upward and downward transitions,  $w_{ij} = w_{ji}$ . The energy absorbed from the exciting field is one quantum  $h\nu_{ij}$  per transition. The power absorbed per unit volume is therefore

$$P_{ij} = h\nu_{ij}w_{ij}(\rho_j - \rho_i). \quad (3)$$

Here  $i$  denotes the higher state and  $\rho$  denotes the density of ions in each particular state. Power is emitted rather than absorbed if the densities are "inverted,"  $\rho_i > \rho_j$ .

The transition probability can be written<sup>8</sup>

$$w_{ij} = \frac{1}{4} \left( \frac{2\pi}{\hbar} \right)^2 g(\nu - \nu_{ij}) |\mathbf{H}_{rf}^* \cdot \mathbf{u}_{ij}|^2. \quad (4)$$

Here  $g(\nu - \nu_{ij})$  is a normalized function describing the line shape as a function of frequency,  $\int g(\nu - \nu_{ij}) d\nu = 1$ ; the line is centered at  $\nu_{ij}$ .  $\mathbf{H}_{rf}$  is the exciting rf magnetic field and  $\mathbf{u}_{ij}$  is the magnetic dipole moment associated with the transition from state  $i$  to  $j$ . Bold face symbols are used to indicate vector (and tensor) quantities. The asterisk (\*) denotes the conjugate complex, that is, a quantity having the opposite time dependence. Using Dirac's bracket notation, this dipole moment is defined quantum-theoretically by

$$\mathbf{u}_{ij} = g\beta \langle j | \mathbf{S} | i \rangle = \mathbf{u}_{ji}^*. \quad (5)$$

Here  $g$  is the spectroscopic splitting factor, a number usually close to 2,  $\beta$  is the Bohr electronic magneton,  $\mathbf{S}$  is the vector spin operator whose components are  $S_x$ ,  $S_y$  and  $S_z$ . It should be pointed out that both  $\mathbf{H}_{rf}$  and  $\mathbf{u}_{ij}$  are varying in time like  $\exp(i\omega_{ij}t)$ . This implies the possibility of phase differences between the components of  $\mathbf{u}_{ij}$  or the components of  $\mathbf{H}_{rf}$ . An important example is that of circular polarization. With respect to some reference system,  $\mathbf{u}_{ij}$  has components  $\mu_x$  and  $\mu_y$  equal in am-

plitude but  $90^\circ$  out of phase. Such a transition is excited by the corresponding circularly polarized RF magnetic field, but not by circular polarization of the opposite sense. This property can be used to give nonreciprocal gain and attenuation in the same way as the gyromagnetic behavior of ferrites is utilized in unidirectional passive devices.

Since  $w_{ij}$  is proportional to the incident power, the absorption can be described, on a macroscopic scale, by the imaginary part  $\chi''$  of susceptibility, where  $\chi''$  is independent of power at low power levels. It is a tensor defined by

$$P_{ij} = \frac{1}{2}\omega_{ij}\mu_0\mathbf{H}_{rf}^* \cdot \chi''_{ij} \cdot \mathbf{H}_{rf}. \quad (6)$$

By comparison with (3) and (4) we find

$$\mathbf{H}_{rf}^* \cdot \chi''_{ij} \cdot \mathbf{H}_{rf} = \frac{\pi}{\mu_0 h} g(\nu - \nu_{ij})(\rho_j - \rho_i)\mathbf{H}_{rf}^* \cdot \mathbf{u}_{ij}\mathbf{u}_{ij}^* \cdot \mathbf{H}_{rf}. \quad (7)$$

This representation shows the tensor character of  $\chi''_{ij}$ . The properties of the tensor with respect to polarization of  $\mathbf{H}_{rf}$  in space and phase are described by the dyadic product  $\mathbf{u}_{ij}\mathbf{u}_{ij}^*$ . This also shows that this tensor is degenerate. Instead of three nonvanishing eigenvalues it has only one, namely  $|\mu_{ij}|^2$  with the associated eigenvector. The eigenvector represents the polarization of the magnetic moment  $\mathbf{u}_{ij}$  with respect to space and phase. Magnitude and polarization of  $\mathbf{u}_{ij}$  in (5) can be calculated in a standard quantum theoretical fashion. Maximum transition probability occurs if  $\mathbf{u}_{ij}$  and  $\mathbf{H}_{rf}$  have the same polarization, which in general will be elliptical.

As an example, we give the numerical values of imaginary part  $\chi''$  of susceptibility for a particular transition in ruby.<sup>8</sup> This transition occurs between  $-\frac{3}{2}$  and  $-\frac{1}{2}$  states (see Fig. 2) at a field of 3.97 kilo-oersted applied perpendicular to the crystalline axis. Its transition frequency is 5.85 mc. It is the same line whose inversion is discussed below and which is employed in the TWM described in the accompanying paper.<sup>5</sup> We compute the quantities  $\chi''_+$  and  $\chi''_-$ , which are the values of  $\chi''$  for excitation with circular polarization. The circular polarization is defined in an  $x$ - $y$  plane where the  $z$ -direction coincides with the applied dc magnetic field. The magnitude of  $\chi''_+$  is defined by

$$|\chi''_+| = (\mathbf{H}_{rf+}^* \cdot \chi'' \cdot \mathbf{H}_{rf+}) / (\mathbf{H}_{rf+}^* \cdot \mathbf{H}_{rf+}) \quad (7a)$$

and similarly for  $\chi''_-$ .

The ruby crystal is the commercial "pink sapphire" produced by Linde Company. The chromium content of 0.05 per cent substituting for aluminum indicated by the manufacturer was verified by chemical

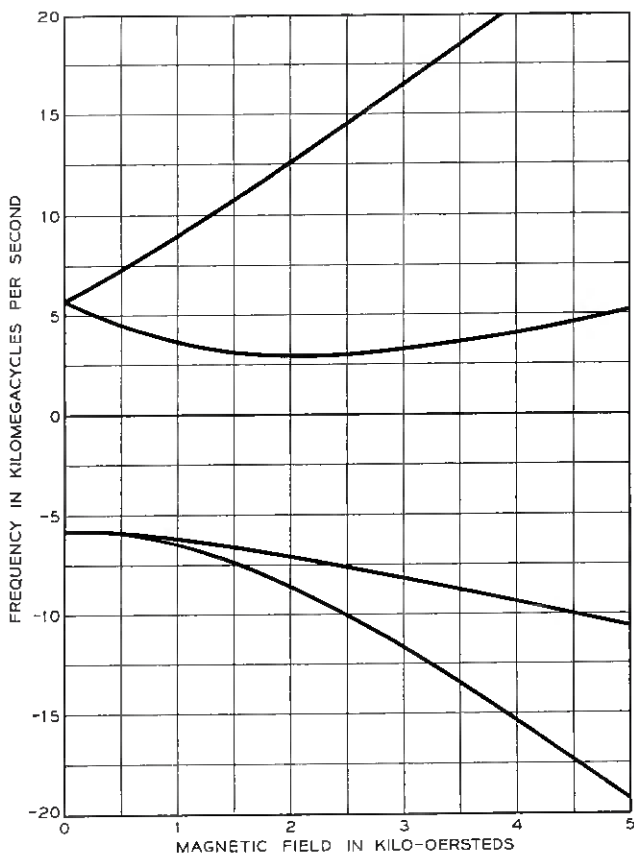


Fig. 2 — Energy-levels of  $\text{Cr}^{+++}$  in ruby as function of magnetic field applied perpendicular to crystalline symmetry axis.

analysis.<sup>9</sup> We thus have  $\rho_0 = 2.35 \times 10^{19}$   $\text{Cr}^{+++}$  ions  $\text{cm}^{-3}$ . For the density difference

$$\rho_{-3/2} - \rho_{-1/2} \approx \frac{\rho_0}{2S + 1} \frac{h\nu}{kT}$$

we find, at  $T = 1.6^\circ\text{K}$ ,  $\rho_{-3/2} - \rho_{-1/2} = 1.04 \times 10^{18}$   $\text{cm}^{-3}$ . Assuming a Lorentzian line shape, at the line center  $g(0) = 2/\pi\Delta\nu$ , where  $\Delta\nu = 6 \times 10^7$   $\text{sec}^{-1}$  is the measured full line width at half intensity. Using the eigenvectors evaluated in Ref. 8 and (5), we find  $|\mu_+|^2 = 5.08 \times 10^{-40}$   $\text{erg}^2$  oersted $^{-2}$  and  $|\mu_-|^2 = 0.57 \times 10^{-40}$   $\text{erg}^2$  oersted $^{-2}$ . The resulting numbers for susceptibility by circular excitation are  $\chi_+'' = 0.0166$  and  $\chi_-'' = 0.0018$ , respectively.

This can be compared with measurements in the TWM which yield  $\chi_+'' F_+ = 0.0062$ , where  $F_+$  is the filling factor for positive circular polarization. By definition,  $F_+ < \frac{1}{2}$ . We find  $F_+ = 0.37$ . Since this filling factor is about what should be expected on the basis of TWM geometry, the comparison of the calculated  $\chi_+''$  and the measured  $\chi_+'' F_+$  shows the consistency of experimental data with theoretical computation.

Saturation effects can be discussed considering both relaxation processes and RF excitation present. The population  $n_1$  then changes according to

$$\frac{dn_i}{dt} = -\frac{n_i}{\tau_{ij}} + \frac{n_j}{\tau_{ji}} - n_i w_{ij} + n_j w_{ij}. \quad (8)$$

With steady-state conditions,  $dn_i/dt = 0$ . From this equation, the following features are easily deduced. If the exciting field is weak,  $w_{ij}\tau_{ij} \ll 1$ , the ratio  $n_i/n_j$  is the unperturbed Boltzmann ratio (1). If the exciting field is strong,  $w_{ij}\tau_{ij} \gg 1$ , saturation occurs; that is,  $n_i = n_j$ . The Boltzmann difference between  $n_i$  and  $n_j$  is reduced to half its value with  $w_{ij}\tau_{ij} = 1$ .

### III. THREE-LEVEL EXCITATION

In the three-level maser, a saturating "pump" signal is applied between levels 1 and 3 (see Fig. 1) so that  $n_1 \rightarrow n_3$ . The population  $n_2$  then will be determined by

$$\frac{dn_2}{dt} = -\frac{n_2}{\tau_{21}} - \frac{n_2}{\tau_{23}} + \frac{n_1}{\tau_{12}} + \frac{n_3}{\tau_{32}}.$$

Applying steady state conditions and relations like (2),

$$\frac{n_2}{n_1} = \frac{1 + \frac{\tau_{12}}{\tau_{23}} \frac{n_3}{n_1} \exp\left(\frac{\hbar\nu_{32}}{kT}\right)}{\exp\left(\frac{\hbar\nu_{21}}{kT}\right) + \frac{\tau_{12}}{\tau_{23}}}, \quad (9)$$

where, with the pump transition saturated,  $n_3/n_1 = 1$ . Under this condition, the equation indicates that it would be rather accidental if  $n_2/n_1 = 1$ . If  $n_2/n_1 > 1$ , stimulated emission could be obtained at  $\nu_{21}$ . This situation is indicated in Fig. 3. If  $n_2/n_1 < 1$ , that is,  $n_3/n_2 > 1$ , maser action could be obtained at  $\nu_{32}$ .

For further discussion, let us identify arbitrarily  $\nu_{21}$  or  $\nu_{32}$  with the signal frequency  $\nu_{\text{sig}}$ , and the other frequency with idler frequency  $\nu_{\text{idl}}$ .

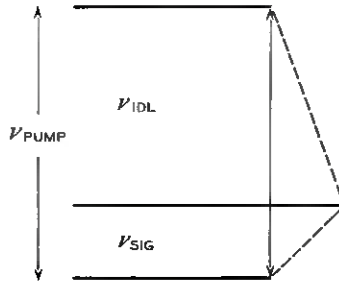


Fig. 3 — Energy-level scheme to demonstrate maser action.

In analogy to (1), we may introduce a spin signal temperature  $T_{sig}$  by

$$\frac{n_i}{n_j} = e^{-(h\nu_{sig}/kT_{sig})}, \quad (10)$$

where  $i$  is the upper state and  $j$  the lower state of the signal transition. Also, we expand the exponential functions in (9) and (10) to the linear term. This is frequently justified under experimental conditions. Even where it is not, the resulting simpler equations show the qualitative features more clearly. We find

$$\frac{T_{sig}}{T_0} = \frac{1 + \frac{\tau_{sig}}{\tau_{idl}}}{1 - \frac{\tau_{sig} \nu_{idl}}{\tau_{idl} \nu_{sig}}}. \quad (11)$$

We may define as “inversion” the quantity  $-T_0/T_{sig}$ . It is easily measured in a TWM as the ratio of gain with saturating pump power to attenuation without pump power, both expressed in decibels. To obtain large gain and bandwidth from a given number of ions in a crystal at  $T_0$ , the inversion should be as large as possible or the negative  $T_{sig}$  should be as small as possible. This suggests that it would be desirable for

$$\tau_{sig}/\tau_{idl} \gg 1 \quad (12)$$

and

$$\nu_{idl}/\nu_{sig} \gg 1. \quad (13)$$

In most experiments performed up to now, however, maser action was based on one of these ratios being large, while the other was not appreciably different from unity. Consequently, it is convenient to distinguish between "relaxation time ratio operation" of 3LSSM, where (12) is satisfied, and "frequency ratio operation", where (13) is satisfied. Both modes of operation will be discussed in more detail below.

Before entering this discussion, however, let us now consider two interesting refinements of (11). The first is concerned with saturation of the signal transition. It will determine the upper limit of the dynamic range of a maser amplifier. For this, a transition probability  $w_{\text{sig}}$  at the signal frequency  $\nu_{\text{sig}}$  is introduced. Instead of (11) we then find

$$\frac{T_{\text{sig}}}{T_0} = \frac{\left(1 + \frac{\tau_{\text{sig}}}{\tau_{\text{id1}}}\right) \left(1 + w_{\text{sig}} \frac{\tau_{\text{sig}} \tau_{\text{id1}}}{\tau_{\text{sig}} + \tau_{\text{id1}}}\right)}{1 - \frac{\tau_{\text{sig}} \nu_{\text{id1}}}{\tau_{\text{id1}} \nu_{\text{sig}}}}. \quad (14)$$

The numerator shows that, in saturating a maser signal, the applied RF field has to overcome the shunted signal and idler relaxation times. Thus, in general, the maser signal saturates at a higher power level than the same line in the absorbing state. If both relaxation times are appreciably different, this shunted value is essentially the shorter of the two. The difference in saturation levels is drastic, therefore, if the idler relaxation time is short compared to the signal relaxation time.

The other refinement considered is the effect of incomplete saturation of the pump transition. Such considerations are important with the application of very high pump frequencies. For a description of incomplete saturation, a pump temperature  $T_{\text{pump}}$  is defined analogously to the signal temperature in (10). The resulting modification of (11) is

$$\frac{T_{\text{sig}}}{T_0} = \frac{1 + \frac{\tau_{\text{sig}}}{\tau_{\text{id1}}}}{1 - \frac{\tau_{\text{sig}} \nu_{\text{id1}}}{\tau_{\text{id1}} \nu_{\text{sig}}} \left(1 - \frac{\nu_{\text{pump}}}{\nu_{\text{id1}}} \frac{T_0}{T_{\text{pump}}}\right)}. \quad (15)$$

The denominator shows that, with comparatively high pump frequencies, appreciable inversion can be achieved with slight saturation of the pump transition. Suppose a certain inversion results from complete saturation ( $T_{\text{pump}} \rightarrow \infty$ ) at pump frequency  $\nu_{\text{pump}}$ . With the relaxation time ratio unchanged, the same inversion occurs with pump frequency  $\nu'_{\text{pump}} = a\nu_{\text{pump}}$  ( $a$  is a number greater than unity) and pump temperature  $T'_{\text{pump}} =$

$aT_0/(a-1)$ . For example, with  $\nu'_{\text{pump}} = 2 \nu_{\text{pump}}$ , this requires  $T'_{\text{pump}} = 2 T_0$ . In this sense, pump frequency can be traded for pump saturation.

#### IV. RELAXATION TIME RATIO OPERATION

We have defined this operation by  $\tau_{\text{sig}}/\tau_{\text{id1}} \gg 1$ , while  $\nu_{\text{id1}}/\nu_{\text{sig}}$  is not specified but not too far from unity. From (11), we thus find

$$T_{\text{sig}}/T_0 = -\nu_{\text{sig}}/\nu_{\text{id1}}. \quad (16)$$

Following the discussion of (14), a particularly attractive property of this operation is that the inverted signal transition saturates at a rather high power level in proportion to the idler relaxation time. By the same token, after a very strong signal resulting in saturation of the signal transition, the amplifying condition is restored in a short time, of the order of the idler relaxation time.

Unfortunately, experimental data about relaxation times are rather scarce. Usually, our experiments have yielded relaxation time ratios close to one; only in exceptions have they been as high as five. Also, there is no adequate theory of relaxation processes that would enable one to compute conditions leading to large relaxation time ratios. This difficulty was bypassed by Scovil and Feher using a technique of impurity doping.<sup>2</sup> We explain this technique by considering the effect of concentration on relaxation times.

At very low concentrations, ions do not interact with each other. The individual resonance lines are narrow, but slightly displaced with respect to each other, as a result of random local fields. The observed over-all line is "inhomogeneously" broadened.<sup>10</sup> In this range, line width and relaxation time should be independent of concentration. With higher concentration, spin-spin interaction comes into play in two ways: (a) the dc magnetic field associated with neighboring spins produces addition inhomogeneous broadening; (b) the rf magnetic field associated with spins during relaxation type transitions leads to "homogeneous" broadening in excess of the inhomogeneous. This can be visualized as a resonant coupling between spins which results in a broader line of identical frequency for every ion. The homogeneous broadening increases proportionally to ion concentration. Gadolinium ethyl sulfate as a maser material is used in a range where homogeneous broadening outweighs the inhomogeneous broadening effects by about a factor of two. This is the case with a concentration of 0.5 per cent gadolinium in a diamagnetic

host crystal of lanthanum ethyl sulfate. Some measurements in this concentration range in our laboratory have indicated a rather strong dependence of relaxation time on concentration. A typical value found is a reduction in relaxation time by a factor of 10 upon doubling the ion concentration. This applies to the pump relaxation time, too, indicating a rather strong concentration dependence of pump power required to saturate the pump transition. In practice, one uses as high an ion concentration as is compatible with the pump power which is available and which can be dissipated in the cryostat, in order to have maximum gain and bandwidth per volume of maser material.

In the doping technique, an additional transition is used, whose frequency coincides with that of the idler transition and whose dipole moment is similar to that of the idler. Spin-spin interaction will then be effective at the idler frequency, which can be regarded as due to an effective increase of ion concentration. As a result, the idler relaxation time is shortened considerably. On the basis of the figure given above, a reduction in relaxation time by a factor of 10 might be expected for an effective doubling of ions in the idler transition. It should be pointed out, however, that at lower ion concentrations such as are typical of inhomogeneous broadening, no doping effects are observed. In this range, the idler relaxation time is essentially unaffected by the doping transition.

The doping transition may be one between other levels in the same ion energy level scheme. We call this case "self-doping condition." Alternatively, the doping condition can be provided by a transition of another ion spectrum within the same crystal lattice. This case we call "impurity doping condition." An advantage of this latter case is the free choice of impurity concentration which allows one to control the strength of doping action.

We will illustrate this type of operation by describing the use of gadolinium in a crystal of hydrated lanthanum ethyl sulfate containing cerium as an additional impurity. Fig. 4 shows part of a measured spectrum of a crystal containing 0.5 per cent gadolinium and 0.2 per cent cerium. Resonance fields for a signal frequency of 6.298 kmc are plotted versus the angle between applied magnetic field and crystalline axis. Experimentally, doping conditions are found at crossover points of lines in an observed spectrum. The energy-level diagrams indicating the doping conditions at points A and B in Fig. 4 are shown in Fig. 5. Relaxation times were measured by the saturation method. With uncluttered  $-\frac{3}{2} \leftrightarrow -\frac{1}{2}$  and  $-\frac{1}{2} \leftrightarrow +\frac{1}{2}$  lines, the relaxation times are nearly the same. At point A, the  $-\frac{1}{2} \leftrightarrow +\frac{1}{2}$  relaxation time  $\tau_{id1}$  is reduced by a factor of 5. The effect is comparatively small because the  $+\frac{3}{2}$  and  $+\frac{7}{2}$

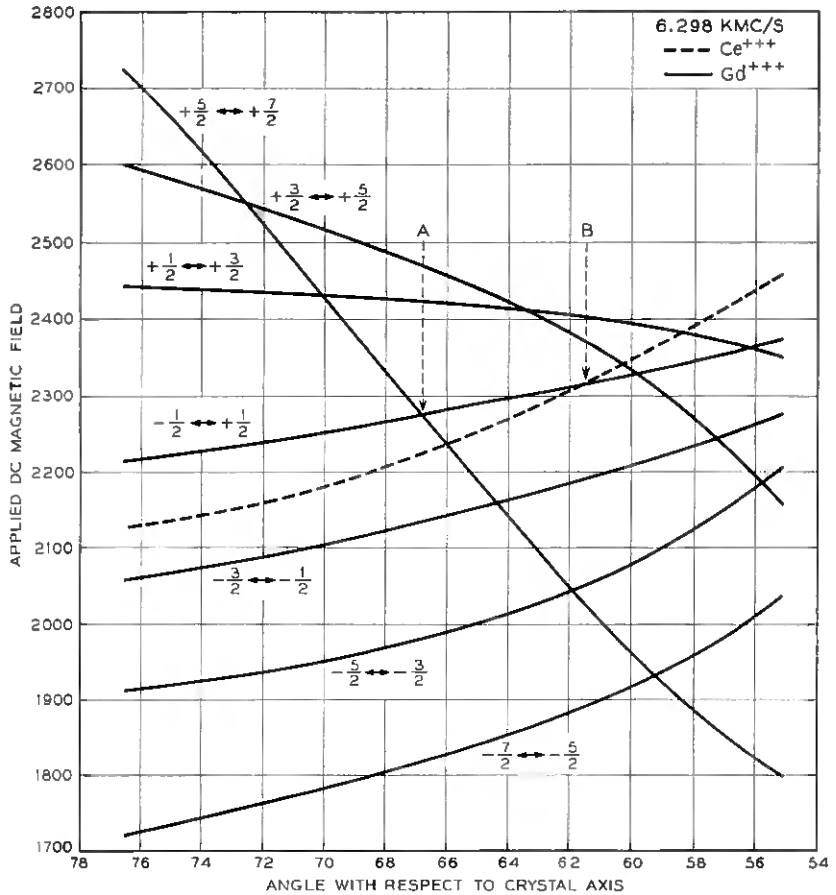


Fig. 4 — Part of measured paramagnetic resonance spectrum of lanthanum ethyl sulfate containing gadolinium and cerium.

levels are not very populated at 1.5°K. As should be expected from (11) with a frequency ratio  $\nu_{id1}/\nu_{sig} = 0.94$ , the measured inversion obtained by applying pump power to the  $-\frac{3}{2} \leftrightarrow +\frac{1}{2}$  transition was  $-T_0/T_{sig} = 0.5$ . At point B, reduction in  $\tau_{id1}$  was by a factor 10. In agreement with this, inversion observed was  $-T_0/T_{sig} = 0.8$ . Possibly the near cross-over of  $+\frac{3}{2} \leftrightarrow +\frac{5}{2}$  is helpful in achieving the large reduction of  $\tau_{id1}$ . For it was found that strong doping was effective even when idler and doping frequency differed by as much as 100 mc, i.e., more than the line width (30 mc). Further tests showed saturation of the inverted signal at about 10 times the saturating power required for the absorption sig-

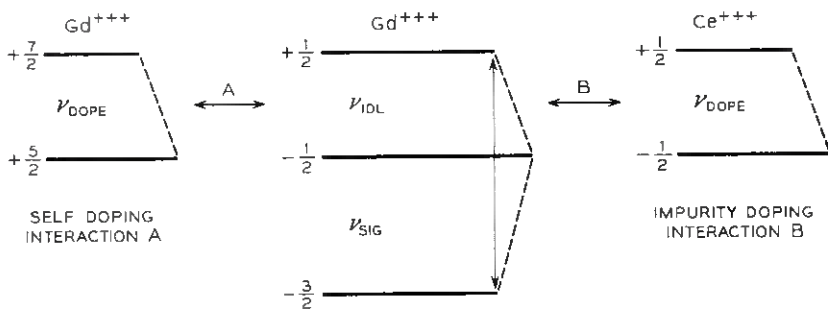


Fig. 5 — Energy-level scheme to describe self- and impurity-doping conditions

nal. In our slow-wave structure, the respective power levels were 32 mw and 3.2 mw. After a complete saturation, the amplification is restored to within  $\frac{1}{8}$  of its steady-state value within 20 microseconds indicating  $\tau_{idl} \approx 10$  microseconds. The signal transition is almost completely circular. Thus, the degree of nonreciprocity in gain is limited by the perfection of the microwave structure only. In a test slow-wave structure exhibiting a slowing of 100 compared to velocity of light, essentially unidirectional gain of 4.5 db/cm was obtained.

While this material shows appreciable power-handling capacity and fast recovery, it is not too well suited for practical application because of chemical instability and mechanical weakness. Somewhat disadvantageous, too, is the low pump-transition probability at the frequencies used in our experiments, which has to be overcome by high pump fields. Also, because of nearly equal level spacing,  $\nu_{idl}/\nu_{sig} \approx 1$  and inversion will be limited to order 1. These disadvantages are avoided by the use of ruby at the expense of somewhat lower gain, lower signal saturation and slower recovery.

## V. FREQUENCY RATIO OPERATION

Equation (11) suggests that inversion can always be achieved by a sufficiently large ratio  $\nu_{idl}/\nu_{sig}$  independent of  $\tau_{sig}/\tau_{idl}$ . From a practical point of view, there are limits to this approach. For a given signal frequency, the highest useful ratio  $\nu_{idl}/\nu_{sig}$  is restricted by pump power sources available at high microwave frequencies. Depending on the power requirements, this limit lies presently between perhaps 35 and 100 kmc, unless optical, incoherent power sources could be utilized. Also, one would like to use for practical masers only such operations where the

relaxation time ratio  $\tau_{\text{sig}}/\tau_{\text{id1}}$  is at least not below unity. If this is satisfied, one might expect an inversion of order

$$-T_0/T_{\text{sig}} \approx \nu_{\text{id1}}/2\nu_{\text{sig}}. \quad (17)$$

The inversion could be improved with a more favorable relaxation time ratio.

For our experiments with frequency ratio operation at low signal frequencies, the energy-level diagram of ruby<sup>8, 11, 12</sup> was used with magnetic field applied perpendicular to the crystalline symmetry axis. This diagram is shown in Fig. 2. Use of the perpendicular orientation is suggested by the observation that all lines are reasonably narrow (of order 60 mc in 0.05 per cent ruby) and correspondingly intense at this orientation and that all possible transitions are reasonably probable. For a signal frequency of about 5.8 kmc, two transitions are available. One is between  $+\frac{1}{2}$  and  $+\frac{3}{2}$  levels at about 1.0 kilogauss. With a pump frequency of about 15 kmc between either  $-\frac{3}{2}$  or  $-\frac{1}{2}$  and  $+\frac{3}{2}$ , no inversion was observed but only saturation of the signal. This indicates an unfavorable relaxation time ratio of about  $\tau_{\text{sig}}/\tau_{\text{id1}} = 0.7$ . The other signal transition occurs between  $-\frac{3}{2}$  and  $-\frac{1}{2}$  levels at a field of 3.97 kilogauss. The  $-\frac{3}{2} \leftrightarrow -\frac{1}{2}$  transition is used for pumping at a frequency of about 18.5 kmc. The inversion found is  $-T_0/T_{\text{sig}} = 0.95$ . Thus, the relaxation time ratio  $\tau_{\text{sig}}/\tau_{\text{id1}} = 1.45$  favors this maser operation.

Both relaxation times are rather long, of the order  $\frac{1}{10}$  second. Consequently, gain saturation at the output sets in at a fairly low level of 6 microwatts c.w. output power in our structure. The power level of saturation can be appreciably higher in pulsed operation. This can be understood by considering the energy stored in the inverted spin system. As long as pulses repeat in a time shorter than the relaxation time, it is only the average power which determines the saturation behavior. Thus, with a  $10^{-3}$  duty cycle, saturation was observed at peak power of 6 mw.

## VI. OPTIMIZATION OF MASER MATERIAL OPERATION

From the preceding discussion, it is apparent that the distinction of relaxation time ratio operation and frequency ratio operation is somewhat artificial. This classification is justified, however, because both cases offer viewpoints for the experimental approach to maser operation. They allow one to predict maser action with a reasonable chance of success from the knowledge of the energy-level diagram only. In the relaxation time ratio operation, the respective ion concentrations are the only critical parameters whose effect has to be investigated experimen-

tally. They have to be compatible with the doping effect and pump power available. In the frequency ratio operation, similarly, maser action is assured if the line is homogeneously broadened, if the pump power available is sufficient for saturation and if the relaxation time ratio is not too unfavorable. It is clear that an ideal maser material should exhibit both a large frequency ratio  $\nu_{\text{idl}}/\nu_{\text{sig}}$  within practical limits set by available pump power sources and a large relaxation time ratio  $\tau_{\text{sig}}/\tau_{\text{idl}}$ . To accomplish the first, paramagnetic materials with high zero field splitting are required. To accomplish the second, another similar spectrum of a different ion or ion site within the same host crystal could be used for doping the idler relaxation time. This approach requires a rather intimate knowledge of the involved paramagnetic spectra, but there is little doubt that more ideal maser materials will be found as development continues.

#### VII. NONRECIPROCAL ATTENUATION

The development of unilateral TWM depends on the availability of elements exhibiting nonreciprocal attenuation. In contrast to conventional ferrite nonreciprocal devices, which operate at room temperature and at a magnetic field adjusted for optimum performance of the device, the nonreciprocal behavior in the TWM must be achieved at a low temperature and at a field dictated by the maser operation. Two practical solutions have been found so far, while others may appear useful in the future.

The first approach uses the same paramagnetic material as that supplying maser gain, but with positive signal temperature. Experimentally it was established that the pump power used in the ruby TWM (of order 100 mw) is not sufficient to saturate the pump transition of a higher concentration (0.9 per cent) ruby. At the signal frequency, only very slight reduction in attenuation was observed. Thus it is possible to place low- and high-concentration materials together into the same structure, with one exhibiting gain and the other attenuation. Suppose a forward wave in the structure produces right circular polarization in one region, left circular in another. Both gain and isolator materials interact with right circular polarization only. Thus, we place gain material in the right circular region so that it amplifies the forward wave. Isolator material in the left circular region does not interact with the forward wave. A reverse wave, however, produces the opposite senses of circular polarization. This can easily be verified by the observation that, aside from absorption, a reversal of direction of propagation is equivalent to a

change in sign of time. Thus, the right circular polarization of the reverse wave interacts with the isolator material, but not with the gain material. Ideally, pure forward gain and pure reverse attenuation should result. In practice, the reverse-to-forward ratio of attenuation has an upper limit,  $C$ , the circularity of the signal transition, which then will be further reduced by variation of the degree of circular polarization in the microwave structure. The same applies to the forward-to-reverse ratio of gain. For the ruby signal transition discussed before,  $C = |\chi''_+|/|\chi''_-| = 8.95$ .

One obvious advantage of using the same paramagnetic ion for amplification and for isolation is that the resonance condition will always occur at the same magnetic field. The isolator will automatically track the amplifying material with electronic tuning. One disadvantage is that pump power will be absorbed by the isolator. It is not saturated at the pump frequency and therefore absorbs a major fraction of the pump power.

This difficulty could be avoided by using a different paramagnetic material as isolator. In practice, this approach may be rather difficult because the resonance line considered should occur at a magnetic field given by the maser operation and, in addition, it should exhibit high circularity.

The other approach is to use ferrimagnetic materials. Investigations on the resonance behavior of ferrimagnetic materials at liquid helium temperature are being carried out by F. W. Ostermayer of Bell Telephone Laboratories. While he shall report his results in detail, we mention some typical features. Three ferrimagnetic polycrystalline materials have shown useful resonance properties at helium temperature. They are yttrium iron garnet, yttrium gallium iron garnet and nickel zinc ferrispinel. From a room temperature line width usually below 50 oersteds, the helium temperature line width is of the order of 1000 oersteds for these materials. The strength of the resonance absorption decreases accordingly. Still, the resonance absorption is very strong compared to gain or attenuation due to paramagnetics. Therefore the ferrite volumes used in a TWM are extremely small. The resonance field can be shifted to the field required for the maser action within a range set by the saturation magnetization by shaping the ferrite sample. The shape follows from the demagnetizing factors, which in turn are calculated from Kittel's<sup>13</sup> resonance condition.

Two such isolators have been tested as parts of a TWM. One used 0.020-inch diameter spheres of yttrium gallium iron garnet and was used in conjunction with the maser operation of gadolinium ethyl sul-

fate described before. The applied field of about 2.1 kilogauss provided resonance conditions for both the active material and the isolator. Reverse-to-forward attenuation at helium temperature was better than 30. The other is a rectangular slab of nickel zinc ferrispinel with 0.010- by 0.020-inch cross section having the length of the maser slow wave structure. Its resonance field is sufficiently close to that of the  $-\frac{3}{2}$  to  $-\frac{1}{2}$  line in ruby at 5.85 kmc and with crystalline symmetry axis perpendicular to the applied magnetic field. Maser operation using this line is described above. At helium temperature, the ratio of reverse to forward attenuation in the nickel zinc ferrispinel isolator is better than 10. In both cases, the isolator reverse attenuation is adjusted to exceed the forward maser gain slightly. Due to the large ferrimagnetic line width, no great care has to be taken to have the maser magnetic field coincident with the field of the resonance isolator. By the same token, tracking over reasonably wide bands by electronic tuning is not difficult. A decisive advantage of ferrimagnetic isolation is the small interaction of the ferrimagnetic material with the pump frequency. Also, the figure of merit favors this type of isolation, so that it appears as the more attractive possibility.

#### VIII. SUMMARY

The use of active materials in three-level solid state masers has been discussed. Experimental data have been presented for two typical paramagnetic salts used as active materials in masers. Maser action in these materials can be analyzed in terms of two important modes of operation that make use of either a favorable ratio of signal to idler relaxation time or a favorable ratio of idler to signal frequency. It has been pointed out that more ideal maser materials can be developed that combine the advantages of both modes of operation. Some mention has been made of the use of paramagnetic and ferrimagnetic materials for low-temperature isolators. While the experimental results warrant the use of some materials presently available in practical traveling-wave masers, appreciably improved characteristics can be expected from better materials yet to be developed. The application of active and isolator materials to a traveling-wave maser is treated in the accompanying paper.

#### REFERENCES

1. Bloembergen, N., Proposal for a New-Type Solid State Maser, *Phys. Rev.*, **104**, October 1956, p. 324.
2. Scovil, H. E. D., Feher, G. and Seidel, H., Operation of a Solid State Maser, *Phys. Rev.*, **105**, January 1957, p. 762.
3. McWhorter, A. L. and Meyer, J. W., Solid State Maser Amplifier, *Phys. Rev.*, **109**, January 15, 1958, p. 312.

4. Makhov, G., Kikuchi, C., Lambe, J. and Terhune, R. W., Maser Action in Ruby, *Phys. Rev.*, **109**, February 15, 1958, p. 1399.
5. DeGrasse, R. W., Schulz-DuBois, E. O. and Scovil, H. E. D., this issue, p. 305.
6. Einstein, A., *Phys. Zeit*, **18**, 1917, p. 121.
7. Fermi, E., *Rev. Mod. Phys.*, **4**, 1932, p. 87; Rosenfeld, L., *Ann. Inst. Henri Poincare*, **1**, 1931, p. 25; Heitler, W., *Quantum Theory of Radiation*, 2nd Ed., Oxford Univ. Press, New York, 1944.
8. Schulz-DuBois, E. O., Paramagnetic Spectra of Substituted Sapphire—Part I: Ruby, *B.S.T.J.*, **38**, January 1959, p. 271.
9. Wood, D. L., private communication.
10. Portis, A. M., *Phys. Rev.*, **91**, 1953, p. 1071.
11. Manenkov, A. A. and Prokhorov, A. M., *J. Exp. Theor. Phys. (U.S.S.R.)*, **28**, 1955, p. 762.
12. Geusic, J. E., *Phys. Rev.*, **102**, 1956, p. 1252.
13. Kittel, C., *Phys. Rev.*, **71**, 1947, p. 270.

# Engineering Aspects of TASI

By K. BULLINGTON and J. M. FRASER

(Manuscript received September 24, 1958)

*The number of telephone circuits carried by a submarine cable system can be doubled by using the normal gaps in speech to interpolate additional conversations. TASI is a high-speed transmission and switching system that assigns a talker to a channel as soon as he starts to talk and disconnects him when he pauses, if someone else needs the channel. Switching from channel to channel may occur many times during a typical call, but the effect on transmission quality is negligible because the switching time is fast compared with the syllabic rate.*

For many years telephone people have been intrigued with the idea of making use of the idle time during a telephone call. TASI, an abbreviation for Time Assignment Speech Interpolation, is a high-speed transmission and switching system based on the principle of using the free channel time to interpolate additional talkers. Although TASI requires considerable terminal equipment, it can approximately double the usefulness of long, expensive channels such as the deep sea submarine cable systems. The first speech interpolation system is expected to be placed in service during 1960 on the transatlantic telephone cable system between London and New York that was opened for service in September 1956.

The basic principles of TASI are old. An extensive investigation of the feasibility of speech interpolation systems was conducted in 1946 and 1947 by A. C. Dickieson, P. G. Edwards and others. An experimental model was demonstrated in 1950 by A. E. Melhose, and this was later extended and improved by R. L. Carbrey.

In a normal two-way conversation each talker ordinarily uses the circuit for only about half of the time. In addition, the circuit may not be used momentarily while the operator is trying to get the right people together, or while an individual comes to the phone or takes the normal pauses between sentences and even syllables. All of these gaps add up to a substantial amount of free time. Measurements on working circuits, shown in Fig. 1, indicate that the average activity (percentage of time

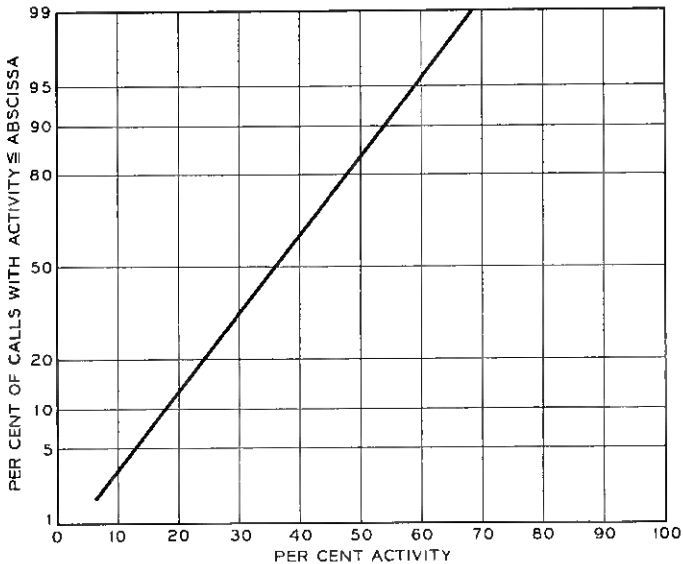


Fig. 1 —Measured activity distribution of transatlantic calls.

that energy above a very low threshold is transmitted in one direction) is no more than 35 to 40 per cent of the time that the circuit is busy at the switchboard. Since long distance circuits use separate pairs of wires or separate carrier channels for the two directions of transmission, it follows that, on the average, each one-way channel is free for 60 to 65 per cent of the time.

An attempt to interpolate two or more independent conversations on a single channel would create considerable delay and mutual interference since the probability of two talkers wanting the same channel at the same time is moderately high. However, when two or three dozen channels are operated as a group, these variations in individual activity tend to average out and the probabilities can be counted on to minimize the mutual interference to a point where there will be no noticeable effect on continuity of conversation. For example, even when all the channels are busy, at least one channel on the average is available for reassignment every  $L/c$  seconds, where  $L$  is the average talkspurt length (which is somewhat less than one second) and  $c$  is the number of channels in the group.

A simplified block diagram for a TASI system is shown in Fig. 2 for one direction of transmission. An identical but independent arrangement is used for the opposite direction. Each of the  $n$  lines from the toll switch-

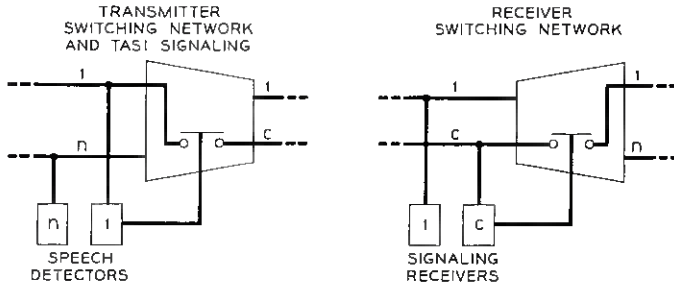


Fig. 2 — Simplified block diagram for a TASI system.

board is equipped with a speech detector which is capable of recognizing the weakest speech within 5 milliseconds or less. When the speech detector on line 1 operates, the TASI switching network connects line 1 to an idle channel, say channel  $c$ , and then sends a 10–15 millisecond coded signal on that channel which instructs the distant receiving terminal to connect that channel to listener line 1. Once a connection has been set up, it is maintained until someone else needs the channel, even though the person may stop talking in the meantime. A similar 10–15 millisecond coded signal is used for disconnect purposes but this is sent over a separate channel reserved for this purpose in order to avoid interference to the listener.

When speech appears on any of the  $n$  lines, the speech must be recognized by the speech detector, which causes some clipping during the first few milliseconds. This type of clipping can be minimized by increasing the sensitivity of the speech detector. The sensitivity cannot be too high, or it will operate too often on noise. This is undesirable because it increases the activity, and hence reduces the TASI advantage. A compromise is needed to achieve minimum activity but maintain satisfactory speech quality for even the weak talkers.

The potential impairment caused by the loss of speech energy that is below the sensitivity of the speech detector and by the time delay required to set up a connection can be made negligible by design. Another possible impairment is inherent in any line concentration arrangement, but this can be minimized to any desired degree by limiting the number of lines to be served. This factor is the possibility that the number of individuals who are talking or starting to talk at a particular instant will exceed the number of available channels. For example, telephone subscribers on a party line must share time with their neighbors on a single pair of wires leading to the central office. In addition, all trunk lines between two or more central offices may occasionally be busy and a call

coming in at that instant will experience some delay. In a similar manner, TASI may occasionally be overloaded by an unusually large number of simultaneous talkers. In this case, however, the information cannot be delayed and any failure to make an almost instantaneous connection results in a loss of speech transmission (called a freezeout) until a channel becomes available. It appears that the effect on transmission quality is negligible as long as the percentage of lost speech (freezeout fraction) is less than 0.5 per cent.

During periods of light traffic, the system's operation is essentially the same as without TASI, and hence there can be no TASI impairment. However, as the load increases, the amount of switching and possible impairment increases. The objective is to limit the number of busy lines to a point where the resulting impairment is not noticeable to the average listener and is not objectionable to the more critical listener.

The number of circuits that can be made available for service at the toll switchboard (for a freezeout fraction of 0.5 per cent) is greater than the number of physical channels by the TASI multiplying factor shown in Fig. 3. As the number of channels in the group increases, the number of potential conversations approaches a limit set by the reciprocal of the average activity. It will be noted that a 36-channel group, such as is available in present submarine cable systems, achieves a substantial TASI advantage, but that the application of TASI to only a dozen channels or less is much less attractive. For an average activity in the range of 35 to 40 per cent, it appears that the use of TASI on a 36-chan-

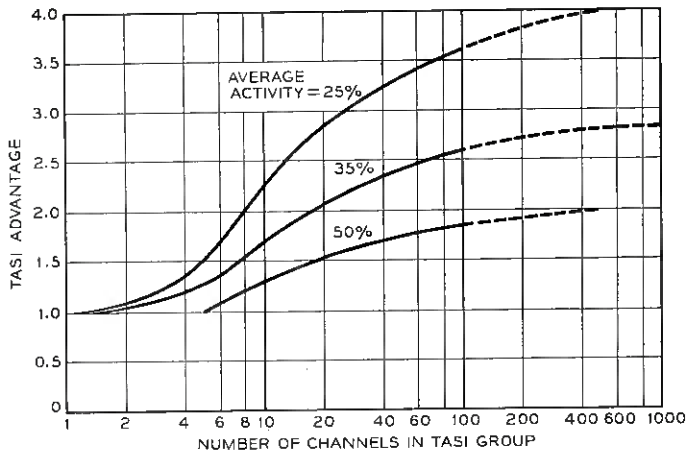


Fig. 3 — TASI multiplying factor for freezeout fraction of 0.5 per cent.

nel group can at least double the number of available circuits and still maintain good quality.

The average number of simultaneous talkers,  $np$ , is the product of the number of busy lines,  $n$  multiplied by the average activity,  $p$ . When the average number of simultaneous talkers is approximately equal to the number of channels,  $c$ , there is a 50 per cent chance that a new talker will be frozen out momentarily. This does not mean that 50 per cent of the speech is lost, but there is noticeable impairment. In order to allow for variations around the average and to achieve satisfactory quality, the average number of simultaneous talkers  $np$  should be limited to a value that will satisfy the approximate condition  $np + \sqrt{np} \leq c$ . This approximate expression is based on a more exact derivation given in the Appendix. When this criterion is met, only a small percentage of the connections will experience any degree of freezeout, except for that required for the connect signaling code.

The expected freezeout fraction is shown in Fig. 4 as a function of the number of busy lines working on 36 physical channels for a talker activity of 30 to 40 per cent. Listening tests have shown that a freezeout

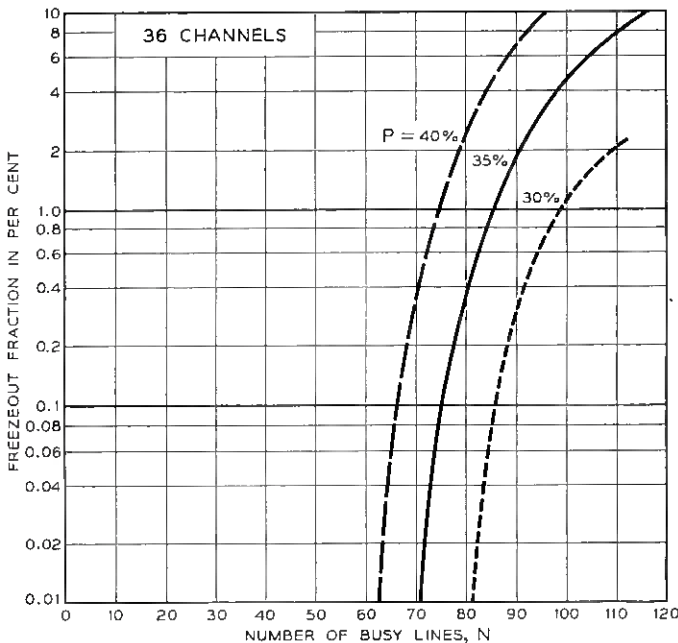


Fig. 4 — Expected TASI freezeout fraction as a function of the number of busy lines.

fraction of 0.1 per cent is barely perceptible by a critical listener. A value of 0.5 per cent is noticeable to the critical listener but not usually apparent to an average listener who is intent on understanding a message. A value of 2 per cent would be somewhat objectionable and a value of 5 to 10 per cent would be definitely objectionable.

The average length of freezeout is roughly proportional to  $L/c$ , where  $L$  is the average talkspurt length and  $c$  is the number of channels. The average talkspurt length for TASI purposes depends not only on the characteristics of speech, but also on the sensitivity, operate time and hangover of the speech detector. In addition, it depends on the number and duration of bursts of noise and echoes on the circuit. A typical measured value of effective talkspurt length is about 0.6 second. Measurements of speech alone (as given by Norwine and Murphy<sup>1</sup>) indicate a median talkspurt length of about 0.6 second and a mean length of 1.5–1.8 seconds.

The probability that a talkspurt will be clipped longer than any specified value is shown in Fig. 5 for a 36-channel system with an effective talkspurt length of 0.6 second. First of all, the chart shows that a 15-millisecond clip occurs for TASI signaling each time a new connection is needed. During the busy hour, this may occur on almost every talkspurt,

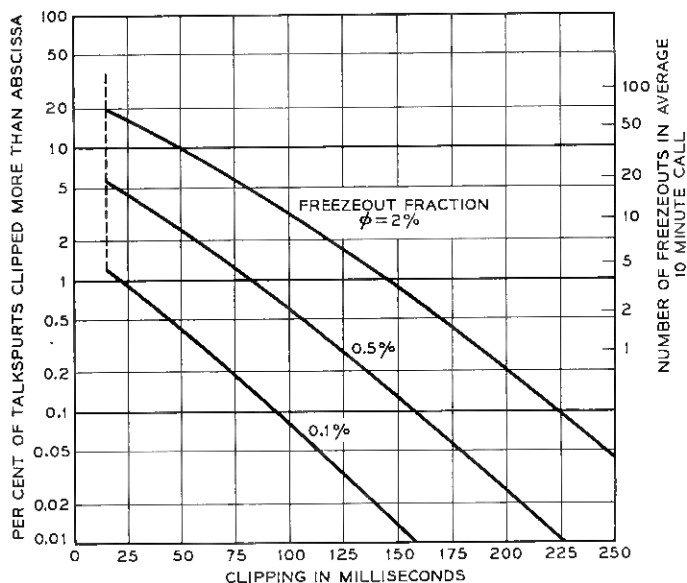


Fig. 5 — Clipping after operation of speech detector.

but the number of operations will be reduced considerably in nonbusy hours. The three lines sloping toward the right represent three different freezeout fractions. For example, the middle curve, labeled 0.5 per cent, indicates that 0.5 per cent of the talking time has been lost because a channel was not available. In this case, about 6 per cent of the talkspurts are frozen out for more than the 15-millisecond signaling time and 1 per cent of the talkspurts are frozen out for 80 milliseconds or longer. A freezeout longer than 80 milliseconds can be expected about four times during an average 10-minute call. For comparison purposes, it is worth noting that the average syllable length is about 125 to 250 milliseconds. On the average, less than one talkspurt in 10,000 will be frozen out for as long as  $\frac{1}{4}$  second, and this will occur only once in about 30 calls during the busy hour.

As mentioned earlier, a talker holds a channel until his speech detector indicates that he is finished talking and until someone else needs his channel. This is true on all but three of the available channels. One channel is reserved full time for disconnect and other control purposes and two talking channels taken at random are disconnected when possible, in order that a channel will be instantly available for the next talker.

Switching from channel to channel during a conversation also causes some variations in circuit noise and net loss. It is expected that a little noise will be introduced in the receiving circuits in order to prevent a completely dead receiver during the silent intervals. The variations in net loss are not expected to be important as long as the plant is maintained to meet the present objectives.

TASI is designed to take advantage of the characteristics of two-way conversational speech. It requires a channel width of about 3,000 cycles in order to accommodate the tones needed for the rapid connect and disconnect signaling.

Telegraph or data systems that use frequency shift or frequency modulation will lock up the TASI speech detector 100 per cent of the time and hence be transmitted satisfactorily. On the other hand, the use of on-off telegraph or data systems will require either a means for locking the speech detector or a separate channel outside the TASI complement. The high activity of telegraph and data systems requires an essentially full-time channel, and hence reduces the number of conversations that TASI can yield.

TASI will be located in the four-wire part of the telephone plant, as shown in Fig. 6. It requires that split-type echo suppressors be used to insure that echoes cannot seize an outgoing circuit at either end. Com-

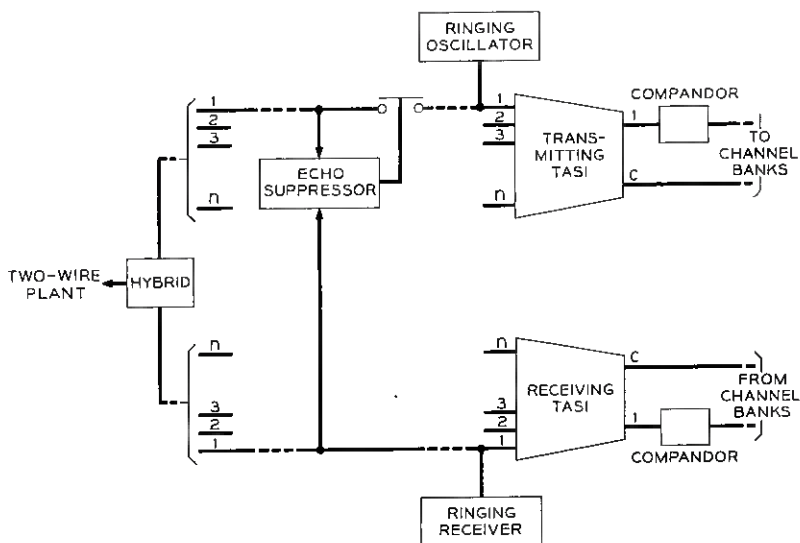


Fig. 6 — TASI location in the four-wire plant.

pandors, which are to be added to deep sea submarine cable systems on a channel-by-channel basis as required by noise conditions, are also compatible with TASI.

Provision will be made to switch out TASI for testing purposes. In order not to affect service, circuits will be removed as they become idle until the number of circuits available to the switchboard is no greater than the number of physical channels before TASI is removed.

Because TASI is a time-sharing device, there are problems involved in transmitting supervisory and dialing pulses. TASI can work satisfactorily with the present ringdown manual arrangement, but it is obvious that continuous supervision by means of a steady tone during the idle time cannot be used. Likewise, dial pulses cannot compete for a TASI channel on the same basis as a talker, because TASI clipping would cause signaling errors. Various schemes using spurt signaling are being investigated for use when dialing over TASI is required.

#### APPENDIX

The TASI principle has been recognized for many years, and several individuals, including R. I. Wilkinson, have contributed to the mathematic analysis of speech interpolation. The following summary is based on a more complete analysis given in an unpublished 1953 memorandum by H. Cravis.

Assume that there are  $n$  independent talkers, each of whom has an average activity  $p$ , competing with an individual test call (total number of talkers =  $n + 1$ ). At any particular instant, the probability that the number of simultaneous talkers will equal or exceed  $c$  (where  $c$  is less than  $n$ ) is given by the cumulative binomial distribution,  $B_{(c,n,p)}$  :

$$B_{(c,n,p)} = \sum_{x=c}^n \frac{n!}{x!(n-x)!} p^x (1-p)^{n-x}. \quad (1)$$

The probability of a freezeout lasting longer than  $t$  seconds is given by  $B_{(c,n,\theta)}$ , where  $\theta = pe^{-t/L}$  for an exponential talkspurt distribution [or  $\theta = p(1 - t/L)$  for a constant talkspurt length].\* In this expression,  $L$  is the average talkspurt length.

It can be shown that the average freezeout length (for an exponential talkspurt distribution) is

$$t_F = L \sum_{k=c}^n \frac{1}{k} \frac{B_{(k,n,p)}}{B_{(c,n,p)}} \quad (2)$$

$$= \frac{L}{c} M, \quad (3)$$

where

$$M = \left[ 1 + \frac{c}{c+1} \frac{B_{(c+1,n,p)}}{B_{(c,n,p)}} + \frac{c}{c+2} \frac{B_{(c+2,n,p)}}{B_{(c,n,p)}} + \dots \right]. \quad (4)$$

This series converges rapidly, so only a few terms are needed for sufficiently accurate results.

The fraction of the speech that is frozen out is

$$\Phi = \frac{t_F B_{(c,n,p)}}{L} = \frac{M}{c} B_{(c,n,p)} = \sum_{k=c}^n \frac{1}{k} B_{(k,n,p)}. \quad (5)$$

Tables of the binomial distribution are available for accurate computations. However, in the range of interest to TASI, this function is almost identical with the cumulative normal probability law, that is,

$$B_{(c,n,p)} \approx \frac{1}{\sqrt{2\pi}} \int_{u=y}^{\infty} e^{-u^2/2} du, \quad (6)$$

where

$$y = \frac{c - np - \frac{1}{2}}{\sqrt{np(1-p)}}.$$

\* The assumption of an exponential distribution of talkspurt lengths is the best simple approximation to the experimental data. The use of a constant talkspurt length does not change the over-all result significantly.

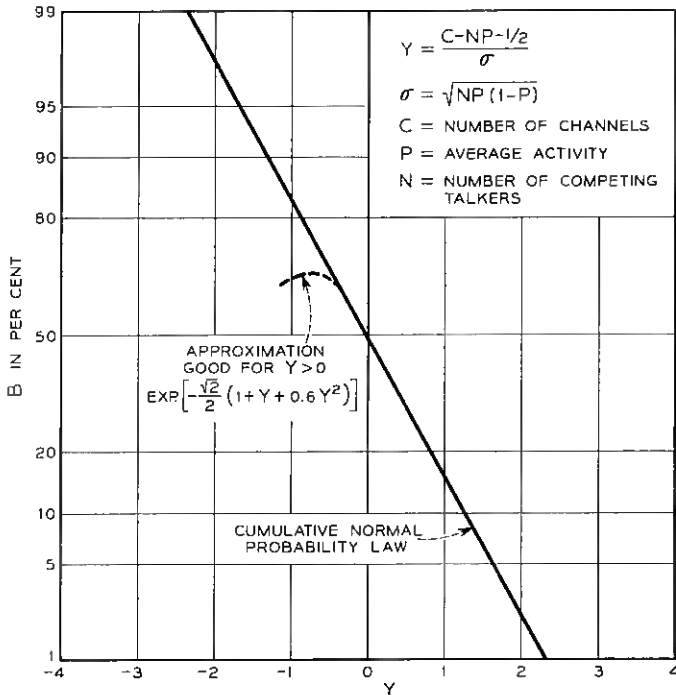


Fig. 7 — Probability of freezout,  $B_{(c,n,p)}$ .

In this expression the mean value is  $np + \frac{1}{2}$  and the standard deviation  $\sigma = \sqrt{np(1-p)}$ .

The probability that a given talkspurt will be frozen out can be obtained from either (1) or (6) and is shown as a solid line on Fig. 7. For example, when  $y = 1$ , 16 per cent of the talkspurts will experience some degree of freezout, because there are more talkers than channels. Most of these freezouts will last only a few milliseconds, so the percentage of speech that is lost is less than 16 per cent by the ratio  $t_F/L$ .

By substituting  $\theta = pe^{-t/L}$  for  $p$  in Fig. 7, it is possible to obtain the probability of a freezout lasting longer than  $t/L$ . Typical values for a 36-channel system are shown in Fig. 5, for various values of the freezout fraction  $\Phi$ .

In all practical cases the probability of freezout is less than 50 per cent and the cumulative binomial distribution and its approximation, the cumulative normal probability law, can be further approximated by the dashed line in Fig. 7; that is,

$$B_{(k,n,p)} \approx \exp \left[ -\frac{\sqrt{2}}{2} (1 + y_k + 0.6y_k^2) \right] \quad (7)$$

for  $B < 0.5$ , where

$$y_k = \frac{k - np - \frac{1}{2}}{\sigma} = y_c + \frac{k - c}{\sigma}$$

This approximation, together with the omission in (4) of the factors  $c/(c + 1)$ ,  $c/(c + 2)$  etc. (which are less than but close to unity), leads to the following approximate expression for the factor  $M$ :

$$M \approx \sum_{k=c}^{\infty} \exp \left[ - \frac{\sqrt{2}}{2} \frac{k - c}{\sigma} \left( 1 + 1.2y_c + 0.6 \frac{k - c}{\sigma} \right) \right]. \quad (8)$$

The magnitude of  $M$  varies from about 1.5 to 3 or more, as shown in Fig. 8. This chart, together with (3), indicates that the average freezeout, when it occurs, is only about 1/10 to 1/20 of the average talkspurt length in a 36-channel system.

By the use of (5) and Figs. 7 and 8, Fig. 4 can be constructed and sim-

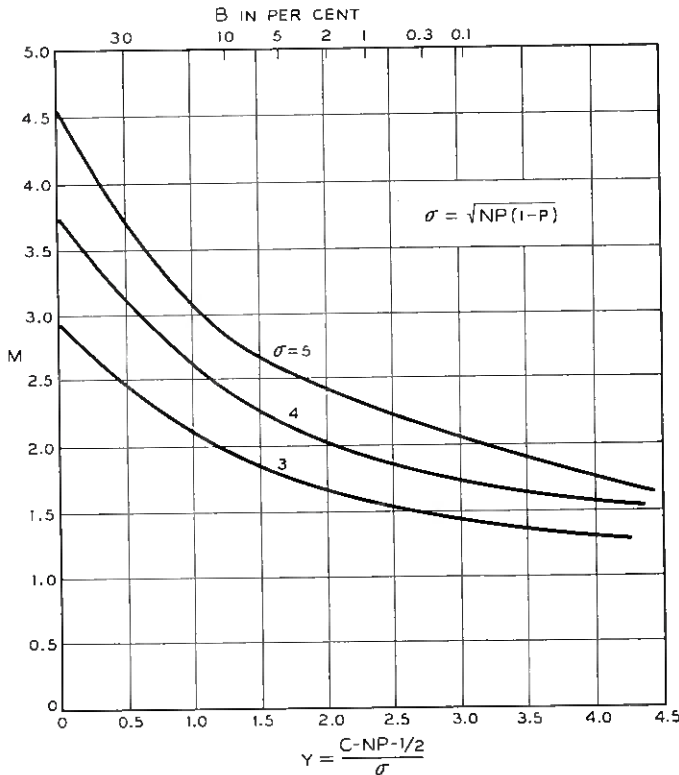


Fig. 8 — Mean freezeout length.

ilar charts for other values of  $c$  can be obtained. A cross plot of such data for a constant value of  $\Phi$  yields curves of TASI advantage like Fig. 3. The TASI advantage is  $(n + 1)/c$ , since there must be  $n + 1$  potential talkers in order to have  $n$  competing talkers.

In order to achieve a value of  $\Phi$  less than 1 per cent, it is necessary for  $y > 1$ ; that is,

$$y = \frac{c - np - \frac{1}{2}}{\sqrt{np(1-p)}} > 1,$$

or

$$c > np + \sqrt{np} - \sqrt{np} (1 - \sqrt{1-p}) + \frac{1}{2}.$$

The last two terms are opposite in sign and each is small compared with the first two terms. This leads to the simple approximate relation that a practical TASI should be limited to the following condition:

$$np + \sqrt{np} < c.$$

#### REFERENCE

1. Norwine, A. C. and Murphy, O. J., Characteristic Time Intervals in Telephone Conversation. B.S.T.J., **17**, April 1938, p. 281.

# System Design of the Flying Spot Store

By C. W. HOOVER, JR., G. HAUGK and D. R. HERRIOTT

(Manuscript received November 5, 1958)

*The flying spot store is a versatile and efficient semipermanent information storage system developed for use in the electronic telephone switching system. Because of the form of the store, many variables enter into system design. In this paper the factors which control speed, capacity, number of channels, physical size and probability of error in readout are discussed. It is shown that these factors are related to the intended application for the store, to the form of the store and to device parameters. A number of scaling operations which involve exchanges between system parameters such as speed and capacity or between system and device parameters are given.*

## 1. INTRODUCTION

### 1.1 Purpose and Organization of the Paper

This paper discusses physical factors which control the speed, capacity, number of channels, physical size and probability of error in readout in the system design of the flying spot store. These factors are related to the form of the store, to the intended application and to device characteristics.

All of the factors which enter into system design interact strongly. For this reason, a number of scaling relationships which involve exchanges between system variables such as speed and capacity, or between system variables and device parameters, are given. A graphical representation for the flying spot store is developed that demonstrates the relationships between the factors entering into physical system design. This representation is used in discussing the range of realizable designs.

In system design, devices and operating conditions are chosen to meet the requirements of speed, capacity, etc., set by the intended application. Electronic circuit design then proceeds and, if necessary, the parameters chosen are modified on the basis of circuit requirements. In all the development to date, very little modification of the physical

system parameters has been necessary in order to permit electronic circuit realization.

### 1.2 Form of the Flying Spot Store

The form of the flying spot store is shown in Fig. 1. Information is stored in the film plane as patterns of transparent and opaque spots on developed photographic emulsion. Access for writing and for reading is gained by means of a number of light beams generated by a single cathode ray tube (CRT) and an array of objective lenses operated in parallel, each lens imaging the working area of the CRT screen on a separate photographic storage area in the film plane. When the image of the cathodoluminescent spot on the phosphor screen of the CRT falls on a transparent spot on the developed emulsion, light passes through the film plane to the photomultiplier tube (PMT) detector. When the image falls on an opaque area, no light reaches the PMT. Light signals are converted into current signals at the photocathode, and these current

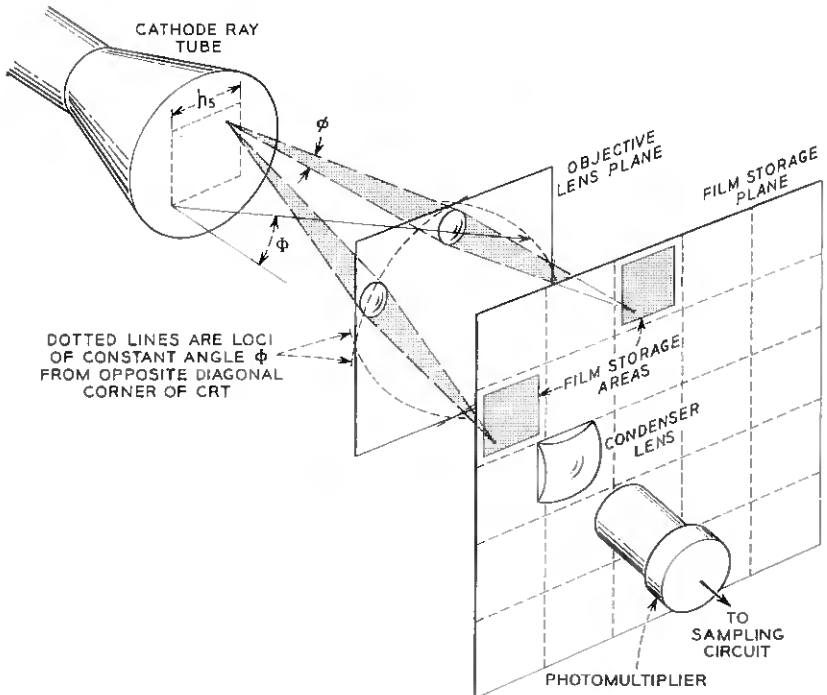


Fig. 1 — Form of the flying spot store.

signals are then amplified in the secondary-emission multiplier stages (dynodes) of the PMT. Thus, the combination of the CRT, optical system and PMT is used to provide an electrical output which indicates whether each spot is transparent or opaque. Transparent spots are used to represent binary "1's," opaque spots to represent binary "0's". The associated objective lens, photographic storage area, condenser lens and PMT are physically located within the solid angle that is subtended at the center of the CRT by the photographic storage area. These, together with the information sampling circuit, constitute an information channel of the system. Fig. 1 shows the system half-field angle  $\Phi$ , the channel field angle  $\varphi$ , and the array size  $h_a$ .

In this paper it is assumed that the electron beam of the CRT is under the control of a feedback beam-positioning system and that a number of channels of the system are used in the optical beam encoder element of this feedback system. The information stored in these channels (called servo channels) is arranged to give a continuous indication of beam position. The mode and speed of operation of the feedback beam-positioning system have been described in an earlier article<sup>1</sup> and additional considerations are given elsewhere in this issue.<sup>2</sup>

### 1.3 Speed of Operation

Cycle time is the time required to complete a readout operation from the store. It is the sum of the beam-positioning time and the sampling time. Beam-positioning time is made as short as possible, consistent with system requirements. The minimum beam-positioning time which has been obtained to date is of the order of 2 microseconds. Information channel sampling has been done, and is practical at 0.3 microsecond. Thus, beam-positioning time is the major part of cycle time. In the design of the servo channels the relative aperture of the lens and the channel magnification are chosen, along with other system parameters, to obtain minimum beam-positioning time and required beam-positioning accuracy. On the other hand, there are a number of very fruitful exchanges which can be made between sampling time and other channel parameters in the design of the information storage channels. These exchanges, which affect sampling time but have a relatively small effect on total cycle time, are discussed in this paper.

### 1.4 Capacity and Word Length

The capacity of the system is given by the product of the number of information channels and the number of spots in the array at the CRT.

It is desirable to provide the total capacity in a number of channels equal to the word length. However, the total capacity required or other system requirements may dictate the use of a larger or smaller number of channels.

The number of bits per channel is the square of the number of spots in one row of the array at the CRT. In almost all cases, this number is set at much less than the total capacity required in the store. This limitation on the number of bits per channel will be shown to be due in part to energy conditions which must be satisfied, in part to device limitations and in part to system requirements. The array size will almost always be less than  $1000 \times 1000$  spots; it now appears practical to design for  $256 \times 256$  spots.

Because of the relatively small capacity per channel and the fact that 16 or more servo channels are used in stores of this type (to define 256 rows and 256 columns), systems with one or few information storage channels are of little interest. Likewise, systems with a number of channels less than the word length require a register to assemble the complete word. Two or more cycle times are required per word readout and, unless the two or more bits of each word in each channel are located remotely from each other, the very desirable property of independence of the bits of the stored word is lost. For these reasons, principal consideration is given in this paper to systems with a total number of channels of 40 or more.

## II. SYSTEM DESIGN

### 2.1 *System Design for the Efficient Use of the Flux from the CRT*

A number of factors combine to set the maximum flux density (radiant power density) in the cathodoluminescent spot and the maximum number of spots which can be resolved on the CRT screen. The maximum flux density, together with the spot size, fixes the maximum flux per spot. The spot size and the maximum usable area of the CRT screen together determine the number of bits which can be stored in each channel. Thus, it is desirable to use as large a CRT screen area as possible. In all tubes we have tested to date it has been possible to obtain sufficient flux per spot in the smallest spot which can be resolved (approximately 0.015 inch). Thus, this organization has been used, since it results in maximum capacity per channel and minimum equipment for given total capacity.

Each channel of the system must be designed to provide a minimum flux level at the photocathode, which is determined by the sampling

time (inversely proportional to channel bandwidth) and the signal-to-noise requirement of the intended application.

Since there are limits on the maximum flux per spot, the maximum number of spots in the array at the CRT and the minimum flux level at the photocathode in each channel, the first consideration in system design is to arrange the optics so that the available flux is used efficiently. The most efficient arrangement is one in which the greatest fraction of the flux from each spot is intercepted by the apertures of the objective lens array. The field angle for which the lenses are designed limits the area in the lens plane, and the ratio of lens aperture to lens mount diameter limits the percentage of the light falling in the plane which is actually used. Any reduction in the flux gathered into the channels of the system results in loss in maximum attainable system speed or capacity.

## 2.2 *Power and Signal-to-Noise Requirements*

### 2.2.1 *Noise Sources*

As readout proceeds in any one channel of a flying spot store, distributions in amplitude are found in the flux signals, incident on the photocathode of the PMT that represent "1's" and "0's." These signal distributions are due largely to spot-to-spot variations and imperfections in the system. Examples are variations in the flux from the CRT screen as a function of beam position, variations with field angle of illumination within the channel and film blemishes. These distributions are very nearly independent of absolute flux level. In the photocathode, the flux signals are converted into current signals, and fluctuations in time may be added to the signal arising from reading of any spot on the film. These fluctuations may be due to shot noise, secondary emission noise or regeneration noise. The most important of these will be shown to be shot-noise-in-signal, which depends on the magnitude of the signal current from the photocathode and, hence, on the flux level at the photocathode, photocathode efficiency and channel bandwidth. Both types of fluctuation — spatial and temporal — as well as the performance of the information sampler circuit, must be taken into account in the channel design. In a design for a high-capacity system with a requirement that the probability of error be very small, it may be necessary to set the flux level so high that shot noise fluctuations introduced in the detector are negligible. In this case, the probability of error depends only on the sampler performance and on the amplitude distributions determined by transmission factors and physical imperfections. In another case, where

the distribution in amplitudes of the incident flux was smaller or where a higher probability of error would be acceptable, some of the total error might be allotted to shot noise fluctuations introduced in the PMT and, in this case, a lower flux level than that of the first example would suffice at the same sampling time. Thus, it is clear that the flux level at the photocathode must be set so that the required electrical signal-to-noise ratio fixed by the system application is obtained in the readout of the most poorly illuminated storage location.

### 2.2.2 Electrical Signal-to-Noise Ratio

The signal-to-noise ratio in the currents leaving the photocathode is given by:

$$\frac{\bar{I}_{pc}}{I_{n,pc}} = \left[ \left( \frac{\bar{I}_{pc}}{2e\Delta f} \right) \left( \frac{1}{1 + \bar{I}_d/\bar{I}_{pc}} \right) \right]^{1/2}, \quad (1)$$

where  $\bar{I}_{pc}$  and  $\bar{I}_d$  are the mean signal and dark emission currents respectively,  $I_{n,pc}$  is the total rms shot noise in the photocathode current,  $e$  is the electronic charge, and  $\Delta f$  is the bandwidth in which the observation is made.  $\bar{I}_{pc}$  is directly proportional to the incident flux and photocathode sensitivity.  $\bar{I}_d$  depends on the area, type and temperature of the photocathode. For a 2-inch diameter, type S-11 (Cs-O-Sb) photocathode of the type commonly used in the flying spot store,  $\bar{I}_d = 1.7 \times 10^{-15}$  amperes at 25°C. The first factor on the right-hand side of (1),  $(\bar{I}_{pc}/2e\Delta f)^{1/2}$ , is the signal-to-shot-noise-in-signal ratio, while the second accounts for the reduction in total signal-to-noise ratio due to shot noise in the dark emission current  $\bar{I}_d$ . As  $\bar{I}_{pc}$  varies through the range  $\infty \geq \bar{I}_{pc} \geq \bar{I}_d$ , the second factor in (1) goes from 0.707 to 1.

At all bandwidths of interest for flying spot store information channels,  $\bar{I}_{pc}$  must be made large compared to  $\bar{I}_d$  to obtain a satisfactory over-all signal-to-noise ratio. The maximum sampling time of interest is of the order of 1 millisecond. The channel bandwidth required in this case is 350 cps. To obtain a signal-to-shot-noise-in-signal ratio of 10 at this bandwidth, the flux level at the photocathode must be set to produce  $\bar{I}_{pc} = 1.1 \times 10^{-14}$  amperes. Thus, at this limit  $\bar{I}_{pc} = 6.5 \bar{I}_d$  and it is seen that the shot-noise-in-signal is the limiting noise. Other factors limit scaling the system in capacity by increasing sampling time before the flux level that corresponds to a sampling time of 1 millisecond at a signal-to-noise ratio of 10:1 is reached. Thus, it is clear that shot-noise-in-signal dominates shot noise in dark current in flying spot store channels.

Equation (1) gives the signal-to-noise ratio at the photocathode. The signal-to-noise ratio in the currents at the anode is found to be slightly less than that at the photocathode due to fluctuations in secondary emission ratio in the first few dynode multiplier stages.<sup>3</sup> Under the operating conditions used in the flying spot store, the maximum reduction in signal-to-noise ratio due to this additional noise source is of the order of one-third. It has been found that regeneration contributes little additional noise under the PMT operating conditions which are used in the flying spot store.

The nearly noise-free current amplification obtained in the dynodes makes it possible to amplify the signal and noise currents originating at the photocathode to a sufficiently high level that the signal-to-noise ratio is not further reduced by Johnson noise in the anode circuit resistance. The condition that the rms shot noise voltage in the output shall be at least  $r$  times the rms Johnson noise voltage leads to the following requirement on the minimum value of anode circuit resistance,  $R_a$  :

$$R_a \geq \frac{2kT}{e} \frac{r^2}{G^2} \frac{1}{\bar{I}_{pc}} = \frac{1}{20} \frac{r^2}{G^2} \frac{1}{\bar{I}_{pc}}, \quad (2)$$

in ohms, where  $G$  is the total current amplification of all of the dynodes,  $k$  is Boltzmann's constant and  $T$  is the absolute temperature of the anode circuit resistor. Note that, in the case of a phototube ( $G = 1$ ), excessively high anode circuit resistance would be needed and that this large resistance, together with tube and wiring capacitance, would result in severe limitation of bandwidth. In photomultiplier tubes, current amplification of  $10^6$  can be obtained. This makes it possible to choose a value of anode circuit resistance compatible with the bandwidth needed in the channel without degrading the signal-to-noise ratio.

It is for this reason that PMT's must be used in the flying spot store. In a typical case, where a channel bandwidth of 1 mc and a signal-to-noise ratio of 10 are required by the application, an anode circuit resistance of 10,000 ohms is chosen in order to provide this bandwidth. The solution of (2) reveals that a minimum current amplification of 820 must be provided in the PMT if the electrical signal-to-shot-noise ratio is not to be reduced by more than 10 per cent by Johnson noise in the anode resistor. In practice, current amplification has been used that is greater than that specified by (2) for the size of the anode circuit resistor  $R_a$  chosen. This increases the output current level and decreases the gain required in the amplifier stages following the PMT.

From the foregoing, it is seen that the limiting noise of a fundamental nature is the shot-noise-in-signal and that it is possible to obtain an

over-all channel signal-to-noise ratio only a little less than this. Channel electrical signal-to-noise ratio is given by:

$$\frac{I_a}{I_{n,a}} = \frac{1}{m} \left( \frac{\bar{I}_{pc}}{2e\Delta f_c} \right)^{1/2}, \quad (3)$$

where the factor  $1/m$  accounts for the maximum reduction due to secondary emission fluctuation noise and  $\Delta f_c$  is the channel bandwidth. Since the bandwidth of the dynode stages is of the order of several hundred megacycles, channel bandwidth is almost always determined by the anode circuit or, as will be shown later, by the frequency response characteristic of the phosphor.

### 2.2.3 Minimum Photocathode Current

We now find the minimum flux at the photocathode required to produce a specified signal-to-noise ratio in channel bandwidth,  $\Delta f_c$ . The total flux incident on the photocathode is given by:

$$F_{pc} = P_{\max} \int_{\lambda_1}^{\lambda_2} \left( \frac{P}{P_{\max}} \right)_\lambda d\lambda, \text{ watts.} \quad (4)$$

The photocathode current is given by:

$$\bar{I}_{pc} = \int_{\lambda_1}^{\lambda_2} P_\lambda S_\lambda d\lambda = P_{\max} S_{\max} \int_{\lambda_1}^{\lambda_2} \left( \frac{P}{P_{\max}} \right)_\lambda \left( \frac{S}{S_{\max}} \right)_\lambda d\lambda, \text{ amperes,} \quad (5)$$

where  $(P/P_{\max})_\lambda$  is the relative spectral emission characteristic of the phosphor,  $P_{\max}$  is the maximum flux per unit wavelength interval (watts/Å) at the photocathode,  $(S/S_{\max})_\lambda$  and  $S_{\max}$  are the relative and maximum photocathode sensitivities respectively, and  $\lambda_1$  and  $\lambda_2$  are chosen to include the entire wavelength region in which the spectral emission and photocathode sensitivity are both nonzero.

The minimum flux which will produce an over-all channel signal-to-noise ratio of  $(\bar{I}_a/I_{n,a})$  in channel bandwidth  $\Delta f_c$  is found by combining (3), (4) and (5). It is given by:

$$F_{pc,\min} = (m)^2 \frac{2e\Delta f_c}{S_{\max} k_m} \left( \frac{\bar{I}_a}{I_{n,a}} \right)^2, \text{ watts,} \quad (6)$$

where  $k_m$  is a normalized factor which depends only on the spectral match between the emission characteristic of the phosphor and the sensitivity characteristic of the photocathode, and is given by:

$$k_m = \frac{\int_{\lambda_1}^{\lambda_2} \left( \frac{P}{P_{\max}} \right)_\lambda \left( \frac{S}{S_{\max}} \right)_\lambda d\lambda}{\int_{\lambda_1}^{\lambda_2} \left( \frac{P}{P_{\max}} \right)_\lambda d\lambda}. \quad (7)$$

### 2.2.4 *Required Transmission per Channel*

A number of factors, singly or in combination, set the maximum flux density in the cathodoluminescent spot at the CRT. Examples are the thermal velocity limitation on the maximum current density in the electron beam, accelerating voltage, phosphor type and efficiency and the maximum phosphor loading which can be used without burn. Likewise, system requirements on the number of bits per channel or device limitations may set the maximum number of spots in the array at the CRT. Once the maximum flux density and spot size have been set, the maximum flux per spot at the CRT screen,  $F_{s,\max}$  is fixed. The minimum flux level at the photocathode which provides the required signal-to-noise ratio in the channel is given by (6). Clearly, therefore, each channel of the system must be designed so that a fraction,  $k_g \geq F_{pc,\min}/F_{s,\max}$  of the light emitted from the cathodoluminescent spot is transmitted to the photocathode. The minimum value of  $k_g$  has been arrived at through consideration of system requirements (sampling time, signal-to-noise, number of bits per channel, etc.) and CRT, phosphor and PMT characteristics. In the further consideration of device characteristics in Section III it will be seen that this is a reasonable approach, since there are a limited number of fast-decay cathodoluminescent phosphors, all of which are quite well matched to the relative spectral sensitivity characteristic of the most efficient photocathode available. Thus, once system speed, capacity, signal-to-noise and number of channels are set, we are led rather quickly to a choice of CRT size, phosphor and photocathode type.

Physically, the value of  $k_g$  is determined by the relative aperture of the channel objective lens and the channel magnification. Thus, we turn next in this paper, as is done in design, to consideration of the range of channel optical designs which will provide a specified value of  $k_g$ . It will be seen that the great flexibility of flying spot store systems derives from the fact that very many different optical systems can be chosen which will provide a specified value of  $k_g$ , set on the basis of system speed, capacity and performance. This allows wide latitude in number of channels, capacity and choice of lens design.

## 2.3 *Geometrical Factors in System Design*

### 2.3.1 *Transmission and Loss Factors*

The fraction of the light emitted from the cathodoluminescent spot which is transmitted to the photocathode in each channel,  $k_o$ , may be written as the product of two factors:  $k_{o1}$ , which represents reflection

and absorption losses in the optics, and  $k_{g2}$ , which is the fraction of the light from the cathodoluminescent spot that is intercepted by the effective aperture of the objective lens of the channel. We define  $k_{g2}$  as the optical acquisition factor.

In general, the range of variation of  $k_{g1}$  is small and in no case is it a controlling factor in design. On the other hand,  $k_{g2}$  varies through an enormous range and is the principal variable of optical system design.

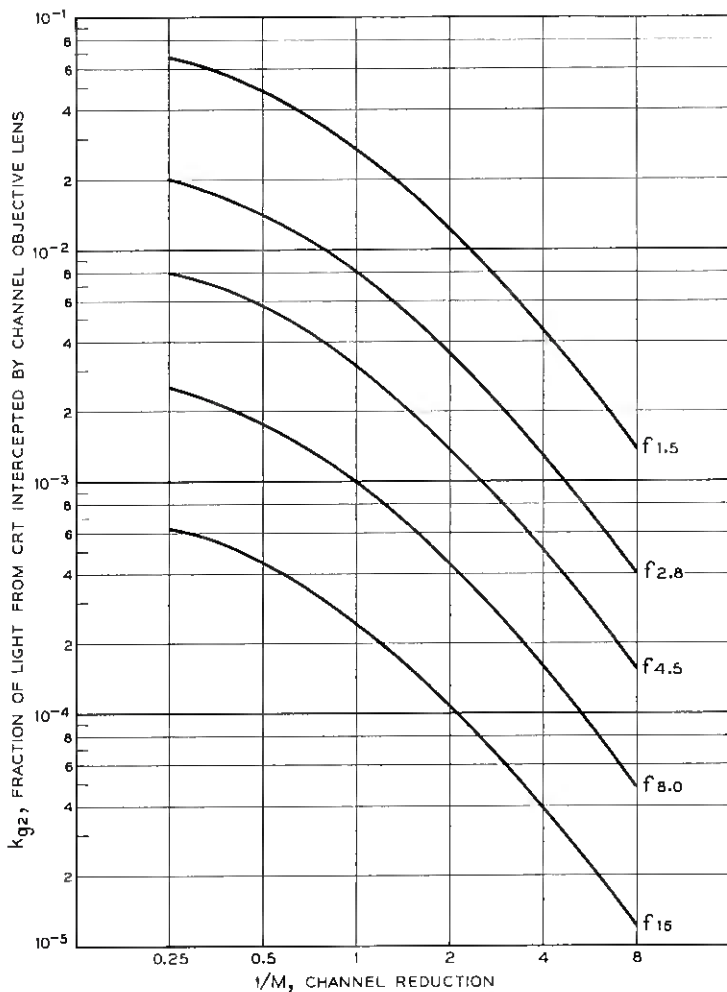


Fig. 2 — The system plane — individual channel designs are represented by points at the channel reduction,  $1/M$ , and channel objective lens  $f$ -number.

At the CRT screen the distribution in intensity has been found to be given approximately by  $I = I_0 \cos \theta$ ,  $\theta \leq 40^\circ$ , where  $\theta$  is the angle between the viewing direction and the normal to the screen. Including the effect of this distribution the optical acquisition factor  $k_{g2}$  is given by:

$$k_{g2} = \frac{1}{1 + 4f^2(M + 1)^2/M^2}, \quad (8)$$

where  $f$  is  $f$ -number of the lens used in the channel ( $f = \text{focal length}/\text{effective lens aperture}$ ) and  $M$  is the channel magnification.

### 2.3.2 Graphical System Design

A plot of the optical acquisition factor,  $k_{g2}$ , as a function of  $1/M$ , the reduction between CRT screen and photographic storage area, is given in Fig. 2 for lenses of various relative aperture. From this plot it is seen at once that the fraction of the flux intercepted in each channel increases with channel magnification and lens relative aperture. Each point of Fig. 2 represents a channel design. Channel designs which satisfy signal-to-noise requirements are those which lie above the values of  $k_{g2}$  given by

$$k_{g2} \geq \frac{k_g}{k_{g1}} = \frac{1}{k_{g1}} \frac{F_{pc,\min}}{F_{s,\max}}. \quad (9)$$

In order to establish the range of required values of  $k_{g2}$  we now consider the following example taken from the case of a practical system. System parameters are as follows: Cathode ray tube — accelerating voltage, 10 kv; beam current, 10 microamperes; spot size, 0.015 inch (90 per cent of current within  $0.015 \times 0.015$  inch area); phosphor, P-16; efficiency, 1.5 per cent. Photomultiplier tube — S-11 photocathode;  $S_{\max}$ , 0.050 ampere/watt; spectral match factor  $k_m$ , 0.88; secondary emission fluctuation noise factor  $m$ , 1.5. Optics — loss factor  $k_{g1}$ , 0.25. The minimum values of  $k_{g2}$  required for sampling in 0.1, 0.3 and 1 microsecond at electrical signal-to-noise ratios of 10:1 and 20:1 are as follows:

Sampling Time, in microseconds	Signal-to-Noise Ratio	Required Value of $k_{g2}$
0.1	10	$1.5 \times 10^{-6}$
0.1	20	$6.0 \times 10^{-6}$
0.3	10	$5.0 \times 10^{-6}$
0.3	20	$2.0 \times 10^{-6}$
1.0	10	$1.5 \times 10^{-6}$
1.0	20	$6.0 \times 10^{-6}$

Flying spot store designs fall within the range  $4 \geq M \geq \frac{1}{8}$ . The reasons for this are easily seen. At  $M > 4$  the very great size of each individual storage area (area = 16 times the area of spot array at the CRT screen) limits systems of reasonable dimensions to few channels and results in inefficient use of the photographic storage medium. At  $M \leq \frac{1}{8}$  three factors enter. First, for even the largest CRT spot sizes contemplated, the small spot size in the film plane makes the system increasingly susceptible to errors due to film blemishes. Second, the problem in repositioning the storage plate in the store after development becomes more difficult in inverse proportion to the size of the bit storage cell. Finally, before this level is reached it is possible to obtain a large enough number of channels for any application now foreseen.

### 2.3.3 Nonoverlapping Channels

In general, a solid angle slightly greater than that required to prevent overlap of images must be allotted to each channel in order to allow mounting of the film storage area, condenser lens and PMT. This requirement leads to a limit on the minimum value of channel magnification which can be used with any particular channel design. This limit is expressed by:

$$\frac{1}{M} \geq \frac{h_s}{h_{lc}} - 1 = \frac{f}{c} \frac{h_s}{f.l.} - 1, \quad (10)$$

where  $h_s$  is the CRT array size,  $f$  is the  $f$  number and  $f.l.$  is the focal length of the channel lens.  $h_{lc}$  is the distance between lens centers, and  $c$  is the ratio of the distance between lens centers to lens aperture.

Fig. 3 shows the minimum value of magnification which can be used for values of the ratio of CRT array size to lens focal length,  $h_s/f.l.$ , from 0.25 to 2.0, and for lens-spacing parameter  $c$ , values of 1.5 and 2.5, along with the data plotted in Fig. 2. Channel designs which satisfy the nonoverlap requirement are those to the right of the curve for the values of  $h_s/f.l.$  and  $c$  chosen for the system.

### 2.3.4 Optical System Length

System length is directly proportional to focal length of the objective lens. It is given by:

$$L_s = \left( M + 2 + \frac{1}{M} \right) f.l. \quad (11)$$

Minimum optical system length is found for the case where  $M = 1$ ,

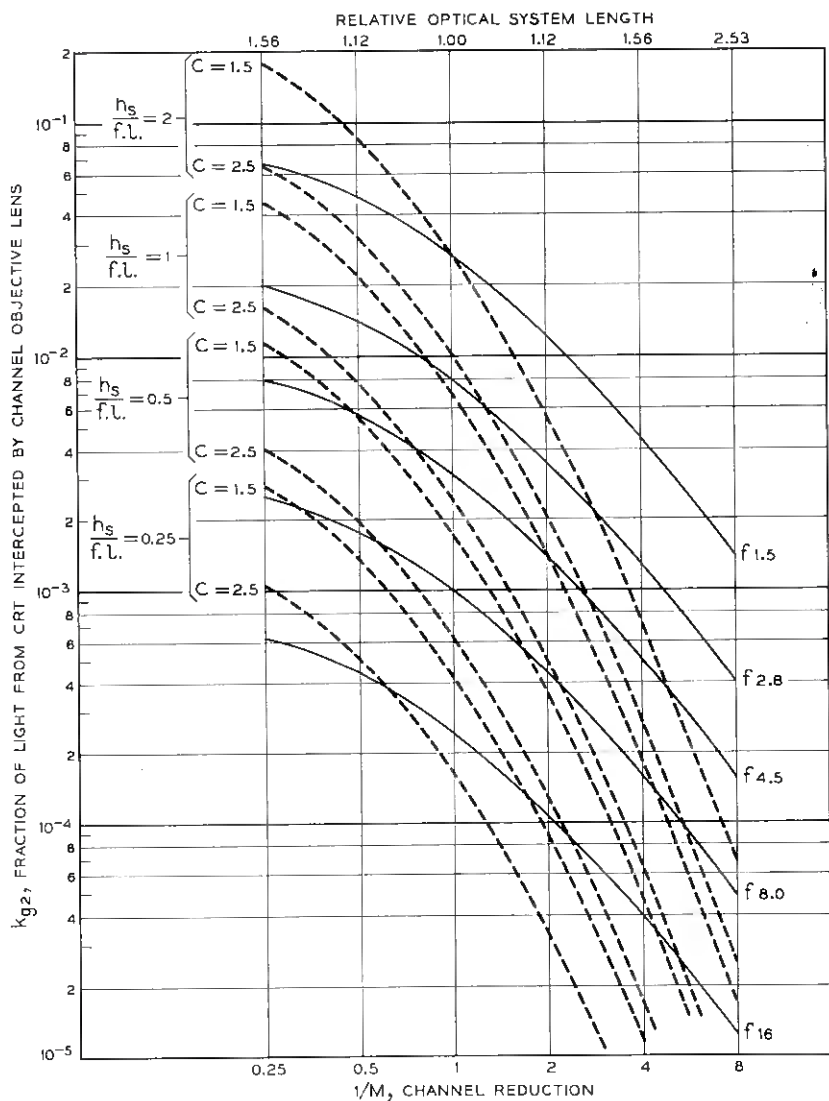


Fig. 3 — Minimum value of magnification which can be used for values of ratio of CRT array size to lens focal length.

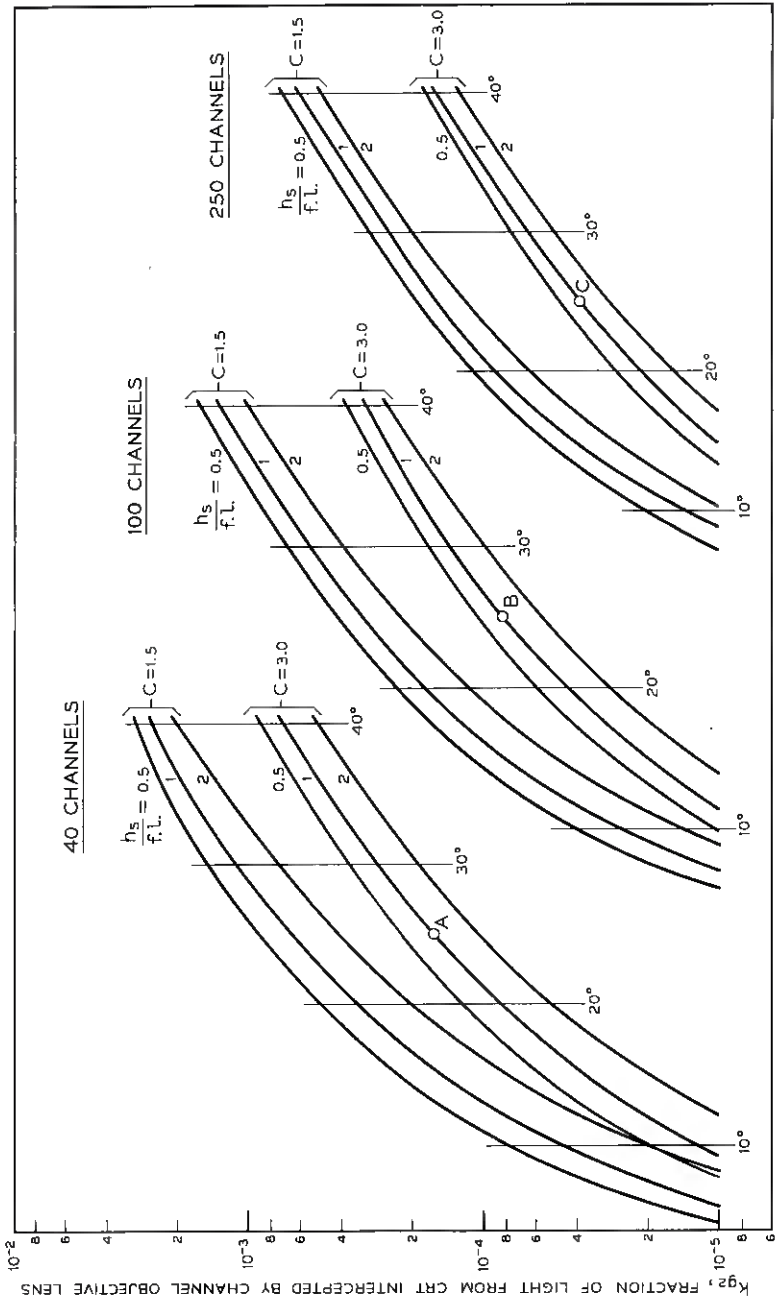


Fig. 4 — Field angle needed to get a specified optical acquisition factor in a specified number of channels.

but system length does not increase strongly with variation in magnification around unity. Thus, at  $M = \frac{1}{4}$  and  $M = 4$  the optical system length is 1.56 times the minimum length. As noted previously,  $h_s$ , the size of the array at the CRT, is usually made as large as possible, since system capacity and the number of bits per channel both increase with this dimension. When  $h_s$  has been fixed by the choice of a CRT the curves for  $h_s/f.l.$  in Fig. 3 become curves of constant focal length and define the minimum focal length which can be used for specified magnification ratio.

### 2.3.5 Number of Channels

The number of channels which can be combined into a system which provides a specified value of optical acquisition factor,  $k_{\rho 2}$ , depends on the field angle of good correction of the lens, the ratio of CRT array size to focal length,  $h_s/f.l.$ , and the ratio of lens mount diameter to operating aperture,  $c$ . Fig. 4 shows the lens half-field angle which must be obtained in order to get 40, 100 and 250 nonoverlapping channels. Each curve is drawn for specified values of  $h_s/f.l.$  and  $c$ . In finding these curves, we have first found the area in the lens plane which can be used. This is the area defined by the intersection with the lens plane of cones of constant half-angle  $\Phi$ , erected from the corners of the CRT array as shown in Fig. 1. This area is a function of the ratio  $h_s/f.l.$  as well as of the lens focal length and channel magnification. The calculation assumes that this area is approximately filled by a rectangular array of objective lenses, spaced on centers, by  $c$  times the working aperture of the lens. The conditions listed thus far do not define a curve, but rather define a set of curves, since a given value of  $k_{\rho 2}$  can be obtained with a large variety of different values of channel magnification and lens  $f$ -number, as shown in Fig. 2. The nonoverlap condition has therefore been used to find the minimum value of  $1/M$  and lens  $f$ -number which can be used for the specified values of  $h_s/f.l.$  and  $c$  in each case. The set of curves shown in Fig. 4 has been obtained using both this condition and those previously stated.

Thus, each curve gives the value of  $k_{\rho 2}$  which can be obtained in the stated number of channels as a function of lens half-field angle  $\Phi$ , with the following additional conditions: (a) values of the ratios  $h_s/f.l.$  and  $c$  are fixed, and (b) the value of  $k_{\rho 2}$  is obtained with the minimum values of channel parameters,  $1/M$  and lens  $f$ -number which can be used without violating the nonoverlap condition.

The curves of Fig. 4 illustrate several important features of flying spot store systems. First, it is important to note that values of  $k_{\rho 2} \geq$

$10^{-5}$  can be obtained in as many as 250 nonoverlapping channels, even at extreme values of the lens spacing parameter  $c$  and the ratio  $h_s/f.l.$ , with lens half-field angles  $\leq 30^\circ$ . As shown in an earlier example, the flux level obtainable at the photocathode in a practical system with  $k_{\rho 2} = 10^{-5}$  is such that sampling can be done in 0.1 microsecond with a signal-to-rms-noise ratio of 10. Most designs operate at a value of  $k_{\rho 2}$  greater than  $10^{-5}$ . Furthermore, sampling time may be increased by a factor of 10 or more without seriously affecting cycle time, since beam positioning requires a minimum of 2 microseconds. This increase in sampling time can be used where necessary to compensate for reduced flux level at the photocathode or to increase the signal-to-noise ratio.

A second fact shown in Fig. 4 is that  $k_{\rho 2}$  does not vary rapidly with number of channels, if  $\Phi$ ,  $h_s/f.l.$  and  $c$  remain constant. Thus,  $k_{\rho 2}$  typically decreases by a factor somewhat less than the factor by which the number of channels is increased. The curves also show that the number of channels which can be obtained with a fixed value of  $k_{\rho 2}$  and  $h_s/f.l.$  increases quite rapidly with the half-field angle of the channel objective lens. In considering the effect of increasing field angle on the number of channels obtainable at constant  $k_{\rho 2}$  (moving horizontally to the right across the curves of Fig. 4), it is noted that the value of  $c$  increases, since lens designs providing larger field angle usually have a greater value of barrel-to-aperture ratio than do those operating at narrow field angles. Thus, the value of the lens spacing parameter,  $c$ , might well be 1.5 for a simple triplet design operating at a field angle of  $15^\circ$  and 3.0 for a wide-angle design which could be used up to a half-field angle of  $30^\circ$ . The curves of Fig. 4 show that a 40-channel system with  $k_{\rho 2} = 10^{-4}$  can be constructed using a maximum half-field angle of  $12^\circ$ , with lenses spaced by 1.5 times the operating aperture ( $c = 1.5$ ), and  $h_s/f.l. = 0.5$ . The use of a wide-angle design with maximum half-field angle of  $24.5^\circ$  and lenses spaced by three times the operating aperture allows us to construct a 100-channel system providing the same value of  $k_{\rho 2}$ , with  $h_s/f.l. = 0.5$ .

### 2.3.6 *Scaling the System in Number of Channels*

One particularly useful method of scaling a flying spot store system to obtain a greater number of channels, starting with an existing design, assumes that the lens design, CRT design and CRT operating conditions remain constant. Thus, system field angle  $\Phi$ , lens focal length and the ratios  $h_s/f.l.$  and  $c$  remain constant. In this scaling operation we proceed along a line of constant half-field angle in Fig. 4, between curves for different numbers of channels with the common values of  $h_s/f.l.$  and

c. In order to provide a larger number of channels than in the starting design, within the same half-field angle and with fixed lens focal length, the channel magnification and/or the lens aperture must be reduced. Both result in decreased values of  $k_{\rho 2}$ .

As an example, consider scaling the system which has the following fixed parameters:  $\Phi = 25^\circ$ ;  $h_s/f.l. = 1$ ;  $c = 3$ . The points labeled A, B and c in Fig. 4 correspond respectively to 40-, 100- and 250-channel systems having these parameters. The values of  $f$  and  $1/M$  which yield given values of  $k_{\rho 2}$  can be found from Fig. 3. The attainable values of  $k_{\rho 2}$ , lens  $f$ -number and channel magnification for these three solutions are given by this table:

Number of Channels	$f$ -Number of Channel Objective Lens	Channel Magnification	Attainable Value of $k_{\rho 2}$
40	11	0.44	$2.2 \times 10^{-4}$
100	12	0.30	$1.1 \times 10^{-4}$
250	13	0.25	$5.0 \times 10^{-5}$

Thus, it is seen that increasing the number of channels and the capacity by a factor of 6.25 results in a decrease in flux level at the photocathode by a factor of 4.4. This reduction could easily be compensated for by increasing the sampling time by a factor of 4.4. In most cases, this increase would have negligible effect on cycle time.

This method of scaling is particularly useful, since it requires a minimum number of device changes: CRT design and operating conditions remain fixed, the lens design and focal length also remain fixed and no difficulty should be experienced in modifying the given lens design for the smaller aperture and slightly reduced magnification ratio which result from scaling to a system with more channels.

### III. DEVICE CHARACTERISTICS

#### 3.1 Phosphor

##### 3.1.1 Frequency Response and Efficiency

Cathodoluminescent phosphors differ widely in efficiency and decay characteristics. For the flying spot store, efficient materials in which the luminescence centers have short mean lifetimes to emission are used. Mean lifetime to emission is an important parameter, since the time for the flux from a given area to decay when the beam is moved to a new location limits the speed of position sensing and of readout. The type

of decay characteristic is also important. A number of materials which have been studied for use in the flying spot store show an exponential decay following the cessation of excitation. When such a phosphor is used, its effect on the over-all frequency response characteristic of the channel is precisely the same as that of a circuit which contributes a 6 db/octave cutoff above a corner frequency given by  $f = 1/(2\pi\tau)$ , where  $\tau$  is the phosphor decay time constant. By the use of an equalizing amplifier, this characteristic can be exactly equalized to provide a flat frequency response to a frequency higher than  $f$ . The amount of equalization which can be obtained depends on the gain-bandwidth product of the active element used in the equalizer.

A number of other phosphors of possible interest show hyperbolic or bimolecular decay characteristics. These are harder to equalize. The required gain-frequency response in the equalizing amplifier can only be approximated, and, unlike materials which show exponential decay, the constants of the decay characteristic are functions of beam current density and screen temperature.

Efficiency and mean lifetime are not independent variables, since efficiency can be exchanged for frequency equalization.

Thus, in comparing phosphors and in the design of circuits in which the phosphor is one element in the transmission path, it is useful to have a phosphor "frequency response" curve. Such frequency response curves plot the amplitude of the ac component of the flux as a function of frequency, at constant average beam power and beam power density, and with 100 per cent beam current modulation. Thus the ordinate at low frequency is proportional to the dc efficiency of the phosphor. The ac component of flux drops off above a cutoff frequency which is inversely proportional to the mean lifetime of the excited states in the phosphor. This is illustrated by the frequency response curves shown in Fig. 5 for two phosphors with different decay time constants (both are assumed to decay exponentially) and efficiencies. At frequencies up to  $f_2$ , electrical equalization can be employed at the output of the PMT to bring the frequency response curve for the system using phosphor A into coincidence with that for the system using phosphor B. If this were done, the signal level and signal-to-noise ratios would be identical in the two systems. The chief disadvantage, in practice, in the use of phosphor A would be the higher PMT output current that would result, since PMT life decreases with increasing anode current. However, if frequency cutoffs of  $f_2$  and  $f_1$  were sufficiently high for the servo and information channels respectively, a real advantage would accrue to the system through the use of phosphor type A, since the total available flux in the information storage

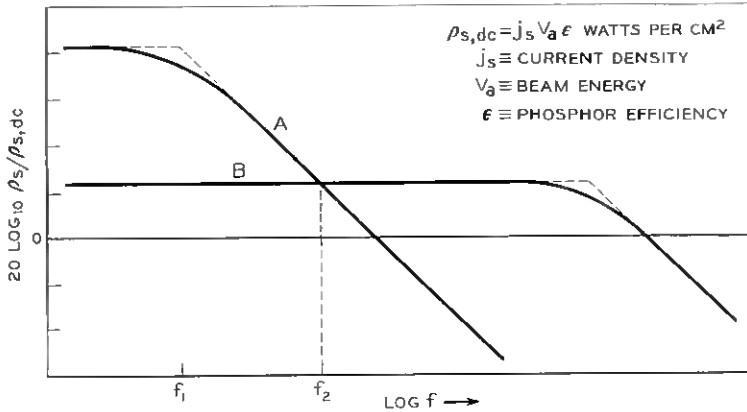


Fig. 5 — Frequency response curves for two phosphors with different decay time constants and efficiencies.

channels would be greater than that obtainable with phosphor type B in the ratio of their dc efficiencies.

Viewed on the basis of frequency response, efficiency and type of decay, P-16 phosphor has a distinct advantage over the slower but more efficient P-5 and P-11 phosphors, for systems requiring very fast beam-positioning times. Its decay time constant is not a function of current density and it does not saturate at any beam current that can be used without damaging the screen. The ultraviolet component of the emission from type P-15 phosphor has an extremely short decay time constant ( $\tau \doteq 0.01$  microsecond) but it is much less efficient than the slower P-16 material. Thus, even in a channel requiring uniform frequency response up to 10 mc, P-16 is superior, since its higher efficiency results in a higher output after equalization.

The efficiencies and decay time constants at 10 kv of three commonly used phosphors are given in Table I. The efficiencies are for aluminized phosphor screens, not for the materials themselves. These are for specific

TABLE I

Type	Material	Screen Efficiency	Decay Time Constant	Spectral Match to S-11 photocathode Factor, $k_m$
P-11	ZnS:Ag	6%	20-40 $\mu$ sec	0.92
P-5	CaWO <sub>3</sub>	2%	7 $\mu$ sec	0.89
P-16	2(CaO)(MgO)2(SiO <sub>2</sub> ):Ce <sup>+3</sup>	1.5%	0.05 $\mu$ sec	0.88

tubes, and it should be borne in mind that the screen efficiency obtained depends strongly on the method of phosphor and screen preparation.

### 3.1.2 Spectral Emission Characteristic

The constant  $k_m$ , defined by (7), is a measure of the quality of the match between phosphor spectral emission characteristic and photocathode relative spectral sensitivity characteristic. Thus, if all of the emission of the phosphor occurs at the wavelength of maximum spectral sensitivity of the photocathode,  $k_m = 1$ . This factor has been evaluated for the actual spectral responses of the three phosphors listed in Table I, and the type S-11 photocathode, and is also tabulated in Table I.

### 3.1.3 Phosphor Loading

Phosphor loading is defined as the power density in the incident electron beam. In quite reasonable electron optical designs, power density in the electron beam at the CRT screen can reach one kilowatt/cm<sup>2</sup> or more. The phosphor loading which can be employed without damage to the screen depends on the phosphor type, screen thickness and method of preparation. Phosphor loading rather than electron optical limitations usually sets the maximum current density in the electron beam and, as a result, the maximum flux density in the spot. Very much higher current densities could be used if the exposure of each spot were limited so that temperature rise would not be enough to damage the screen, and if it were possible to insure that the time between exposures of any single spot of the screen would be comparable to or greater than the thermal time constant of the screen. These conditions cannot be met in a random-access memory without slowing the system. However, phosphor loading could be increased in serial-access systems. A maximum phosphor loading of 200 watts/cm<sup>2</sup> can be used with a P-16 screen, provided that no spot is continuously exposed to the beam for more than 1000 microseconds, and that the average loading at any spot is less than 5 watts/cm<sup>2</sup>.

A special "time out" circuit has been incorporated in the store which prevents screen exposure of greater than 1000 microseconds at any one point, by deflecting the beam off the working area whenever no new address is received within this period of time.

## 3.2 Cathode Ray Tube

### 3.2.1 System Considerations

System considerations strongly influence the choice of CRT parameters. The CRT screen is made large, since total available flux and

number of spots both increase with screen area. Fast-feedback beam-positioning systems introduce the requirement for electrostatic deflection systems. Accelerating voltage, and therefore phosphor efficiency and flux density, is limited to set a bound on deflection amplifier power (this power is very significant — in the wideband deflection amplifiers used in maximum-speed feedback beam-positioning systems it is a large fraction of the total power consumption). Finally, phosphor loading, rather than the thermal velocity or space charge limitations, sets the maximum current density in the cathode ray tube beam.

### 3.2.2 *Spot Size Spacing and Uniformity*

Spot size may be set to produce the required flux per spot, given a maximum flux density, or the flux level attainable in the minimum size spot that can be resolved may be accepted and the rest of the system adjusted to work at that level. In both cases, spot spacing and uniformity must be set to provide satisfactory discrimination between stored "1's" and "0's" in readout.

The ability of the system to distinguish between stored "1's" and "0's" depends on the fraction of the total flux in the reading beam that is intercepted by the individual square bit storage cell in the photographic storage area. Flux falling outside the cell decreases the amplitude of the signal representing a "1" and increases the amplitude of a signal representing a "0". The size of the bit storage cell is chosen so that satisfactory discrimination can be obtained between the lowest-amplitude "1" and the maximum-amplitude "0". Many factors contribute to the spatial distribution of flux in the reading beam. Among these are the distribution in intensity in the cathodoluminescent spot, optical aberrations, variations in illumination and local imperfections. Since the distribution in intensity in the cathodoluminescent spot is only one of the factors contributing to the spread in the reading image, spot spacing on the CRT screen must be set at a greater fraction of spot diameter than would be the case if this were the only distribution that had to be considered.

In the flying spot store application, the relevant measure of CRT spot size is the size of the centrally located square within the cathodoluminescent spot, with sides parallel to the sides of the bit storage cell, which includes within it a specified fraction of the total flux from the spot. All measurements of CRT spot size have been done with equipment which allows us to find the fraction of flux as a function of the length of side of the central square. Spot spacing has been set so that a minimum of 90 per cent of the total flux falls within the square area

at the CRT screen, corresponding to a bit storage cell. Since the spot spacing at the CRT is set to meet this criterion in the case of the worst spot on the screen, it can be seen that efficient use of the CRT screen demands good uniformity of spot size over the surface.

The principal factors that reduce spot uniformity are defocusing due to the cylinder lens effect of the deflection plates and deflection aberrations. In order to minimize both types of distortion, deflection angles must be kept small.

Spot uniformity is also an important variable in the exposure process. Variations in the image area due to spot defocusing result in variations in density and size in the developed image and also reduce discrimination ratio in readout.

### 3.2.3 *Tube Length and Magnification Ratio*

The distance between the deflection plates and the screen in the CRT is determined by the array size and the maximum deflection angle. Since array size tends to be large and deflection angles small, CRT's for flying spot stores tend to be long. In order to get the long throw between deflection plates and screen without excessive total length electrostatically deflected CRT's usually image the first crossover at a magnification of 3 to 5.

### 3.2.4 *Beam Current and Cathode Loading*

In the usual electrostatically deflected CRT, operated at an accelerating voltage of 10 kv, the maximum current density which can be obtained at the screen is set by thermal velocity limitations. The current density which can be obtained at this limit, with conservative cathode loading that gives good CRT life, is considerably in excess of the current density which produces the maximum allowable phosphor loading. Likewise, the space-charge limitation on the maximum current density in the beam is not approached. We have tested tubes which provide maximum current densities in the focused spot of 20 to 100 ma/cm<sup>2</sup> and beam currents in the range from 5 to 30 microamperes.

These considerations might be interpreted to mean that the optimum CRT design would be one in which the accelerating voltage had been reduced to the point where electron optical and phosphor limitations are met at the same point. This is not the case, since uniformity of flux output and efficiency of the phosphor fall off rapidly with decreasing voltage.

### 3.2.5 Cathode Ray Tube Performance

The performance of a cathode ray tube depends strongly on the fabrication techniques used in its assembly as well as its design. Therefore a "benchmark" is given at this point rather than a theoretical prediction of spot size. We have tested CRT's at an accelerating voltage of 10 kv and a beam current to the screen of 5 microamperes, which produce an undeflected spot size of 0.015 inch (90 per cent of the light within a 0.015-inch square). Spot size in these tubes varies by at most 1.5 to 1 in a  $256 \times 256$  array.

## 3.3 Optics

### 3.3.1 Requirement for Correction over a Wide Field Angle

The basic optical system arrangement discussed here, in which the lenses are mounted in a plane with their axes parallel to the normal to the cathode ray tube screen, results in considerable simplification in the mounting of components and allows for more than one photographic storage area on each photographic plate. This arrangement requires that the lenses be corrected over the field angle between the ray from one corner of the CRT array to the lens farthest away from that corner in the diagonal direction. Thus, the lens must be well corrected over a half-field angle, which typically is  $25^\circ$  instead of the  $10^\circ$  or less subtended in the individual channel.

### 3.3.2 Requirement on Uniformity of Illumination

It is necessary that the illumination in the poorest channel of the system meet minimum requirements imposed by sampling considerations. A more critical requirement is that of uniformity of illumination within each channel, since variations here cause signal amplitude to vary from point to point and contribute to the probability of error in readout.

The average illumination in a channel varies with the field angle of the channel to the center of the CRT. Within the channel, illumination varies with spot position on the CRT screen. The variation in any one channel is greater than the cube of the cosine of the channel field angle and may amount to 10 per cent in an on-axis channel and to 20 per cent or more in a channel at the edge of the field. An improvement in this per-channel variation has been obtained by placing a stop in front of the lens to vignette the high illumination side of the field.

### 3.3.3 *Requirement on Condenser Lens*

Photocathodes show variations in sensitivity from point to point over their surface. Likewise, electron collection efficiency varies with position over the photocathode. Thus if the reading beam passing through the film were allowed to fall directly onto the photocathode, large fluctuations in signal amplitude as a function of beam position would result. The condenser lens is introduced to prevent this. It images the aperture of the lens onto the photocathode, and all flux passing through the photographic storage area in the channel falls within this area. Ideally, this image is stationary and independent of the position of the reading beam. Condenser aberrations tend to cause the image on the multiplier to move with variations in position of the reading beam. This motion must be small compared to the image size on the photocathode.

### 3.3.4 *Optical Requirements of the Optical Beam Encoder*

In many cases, it is desirable to use lenses in the servo channels that are faster than those in the information storage channels, since the feedback beam-positioning system operates at wide electrical bandwidths (e.g. 10 mc in maximum speed feedback beam-positioning systems) and because the beam is half covered by the servo edge at the readout position. Uniformity of illumination is more critical here, since it affects the spacing of the spots in the array at the CRT through the action of the feedback system.

### 3.3.5 *Lens Designs*

Almost all flying spot store designs result in the choice of lenses which are not diffraction-limited. This is a result of the fairly wide spacing of stored information used to minimize the effect of blemishes on the developed photographic storage plate. Thus, illumination and aberration performance are the critical lens characteristics.

The number of channels that may be used is limited by the field angle of good correction and good illumination that may be obtained with a given design. It also depends on the outside diameter of the lens mount. A lens designed to cover a relatively narrow half-field angle such as  $15^\circ$  will be much smaller in mount diameter than one which will cover  $30^\circ$  without vignetting. Thus, it may be desirable in some cases to use different lens designs and channel spacings in different areas of the lens array.

Two design modes are possible. A relatively narrow field design, such as a triplet, may be used over its limited field of view with efficient

channel packing, due to the small barrel-to-aperture ratio in this design. At the other extreme, a very wide angle lens may be used over a wide field with poorer channel packing efficiency.

A moderate field angle lens of the six-element double-Gauss type has been used in experimental work with excellent results. A  $25^\circ$  half field may be obtained at  $f/8$  relative aperture and channel magnification in the range from 4:1 to 6:1. The diameter and length of this design are relatively large, and illumination has been found to fall off at a rate greater than the cube of the cosine of the field angle. Tessar types have also been used which show only slightly poorer performance at these field angles.

The image characteristic important in lenses for a flying spot store is measured in terms of contrast at the spacing of the stored information in a flat focal plane. The lens must be designed to concentrate the maximum flux into the individual bit storage cell rather than to concentrate it into a sharp core surrounded by flare. The flare light in such a lens may not deteriorate photographic performance, due to its low density, but it does reduce the difference between the minimum "1" and the maximum "0", since it may represent a sizable fraction of the total light in the reading beam. All measurements of lens performance have been made in terms of the sine wave response or by methods which allow us to determine the fraction of the light falling within a specified area. The method of measurement is described in another paper in this issue.<sup>4</sup>

Distortion is not critical, because the stored information is written through the lens that it is later read through.

### 3.4 *Photomultipliers*

#### 3.4.1 *Photocathode Sensitivity*

The type S-11 photocathode has a wide region of high sensitivity and is well matched to most of the phosphors suitable for use in flying spot stores. This photocathode is the most efficient of the types commercially available. Photocathode sensitivities of 0.040 microamperes/microwatt, averaged over the photocathode, can be obtained at 3900 Å. This corresponds to a quantum efficiency of 12.7 per cent.

#### 3.4.2 *Noise and Current Amplification*

Noise in the photomultiplier detector plays an extremely important role. Provided it is no greater than shot noise, a very wide range of

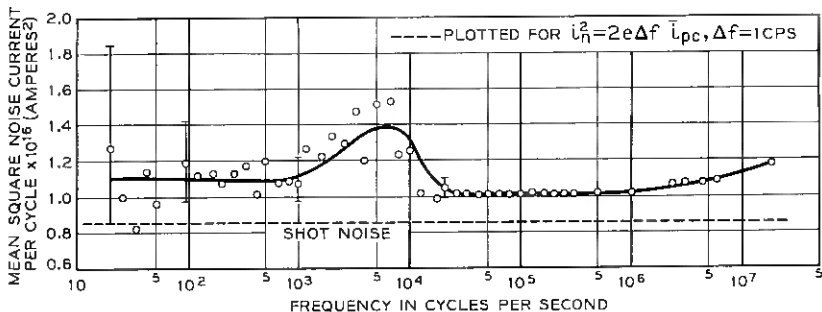


Fig. 6 — Noise power spectrum for photomultiplier.

systems can be built. Early studies on photomultipliers revealed noise in the anode current which was in excess of the expected shot noise by 20 db or more, plus sudden changes of total amplification by a factor of two or more. These anomalies caused great concern, since they would have seriously limited both the range of stores which could be built and the system reliability. It was found that the anomalous noise was associated with the piling up of "after-pulses." In a new design, "after-pulsing" and the sudden amplification changes in time have been largely eliminated. Tubes of this design show noise which is very little in excess of shot noise under the operating conditions commonly encountered in the flying spot store. Current amplification up to  $10^6$  at anode current levels of 350 microamperes can be obtained in this design without increase in noise power at the output due to regeneration. A measured noise power spectrum typical of those obtained for tubes of this type is given in Fig. 6.

#### IV. SAMPLING CONSIDERATIONS

##### 4.1 Sources of Error

Fluctuations in signal amplitude which affect probability of error in readout from an information channel include spot size and intensity variations at the CRT, phosphor blemishes, noise and gain variations in the PMT, blemishes on the developed photographic plates, CRT beam-positioning error, optical error and information sampler error. This section discusses means which have been used to minimize the probability of error due to these factors. Approximate criteria for allowable error probabilities are given, and the way in which early sampler designs were arrived at is described.

#### 4.1.1 *Variation in CRT Spot Size and Shape*

Local variations in spot size as well as variations which are a function of deflection angle are found in electrostatically deflected CRT's. In general, the distribution of intensity in the spot is not cylindrically symmetric. The straightforward way used to control error due to this variation is to set spot spacing on the basis of the poorest spot in the array.

#### 4.1.2 *Intensity Variations at the CRT Screen*

It has been found that the flux level varies from spot to spot on the CRT screen. When one set of spots is used more frequently than the others in a flying spot store the situation is further aggravated, since the phosphor fatigues more rapidly at these spots. In the case of a P-16 screen, the initial fatigue rate is rapid, but the rate decreases with time and a quasi-equilibrium state is reached after a few weeks. Thus, pre-aging of the tubes helps reduce signal fluctuations due to this cause. Even so, after a few weeks of continuous operation spot-to-spot flux variations of as much as  $\pm 15$  per cent have been observed.

In the flying spot store, a narrowband feedback control system which acts on beam current is used to hold average intensity constant to within  $\pm 1$  per cent. However, this circuit does not compensate for spot-to-spot variations in intensity. Such variations affect probability of error in two ways. The feedback beam-positioning system locks the image of the beam to a mechanical reference edge located in one of the servo channels.<sup>1,2</sup> An electrical "half-light" reference determines the final beam position. If a constant electrical signal were used as reference, beam position with respect to the storage location would vary with spot intensity. Beam-positioning error is especially serious, since it results in highly dependent bit-error probabilities. To reduce this serious source of error, one channel of the system is used to sense the flux level at each spot. Its electrical output is used to provide a dynamic half-light reference for the feedback beam-positioning system, which is nearly correct for all spots within the range from +20 per cent to -50 per cent of average intensity.

Even when the beam is correctly positioned, spot-to-spot variations in intensity contribute to signal amplitude fluctuations in the information storage channels. The sampler circuit has been designed to operate properly with these distributions in signal amplitude.

#### 4.1.3 *Phosphor Blemishes*

The best screens made by commercial setting techniques have been found to have a few phosphor blemishes of a maximum diameter of 0.004

inch per tube. Phosphor screen blemishes give rise to dependent bit-error probabilities in a word, which cannot be reduced by means of redundancy in the stored word. The use of spot spacings larger than the spot diameter is a straightforward way of minimizing phosphor blemish effects, but this is very costly in terms of capacity.

Phosphor blemish specifications are arrived at by considering their effect on readout. Clearly, no CRT screen with a phosphor blemish exceeding one spot diameter in extent may be used, since a blemish of this size would displace the writing beam enough to superpose some of the stored information. Some smaller blemishes can be tolerated, but the probability of occurrence of two such blemishes separated by one spot diameter or less must be negligible.

#### 4.1.4 *PMT Current Amplification Variations*

Variations in current amplification in the PMT can easily introduce error by causing some of the signals representing "1's" and "0's" to fall outside the corresponding discrimination levels in the sampling circuit. PMT's generally show an initial increase in current amplification followed by a slow, steady decrease over a long time, which is due to decrease in the secondary emission ratio of the high-current dynodes. A stabilizer circuit has been built which holds the over-all PMT current amplification constant to within  $\pm 10$  per cent without adjustment for relatively long periods of time.

#### 4.1.5 *PMT Noise*

As has been shown in Section 2.2.2, the electrical signal-to-noise ratio is determined very largely by the shot-noise-in-signal. The standard deviation of the electrical fluctuation noise in the channel is given by  $\sigma = m(2e\Delta f_c \bar{I}_a)^{1/2}$ . In a typical application,  $\Delta f_c = 1$  mc,  $\bar{I}_a = 350$  microamperes and  $m = 1.5$ . The calculated value of  $\sigma$  in this case is 5.8 microamperes. A  $\pm 3\sigma$  variation then corresponds to about  $\pm 7.5$  per cent.

#### 4.1.6 *Flux Variations Within and Between Channels*

Variations in flux level within and between channels lower both the optical discrimination ratio and window, and contribute to the probability of error. By the use of vignetting blades and varying stop sizes, flux variations within and between channels are limited to  $\pm 10$  per cent. This allows the use of a constant exposure time for all spots in plate-making, and makes it possible to use the same sampler circuit with both on-axis and off-axis channels.

4.1.7 *Storage Plate Blemishes*

A few blemishes are found on the photographic storage plates after development. These may be due to defects in the material or may originate during handling or processing.

One can arrive at a storage plate blemish<sup>4,5</sup> criterion from system operation requirements. In this discussion, a parallel channel arrangement is considered in which one bit of each word is placed in each storage area of the film plane. A storage plate blemish can then affect at most one bit of the stored word. Use of a single-error-correcting, double-error-detecting Hamming code makes it possible to detect single or double errors and correct single errors in each word.<sup>6</sup> System requirements may impose the condition that all words must be correct or correctable. Thus, when the photographic storage plates are tested after preparation, any plate in which one or more words contain a double error is rejected. The practical problem is, therefore, that the probability of making a satisfactory set of plates in a small number of trials be high.

As an example, we consider the case of a system in which one block of stored information consists of 30,000 19-bit words. Table II gives a summary of an arrangement which might be used.

The efficiency is the amount of correct information obtainable from a set of plates over the total information on the plates (redundant bits plus stored bits). In order to employ the Hamming code, six additional channels are added and the complete word, including the redundant bits, is obtained in one readout. We now calculate the probability of the occurrence of a noncorrectable word. Assuming that the probability of an individual bit being in error,  $p$ , is small ( $p^2 \ll p$ ), the probability  $P$  of two errors occurring within a 25-bit word is given by

$$P = \binom{25}{2} p^2.$$

If this expression is multiplied by the total number of words,  $w$ , the

TABLE II — SINGLE-ERROR-CORRECTING, DOUBLE-ERROR-DETECTING HAMMING ARRANGEMENT — SYSTEM PARAMETERS

CRT Array Size.....	173 × 173
Number of Channels.....	25
Word Length.....	19 bits
Redundant Bits.....	6 bits
Single-Error Correction.....	5 bits
Double-Error Detection.....	1 bit
Readouts per Word.....	1
Efficiency.....	0.760

TABLE III — PROBABILITY OF MAKING AN ACCEPTABLE SET OF PLATES

Probability of a noncorrectable word, $P = 300 p^2$	
Average Number of Plates, $U$	Individual Bit Probabilities, $p \times 10^{-4}$
2	2.8
4	3.9
6	4.5

average number of noncorrectable words,  $a$ , is obtained. That is,

$$a = \binom{25}{2} p^2 w,$$

which for this example becomes  $9 \times 10^6 p^2$ . A reasonable and convenient assumption — that the distribution of double errors on the plates is Poisson — is made. It follows from this assumption that the probability of having no double errors on the plate is  $a^0 e^{-a}/0! = e^{-a}$  and that the average number of plates,  $U$ , which must be made to obtain an acceptable plate, is just  $e^a$ .

Table III gives the value of  $p$  corresponding to  $U = 2, 4$  and 6. Thus, from simple considerations of system requirements, a reasonable criterion for maximum individual bit-error probabilities due to storage plate blemishes can be found. If we wish to obtain a satisfactory set of plates in two or less trials on the average,  $p$  must be  $\leq 2.8 \times 10^{-4}$  under the conditions of our example. Recent laboratory studies of the storage plate blemish problem indicate that this criterion will be easily met and in fact exceeded in practical systems.<sup>4</sup>

Plate acceptance can also be based on a count of the single errors on a plate, without regard to the location of these errors, the acceptance count being such as to virtually guarantee that no double errors exist in a single word. Plate verification by this means is also faster.

#### 4.2 Estimate of Nondependent Error Rate

An estimate of allowable bit-error rates from all nondependent error sources is now made. Since two plate errors do not occur in the same word in an acceptable plate, the most probable uncorrected errors result from the combination of a storage plate error and a single-bit error due to one or more nondependent error sources, or of two such nondependent single-bit errors occurring within the same word. Thus, let  $p_1$  be the probability of a bit being in error from all sources, other than storage plate blemish, which give rise to sensibly independent bit-error probabilities in a word. Assume that one uncorrected error every four hours in

the store readout is the maximum tolerable. For the 25-bit word of our previous example, the probability of a noncorrectable error is given by:

$$\binom{25}{2} \times (2pp_1 + p_1^2) = 600pp_1 + 300p_1^2.$$

In four hours, the number of incorrect readings is given by the product of the number of words read out and the probability that a word has a noncorrectable error. In a typical system,  $2 \times 10^5$  words might be read every second. Therefore, in our example,  $1 > (600 pp_1 + 300 p_1^2) \times 2 \times 10^5 \times 14,400$ . If  $p$  is  $10^{-4}$ ,  $p_1 < 5.8 \times 10^{-9}$ ; if  $p$  is  $10^{-5}$ ,  $p_1 < 5.8 \times 10^{-8}$ .

As a "benchmark", it can be noted that, for Gaussian noise and ideal conditions, the calculated values of  $p_1$  correspond to a minimum signal to rms noise power ratio of 21 db.<sup>7</sup>

One method of fast and relatively uncomplicated system operation involves the abandonment of the double-error detection feature in reading out the information. The additional redundant channel is still used for parity check. Should the parity check fail, single-error correction is initiated. Nonfailure of the parity check is taken to mean that the word is correct.

#### 4.3 Beam-Positioning Error

Beam-positioning error can give rise to highly dependent bit-error probabilities. In the preceding discussion, this error was assumed to be zero. The feedback beam-positioning systems which have been built generally position the beam to within  $\pm \frac{1}{16}$  spot diameter of the center of the bit storage cell. It has been found that this degree of mispositioning causes little degradation in over-all system signal-to-noise ratio.<sup>4</sup> However, when an occasional larger misposition occurs due to noise in the servo system, many bits in a word can be affected. Dependent errors of this type cannot be completely overcome by the means that have just been described. If the sampling circuit responds more slowly than the positioning circuit it is possible to hide rapid short duration mispositions from the information channels. If it can be determined that a misposition error has occurred during sampling, the system can be arranged to repeat the sample. The error rate in an experimental system has been reduced using these techniques.

#### 4.4 Optical Discrimination Ratio and Optical Discrimination Window

The information sampler circuit must be designed to work with the flux distributions representing "1's" and "0's" at the photocathode.

These distributions are a function of spot size; intensity variations and the distribution in intensity in the flux from the cathodoluminescent spot at the CRT screen; spot spacing in the CRT array; phosphor blemishes; halo and reflections in the CRT faceplate; optical aberrations; exposure time; film density and contrast and many others. At the time design was started these distributions were not known. However, experimental data were available on the minimum amplitude signal for a "1" and the maximum amplitude signal for a "0" when the "worst" spots were read by a spot of average flux level at the CRT. Two parameters chosen to be used with these data are optical discrimination ratio,  $R_{\text{optical}}$ , and optical discrimination window,  $W_{\text{optical}}$ . Optical discrimination ratio is given by  $R_{\text{optical}} = S/N$ , where  $S$  is the photocathode current corresponding to the lowest-amplitude "1" read by a spot of average flux level at the CRT screen, and  $N$  is similarly defined for the highest-amplitude "0". Optical discrimination window is given by  $W_{\text{optical}} = S - N$ , measured in terms of photocathode current.

#### 4.5 Worst-Circuit Approach to Combination of Errors

Since the amplitude distributions are not precisely known and since limits are known in most cases, the "worst-circuit" approach has been used in the design of the sampler circuit.

Let the maximum variations of each of  $k$  individual noise sources be  $\pm\alpha_i$ . Then the minimum discrimination ratio that is presented to the sampler is:

$$\frac{S(1 - \alpha_1)(1 - \alpha_2) \cdots}{N(1 + \alpha_1)(1 + \alpha_2) \cdots} = \frac{S}{N} \prod_{i=1}^k \frac{(1 - \alpha_i)}{(1 + \alpha_i)}. \quad (12)$$

Likewise, it is seen that the discrimination window at the sampler circuit is reduced from  $A(S - N)$  amperes to:

$$A \left[ S \prod_{i=1}^k (1 - \alpha_i) - N \prod_{i=1}^k (1 + \alpha_i) \right] \quad (13)$$

amperes, where  $A$  is the total amplification (in PMT and sampler circuit) up to the point where the sampler actually discriminates between a "1" and a "0". It is clear that the sampler discrimination levels for a "1" and "0" must be set within this window. These considerations are illustrated in Fig. 7.

Economic samplers having the bandwidths required for use in flying spot stores ( $\sim 1$  mc) do not have zero window width and, in addition, constitute a small but nonnegligible error source, due to component

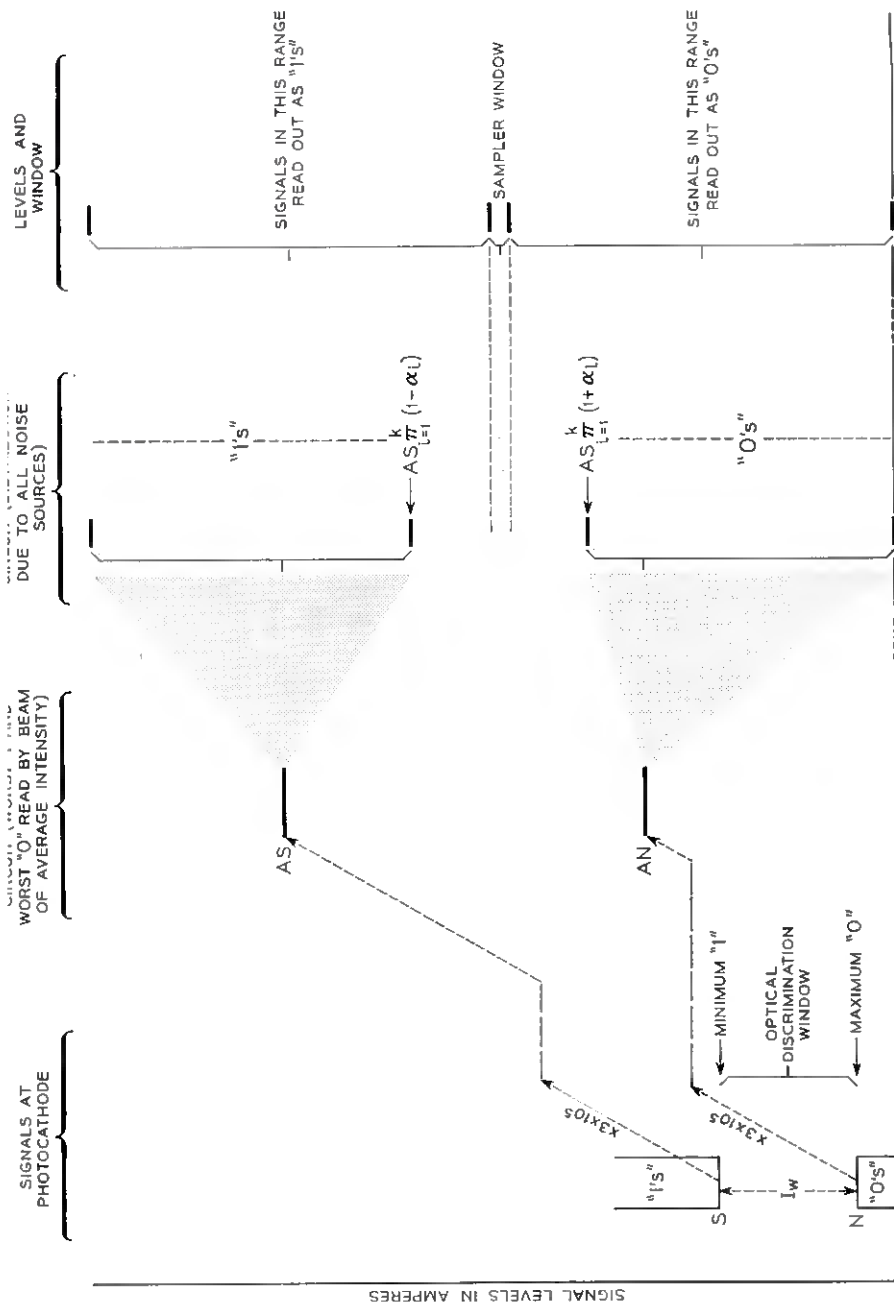


Fig. 7 — Signals representing "1's" and "0's" throughout the system, and optical discrimination window.

aging, power supply drift and residual error due to past history. An example follows:

*Estimated Error Source Variations*

Photomultiplier Noise	$\pm 7.5\%$
Photomultiplier Gain Variation	$\pm 10\%$
Light Variation Due to Optics (Within and Between Channels)	$\pm 10\%$
Light Variation Due to Phosphor (With Intensity Servo)	$\pm 5.0\%$
Positioning and Sampler Error	$\pm 10\%$
Minimum Optical Discrimination Ratio, $R_{\text{optical}}$	23:1
Minimum Optical Discrimination Window, $W_{\text{optical}}$	$1.5 \times 10^{-9}$ amperes

*Other Design Information*

Minimum Window at Photomultiplier output, $I_w$	$3.0 \times 10^{-4}$ amperes
---	------------------------------

The discrimination levels for "1" and "0" in the information sampler circuit are set by the circuit design. Sufficient amplification must be provided so that the signal distributions found at the photocathode fall outside of the sampler discrimination levels as shown in Fig. 7. The total PMT and circuit gain required is given by

$$A = \frac{I_w(R - 1)}{W \left[ R \prod_{i=1}^k (1 - \alpha_i) - \prod_{i=1}^k (1 + \alpha_i) \right]}. \quad (14)$$

For the example above  $A = 3.32 \times 10^9$ .

An approach somewhat better than worst circuit can be taken by assuming normality of the distributions when physical reasoning tells us that the true distributions cannot be far from normal. However, the complete problem involves not only the probability that a signal shall exceed certain bounds for a certain percentage of the time but also the indicator, or sampler response. Thus, the requirements on the sampling circuit response prior to and during the sample period must have satisfied a certain criterion. In a simple instance, the criterion might be that the integral of the signal pulse noise in the period of sampling remain within a certain bound.

#### 4.6 Information Sampler Design

An early electron tube sampler design is shown in Fig. 8. The first stage supplies gain and frequency equalization for the PMT anode circuit cutoff, and sets the bias voltage level at the suppressor grid of the following stage. The second stage employs a vacuum tube with two control grids. Coincident gating is accomplished in this stage by applying

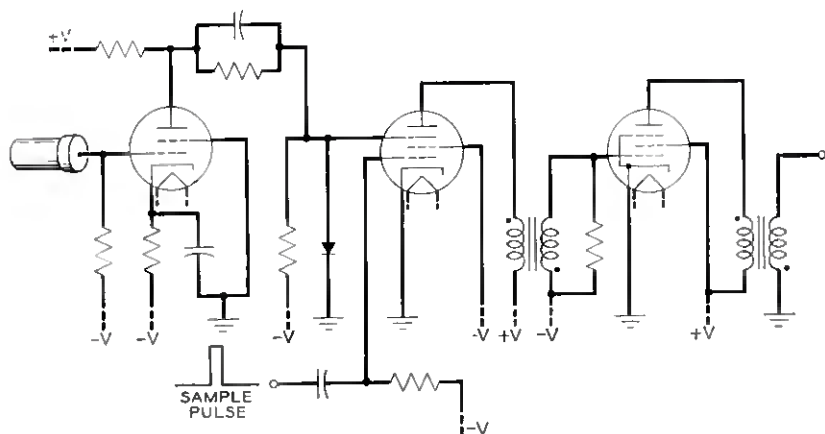


Fig. 8 — Information sampler circuit.

the signals representing "1's" and "0's" to the suppressor grid and a sampling pulse to the control grid. The bias set at the suppressor grid by the first stage is such that the maximum amplitude "0" does not take the tube above cutoff. Likewise, the minimum amplitude "1" carries the tube into the region of operation where output signal is only a function of the size of the sample pulse. The output stage is a pulse amplifier arranged to drive a low-impedance cable.

## V. DISCUSSION

### 5.1 Introduction of System Requirements

Maximum store cycle time is set by the intended application, and the phosphor type is then chosen on the basis of its speed of response and efficiency, because of the strong effect which these variables have on beam-positioning time. The phosphor type sets the maximum screen loading which can be used. In high-speed systems, the type S-11 photocathode is usually chosen because of its high efficiency and good match to the emission spectrum of the fast phosphors. The minimum CRT-accelerating voltage, consistent with the requirements on the number of spots to be resolved, spot size uniformity and flux uniformity, is then selected, since this minimizes deflection amplifier power and since, in any case, the additional beam current and power density available at

higher accelerating voltages could not be used due to the phosphor loading limit.

Since the number of spots which can be resolved and the total flux both increase with the size of the CRT screen, this dimension is usually made as large as space or the existing technology will allow and, in order to obtain maximum capacity with minimum equipment, the number of spots on the screen is often set at the maximum number which can be resolved. The degree of resolution required is set by sampling considerations. Channel capacity is set at the maximum number of bits which can be resolved, to provide the maximum number of stored words of a specified length. These factors set spot size and, together with phosphor efficiency and screen loading, they determine the maximum flux per spot.

From the foregoing, it is seen that, once store cycle time and channel capacity have been fixed by the intended application, the only independent variable left in the determination of the optical acquisition factor,  $k_{o2}$ , is the sampling time, since signal-to-noise ratio in sampling is also set by system requirements. Fortunately, fairly wide latitude is possible in the choice of  $k_{o2}$  in the case where sampling time is a small part of total cycle time.

### 5.2 Determination of Channel Parameters

The usable area in the lens plane approaches the area intercepted by a cone of half angle equal to the maximum field angle of the lens for low values of the ratio of screen height to focal length, where the variation in spot position in the array accounts for little of the total field angle. Screen height,  $h_s$ , is made large to maximize flux and channel capacity. If the ratio  $h_s/f.l.$  is made small, long optical systems result (assuming  $1/M > 1$ ). Thus, we see that efficient production of flux demands the use of a large CRT and that efficient use of this flux precludes the use of very short optical systems. Therefore, increasing capacity and speed almost invariably result in increasing system dimensions.

Having fixed the value of  $h_s/f.l.$  and  $c$ , the minimum value of  $1/M$  (and therefore the minimum system length) and the maximum  $f$ -number lens which can be used in the channel while meeting the requirement of nonoverlapping film storage areas are found by proceeding along the ordinate in Fig. 3 at the required value of  $k_{o2}$  to the intersection with the curve drawn for the given value of  $h_s/f.l.$  and  $c$ , the lens spacing parameter. All points to the right require a lens with larger aperture, and hence smaller  $f$ -number, and result in a longer system.

The curves of Fig. 4 show the half-field angle which must be obtained to set a specified value of  $k_{g^2}$  in 40, 100 and 250 nonoverlapping channels, and demonstrate the relationships between  $h_a/f.l.$ ,  $c$  and number of channels. They also demonstrate that a wide range of systems in terms of capacity and number channels can be realized, all providing a value of  $k_{g^2}$  sufficiently high to permit sampling in fractional microsecond times at high signal-to-noise ratios.

#### VI. ACKNOWLEDGMENTS

We wish to acknowledge many helpful discussions with R. W. Sears, M. Nesenbergs, W. Ulrich and H. Raag in the course of this work. The advice and encouragement of R. E. Staehler, R. W. Ketchledge and C. A. Lovell have been of great value throughout the project.

#### REFERENCES

1. Hoover, C. W., Staehler, R. E. and Ketchledge, R. W. Fundamental Concepts in the Design of the Flying Spot Store, B.S.T.J., **37**, September 1958, p. 1161.
2. Gallaher, L. E., this issue, p. 425.
3. Shockley, W., and Pierce, J. R., A Theory of Noise for Electron Multipliers, Proc. I.R.E., **26**, March 1938, p. 321.
4. Purvis, M. B., Deverall, G. V. and Herriott, D. R., this issue, p. 403.
5. Hollander, G. L., *Design Fundamentals of Photographic Data System*, Clevite Brush Development Corp., Cleveland, Ohio.
6. Hamming, R. W., Error Detecting and Error Correcting Codes, B.S.T.J., **29**, April 1950, p. 147.
7. Oliver, B. M., Pierce, J. R. and Shannon, C. E., The Philosophy of PCM Proc. I.R.E., **36**, November 1948, p. 1324.



# Optics and Photography in the Flying Spot Store

By M. B. PURVIS, G. V. DEVERALL and D. R. HERRIOTT

(Manuscript received November 3, 1958)

*The flying spot store is a semipermanent binary information storage system in which a cathode ray tube display is imaged on photographic emulsion by parallel optical channels. One section of the lens system provides the cathode ray tube with spot-positioning information for a closed-loop servo; the remainder of the channels are used for storage of the desired information. This paper discusses some of the optical and photographic problems to be considered in the construction of a flying spot store.*

## I. INTRODUCTION

The experimental electronic switching system uses as its large, semi-permanent memory a flying spot store which has been developed to meet the needs of the system.\* The flying spot store holds the telephone translation records and the operational program. Because it is desirable to handle this information on a word-organized basis, many parallel optical channels are desired.

Stores of several capacities and configurations have been proposed.<sup>3</sup> Discussion in this paper will be limited to the optical and photographic problems of an initial laboratory model flying spot store assembled to show the feasibility of the switching system at as early a date as possible,<sup>2</sup> and to bench tests of an optical configuration proposed for a store of approximately two million bits capacity. In each instance, reference is made to optical channels containing the stored information and to the optics of the closed-loop beam positioning servo.

---

\* The system was described in a paper<sup>1</sup> in a previous issue of this publication. The flying spot store<sup>2</sup> has been described in a previous issue and system considerations<sup>3</sup> of the flying spot store are discussed elsewhere in this issue. These articles provide pertinent background for this paper.

## II. SYSTEM CONSIDERATIONS

## 2.1 Flux Distribution

Fig. 1 shows the physical nature of a single channel. An optical channel consists of an objective lens, a photographic plate, a condenser lens and a photomultiplier tube. Ref. 2 points out the limits of the physical parameters involved in the realization of a flying spot store. The maximum flux per unit area which can be obtained from the phosphor screen on the cathode ray tube is the limiting physical parameter. The cathode ray tube characteristics which also influence optical system performance include light scattering within the phosphor, which affects the distribution of light within the spot; halo; defocusing of the spot with deflection; and local variations of light output with beam position, due to defects in the phosphor. The cathode ray tube face plate is one of the optical elements of the system.

The radiant flux required at the photocathode of the photomultiplier can, within the limitations of phosphor efficiency and aging characteristics, be achieved even for very high speed systems with lenses of relatively high  $f$  number. The lens aperture and focal length and the system magnification ratio may be selected to give as little as  $1/45,000$  of the 1500 microwatts total flux from a typical spot operated at the phosphor loading limit of a P-16 screen and yet operate at an output circuit bandwidth of 10 mc.

At the image plane, flux distribution within the spot is important. The flux density of the spot focused at the image plane must be sufficiently high to produce a relatively dense spot for an exposure time of a few

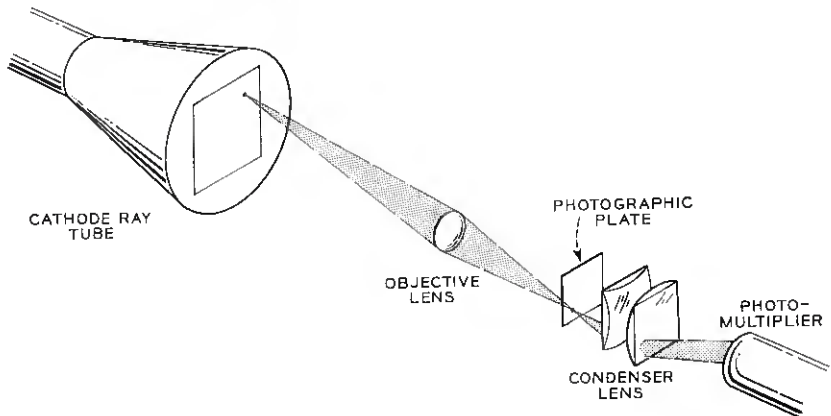


Fig. 1 — Single information channel of a flying spot store.

hundred microseconds. Flux levels which meet the signal-to-noise requirements of the photomultiplier will produce such spots in emulsions which are characterized by the spectroscopic types readily available. These are generally high-contrast, blue sensitive emulsions of medium to low granularity.

## 2.2 *Information Channels Organization*

In a multiple-channel store one or more bits from each word may be stored in each information storage area of the photographic plate. In general, the number of channels may be made equal to or greater than the word length, so that a single beam positioning yields a readout of the entire word. The total storage capacity is seen to be equal to the number of spots on the cathode ray tube raster times the number of channels viewing the raster. The maximum number of channels depends on the maximum off-axis angle at which the objective lens may be used and the limit of the flux level required at the photocathode. The off-axis angle and the distance from lens to cathode ray tube screen fix the size of the lens board. The number of lenses which may be placed in this area is a function of the diameter of the lens barrel and the magnification ratio of the system. Because the image areas may not overlap, the magnification ratio is usually less than 1 and decreases with increasing numbers of channels. Magnification may be selected such that both adjacent lens barrels and condenser systems have suitable mounting space. For a given flux level at the photocathode, the number of spots on the phosphor-loading-limited cathode ray tube will have to be decreased with increasing numbers of channels, since the spot size must be increased to provide more flux with the increasing  $f$  number of the objective lens. The general problem, then, is to ascertain the required number of addresses for the system application and predicate as large a spot size as feasible within the limitations of the cathode ray tube raster. Following this, a lens must be sought with an adequate field angle to allow enough parallel channels for the length of the word required by the system.

The exposure of the photographic plates containing the stored information is carried out by the store itself, under control of an external exposure unit. A shuttering system, normally open, is used to close off all image areas except the one to be written. The information to be stored is organized image area by image area and read to the store from magnetic tape. When a complete plate has been written, it is removed, processed and reinserted in the store. Optical variations between lenses in quadrants otherwise symmetrical preclude exchange of plates between quadrants or between parallel stores.

### 2.3 *Optical Channels of the Closed-Loop Beam-Positioning Servo*

The optical channels of the closed-loop beam-positioning servo provide the spatial division of the cathode ray tube raster area by means of code plates fixed in the image plane. Code plates are required for both the  $x$  and  $y$  coordinates, so that readout from the photomultipliers of these channels gives a spot's address on the raster in both coordinates in parallel binary words.

Beam positioning is accomplished by comparing the position readout of the servo channels with the desired address and deriving therefrom an error signal, which is used to deflect the beam to the desired position.

With these aspects of the system in hand, the individual characteristics of the optical and photographic elements of the system may be analyzed with respect to their contribution to system performance.

## III. OPTICAL DISCRIMINATION RATIO

### 3.1 *Definition*

The measure of success of the optical system in performing its function in the flying spot store can be determined from a single parameter, the optical discrimination ratio, which is defined as follows:

$$\rho = \frac{S_{(1,\min)} - S_{(0,\max)}}{S_{(0,\max)}}$$

where  $\rho$  is the optical discrimination ratio,  $S_{1,\min}$  is the relative amplitude of the minimum "1" in the channel, and  $S_{0,\max}$  is the relative amplitude of the maximum "0" in the channel.

All elements in the optical path — cathode ray tube, objective lens, photographic plate, condenser lens and photomultiplier — may be evaluated with respect to the effect they have upon the discrimination ratio.

### 3.2 *Experimental Approach*

Photography may be discussed in terms of many different parameters, but the most fundamental difference for the flying spot store application is whether one uses opaque spots on a clear background (negative) or clear spots on an opaque background (positive). A negative plate and a positive plate, as used in one information channel of the laboratory model of the flying spot store, are shown in Fig. 2.

It has been verified by experiment that it is very desirable to use a positive plate instead of a negative plate in the image plane. The positive

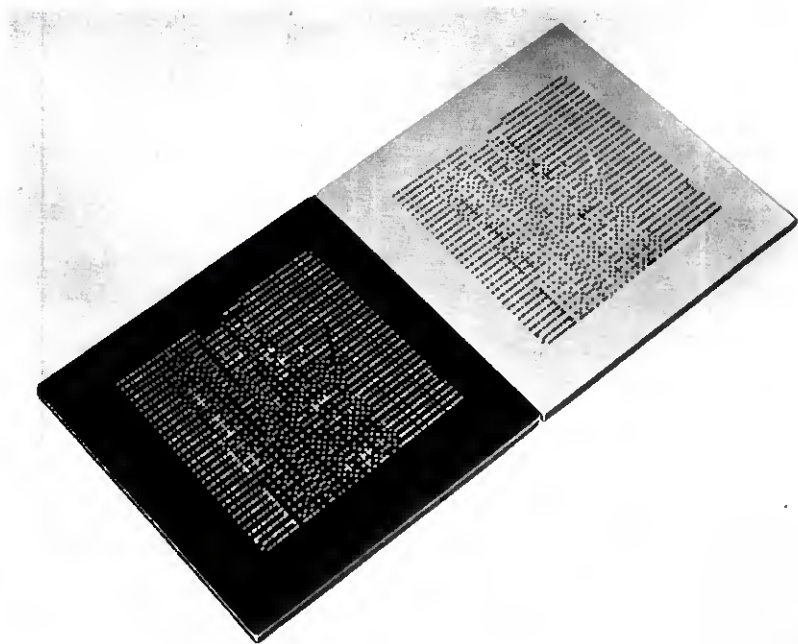


Fig. 2 — Positive and negative information storage plates.

plate gives an appreciable gain in the discrimination ratio of the optical system. Since this gain is often a factor of two or more, it is necessary to restrict the photographic emulsions to those which can be readily and reliably reversed in processing. This requirement, together with the speed requirement, reduces the possible emulsions to a very small number. Fig. 3 shows the basic quantities of the optical discrimination ratio for either negative or positive plates.

The following experimental procedure describes the method of measuring the optical discrimination ratio for positive plates. (The procedure applies equally for negative plates.)

A lens or array of lenses is set up together with the other optical elements of a flying spot store, and arrays of spots are written on a photographic plate. These spots are written in two ways: first, as isolated clear spots on the emulsion (1's) surrounded by dark spots (0's); second, as arrays of boxes in which a 0 is surrounded by 1's, as shown in Fig. 4. After the arrays are written, the photographic plate is removed, processed, reinserted in its original position and read out with the same experimental setup. The minimum 1 ( $S_{1,min}$ ) and the maximum 0 ( $S_{0,max}$ ),

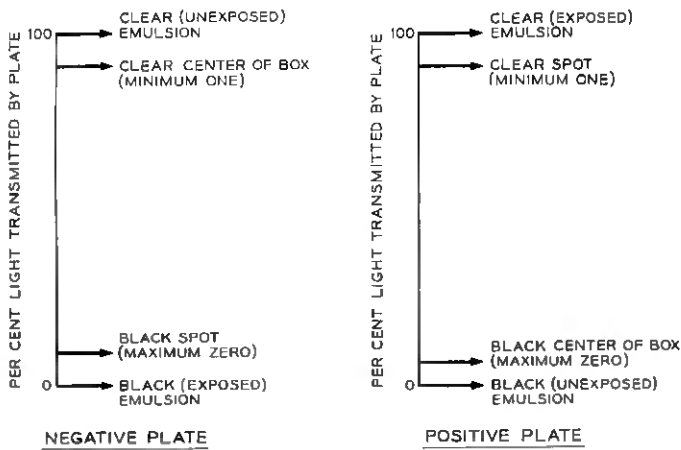


Fig. 3 — Definition of optical discrimination ratio.

as determined by the relative photomultiplier response of the channel, are then used to determine  $\rho$ .

The instrumentation for such tests must be very stable both electrically and mechanically, and also must permit measurements to be made at considerable distances off the system axis. Since conventional lens benches did not prove satisfactory, a standard machine shop surface plate was used to mount the various parts of the system, as shown in Fig. 5. This type of bench, together with the usual box parallels, straight edges, milling machine cross slides and rotary motions ordinarily found

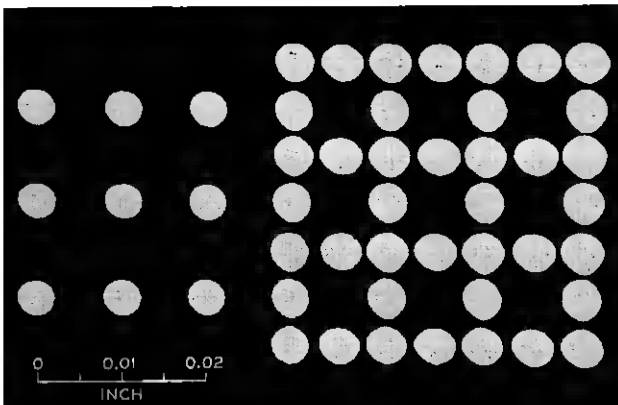


Fig. 4 — Enlargement of an array used to determine optical discrimination ratio.

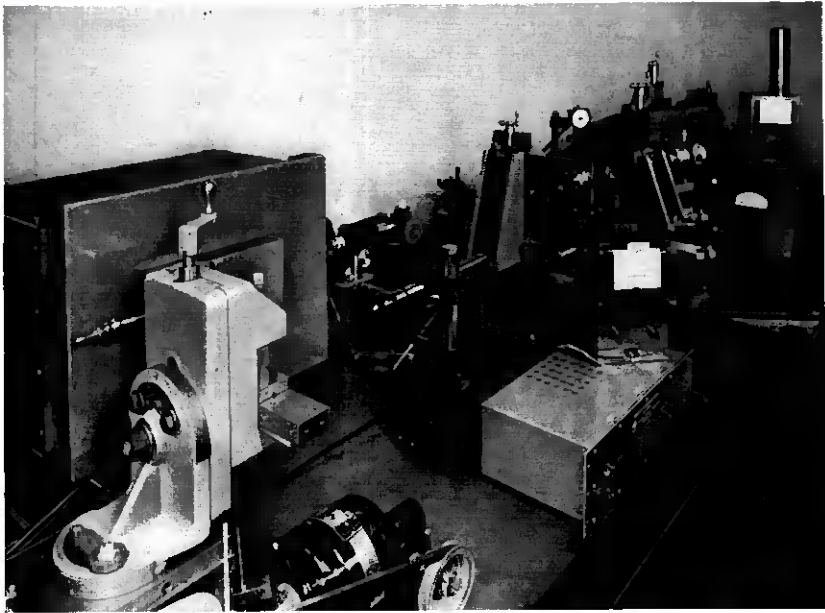


Fig. 5 — Typical experimental setup for optical measurements.

in a machine shop, has supplied the rigidity and versatility necessary in three-dimensional optical measurements.

While specific test results are inevitably a function of the many variables of the system, optical discrimination ratios of 10 to 1 or better may be achieved using a 6-inch  $f/8$  lens corrected for field angles to  $25^\circ$  imaging 0.018-inch cathode ray tube spots on 0.021-inch centers at 4 to 1 reduction.

#### IV. DISCRIMINATION RATIO AS A FUNCTION OF RESOLUTION

##### 4.1 Cathode Ray Tube Resolution

The maximum cathode ray tube resolution is determined by the light intensity distribution in the spot achieved by the tube. It has been experimentally verified that shrinking-raster methods of measuring spot size may be in error by as much as a factor of two when compared with results based on energy considerations. The intensity distribution of light within the spot is essentially Gaussian:

$$I = I_0 e^{-(r^2/2\sigma^2)}.$$

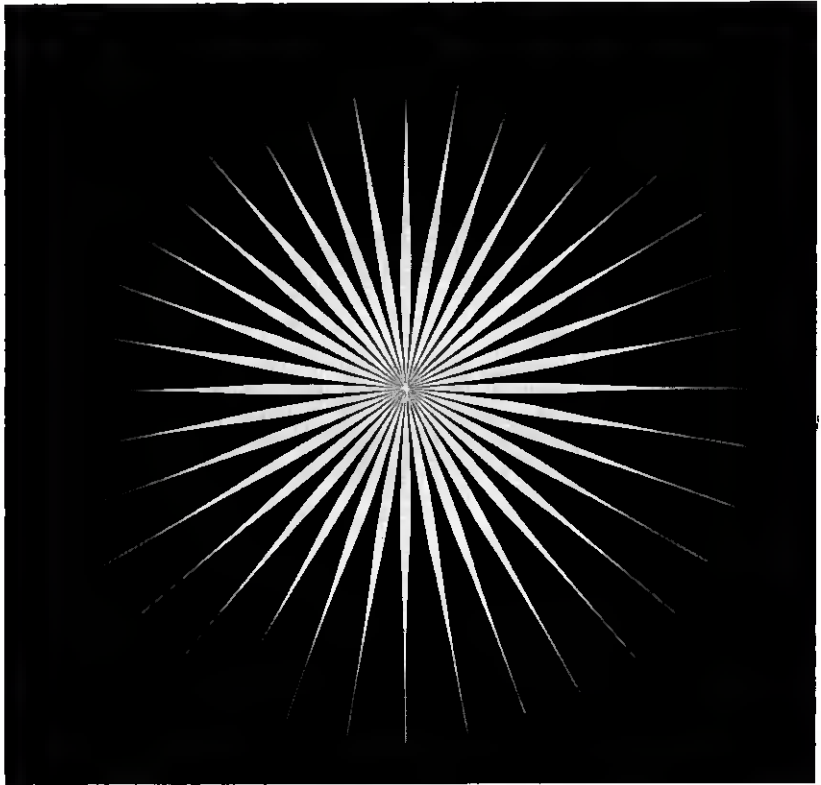


Fig. 6 — Reticle used to simulate intensity distribution of cathode ray tube spot.

A square whose side is  $4\sigma$  will contain 90 per cent of the energy of the spot. A mechanical simulation of the light source for initial test work was produced by making a reticle in the shape of a "Gaussian star," (Fig. 6) which, when imaged through a microscope, gives a light spot whose intensity distribution is Gaussian. Suitable filters effectively simulate the desired spectral region. A cathode ray tube, as characterized in Ref. 2, with a  $256 \times 256$  array of 0.018-inch spots on 0.021-inch centers would present an object plane 5.4 inches on a side and could be contained on a 10-inch tube. In the laboratory model store, a 3-inch raster of  $64 \times 64$  spots is used on a 7-inch tube. Clearly, as the limiting resolution of the cathode ray tube is approached, the problems of deflection defocusing, phosphor aging, phosphor blemishes and uniformity of the phosphor screen become more and more important. If the cathode ray tube spot varies with time in any of the parameters mentioned above, the value

of  $S_{1,\min}$  will also vary and tend to be smaller. If the apparent position of the spot on the tube face varies for any reason, both  $S_{1,\min}$  will be decreased and  $S_{0,\max}$  will be increased, with a resultant decrease in  $\rho$ , the discrimination ratio.

#### 4.2 *Lens Resolution*

The objective lenses used in a flying spot store image the spots from the flat face of the cathode ray tube onto the photographic plate. The phosphor screen of the cathode ray tube must either be planar or approaching planar quality or the objective lens must have a small aperture so that the depth of focus and field curvature characteristic of the lens can absorb the deviation. In general, this would be possible only with low-resolution systems working close to system axis, such as the laboratory model which employs a cathode ray tube face plate with a 30-inch radius of curvature. The 10-inch tube with a  $256 \times 256$  array will require a flat faceplate.

The objective lens must be designed to have very little curvature of field. The Petzval lens of the laboratory model, which exhibits excellent resolution characteristics on axis, also had satisfactory curvature of field at its aperture of  $f/13$ . In later flying spot store designs, a lower  $f$ -number lens was required and, for this problem, the curvature of field of the Petzval design is much too great, and, therefore, a six-element, double-Gauss type of objective lens was used. While the influence of several aberrations may be eliminated by writing and reading through the same optical channel, any aberrations which cause images of adjacent spots on the cathode ray tube to overlap must be reduced below that point. Chromatic aberration corrections are a function of the spectral emission characteristic of the phosphor. For example, P-16 phosphor emits energy over a relatively narrow spectral range, while P-24 phosphor covers a much broader spectral region. Therefore, the chromatic correction for a lens is smaller with P-16 phosphor than with the use of P-24 phosphor.

#### 4.3 *Experimental Measurements on Lens Resolution*

The resolution of the various lenses that have been tested has been determined by two different means.

##### 4.3.1 *Measurement of Contrast*

The contrast of the lens is measured by determining its sine wave response, using the technique described by W. Herriott<sup>4</sup> and D. R.

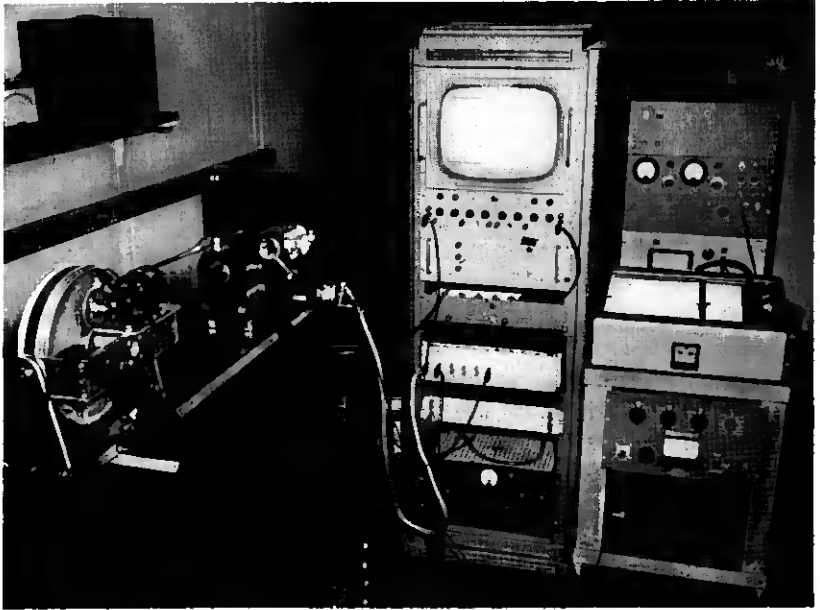


Fig. 7 — Equipment for measuring sine wave response of lenses.

Herriott.<sup>5</sup> This method has the advantage of speed in routine testing and permits both inspection and determination of the precise conjugates which optimize the operation of each particular lens in the flying spot store. The lens bench equipment used in measuring the sine wave response is shown in Fig. 7.

The contrast of the image of a sinusoidal target as a function of target spacing through focus on a lens sample is shown in Fig. 8.

#### 4.3.2 Measurement of the "System" Conditions

This method involves the use of the image analyzer shown in Fig. 9. This instrument, designed by D. R. Herriott, consists of a microscope that images the spot on a square aperture of variable size. Behind the aperture is mounted a photomultiplier tube. A beam-dividing prism and eyepiece allow visual observation of the spot. Measuring spot size in either the image or object plane consists of determining the aperture size which contains 90 per cent of the light, which may be considered a measurement of spot size as defined above. If the aperture is set at an opening small compared to the spot size, the image analyzer or the spot may be traversed to measure the intensity distribution of the spot or,

DATE 12-15-58  
 FIELD ANGLE 0°  
 FOCAL POSITION RELATIVE MM MARKED  
 INITIALS DRM

LENS TYPE 6 ELEMENT  
 CONJUGATE 4-1  
 WAVE LENGTH BLUE

LENS B & L  
 APERTURE f/8  
 FOCAL LENGTH 6"

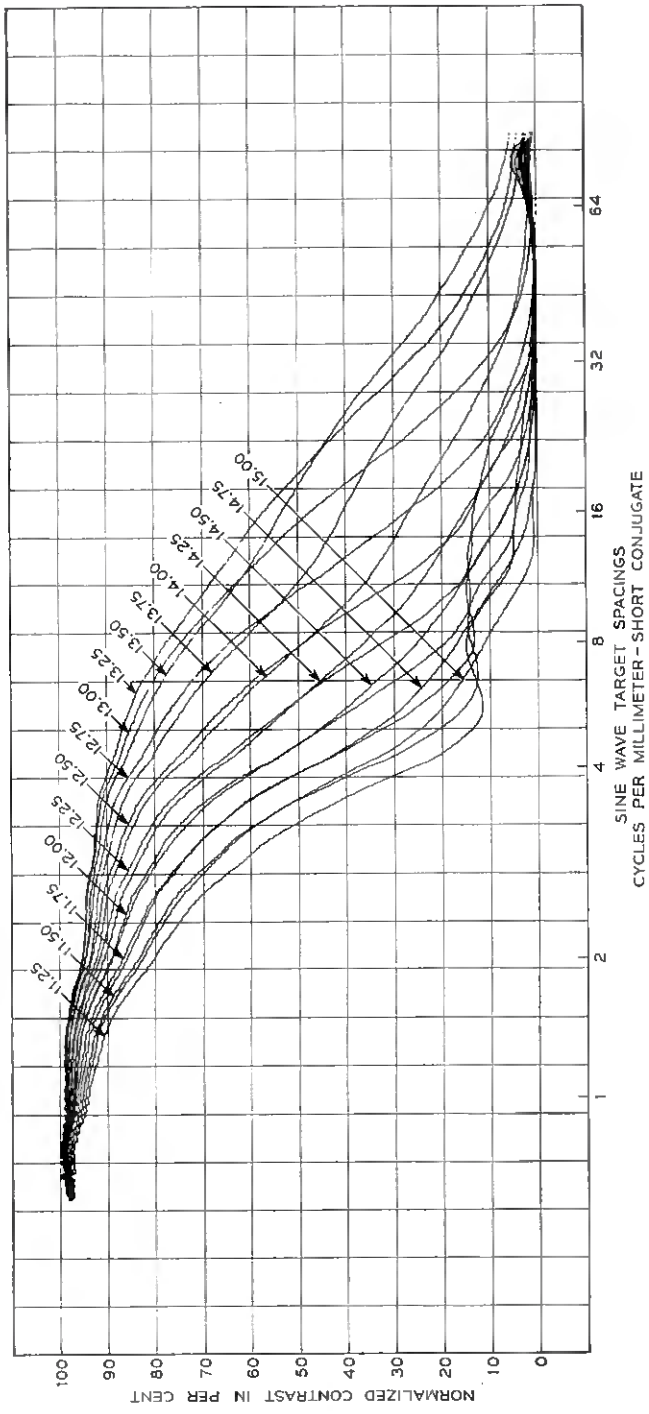


Fig. 8 — Sine wave response of a sample lens measured on a photoelectric lens bench.

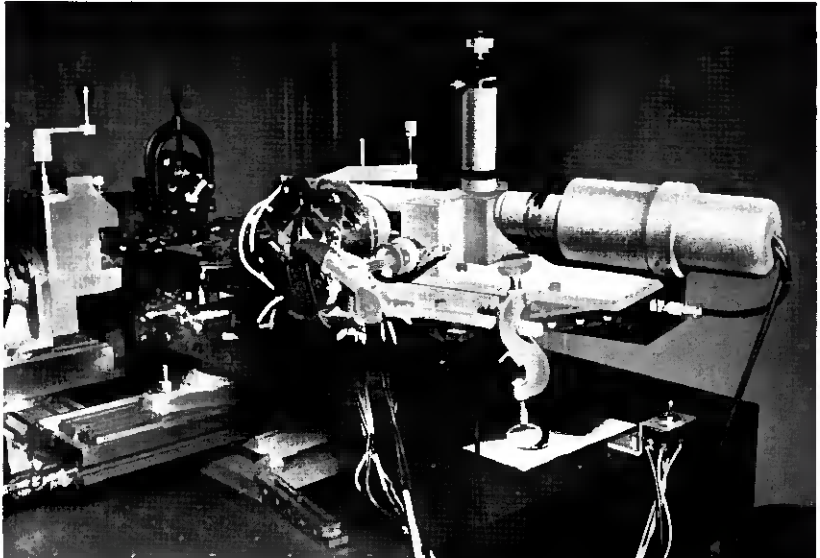


Fig. 9 — Image analyzer.

of course, the square aperture can be replaced by a slit and the intensity distribution measured in that way.

In operation, the square aperture is centered on the image by both the visual observation provided and by maximizing of the electrical output at a suitable aperture. The electrical signal is then recorded as the aperture is driven through its range of opening. Such a recording is shown in Fig. 10. The percentage of light incident upon various-sized squares is meaningful, in a system sense, since the square array used on the cathode ray tube assigns a square area to each bit of information. If the image quality of the lens is such that this percentage of incident light is relatively low for a square whose side is the spot spacing, then the remaining light must fall on adjacent areas, and the discrimination ratio will be reduced. Experience has shown that a 6-inch  $f/8$  lens corrected for a  $25^\circ$  field angle, as characterized in Ref. 2, may be expected to yield 90 per cent of the energy from a cathode ray tube spot into a square whose size is the spot spacing at the image plane.

#### 4.4 *Photographic Emulsion*

The resolution used in the flying spot stores now under investigation does not approach the resolution of the currently available photographic

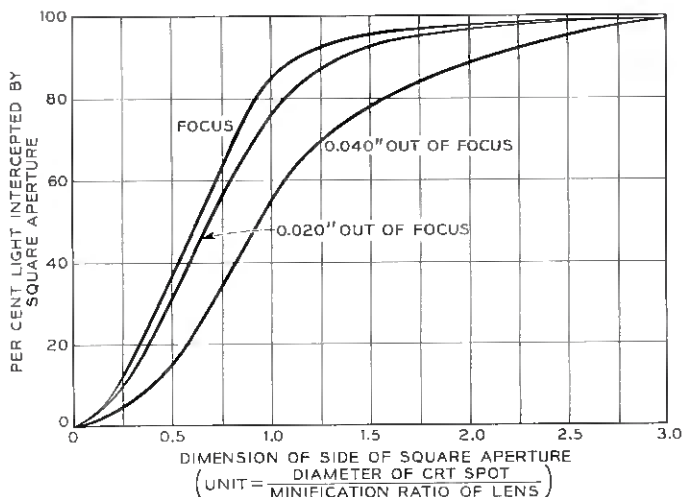


Fig. 10 — Percentage of light incident upon a square aperture for a 6-inch  $f/8$  lens and a 0.015-inch diameter cathode ray tube spot.

emulsions; therefore, the granularity of emulsion is not a limiting factor. However, care must be taken to avoid dust particles or emulsion blemishes which would affect readout of the store. With the resolutions now being considered, neither dust nor blemishes poses a serious problem.

## V. UNIFORMITY OF ILLUMINATION

After a flying spot store has been designed so that the cathode ray tube supplies enough light and the photomultipliers receive enough, it is still necessary to provide the same flux level through the various channels and uniform flux over the field of each individual channel.

### 5.1 Uniformity as Influenced by the Objective Lens

The problem of uniformity of illumination from channel to channel must be considered at the image plane, where the radiant flux varies as  $\cos^4\theta$ , and in the photomultiplier output. Both variations may be corrected to within  $\pm 10$  per cent by making the lens stop diameter a function of the position of the lens relative to the system axis. To make the light more uniform over the field of a particular lens, a front stop or "vignetting blade" is used to partially compensate for the  $\cos^4\theta$  and vignetting effects. Operating uniformity to  $\pm 10$  per cent can be achieved by these methods. Fig. 11 shows the effect of adding vignetting blades.

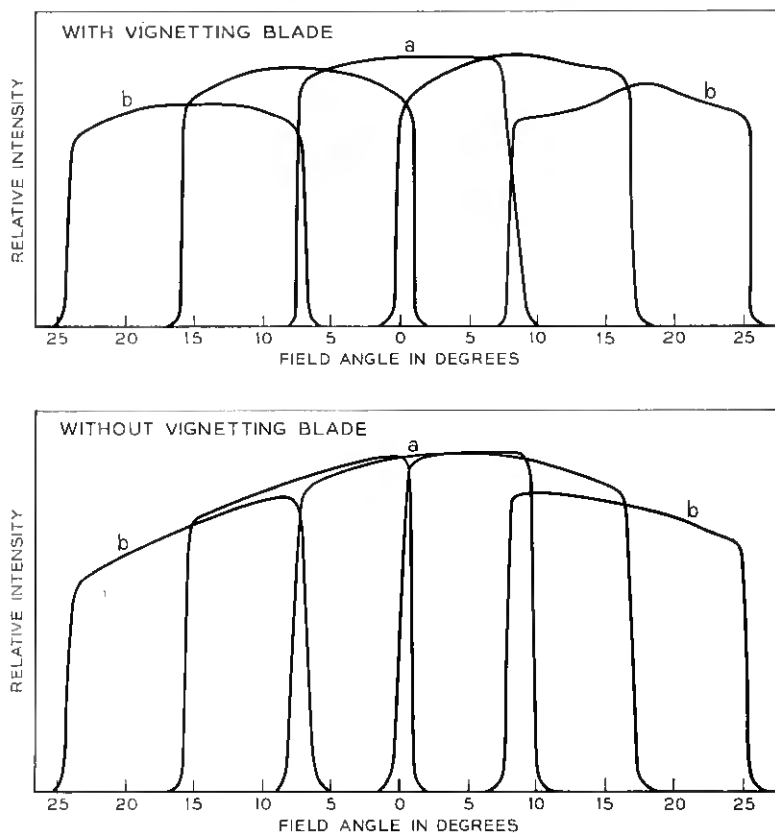


Fig. 11 — Uniformity of illumination across the field of the information channel lenses, showing illumination across the field of the lens on (a) the system axis and (b) the outside of the lens array.

### 5.2 Uniformity as Influenced by the Condenser Lens

The condenser lens in each optical channel is mounted at an angle to the photographic plate such that its optical axis passes through the center of its objective lens stop. This type of mounting allows the condenser system to operate on axis. The requirements that must be met by the condenser are that it shall image the objective lens stop and pass the intercepted light with a minimum loss to the photomultiplier. Since the light intercepted for any given address on the cathode ray tube lies in a rather small cone, which may pass through any zone of the condensing lens, the condenser must be corrected for spherical aberration to prevent the image from moving too greatly on the photomultiplier tube face.

Even rather small motions of the image are important, since the photocathodes of the photomultiplier tubes may be quite nonuniform in response, as shown in Fig. 12, and the resultant variation in photomultiplier tube output reduces the discrimination ratio as defined above.

In practical systems, it is necessary to provide adequate mounting space between channels for the lens, photographic plates and condensers. Because the condenser is mounted at an angle so as to be working on axis, it must be spaced some distance behind the photographic plate and therefore must be of larger aperture. The selection of magnification should be made to give just adequate mounting space for both the lens and condenser. This usually provides enough space between adjacent image areas for mounting parts. As the speed of the objective lens is increased, the angle of the cone of light passing through a point of the photographic material likewise increases, requiring larger condenser apertures.

## VI. THE OPTICS OF THE SERVO SYSTEM

The spot of light on the cathode ray tube is positioned to a given address in the raster by means of a servo system.

### 6.1 *The Laboratory Model Servo Optics*

In the laboratory model, a cylinder lens forms a line of light which is focused on a code plate. This code plate is made so that the complete  $x$

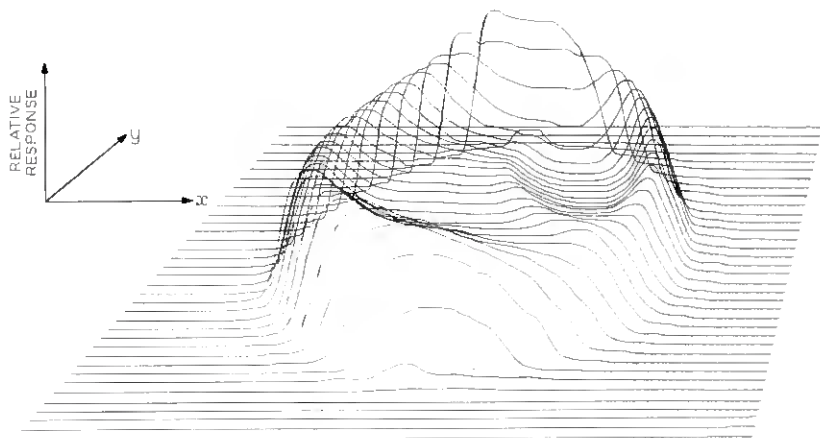


Fig. 12 — Sensitivity variation over photocathode on typical photomultiplier.

address of the cathode ray tube spot is given directly in the binary or Gray code. Another cylinder lens and code plate oriented at a  $90^\circ$  angle to the first gives the  $y$  address. Individual Lucite light pipes gather the light for each address bit from behind the code plate and conduct it to the photomultiplier tube. A unique cylinder lens system based on the Petzval design was used in the laboratory model. The line of light formed by the servo lens is about four inches long, and there is a considerable variation in intensity along this line, in spite of a front rectangular stop used to control the intensity distribution along the line. As in the case of the spherical Petzval, the curvature of field of the cylinder lens is quite severe and, over a flat image plane, this results in a 4-to-1 line-width variation. Although the lens performance is undesirable, the flying spot store has been operated very successfully.

### 6.2 Spherical Lens Servo Optics

When systems with many channels are considered, the use of a spherical lens encoder requiring one lens per address bit is preferred. Fig. 13 shows a sample lens assembly for a single channel. For example, a  $256 \times 256$  array would require 16 servo channels ( $2^8 = 256$ ) to read out the  $x$  and  $y$  coordinates of a cathode ray tube spot in binary form.

The cathode ray tube spot is positioned reproducibly to within  $\frac{1}{10}$  spot diameter by an analog method which assures that the image of the cathode ray tube spot in the servo channel lies half on and half off the controlling reference edge. The analog part of the servo response, as seen

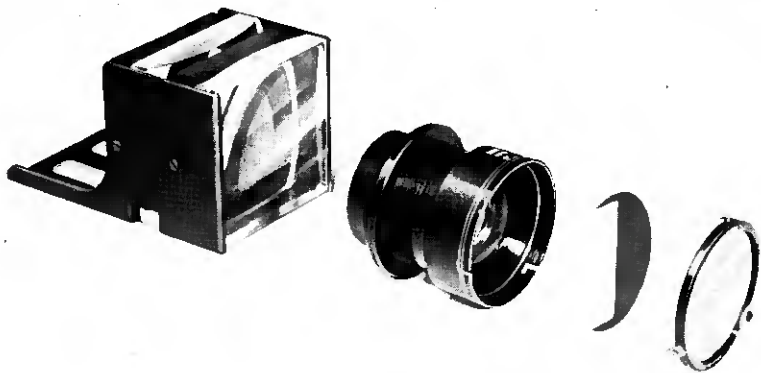


Fig. 13 — Sample lens assembly.

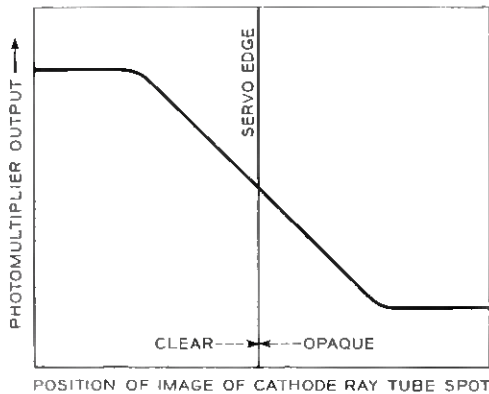


Fig. 14 — Optical crossover characteristic of servo system.

by the photomultiplier tube, should be of the form shown in Fig. 14. This curve is referred to as the optical crossover characteristic of the servo. If the slope of the crossover is greater, the spot is more accurately positioned but the positioning operation must be slower. If the slope is less, the positioning accuracy is decreased and the servoing speed may be increased.

Since the shape of this curve is important to the operation of the flying spot store, it must be controlled as accurately as possible. In the experimental electronic switching system, the crossover characteristic was controlled by defocusing the cylinder lens. In the spherical servo system, the same effect is produced and lens distortion eliminated as a problem by choosing a lens with an appreciable longitudinal chromatic aberration, and then photographing the servo code plates through the lens in red light, for which it is focused, and reading back with the blue-violet light produced by P-16 phosphor. Code plates produced for such a system are shown in Fig. 15. Another method of controlling crossover consists of using a combination of a weak cylinder lens and a spherical lens to produce a short line of light. This line is oriented at a slight angle to the positioning edge so that, when the image of the spot crosses the edge, the crossover characteristic is produced. By shaping the stop of the lens and rotating the cylinder lens, it is possible to control the crossover quite closely. Fig. 16 shows an oscillogram obtained on a test bench and indicates the excellent control that can be achieved. The oscillogram shows the crossover obtained for a 0.005-inch spot as imaged from a cathode ray tube and swept across alternate opaque and clear 0.010-inch bars.

The accuracy with which the spot is positioned on the cathode ray

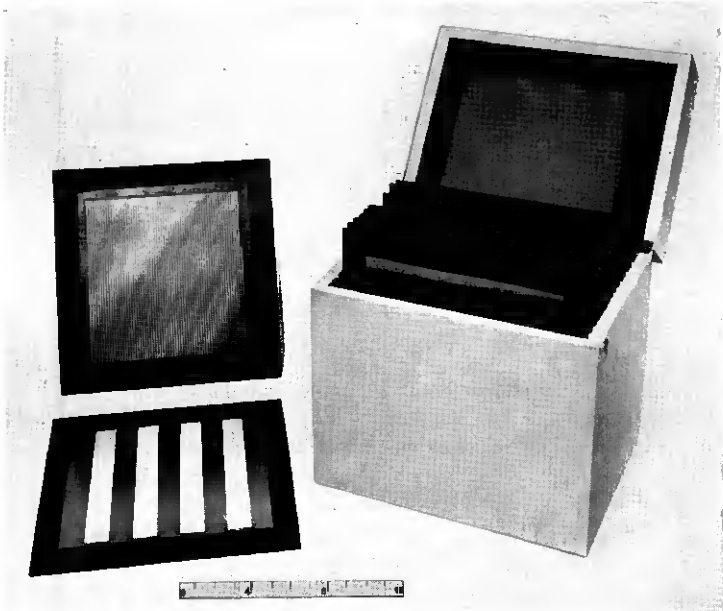


Fig. 15 — A set of master code plates for an optical beam encoder.

tube has a direct effect upon the optical discrimination ratio. If, for read-out, the image of the spot is not centered exactly upon a clear spot in the emulsion, then the value of  $S_{L,\min}$  is reduced and, for an opaque area,  $S_{O,\max}$  is similarly increased. The servo system will misposition the cathode ray tube spot if the light level in a servo channel varies with time. For this reason, it is important to control the radiant flux produced by the cathode ray tube as the phosphor ages.

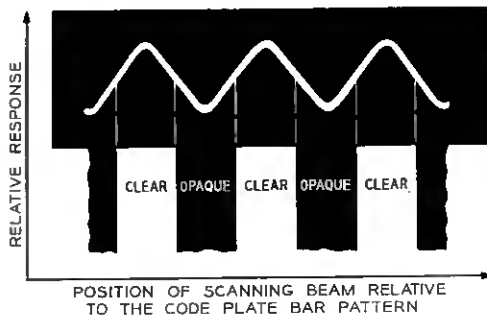


Fig. 16 — Oscillogram of the crossover characteristic of an optical beam encoder.

## VII. TOLERANCES AND DEFECTS

The major problem encountered in the construction of a flying spot store is that of distributing the mechanical, optical and electrical tolerances so that an optimum design is achieved.

For the laboratory experimental switching system, the spot spacing is so large, 0.048 inch, that the written spot may be "burned in" to a large size relative to the  $4\sigma$  spot. Conventional reversal processing gives clean, clear spots and blacks with a density of 2.0 or more. Under these conditions, optical discrimination ratios of 50 can be maintained.

A more difficult problem arises with higher resolution systems. A schematic drawing of this type of flying spot store is given in Fig. 17 to show the servo system and a typical information channel.

The servo channels are arranged in the form of a cross having its center on the axis of the system. The horizontal row of lenses controls the vertical position of the cathode ray tube spot and the vertical row, the hori-

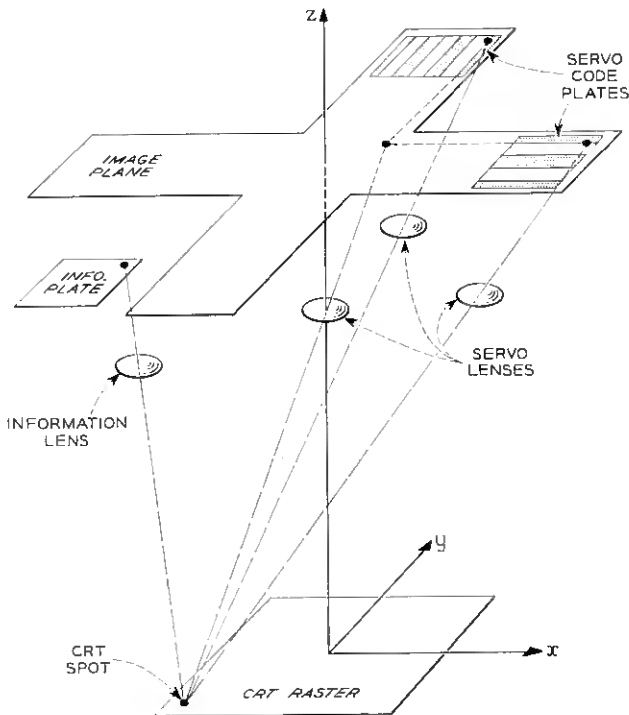


Fig. 17 — Optics of servo system.

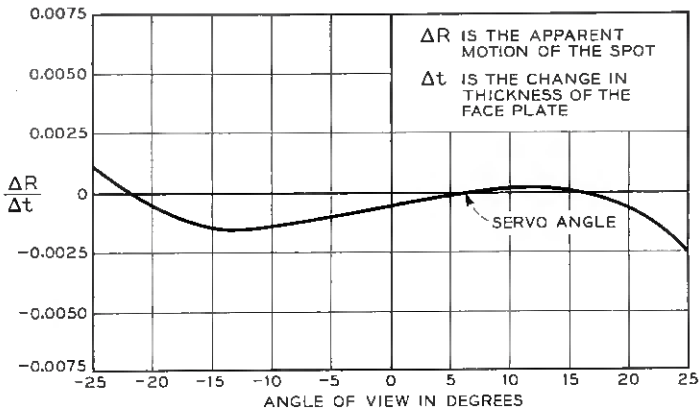


Fig. 18 — Motion of the servo-locked image in an information channel due to the change in the face plate thickness when the cathode ray tube is replaced.

zontal position of the spot. This type of geometric arrangement relaxes the mechanical tolerances for initial positioning of the cathode ray tube.

When a cathode ray tube must be replaced in the flying spot store, it is very desirable that the information in the store can be read without re-exposure of the plates. With the servo system shown in Fig. 17, and the present tolerances of cathode ray tube face plates, it is expected that a tube may be replaced without serious difficulty. Fig. 18, for example, shows a curve for the amount of spot motion, in the image plane, when the face-plate thickness of a cathode ray tube varies from tube to tube and the spot is locked to give a servo address.

The effect of the movement of the image of the readout cathode ray tube spot relative to the written spot is shown in Fig. 19. The amount of movement permitted by the system will be determined by the cathode ray tube spot size, the intensity distribution and spacing, the imaging quality of the lens, the exposure time, the emulsion speed and contrast and the photographic processing methods.

Other elements in the optical system which influence the optical discrimination ratio are defects in the cathode ray tube phosphor and in the photographic plate. The optical discrimination ratio will be reduced if the cathode ray tube phosphor has blemishes which cause the servo system to crowd spots together, or if the aging of the phosphor is so severe that the radiant flux cannot be held constant by the intensity monitor. Any blemishes or dust particles on the photographic plate which block clear areas or produce unwanted clear areas will also reduce the discrimination ratio.

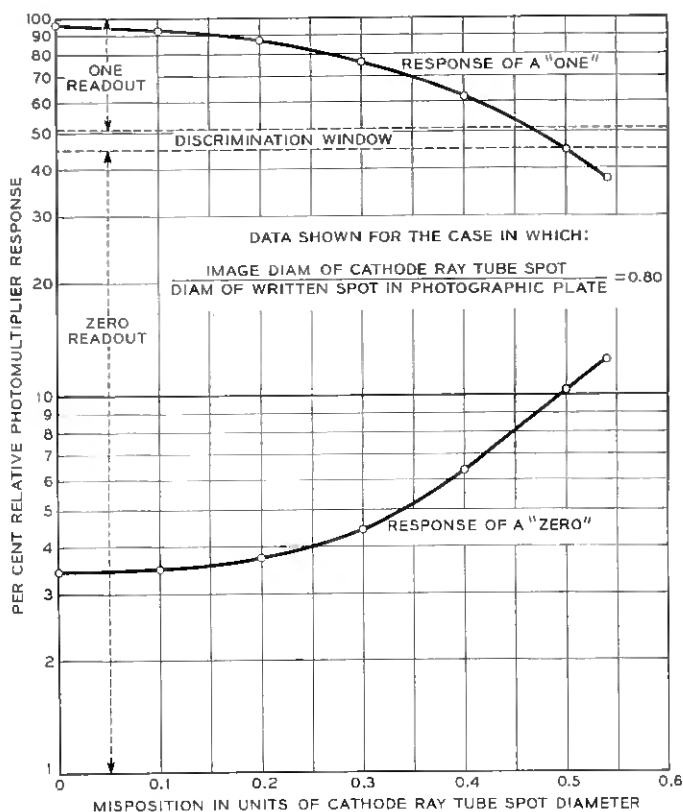


Fig. 19 — Effect of mispositioning of readout spot relative to the written spot for a typical information channel using a positive plate.

Experience with carefully made phosphors and standard photographic materials shows that, in both cases, adequate quality may be obtained to meet system requirements.

#### VIII. CONCLUSIONS

An experimental laboratory model flying spot store has been built and operated, and the feasibility of a multiplexed optical-photographic permanent memory has been demonstrated. Laboratory experiments on other possible optical systems have extended the art to demonstrate the feasibility of multichannel systems using a spherical lens optical beam encoder for servo control of the cathode ray tube spot. Studies of

tolerances on this system indicate satisfactory margins for reliable operation can be achieved.

#### IX. ACKNOWLEDGMENTS

The authors wish to acknowledge the aid of their colleagues in carrying out the many laboratory experiments conducted over the past three years. Especially acknowledged are the contributions of W. Herriott, F. W. Clayden, C. W. Hoover, D. C. Koehler, R. F. Schunneman, G. E. Reitter, Mrs. R. K. Dudek, R. Call and H. Robertson. The Bausch and Lomb Optical Company has provided lens designs and the Eastman Kodak Company has given advice and assistance on the photographic problem for which the authors are appreciative. The John F. Klarmann Co. ruled the master code plates shown in Fig. 15. The encouragement of R. E. Staehler and R. W. Ketchledge has been invaluable.

#### REFERENCES

1. Joel, A. E., Jr., An Experimental Switching System Using New Electronic Techniques, *B.S.T.J.*, **37**, September 1958, p. 1091.
2. Hoover, C. W., Jr., Staehler, R. E. and Ketchledge, R. W., Fundamental Concepts in the Design of the Flying Spot Store, *B.S.T.J.*, **37**, September 1958, p. 1161.
3. Hoover, C. W., Jr., Haugk, G. and Herriott, D. R., this issue, p. 365.
4. Herriott, W., A Photoelectric Lens Bench, *J. Opt. Soc. Am.*, **37**, June 1947, p. 472.
5. Herriott, D. R., Recording Electronic Lens Bench, *J. Opt. Soc. Am.*, **48**, December 1958, p. 968.

# Beam-Positioning Servo System for the Flying Spot Store

By L. E. GALLAHER

(Manuscript received November 5, 1958)

*This paper describes the cathode ray tube beam-positioning servo system essential to the accurate and reliable microsecond access to the photographic information in the flying spot store. The characteristics of both the basic servo loop and its components are discussed and several variations of the basic scheme are compared in relation to the system requirements.*

## I. INTRODUCTION

The flying spot store, a large, high-speed semipermanent memory, has been described by Hoover, Staehler and Ketchledge.<sup>1</sup> They have discussed the fundamental concepts and purposes of such a store and have clearly indicated that an essential feature of such a store is a servo-controlled positioning system. One form of such a positioning system has been described by them. This paper will consider to a greater extent the forms such systems may take and their relationship to the design objectives of the store.

### 1.1 System Objectives

Although the specific system environment for which the store designs were executed is a telephone switching system,<sup>2</sup> the use of the store in more general real-time data processes imposes very similar requirements. The use for which the highest speed of operation is required in the telephone switching application is for real-time operation from a stored program. Random access to tabular information, although needed rapidly, is not usually controlling because of the more infrequent reference. In the case of program information, two important access actions can be distinguished. The first and most common is a sequential access, stepping word by word along the program; the second is a random access occasioned by transfers to other parts of the program or to subprograms.

The first is referred to as an "advance" operation and the second as a "transfer" operation. Since the "advance" is more common in the systems we are concerned with, it is the most critical in speed. Thus, the objectives which are appropriate to the present positioning systems are to make advances as fast as possible and to allow two to three times longer for transfers where necessary. The speeds which are feasible with present systems result in an over-all advance cycle time in the range of 2.5 to 5.0 microseconds.

The size of the flying spot store array is, in the usual case, limited by the devices within the store rather than by the system. This limitation presently places the optimum raster size between  $256 \times 256$  and  $512 \times 512$ .

### 1.2 Background

Realization of a useful flying spot store hinges to a great extent upon the development of an accurate beam-positioning system. The positioning problem is made difficult both by the large number of spot locations required in the array and by the difficulty of returning repeatedly over a period of several months to the desired spot locations with sufficient accuracy to obtain useful readout.

Development of the positioning system for the barrier grid store<sup>3,4</sup> has demonstrated the practicality of high-speed digital-to-analog converters for beam positioning where short-term accuracy is the primary requisite. Assuming a flying spot store array size of  $256 \times 256$  and a positioning tolerance of  $\pm 0.1$  of a spot spacing (to obtain a reasonable signal-to-noise ratio), the positioning accuracy required is  $\pm 0.04$  per cent. To build a forward-acting positioning system with a  $\pm 0.04$  per cent long-term cumulative stability in the digital-to-analog converter, deflection amplifier, cathode ray tube and associated power supplies is considered unrealistic. Hence, a closed-loop or feedback positioning system is mandatory.

The use of a servo positioning system offers additional advantages. In the servo positioning system, both the stored information and the edges used for servoing are mounted on a common frame. Thus, if a cathode ray tube is changed, rewriting of the information plates is not required. Moreover, the deflection error caused by stray magnetic fields and mechanical vibrations is nullified by the servo action.

### 1.3 Organization of Paper

This paper describes, first, the basic servo loop, its components and their characteristics; second, several positioning schemes making use of

the basic servo philosophy; and last, a comparison of the various schemes relative to the system requirements.

## 11. BASIC SERVO LOOP

### 2.1 *Components of the Loop*

A block diagram of the basic servo system is shown in Fig. 1 for one of the two independent axes of the flying spot store. The comparator output is a function of the difference between the address recorded in binary form in the input register and the binary-type positioning information obtained from the optical beam encoder. The comparator output or outputs are connected to the integrating amplifier, which is a high-gain shaping amplifier used to establish the desired loop gain frequency characteristics. The deflection amplifier is a wideband power amplifier designed to drive the deflection plates of the cathode ray tube. The cathode ray tube beam is electrostatically deflected with no post-acceleration. The phosphor must have very fast rise and decay characteristics to meet system objectives. For the purposes of this paper, type P-16 will be assumed. Each photomultiplier tube output is amplified and buffered by its associated amplifier before being fed to the comparator

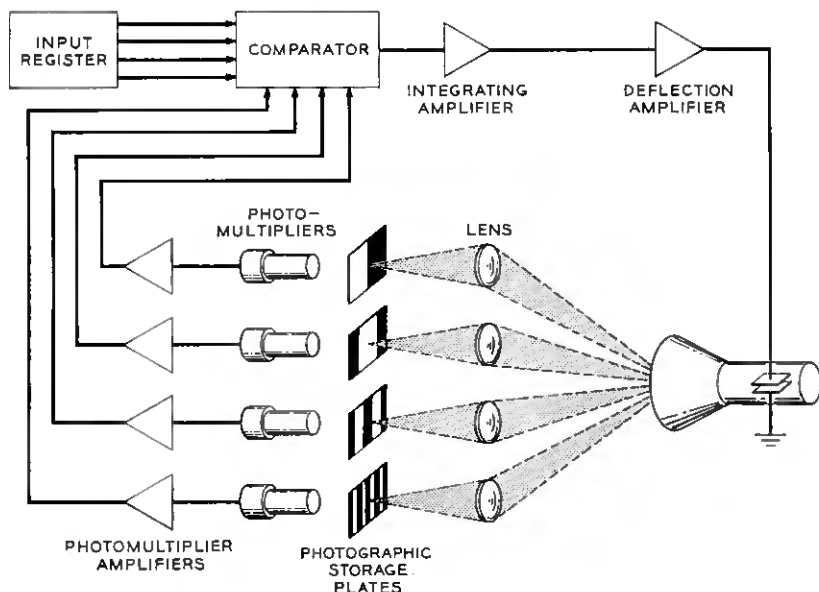


Fig. 1 — Block diagram of basic servo loop.

TABLE I—TRANSIT-TIME DELAY AND CUTOFF FREQUENCIES  
OF MAJOR LOOP COMPONENTS

Component	$\tau_d$ ( $\mu\text{sec}$ )	$F_{co}$ (mc)
Photomultiplier tube.....	60	—
Photomultiplier tube output circuit.....	—	0.4
Comparator.....	14	2.0
Integrating amplifier.....	10	10.0
Deflection amplifier.....	4	5.0
Cathode ray tube (P-16 phosphor).....	11	2.5
Optical path.....	5	—
Connecting cables.....	12	—
Photomultiplier amplifier.....	3	5.0
Total.....	119	

Table I lists the components contributing appreciably to the true transit-time delay and the limiting cutoff frequencies of the various components. Most of the transit-time delay is inherent in the photomultiplier tube. This is to be expected, since, at each stage of a photomultiplier tube, the electrons are emitted with very low energies and are accelerated by only 100 to 150 volts per stage. The photomultiplier output circuit is responsible for the lowest cutoff frequency in the servo loop. This output response is limited by the amount of current that can be obtained from the photomultiplier anode consistent with a reasonable life expectancy.

## 2.2 Servo Loop Characteristics

The maximum crossover frequency that can be obtained is limited both by the loop transit time delay and by the cutoff frequencies of the loop components.

The minimum time delay obtainable, from Table I, is in the order of 100 millimicroseconds. This transit delay sets the maximum possible crossover frequency of the loop at 5 mc, corresponding to  $180^\circ$  phase shift. To be a bit more realistic,  $90^\circ$  should be allowed for the first-order integration characteristics of the shaping amplifier at crossover, plus at least a  $30^\circ$  phase margin to achieve reasonable stability. This leaves only  $60^\circ$  for transit delay phase, bringing the maximum frequency at gain crossover down to 1.7 mc.

The numerous frequency cutoffs listed impose a further practical limit to crossover frequency. Since the asymptotic slope is in the order of 48 db/octave above 10 mc, compensation beyond this point is not practical. Under this condition, the establishment of the crossover

frequency requires an assessment of the expected gain variation to allow adequate gain margin.

Where possible, local feedback is provided to control the gain of each component of the loop. The cathode ray tube beam intensity is controlled by a feedback loop utilizing an optical channel and photomultiplier tube, along with a carrier amplifier to feed a correction signal to the cathode ray tube grid. This brightness stabilizer, as shown in Fig. 2, must have a response speed comparable to that of the positioning servo, since any variation in beam brightness affects the servo loop gain as well as the readout signal.

An intensity monitor circuit, using the same photomultiplier as the brightness stabilizer, is also shown in Fig. 2. This circuit provides a half-light reference signal for all the servo channels. It is the difference between this reference signal and the signal from the encoder channel that is used to position the beam. The purpose of this action is twofold. First, the intensity monitor prevents undesirable interactions between the position servo and the brightness stabilizer from occurring, since, with the monitor, the final beam position is independent of the beam brightness. Second, the intensity monitor provides additional correction for brightness changes that are beyond the speed or control range of the brightness stabilizer.

The photomultiplier tube gains are controlled by feedback techniques. In this case, a relatively slow sampled-data feedback system is sufficient, since the differential of gain with time is small.

All the amplifiers are gain-stabilized, either by a local feedback loop or by cathode degeneration. The integrating amplifier, shown in Fig. 3, is composed of a dc and an ac amplifier operating in parallel. The dc

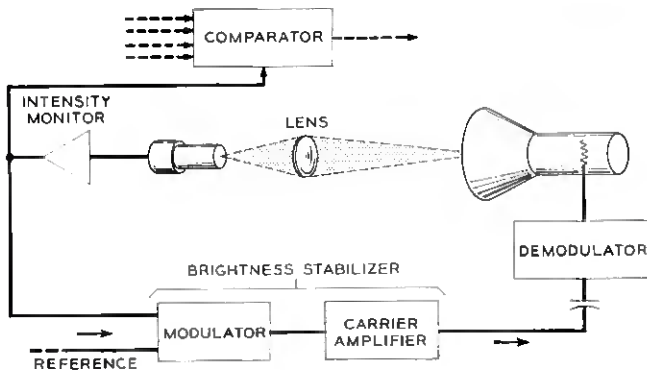


Fig. 2 — Block diagram of intensity monitor and brightness stabilizer.

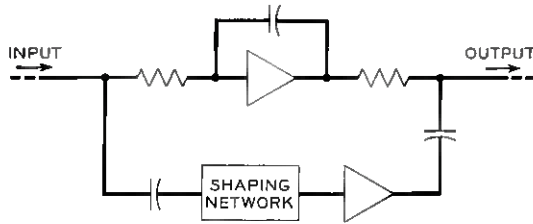


Fig. 3 — Block diagram of integrating amplifier.

section is a high-gain operational-type amplifier, while the ac section is a single-stage, low-gain shaping amplifier stabilized by cathode feedback.

Unfortunately, the optical section of the servo loop contributes three basic types of variations in gain which cannot be stabilized by feedback. Fig. 4 shows a typical crossover characteristic, along with an ideal crossover characteristic. The curves shown plot the luminous energy received on a photomultiplier tube face as a beam is passed over a servo edge. Since the spot on the phosphor has essentially a normal distribution in both axes, the crossover characteristic has a cumulative normal distribution. The slope of this characteristic curve determines the encoder gain and, thus, the loop gain. Since the servo tends to position the beam so that it is half hidden by the edge, it is observed that the servo loop gain is highest when the beam is settled in position. This gain is about 1.6 times the gain corresponding to the ideal crossover characteristic.

Variations in focus also vary the loop gain. This variation is a compounding of the focus obtained on the phosphor with that obtained by the lens. Both of these vary with beam position and may together con-

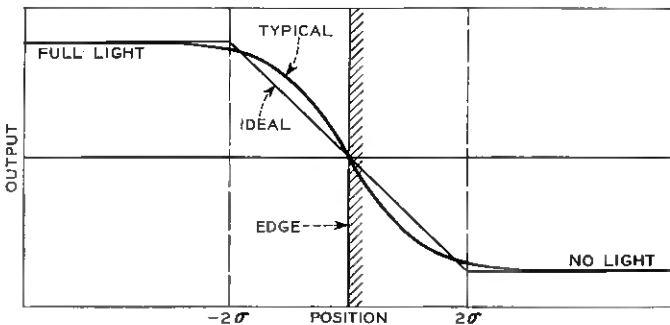


Fig. 4 — Optical encoder crossover characteristics.

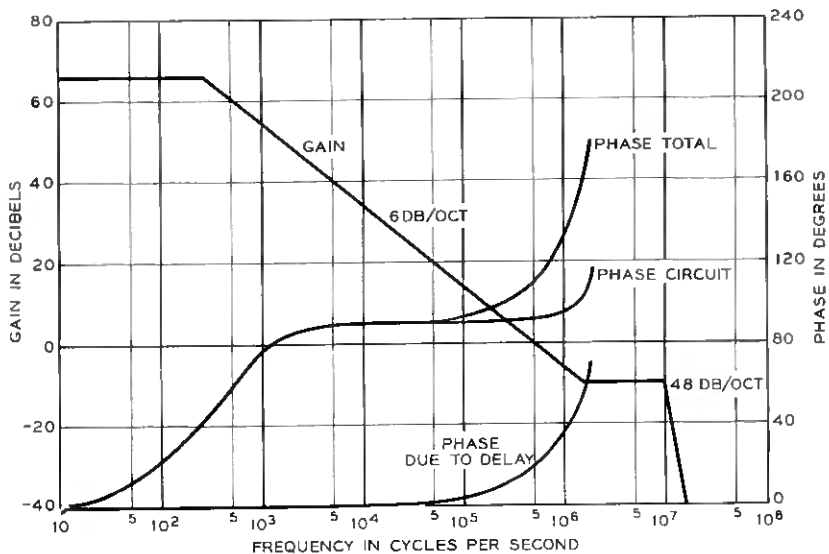


Fig. 5 — Open loop phase and gain vs. frequency.

tribute a variation of  $\pm 20$  per cent to the loop gain. The light intensity varies across the field in the off-axis optical channels and causes an additional  $\pm 10$  per cent variation in the loop gain.<sup>5</sup>

To provide for the expected gain variations, a design gain margin of 10 db is required. Fig. 5 shows curves of phase and asymptotic gain versus frequency that represent the optimum frequency crossover consistent with the findings of the previous sections.

It should be noted that a phase margin of  $30^\circ$  or better is maintained up to about 1.3 mc. Thus, system stability is assured, even with the gain variations discussed above. The crossover frequency shown is for the ideal optical crossover characteristic of Fig. 4. The difference between the typical and ideal crossover characteristic is absorbed as part of the gain margin.

A basic servo with these characteristics forms the basis for the beam positioning systems to be discussed next.

### III. BEAM SERVO POSITIONING SYSTEMS

All the positioning systems which have been studied utilize either the sign-only, the approximate proportional or the true proportional comparator discussed in detail by Ketchledge<sup>6</sup> and Nesenbergs and Mowery.<sup>7</sup> The binary-Gray version of each of the above comparators is used to

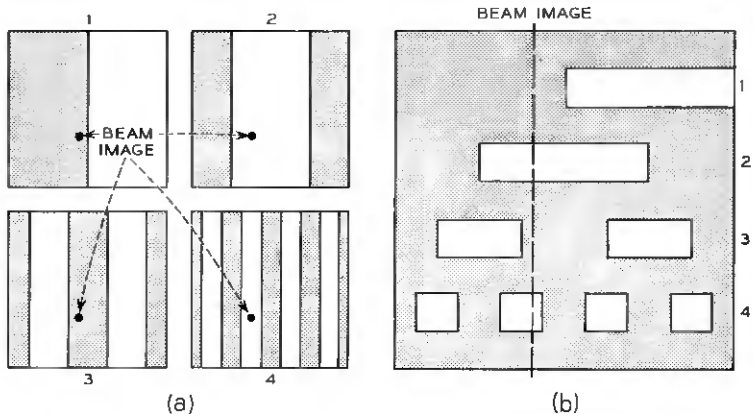


Fig. 6 — Gray code plates (a) for four channels of encoder, with (b) diagrammatic representation.

avoid the transition problem inherent in encoding analog information with a binary code plate system.

The Gray code plates shown in Fig. 6(a) are representative of the servo plates used in the four most significant digits of each axis of the beam position encoder. Fig. 6(b) shows diagrammatically the relative positions of the servo edges contained on the plates of Fig. 6(a).

In the following paragraphs the characteristics of positioning systems making use of the above comparators will be discussed. The digital-to-analog converters utilized in some of the systems are similar to those in the barrier grid store that are described by Ault<sup>3</sup> in this issue.

The system response data quoted in the following sections were obtained initially from measurements made by simulating the system on an analog computer and later from measurements made on a series of laboratory models.

In the following sections note that the times indicated for various sizes of jumps are beam-positioning times that include settling but do not include other portions of the cycle necessary to obtain a complete readout.

### 3.1 Sign-Only Servo

The sign-only servo is one in which the magnitude of the error signal is developed by a sign-only comparator and is a linear function of the true error for small errors and a constant for larger errors. This results in a velocity-limited or saturated servo system.

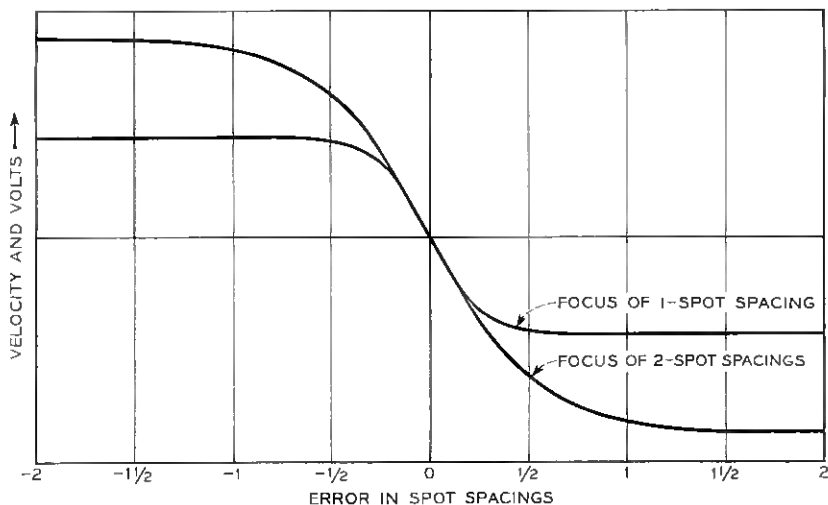


Fig. 7 — Effect of focus on optical crossover characteristic.

The extent of the linear range determines the magnitude of the drive and, thus, the slewing velocity outside the linear range. Fig. 7 shows plots of servo error signal versus spot displacement for two conditions of focus. The maximum slope is held constant for each curve, since the loop gain is a function of this slope, as discussed in Section 2.2. The maximum linear range obtainable with a conventional Gray code plate is reached at  $\pm 1$  spot spacing. This can be achieved by defocusing the optics of the servo channels so that the diameter of the light beam falling on the encoder occupies 2 spot spaces. Since the bars and windows of the least significant digit are each 2 spot spacings wide, this is the largest spot that can be used without reducing the drive signal. Obviously, if a tighter focus is used, the linear range is reduced; consequently, the velocity in the saturated region is likewise reduced.

Unfortunately, as the beam is defocused the optical gain is decreased, thus requiring an increase in the gain of one of the amplifiers contained in the loop. Also, the signal-to-noise ratio is degraded as the focus is degraded. This results because the main source of noise is the photomultiplier tube, and the additional gain needed to counteract the gain lost by defocusing must be supplied between the photomultiplier tube and the deflection plates.

The effect of light variations across the field on signal-to-noise ratio is also accentuated by defocusing the beam on the encoder plates. Consider an off-axis channel where variations in the light intensity may be  $\pm 10$

per cent. When the beam intensity in this channel is down 10 per cent, approximately 55 per cent of the beam must be exposed over the servo edge to balance the signal from the intensity monitor channel. It follows that, with a defocused beam, a larger shift in the position of beam center is required to obtain 55 per cent of the beam over the servo edge. The result is a crowding of some of the rows and columns in the matrix. A small amount of crowding is tolerable, since crowding is a physical constant of the system and would be present both when the storage plates are written and also when they are interrogated. Severe crowding, however, may result in the partial overlapping of spot locations, resulting in a degraded signal-to-noise ratio.

A balance must be made between the obtainable signal-to-noise ratios as a function of focus and the slewing speed. It is generally felt that defocusing the beam in the servo channel so that the  $\pm 2\sigma$  limits of the beam occupy one spot spacing results in the best compromise performance. The resulting slewing speed is 1.5 spots per microsecond. When operation is at the maximum defocusing of 2 spot spacings the slewing speed can be increased to 3 spots per microsecond. The slower speed resulting from the tighter focus will be assumed in calculating beam-positioning times in this paper.

The time required to reposition the beam one spot spacing is roughly 1.2 microseconds, 0.8 microsecond of this being the settling time. The settling time is defined as the time required for the beam to settle within 0.1 of a spot diameter, starting from the time the beam enters the linear region ( $\pm 0.5$  spot). On long jumps, the positioning time is primarily the time spent in slewing the beam. On a 100-spot jump, 67 microseconds are required to move the beam to within 0.5 spot and, again, an additional 0.8 microsecond being settling time.

The logic for sign-only servo comparison is relatively simple and, with the exception of the "exclusive or" function, easy to implement. The "exclusive or" is complicated because it must transmit the analog signal obtained from the encoder without appreciable distortion. Fig. 8 is a vacuum tube version of one digit of the sign-only servo comparator.

Since each channel of the servo system has at least one servo edge, each channel should have high-quality optics to prevent bowing of the rows and columns of the array due to light variations across the field. The least variation in light will occur in those channels located on or near the optical axis of the cathode ray tube. These channels are used, therefore, for the reference channel (intensity monitor) and the least significant digit servo channels. Since the two least significant digit channels (one for each axis) determine the location of every other row

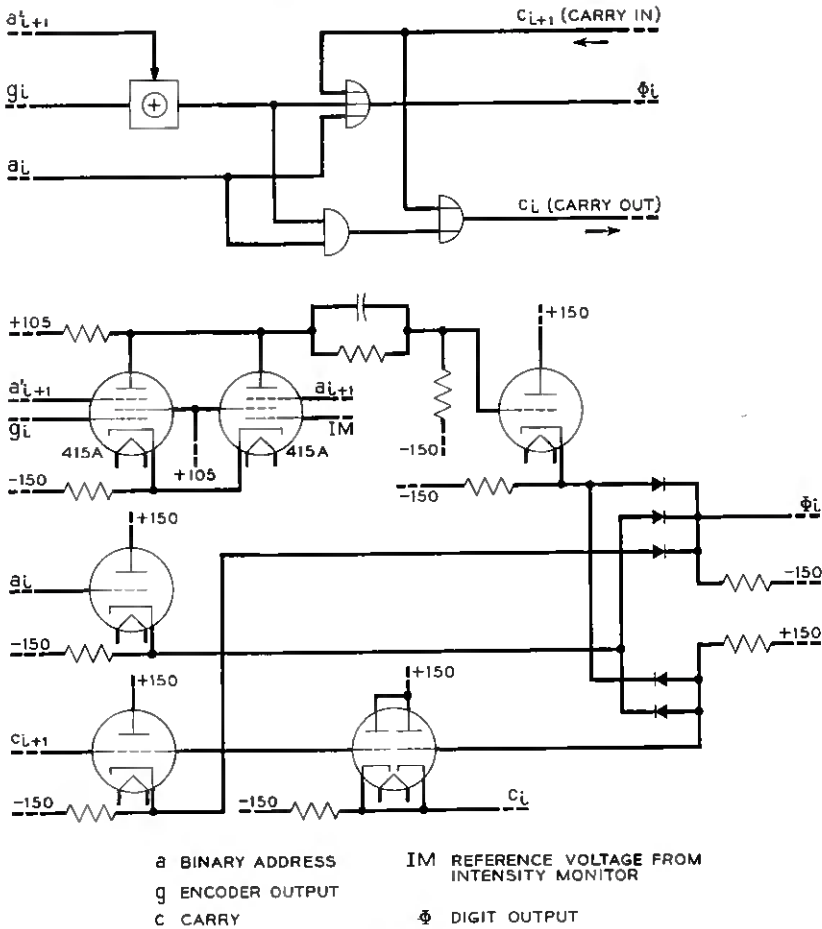


Fig. 8 — One digit of sign-only servo comparator logic.

and column in the array, they will be located near their ideal locations, allowing more latitude for the bowing in the remaining rows and columns.

### 3.2 Sign-Only Servo Plus Digital-to-Analog Converter (DAC)

In order to overcome the long positioning times required on long jumps with a sign-only servo, a DAC may be utilized as in Fig. 9. In this application, the DAC is used to rapidly position the beam as close as possible to the desired location, and the sign-only servo is used to correct any DAC error and establish the final location of the beam.

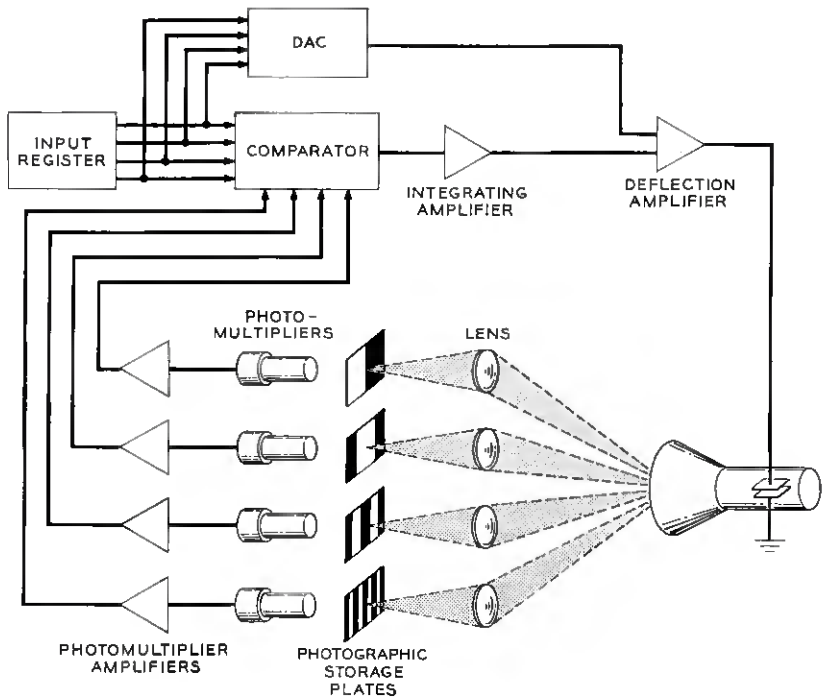


Fig. 9 — Block diagram of servo loop with DAC.

The DAC used in this application should have a sufficiently fast rise time (on the order of 90 millimicroseconds) so that its output will have arrived at its final value before the integrating characteristic of the servo loop has had time to accumulate a deflection signal that later must be integrated out to arrive at the desired location. This situation can be clarified by reference to Fig. 10.

The DAC is free of all dc drift-stability problems, since the servo will retain any DAC drift as a correction signal. Gain variations of the DAC, however, will cause the positioning system initially to overshoot or undershoot, which must be corrected by servo loop action. Distortions in the cathode ray tube such as "barrel" or "pincushion," as well as lack of orthogonality between the two deflection plate assemblies, also require the servo to make greater corrections, which increases the positioning time. These distortions are minimized by the advanced design techniques used in the development of the cathode ray tubes.

Use of the DAC tends to increase the time required to move a single spot location. The error is greatest when the address is changed from

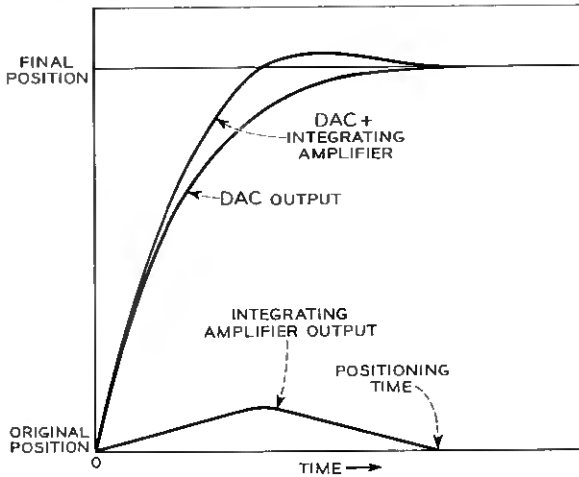


Fig. 10 — Effect of DAC rise time on positioning time.

0111...1 to 1000...0. Here a jump of only one spot position is called for, but the condition on every DAC input is reversed. The error that may result is controlled almost entirely by the accuracy of the resistors in the weighting network. It appears reasonable to expect that the worst error that can occur due to this effect can be held to 0.4 per cent of the raster's dimensions. Thus, for a  $256 \times 256$  array, the worst error in adding one across the center of the array is one spot. That is, the output of the DAC either would not change or it would give an output corresponding to a 2-spot jump. This will increase the positioning time necessary to add one by 0.2 microsecond over the time required by the sign-only servo to position the beam. On the same size array, a large jump requires a worst time of 2.7 microseconds (0.6 DAC, 1.3 correction, 0.8 settling time). For larger arrays, correspondingly larger times are required.

Thus, by the addition of a DAC unit around the comparator, we have greatly decreased the time required for random beam positioning and only slightly affected the time required to add one.

### 3.3 Approximate Proportional Servo System

The approximate proportional servo using the corresponding binary-Gray comparator is a somewhat more elegant positioning system and, as might be expected, it is more complicated and costly. Basically, this system produces a nonlinear error signal that is bounded within

$\pm 6$  db of the true proportional error signal. As with sign-only servo, the error is linear when the displacement is within  $\pm 0.5$  spot.

Assuming a crossover frequency of 500 kc, as in Fig. 5, and a  $256 \times 256$  raster array, the theoretical time required to reposition 256 spots is about 11 microseconds. The time required to move one spot location is the same as that required by the sign-only servo, approximately 1.2 microseconds.

The approximate proportional servo introduces two new problems. The first is a result of the large weighting factors which must be used on the outputs of the more significant digits of the comparator. The most significant digit channel of an eight-channel comparator would carry a weighting factor of 128, relative to 1 for the least significant digit channel. This high factor demands an extremely high signal-to-noise ratio to obtain a sufficiently low probability of a noise pulse occurring that would correspond to a half light condition. If such a pulse should occur in a digit with a high weighting factor, the resulting drive would temporarily displace the beam from its desired location. Because of this weighting problem, it is difficult to think of an approximate proportional servo with weighting factors much greater than 10. Thus, this system would be relatively slow on long jumps. Here again, the approximate proportional system could use a DAC system with the faster correction inherent in the approximate proportional servo.

A second problem results from the difficulty of maintaining dc stability and short transit time in the more complicated logic. The comparator output signal is always derived from the least significant digit channel (the only channel with unity weight) when the beam is settled in position, regardless of which channel receives the half light information as its input. Thus, the servo signal may enter the comparator's most significant digit input, proceed down the carry string (path) to the least significant channel and thence go to the output. The long transit time will appreciably increase the loop transit time, resulting in a lower servo speed. Moreover, the dc stability expected from this form of logic is not compatible with system reliability requirements. The latter problem is alleviated by a modified system discussed in Section 3.5.

### *3.4 True Proportional Servo System*

The true proportional servo will not be discussed in detail. Although it provides a reduction in the random access time by a factor of about 1.5, its logic is somewhat more complicated and has the same inherent problems as the approximate proportional servo and, thus, the same limitations.

### 3.5 Minimization of Number of Transmission (Linear) Channels Required

In the previous articles,<sup>1,6,7</sup> and up to this point in this paper, each logical channel of the encoder and comparator had to be designed to handle linear positioning information, since the servo edges in each channel were used for locking the beam. The carry strings in the approximate and exact proportion comparator must also be linear. In order to overcome these and other similar problems, it is desirable to minimize the number of channels required to transmit the servo edge characteristics. This removes the linear design requirement from the remaining channels, which can now be concerned solely with logical selection of the desired edge and not with linear transmission.

#### 3.5.1 A Double Quantizing Channel System

One scheme for implementing this minimization uses a coding scheme as shown in Fig. 11. Here, the least significant digit is displaced one-half spot spacing to the left and an additional least significant digit is placed one-half spot spacing to the right of the normal location. Only the edges in these two quantizing channels define the desired location, and thus they are the only edge characteristics transmitted for servoing. The rest of the channels are used only to create the direction of drive and therefore can use switching-type logic, which is characterized as two-state logic with inherent regeneration of the levels at each stage. Only speed and logical requirements are imposed on the transition between states. A diagram for a sign-only servo comparator for this system is shown in Fig. 12. Similar logic changes can be made for the proportional positioning systems.

At a focus corresponding to one spot spacing this system gives a

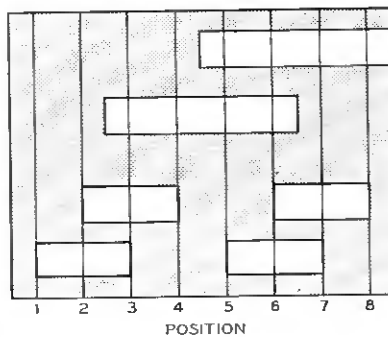


Fig. 11 — Diagrammatic representation of code plates for double-channel quantizing scheme.

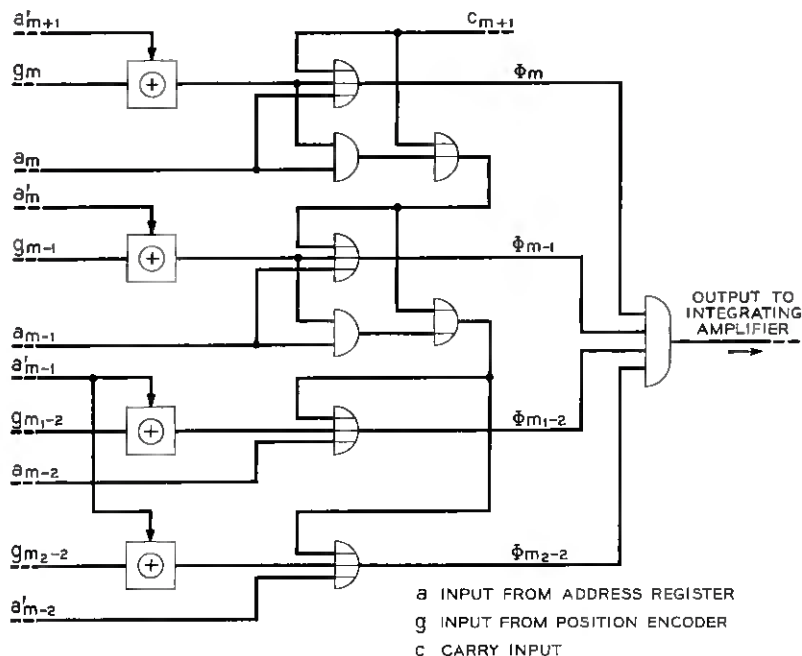


Fig. 12 — Comparator logic for a double quantizing channel system.

speed behavior identical to the normal coding system described in Section 3.1. However, as the focus is degraded, this system suffers a slight degradation in speed, which does not exceed 5 per cent at a focus corresponding to two spot spacing.

This scheme, at the cost of one servo channel, offers the following improvements:

i. A higher signal-to-noise ratio can be realized, since the two linear channels can be placed in preferred optical locations where the variations of focus and light across the field are small.

ii. The number of adjusting controls is greatly reduced, since the switching channels require no adjustments during alignment.

iii. The transit time of the comparator carry string does not affect the servo response time.

iv. The dc stability problems inherent in linear dc logic are removed by the use of switching logic.

### 3.5.2 A Single Quantizing Channel System

Another scheme for implementing the minimization also utilizes an additional channel. This extra channel corresponds to the next significant

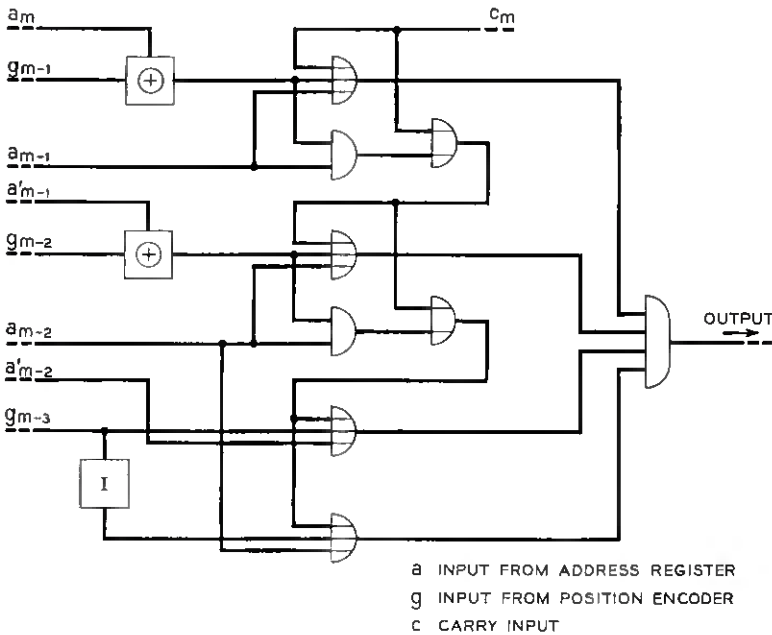


Fig. 13 — Comparator logic for a single quantizing channel system.

digit lower than the conventional least significant digit and contains an edge half-way between each edge of the conventional channels. With this system, only the edge characteristics in the single quantizing channel are transmitted to determine the final beam location. Fig. 13 shows the logic required for a sign-only servo comparator as modified to accommodate this scheme. An example of the simplification which was sought from this philosophy can be seen here. The only stage which must transmit servo information (the last stage) no longer requires an explicit "exclusive or" logical function, and the problem of designing this logic circuit to strict transmission requirements has disappeared. The "exclusive or" circuits in the higher stages are also made simpler by the removal of their transmission requirements.

This scheme has only one linear or transmission channel per axis, with even more simplification of the optical requirements and the adjustments. Greater reliability is maintained, since there are fewer components that can affect the beam position.

The positioning speed using this scheme is the same as that of the previous scheme when the beam is focused to one spot spacing on the encoder and is somewhat less than the previous encoder for larger spot sizes.

TABLE II—SYSTEM POSITIONING TIMES

Size of Array	256 x 256			512 x 512		
	1	25	256	1	25	512
Jump Length (Spots)						
System	Time in microseconds					
Sign-only servo	1.2	17.5	172	1.2	17.5	342
Sign-only servo plus DAC	1.4	1.7	2.7	2.3	2.5	4.7
Approximate proportional servo	1.2	8.2	11.2	1.2	8.2	12.1
Approximate proportional servo, with weighting factor limited to 10	1.2	8.3	24	1.2	8.3	41
Approximate proportional servo, with weighting factor = 10, plus DAC	1.4	1.7	2.7	2.3	2.5	4.5
Exact proportional servo	1.2	4.5	6.5	1.2	4.5	7.0
Exact proportional servo, weighting factor = 10	1.2	5.0	21	1.2	5.0	38
Exact proportional servo, weighting factor = 10, plus DAC	1.4	1.7	2.3	1.9	2.2	4.1

## IV. COMPARISON OF SYSTEMS

Table II lists the longest positioning times that may be required for the various positioning systems as a function of jump distance and raster size. Reference to the table bears out the necessity of using a DAC to obtain a random-access time consistent with the design objectives, regardless of the comparator employed. The proportional schemes with DAC are faster on long jumps than with the sign-only plus DAC system, but their use may be unwarranted in view of the increased complexity of the proportional systems.

On an advance type of operation the DAC tends to degrade the positioning time, particularly on the larger raster size. This degradation is caused when digits of high significance are changed in the advance operation, the worst case occurring when crossing the center of the array, as discussed in Section 3.2. To circumvent this problem, the DAC input circuitry may be modified as shown in Fig. 14.

The modification of Fig. 14(a) reduces the worst possible error of the DAC by a factor of two, resulting in an improved advance time. In fact, this modification reduces the advance times listed for systems using a DAC on a  $512 \times 512$  spot array so that they are identical to the times listed for a  $256 \times 256$  spot array. Fig. 14(b) carries the modification one step further, resulting in a reduction of the worst possible error by a factor of four. With this modification, the advance positioning times for systems utilizing the DAC will be very nearly the same as those without the DAC. Thus, the time required to advance is essentially the same, regardless of the positioning system employed. This

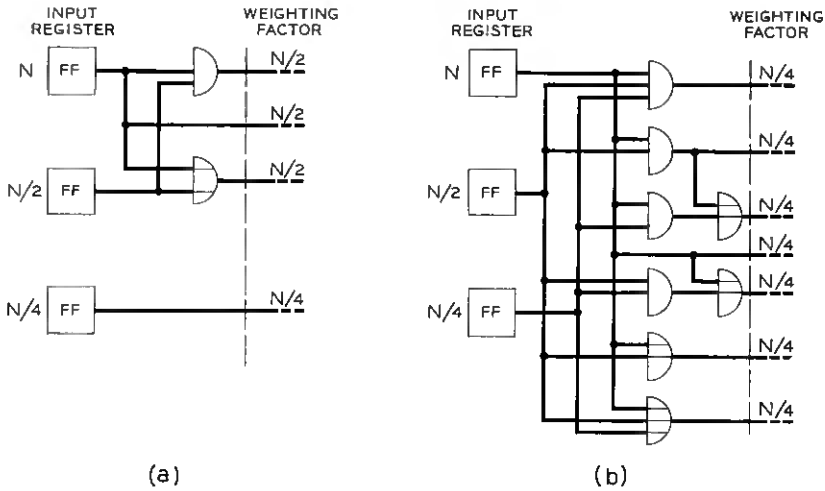


Fig. 14 — DAC input improved by (a) single-stage and (b) dual stage logic

factor accentuates the importance of basic servo loop component characteristics, as it is these components that will determine the advance time, rather than the positioning system.

Since the servo loop components play such a major role in determining the positioning time, it may be worthwhile to review the characteristics of some of the major components listed in Section 2.1.

Instead of utilizing a P-16 type phosphor, as previously assumed, other phosphors may be used because of their higher conversion efficiency or longer life. To date, no phosphor is available with rise and decay characteristics as fast as the P-16 type, although phosphors approaching the P-16 speed and offering higher efficiency and longer life have been noted. Phosphor efficiency and speed are almost equally important, as both affect the signal-to-noise ratio and, thus, the allowable gain crossover frequency. The importance of phosphor life must be evaluated on a basis of system requirements and economic considerations.

The only other component that may be modified to appreciably improve the servo loop characteristics is the photomultiplier tube. The stability of the photomultiplier dynodes may be improved so that a higher anode current may be utilized while a reasonable life is maintained. Also, changes in the structural design might result in a lowering of the electronic transit time in the photomultiplier, with a corresponding improvement in servo characteristics.

No ultimate servo loop characteristic can be given, as removing the limitations from any component increases the importance of the limitations of the other loop components, which may, in turn, be improved by further research.

#### V. CONCLUSION

Several systems making use of the basic servo loop characteristics have been discussed. It has been shown that the advance positioning time is primarily a function of the basic servo loop characteristics rather than the comparator system that is used. The random-access positioning time, on the other hand, depends considerably on the positioning system employed, although the servo loop and DAC characteristics are important factors.

To meet the system objectives, where the advance time is of greater importance and the transfer time is of lesser importance, the sign-only servo comparator plus DAC utilizing quantizing channels represents the best positioning system choice, because of its relative circuit simplicity and higher reliability. For different system requirements, where random-access time is critical, an approximate or true proportional comparator with DAC utilizing quantizing channels may be provided. The true proportional comparator, due to its considerably greater complexity, is justified only under the most severe system requirements, and where basic loop components have been used to their maximum capabilities.

#### VI. ACKNOWLEDGMENTS

Of the many people who have contributed to this project, the author is particularly indebted to the suggestions and guidance provided by R. W. Ketchledge, R. E. Staehler, T. S. Greenwood and C. W. Hoover, Jr.

#### REFERENCES

1. Hoover, C. W., Jr., Staehler, R. E. and Ketchledge, R. W., Fundamental Concepts in the Design of the Flying Spot Store, *B.S.T.J.*, **37**, September 1958, p. 1161.
2. Joel, A. E., Jr., An Experimental Switching System Using New Electronic Techniques, *B.S.T.J.*, **37**, September 1958, p. 1091.
3. Ault, C. F., this issue, p. 445.
4. Greenwood, T. S. and Staehler, R. E., A High-Speed Barrier Grid Store, *B.S.T.J.*, **37**, September 1958, p. 1195.
5. Purvis, M. B., Deverall, G. V. and Herriott, D. R., this issue, p. 403.
6. Ketchledge, R. W., Logic for a Digital Servo System, *B.S.T.J.*, **38**, January 1959, p. 1.
7. Nesenbergs, M. and Mowery, V. O., Logic Synthesis of Some High-Speed Digital Comparators, *B.S.T.J.*, **38**, January 1959, p. 19.

# Stable High-Speed Digital-to-Analog Conversion for Storage Tube Deflection

By C. F. AULT

(Manuscript received October 30, 1958)

*This paper covers the design of access circuitry for a barrier grid tube temporary memory. The circuitry converts a 14-bit binary address into the analog deflection voltage necessary to deflect the electron beam in the barrier grid tube to a specific geometrical storage area defined by the address.*

*A special feedback circuit and raster reference tube deflected in parallel with the barrier grid tube control the size and centering of the array of storage spots. Novel methods of measurement were developed to certify the accuracy of the deflection system.*

*The system meets the requirements of high speed, accuracy, stability and reliability.*

## I. INTRODUCTION

A barrier grid tube is a specialized cathode ray tube developed for high-speed electrostatic storage. Instead of a phosphor screen which changes the electron beam into visible light, there is a target area which stores isolated regions of charge under beam action. A binary "1" is recorded by charging a small target area ("spot") to equilibrium with the beam when the target surface is modulated by a back plate voltage pulse, while a "0" is stored by charging a spot to equilibrium in the absence of the back plate voltage pulse. Information is "read out" the next time the beam is turned on a spot (in the absence of a back plate pulse), the "1" giving a large output until the spot reaches equilibrium.

The barrier grid store, which is a random-access, single-bit, binary memory, utilizes the barrier grid tube as the storage device. To function properly, the store must have a deflection system which converts a binary address to an analog voltage that deflects the barrier grid tube beam to a unique physical storage location. A barrier grid store<sup>1</sup> and a

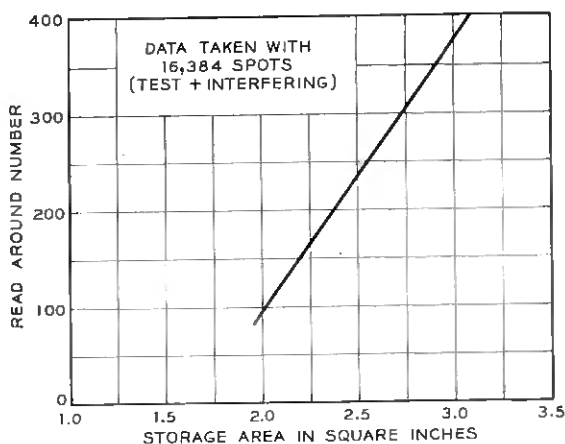


Fig. 1 — Effect on Read Around Number (RAN) of variations in spacing.

barrier grid tube<sup>2</sup> have been described in previous issues of the Bell System Technical Journal.

The deflection requirements for a particular barrier grid store are derived primarily from the capabilities of the barrier grid tube and secondarily from system requirements governing allowable time for regeneration of stored information in the memory. The spacing between stored charges and the total number of charges determine the interference resulting from operations on adjacent and distant spots, and hence determine the system time required for regeneration.

The effect of changing the spacing between storage centers on the interference due to reading and writing on other storage spots is illustrated in Fig. 1. The measure of interference used is the number of times the spots adjacent to a particular or test spot may be operated on before the storage of the test spot is degraded below usable levels. The actual measurement is made by writing a double-spaced checkboard of test spots over the storage area and then writing  $m$  frames of interfering spots in the skipped spaces. Each frame is counted as a "Read Around Number" (RAN) of four, since each test spot has four adjacent interfering spots. A 10 per cent decrease in the size of the storage area decreases the RAN by 50 per cent.

Minimum cost per storage location can only be achieved by utilizing the tube storage area to the fullest extent, commensurate with satisfactory immunity from interference and economical use of access or deflection circuitry. The more efficient access circuit schemes utilize a binary address of  $2n$  bits, which will define an  $n$  vertical by  $n$  horizontal

square array of  $2^{2n}$  discrete storage sites. However, the storage area of the barrier grid tube currently used is circular, and a circle with an inscribed square has about one third its area outside the square. It is not always possible to deflect the beam to the edge of the storage area without its first hitting a deflection plate; consequently, the area outside the inscribed square that can be safely used requires extra addressing circuitry, which the additional number of storage sites may not justify. If necessary, some of this outside area could be used. The best access compromise appears to be a square binary array with just enough separation between spots to yield the required freedom from interference.

The binary-to-analog conversion system discussed in this paper produces an array of  $128 \times 128$ , or 16,384 spots. The spot spacing is sufficient to guarantee a RAN of 150. This RAN is maintained by utilizing the inscribed storage area to the fullest extent, so that no appreciable guard space is allowed to absorb any drift of the deflection system. This was accomplished by designing a servo (raster reference system to be described later) which holds the storage array in a fixed geometrical location.

## II. DESIGN CONSIDERATIONS

A deflection system must have a method for remembering the address of the latest storage location received and a method for converting the address to the correct deflection voltage. To these primary considerations are added those of speed, accuracy, power and reliability. These are not separate problems; a decision about one affects all the others. The energy available at the output of the barrier grid tube is at a maximum if the beam is repositioned exactly where it was at the time of writing. Fig. 2 is a plot showing how the read out signal decreases as the beam is moved off the initial storage location. From this figure, it is apparent that the beam center can be 20 per cent of the beam diameter off the spot without the voltage output being significantly decreased. The beam diameter may only be one-half to one-third as large as the spot spacing. This means, for a  $128 \times 128$  array, an accuracy of deflection better than 0.1 per cent.

It takes a fixed amount of time to read and write information in a barrier grid tube. The tube for which this development was intended required 0.75 microsecond to be read and 0.75 microsecond to be written. A reasonable time for deflection would be one that would not increase the cycle time more than 30 to 50 per cent. The deflection time should not be made any faster than necessary, because the amount of power used for deflection increases with speed.

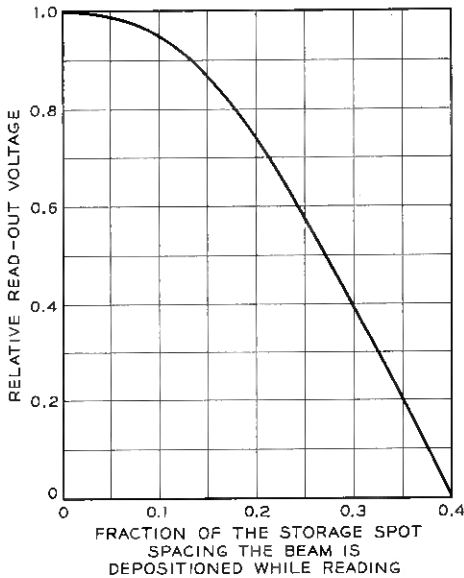


Fig. 2 — Degradation of barrier grid tube output voltage occurring when the beam is repositioned for reading off of the center of the stored charge.

The cycle time for a store consists of (a) time for deflection, (b) time for reading, (c) time for writing and (d) time for writing transients to decay. Item (d) does not increase the cycle time if the transients are present only during the following deflection. However, if they should last into the following reading time, they might cause errors in the read out. If the transients last longer than the deflection time, no decrease in cycle time could be obtained from a decrease in deflection time. Before reading could commence, the start of the next cycle would have to wait until all transients had decayed sufficiently to permit complete recovery.

### III. DESIGN OBJECTIVES

The deflection system developed for the barrier grid store was allowed 0.3 microsecond to settle. The balance of the 2.5-microsecond period (system objective) is 0.1 microsecond for jitter of order pulses with respect to address pulses, 0.75 microsecond for reading, 0.75 microsecond for writing and 0.1 microsecond for turning off the beam. The rest of the period, 0.6 microsecond, is used for transient recovery. The deflection time is not as long as the recovery time because it is desirable to have the readout from the barrier grid store available to the central

control of the electronic switching system as soon as possible after the order pulses are received.

The deflection objective of 0.3 microsecond may seem quite modest until the required accuracy is considered. An  $RC$  circuit will settle to 0.1 per cent in about seven times the time constant. The 10 to 90 per cent rise time of this deflection voltage then must be better than 0.09 microsecond. The rise time (10 to 90 per cent) of most amplifiers equals  $2.2 RC$ :

$$7(\text{time constant}) = 0.3 \mu\text{s},$$

$$\text{time constant} = \frac{0.3 \mu\text{s}}{7},$$

$$\text{rise time (10-90 \%)} = 2.2 \times \left( \frac{0.3 \mu\text{s}}{7} \right) = 0.09 \mu\text{s}.$$

The total tolerance for deflection cannot be allowed for settling, because there is some noise coupled to the deflection plates from other pulse circuits in the store. The design objective was therefore set at 0.05 microsecond rise time.

The deflection circuit used in the barrier grid store satisfies the following requirements:

i. The push-pull output of 140 volts is sufficient to deflect the tube over a square raster inscribed in the circular target of the tube. Push-pull deflection is necessary to prevent a change in average voltage for a pair of deflection plates which would defocus the beam.

ii. The output of 70 volts per deflection plate is developed across 72  $\mu\text{f}$  in 0.05 microsecond. The capacity is divided: tube plus wiring, 40  $\mu\text{f}$ ; amplifier, 32  $\mu\text{f}$ . To develop this output requires an average current of 100 ma.

iii. The voltage to one deflection plate should be the complement of that to the other, so that capacitive coupling to the target by one plate will be cancelled by the capacitive coupling from the other plate.

iv. The average voltage per pair of deflection plates is 0 volts. The average voltage of a pair of plates has to be at ground potential because, if it is different from the target voltage, defocusing occurs. It was found to be impractical to run the target at other than ground potential because of the increased recovery time of transients due to the back plate drive.<sup>1</sup> With the deflection voltage at ground potential, the coupling of the deflection voltage to the raster reference tube (described in Section V), dynamic focus circuit and deflection monitor is facilitated.

## IV. SYSTEM DESIGN

With the requirements for deflection defined, a comparison can now be made of various ways to satisfy them. The methods considered fall into two general categories, which are generally referred to as "high-level" and "low-level" conversion.

A low-level system converts the digital address to a proportional current or voltage at a small value and then amplifies this low value to the correct voltage necessary to deflect the barrier grid tube. A high-level conversion system converts the address to a voltage which is large enough to deflect the tube without amplification.

If an electronic switch is available which is good enough to meet the exacting requirements of a high-level system, it is probably the preferred method of deflection, even though it might use more power than a low-level system would.

A low-level system also requires a good switch, but this switch need only control low currents with small voltage swings. Electron tube diodes such as the 6AL5 and some of the newer silicon diodes are satisfactory for this application. At high currents the electron tubes have too much and too variable a voltage drop, and at high voltages the silicon diodes fail.

## 4.1 High-Level System

Fig. 3 is a schematic of a particular type of high-level decoder. The output has to be at ground potential, so equal positive and negative voltages are used. A switch for each digit connects a resistor to the plus

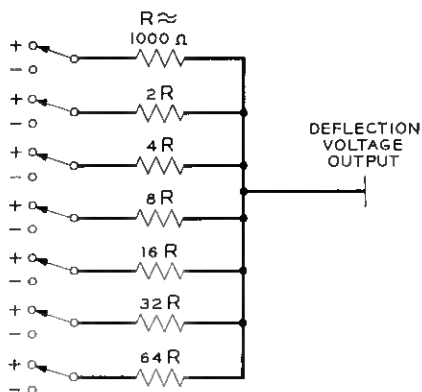


Fig. 3 — High-level digital-to-analog conversion.

voltage for a "1" address and to the minus voltage for a "0" address. The resistors determine the correct current for each digit, thereby controlling the spacing between storage spots; the magnitude of the plus and minus voltages determines the size of the array. For a 0.05-microsecond rise time,  $R$  must equal 1000 ohms;  $V = 35$  volts, so the current through the switch of the msd (most significant digit) varies from zero to 35 ma. The stiffest requirement on the switches occurs for the msd. When the switches are closed, the voltage across each must be constant with time and temperature to 0.1 volt. The switch may have some resistance, since  $R$  may be decreased to compensate for it. The switch must be able to withstand 70 volts and open and close in less than 0.05 microsecond.

#### 4.2 Low-Level System

Fig. 4 is a schematic of a particular low-level system. There are three major divisions: (a) an input register for remembering the address, (b) a digital-to-analog converter to change the register output to an analog current and (c) an amplifier to change the analog current into the deflection voltage.

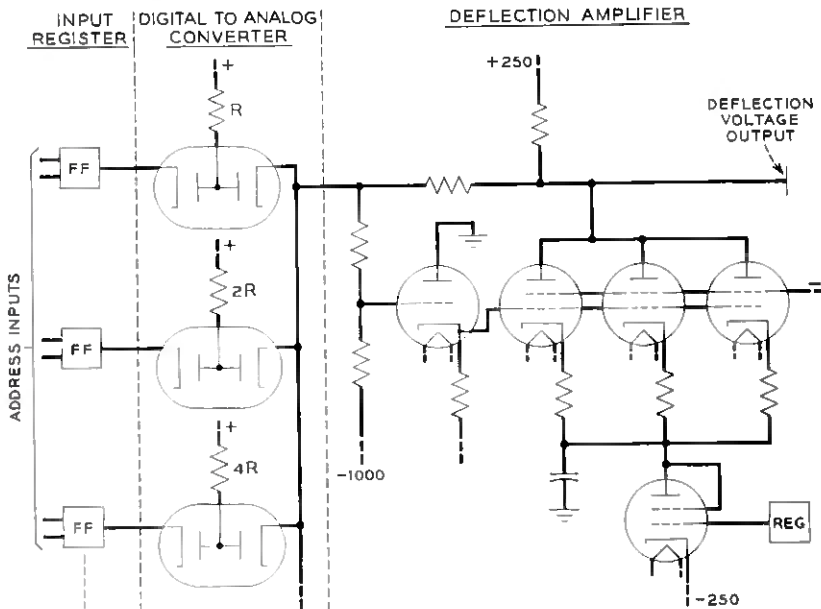


Fig. 4 — Low-level deflection.

The input register consists of flip-flops which produce a larger current than any digit current in the D-A (digital-to-analog) converter. The voltage swing of the output of the flip-flops must be greater than the largest digit current multiplied by the diode resistance, plus twice the largest digit current times the input impedance of the amplifier. When the flip-flop output voltage swing is larger than necessary, it is reduced to prevent excessive capacity coupling through the diodes. Both the rise and fall time must be faster than the 10-90 per cent rise time required of the deflection system or else it will limit the speed.

The D-A converter converts the digital output of the flip-flops to the correct current for the digit it represents. The practical limit for a D-A converter, at speeds of 0.05 microsecond and accuracies of a tenth of a spot, is about eight digits. This limit is certainly true using vacuum tube diodes, whereas by using some of the new silicon diodes possibly nine digits might be switched. To switch nine digits the maximum current possible should be switched by the msd. A reasonable current for this might be 30 ma. The flip-flop must then be able to produce 30 ma. No problem will be encountered using this current through the diode, but the current into the amplifier is rather high, so that the feedback resistor will have to handle four or five watts, which is objectionable. The average current through the amplifier load resistor will have to be increased by an amount equal to the current in the feedback resistor.

If the msd current is 30 ma, the least significant digit current must be 30 ma divided by  $2^8$ , or about 120 microamperes. If the drop across the diodes is 1 volt and the input impedance of the amplifier at high frequencies is 100 ohms, the flip-flop voltage swing must be greater than 7 volts. Assuming a 10-volt swing, a current of 120  $\mu$ a must charge any distributed capacity associated with a diode and the resistor supplying the 120  $\mu$ a. The capacity is not less than 2  $\mu$ mf, so the rise time of this diode for the 10 volts it must charge through before any current flows is 0.17 microsecond. The next digit will take 0.085 microsecond, which is still marginal. To speed up these two slow digits and to make them less subject to noise, a system of adding and subtracting currents that makes it possible to switch reasonable currents may be adopted. The diode switch is connected as shown in Fig. 5. To produce a one-unit increase in current at the output, five units of current are added and four units are subtracted. It is important not to switch currents any larger than necessary, because any drift of the resistor tolerance is multiplied by the amount by which the current exceeds the difference in currents.

Solid state diode recovery time specifications are usually to 90 per

cent recovery from an initial forward current. Some of these, in which this 90 per cent time is 0.01 microsecond, are satisfactory for this application. Since the time of recovery after the 90 per cent time is not usually specified or controlled, some care must be exercised in their use. Some fast silicon diodes have long current decay times from 10 per cent to zero. The diodes with short decay times generally have larger initial current flow when switching occurs than do the diodes with long decay times.

When vacuum tube diodes are used, it is useful to limit the current to about 4 ma through any one diode. If more current is needed, another diode is used. If too much current is used, the diode voltage drop becomes large and the voltage across the current determining resistors must be increased. If too low a voltage is used across the current-determining resistors, the output per unit digit change decreases as more digits feed current into the amplifier. If the amplifier input voltage changes 2 volts and the voltage across the resistor is 100 volts, then the input current decreases 2 per cent. A 2 per cent change in input current causes a change in voltage across the feedback resistor of 0.8 volts. This results in an increase in average voltage for a pair of deflection plates and causes slight defocusing at the edges. If the input impedance of the amplifier were higher or the D-A current higher, this shift in average voltage could cause excessive defocusing.

A brief review of the amplifier requirements for a low-level system may help at this point:

- i. Input and output approximately at 0 volts average per pair.
- ii. Current necessary to charge and discharge 70  $\mu\text{f}$  70 volts in 0.05 microsecond is 100 ma.
- iii. Low input impedance necessary to sum digital-to-analog current output correctly.

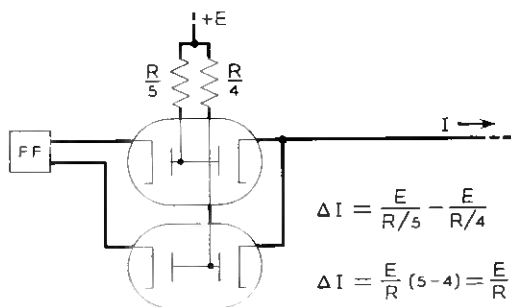


Fig. 5 — Low-level digital-to-analog converter — least significant digit.

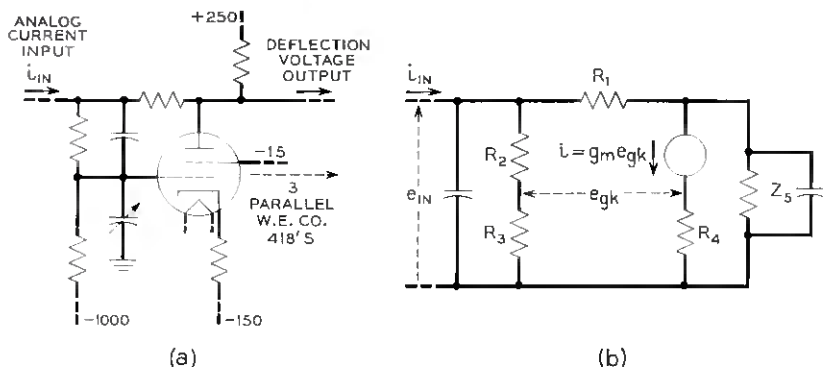


Fig. 6 — (a) Deflection amplifier and (b) equivalent circuit for determining input impedance.

iv. Low output impedance necessary to be immune to interfering capacitively-coupled noise.

v. Must be all dc coupled or else have the direct current reinserted by some means such as a clamp.

The low-level digital-to-analog conversion easily meets the requirements for seven binary digits. The amplifier requirements are also reasonable, so the low-level system was chosen over the high-level system.

Fig. 6(a) is a simplified schematic of the deflection amplifier circuit chosen for use in the barrier grid store developed for the electronic switching system. Fig. 6(b) is the simplified equivalent circuit with the approximate component values. The input impedance (Appendix A) is 73 ohms at low frequencies. At higher frequencies the loop gain decreases, because the impedance of  $z_5$  (output load resistor in parallel with distributed capacity) decreases, causing the input impedance to increase. At still higher frequencies, the input impedance decreases because of the distributed capacity at the input.

Fig. 7(a) gives the equivalent circuit for determining the output impedance. The calculated output impedance (Appendix B) is 34 ohms at low frequencies. At higher frequencies, the output impedance increases, as in Fig. 7(b). At still higher frequencies, the impedance decreases because of the capacitive component of  $z_6$ .

The design of this particular amplifier had to fit within the power supply voltages compatible with and necessary to the rest of the store. The voltages and tubes available permit a design not usually practical. The tubes, Western Electric Company type 418, have a very high GM (25,750) and a figure of merit such that only one stage of amplification

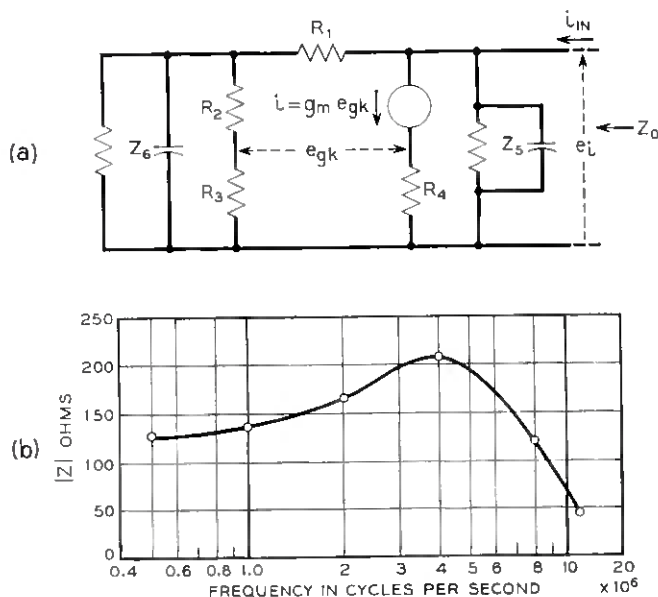


Fig. 7 — (a) Equivalent circuit for determining output impedance of deflection amplifier and (b) measured output impedance.

was necessary to attain the rise time and low input and output impedances desired. Even the requirement that the input and output be at ground potential average was not a handicap, because  $-1000$  volts was available for the voltage divider from the input to the grids, which permits a shift of 150 volts between the input and the grids, with a loss of only 15 per cent of the input voltage.

The average current through  $R_5$ , the plate load resistor, is 100 ma. To handle this current conservatively requires three tubes in parallel. To minimize the screen dissipation, the screens are run at  $-15$  volts with respect to ground potential or 135 volts with respect to the cathode. The three tubes were chosen over one tube with larger power-dissipating capabilities because of the resulting very high composite transconductance. If one large tube had been used it would have necessitated an extra stage of amplification, thus complicating the design considerably. Cathode degeneration is employed to equalize the currents through each of the three tubes.

One problem encountered at the junction of the cathodes of the six push-pull tubes was making this point stay at a constant voltage. Any change in voltage at this point can make the deflection very inaccurate.

The problem was solved by building a regulator on each deflection amplifier chassis that compares the cathode voltage to a reference obtained from the  $-1000$ -volt supply. The regulator holds the voltage constant from 0 to several hundred cycles, after which the capacitors take over.

#### V. RASTER REFERENCE

The optimum condition for storage in a barrier grid tube occurs when the array of spots (raster) is centered so that each corner spot is the same distance from the edge of the barrier grid storage surface as are the other three corner spots. This distance should be as small as possible, so as to avoid crowding the other spots and thereby reducing the RAN. A reduction in spacing of even one spot has a measurable effect on RAN.

However, the deflection amplifier will drift and the voltage from the different power supplies will change with time. The power supplies have a definite drift limit, beyond which an automatic voltage-monitoring system in the electronic switching system would sound an alarm. If a guard band were left between the storage array and the edge of the barrier grid assembly by shrinking the size of the raster, drift of the supplies could be accommodated. Each axis would decrease in length by 1 per cent. If the voltages now change so as to decrease the size of the array it may end up with each axis 2 per cent shorter. A similar guard band must be left to compensate for drift of the amplifier and of the power supply voltage used for centering the array. This could amount to a 2 per cent decrease at each end or a 4 per cent decrease in length of each axis. It is almost impossible to set these tolerances in practice with any great accuracy, so a workable guard band might be about an 8 per cent decrease in length of each axis. This guard band is sufficient to reduce the RAN by almost 50 per cent.

A special raster reference system was developed to control the position of the array, thereby permitting the reductions of this guard band from 8 per cent to less than 1 per cent.

The flying spot store<sup>3</sup> has a servo which controls the position of the beam at every address. This complex circuitry can only be justified for very large amounts of storage. The raster reference system used in the barrier grid store is a compromise system where only the edges of the array are controlled and the addresses in between the extremes depend on the stability of the digital-to-analog converter to maintain the correct spacing. Since a converter may drift, an increase in spacing for each digit is allowed. Each digit is about 101 per cent larger than

the preceding digit, which amounts to each axis being about 4 per cent shorter in effective length.

An ideal reference for the raster in a barrier grid tube would be one where the reference was inside the tube. This is difficult to accomplish, however, so the next best thing is to use a tube operated in parallel with the barrier grid tube which uses the same acceleration voltage and has similar conditions in general.

Fig. 8 is a drawing of the raster reference tube. At one end is an electron gun similar to that of the barrier grid tube, in the middle are two pairs of deflection plates and at the end are four pairs of overlapping plates, each with a knife edge at the overlapping edge nearest the gun. The edges are located in the position equivalent to the center of each edge of the array in the barrier grid tube.

In the electronic switching system the barrier grid store is regularly addressed to the center of one of the sides of the array and a pulse is sent to the store identifying the edge corresponding to the address. The address is not changed for the next 7.5 microseconds (three normal periods).

The raster reference tube beam will normally strike the knife edge, half of the current going to one of the pair of plates and half to the other. The plates have a secondary emission ratio which gives a current gain of about two. If there is an error in the position of the beam, one plate goes more positive than the other.

Fig. 9 is a simplified drawing of the raster reference tube circuitry. Approximately every 2.5 milliseconds the store is addressed to one of the pairs of plates in the raster reference tube. The error signal derived from each visit is stored in a capacitor. (There is a capacitor for each pair of plates.) From the voltages on the two capacitors from a particular axis, a centering and a size correction is generated.

If the barrier grid and the raster reference tubes all had the same sensitivity and centering they could be deflected in parallel by simply connecting each raster reference tube deflection plate to the correspond-

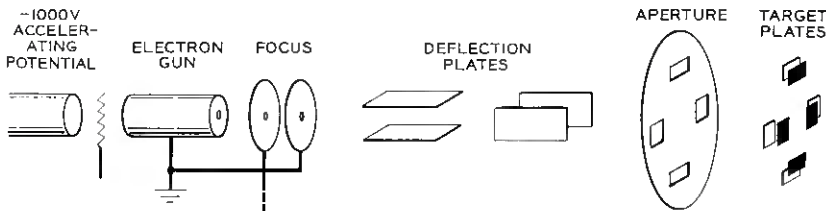


Fig. 8 — Raster reference tube.

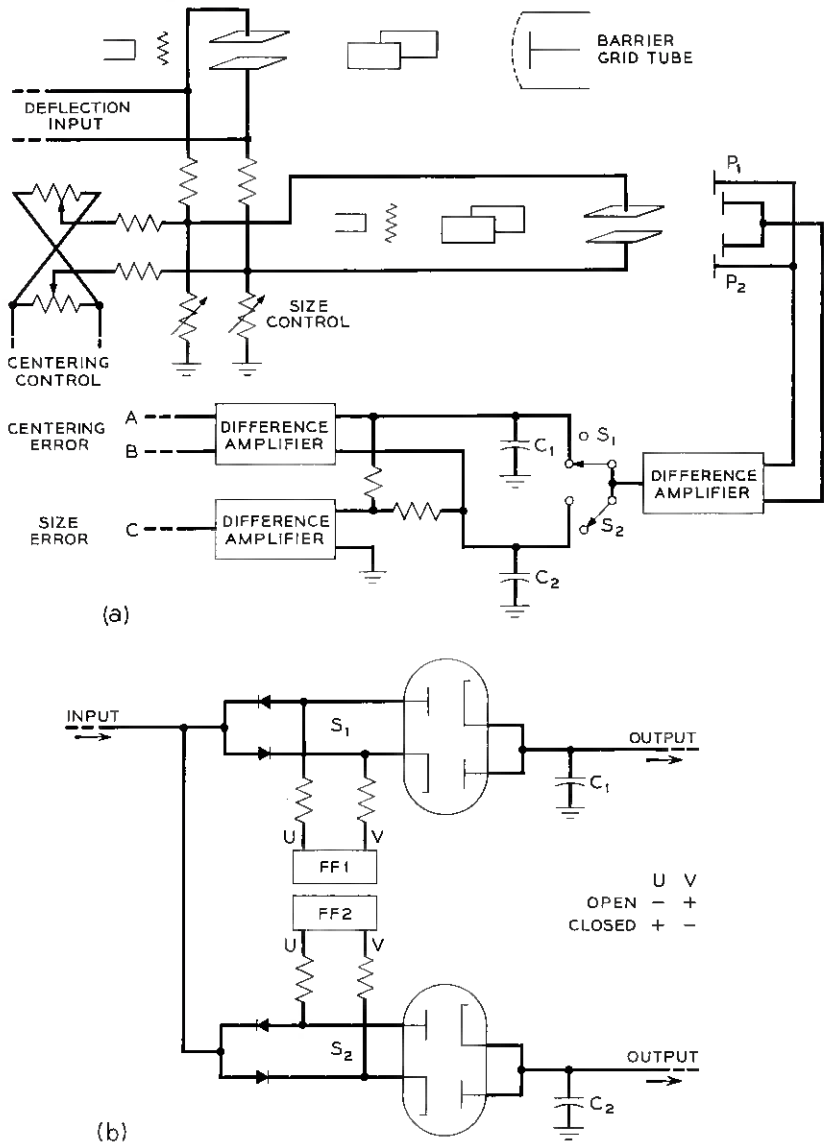


Fig. 9 — (a) Raster reference system circuitry, with (b) flip-flop switches in detail.

ing plate of the barrier grid tube. Since they are not alike, some means must be provided for adjusting the deflection of the reference tube. To facilitate this adjustment, the reference tube was designed with twice the sensitivity of the barrier grid tube and a dividing network was placed between the tubes. This network is not compensated, because the reference is not required to settle as fast as the barrier grid tube, since the error output from the reference tube is the result of the average output for 7.5 microseconds.

The dividing network provides resistance between the tubes, across which a centering voltage is developed. The centering voltage is the algebraic difference in centering voltages of the two tubes. The current through the resistors used for centering must be held very constant, because any change in it causes the raster on the barrier grid tube to be decentered. The two tubes now in use have centering errors that require a 0.5 per cent accurate voltage supply to hold the centering to about half a spot. The centering output of the raster reference system is a differential current fed to the differential inputs to the deflection amplifier. The size output is the voltage used in the digital-to-analog converter, which determines the current for each digit.

The pairs of target plates in the raster reference tube are connected together in two groups, the outside plates making one group and the inside plates another. The operation of the raster reference system can best be explained if an error in position is assumed, either in centering or size.

Assume first an error in centering, with a deflection voltage drift so as to move the raster toward  $P_1$  (Fig. 9). Whenever the beam is on  $P_1$ ,  $s_1$  connects to  $c_1$  and will, in this case, charge it to a negative voltage because more of the beam hits the outer target than hits the inner target. When the beam is at  $P_2$ , the beam is mostly on the inner target and the switch connects to  $c_2$ , which is charged positive. The size amplifier output equals  $K_1(VC_1 + VC_2)$ . The centering amplifier equals  $K_2(VC_1 - VC_2)$ . When there is drift,  $VC_1 = -VC_2$ ; therefore, the centering output is  $2K_2 VC_1$  and the size output is zero.

If there is a size error but no drift, the size is too small, the beam hits the innermost plates at both  $P_1$  and  $P_2$ , both capacitors  $c_1$  and  $c_2$  are charged positive, and  $VC_1 = VC_2$ . The centering output in this case is zero and the size output is  $2K_1 VC_1$ . For either drift or size errors, the output of the raster reference system is in a direction to minimize the error.

The switches [Fig. 9(b)] are opened and closed by flip-flops, which are controlled by the central control portion of the electronic switching

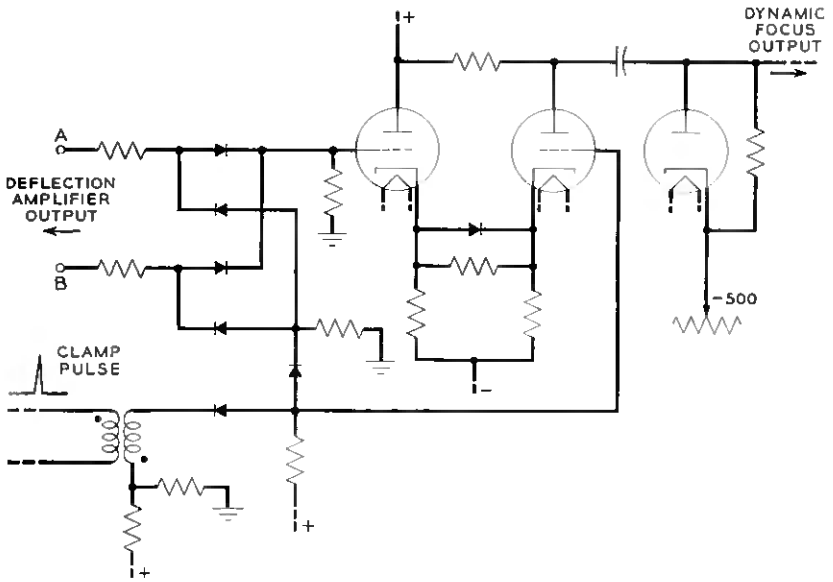


Fig. 10 — Dynamic focus circuit.

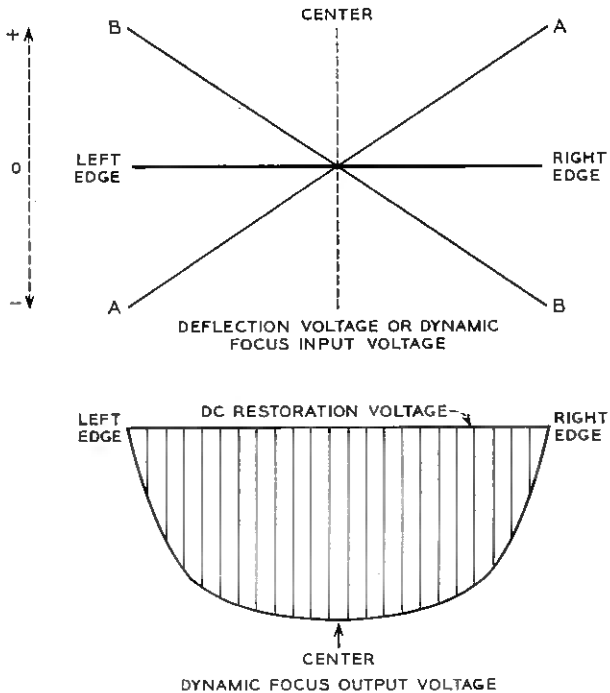


Fig. 11 — Dynamic focus voltage waveforms: (a) deflection voltage or dynamic focus input voltage; (b) dynamic focus output voltage.

system. When closed, a switch permits the circuitry to either charge or discharge the capacitors. Solid state diodes are used for one side of the switch because of their low forward impedance, and vacuum tube diodes are used for the other side because of their high back impedance. It is important that the charge not leak off the capacitor because the switch supplies current for only 7 microseconds and leakage drains the charge for 10 milliseconds.

The raster reference system is a sampled-data servo system where the sampling rate per axis is once every 10 milliseconds. Gain crossover for the loop must be below 50 cycles. There is no reason why the raster reference system has to be fast, so no effort was made to push the response to the limit. The open-loop gain depends on the beam current of the reference tube and the secondary emission ratio of the targets, consequently the break frequency has to be low enough so that the system is stable for any possible raster reference tube.

To make certain that noise in the raster reference circuitry does not cause errors in deflection, the integrating network was placed as near the output of the size and centering correction voltages as possible. The only tubes beyond the integrating network are cathode followers. The size output is single-ended, so that it is particularly susceptible to noise transients. A tetrode cathode follower is used whose screen voltage is carefully filtered.

The sampling rate and the duration of the sampling time were selected so as to fit simply into the electronic switching system<sup>4</sup> method of operation and still hold the array in place for reasonably fast changes in power supply voltages or other circuit drifts.

To a small extent, some of the circuitry that could have been built into the barrier grid store was replaced by the program stored in the flying spot store. The program tells the raster reference system when and at what address to operate. The servoing could have been accomplished without the help of a stored program but at a considerable increase in circuitry.

## VI. DYNAMIC FOCUS

The operation of the present barrier grid tubes is improved if the beam is refocused when deflected near the edge of the raster. The beam-focusing voltage must be adjusted at each address before the beam is turned on. The dynamic focus circuit derives its input from the output of the deflection amplifier (Fig. 10). Fig. 11(a) is a plot of the output voltage of the deflection amplifier for one axis as the beam moves from one side of the tube to the other. Fig. 11(b) is a plot of the required output of the dynamic focus circuit.

The maximum dynamic focus voltage change occurs when the beam goes from the center to either edge. The correction may be as large as 20 volts, with a correction voltage being developed for each axis and applied to a corresponding dynamic focus electrode. The dynamic focus electrode is at approximately  $-500$  volts. It would be difficult to couple the correction voltage from ground potential, where it is generated, to the correction electrode with dc coupling. To make it possible to avoid dc coupling, the correction voltage has a reference inserted at the time the orders are received. The reference is the most positive the correction will ever be, so it is possible to capacitively couple the correction from ground potential to the dynamic focus electrode at  $-500$  volts and there use a diode to reinsert the dc level.

#### VII. METHOD OF MEASUREMENT

The required deflection accuracy is better than 0.1 per cent, and determining just how well a deflection circuit is performing is a difficult task. The deflection circuit is under the most strain when the deflection is from one edge to the other. Then, a 70-volt step must be measured to better than 0.1 per cent from 0.3 microsecond after the initial change to several seconds later. Three methods of measurement have been used to determine deflection accuracy.

The first method tried was to apply the deflection output to the plates of an oscilloscope. When the deflection voltage is a maximum, the area of interest is off the screen, so it was necessary to add a dc voltage in each lead between the deflection amplifier and the deflection plates. This voltage was positive in one lead, negative in the other. By taking successive photographs of the deflection voltage at one-spot increments, the accuracy of deflection could be seen to be within 0.1 spot at 0.3 microsecond.

The second method made use of the raster reference tube. The test equipment which supplied orders and addresses to the store and barrier grid tube normally addresses the store in an orderly sequence of one line at a time, each new spot being adjacent to the preceding spot. This orderly sequence must be interrupted to service the raster reference system. There is one clock which drives the sequential deflection and another, in no way related, which drives the servo. Since the two clocks are not related, the deflection sequence may be interrupted at any of the 16,384 storage addresses and changed to one of the four servo addresses in a random manner. If the servo is disabled, the error signal out of the raster reference tube may be calibrated and used to measure deflection errors equivalent to those resulting from random addressing.

Full output of the servo results from a less than one-spot error, so small errors are easily measured.

The third method which was tried utilizes the output from the barrier grid tube. A deflection error is deliberately caused by adding a small current to the output of one side of the digital-to-analog converter and subtracting a like current from the complementary side. If the deflection is accurate before the error current is added, a reduction in readout voltage will result both when the error current is added positive to one side and negative to the complement and when the current is switched negative to the first side and positive to the complement. If there is a deflection error prior to adding the error current, switching the error current will cause a decrease in readout when it is switched in one sense and an increase in readout when it is switched in the other sense.

This method of measurement is the most accurate, because the error current is easily made as accurate as is the current for the digits in the digital-to-analog converter. This method revealed that an overshoot on the beam drive pulse caused the beam to miss the center of the stored charge, by as much as 0.1 spot on some barrier grid tubes, during the time the readout was being developed. An immediate improvement in the operation of the store resulted when the overshoot was reduced.

#### VIII. SUMMARY

The barrier grid tubes which are used guarantee a RAN (Read Around Number) of 150 for a  $128 \times 128$  array of storage spots. To utilize the storage capabilities of the tube fully, a deflection system with an accuracy better than 0.1 per cent was developed. The speed of the deflection system had to be compatible with the 0.75-microsecond reading and 0.75-microsecond writing time capabilities of the tube. For the deflection to settle as accurately as this in a compatible time a 10 to 90 per cent rise time of 0.05 microsecond is required.

A comparison of high- and low-level digital-to-analog conversion systems resulted in the choice of the low-level system for present designs.

To insure a high RAN with a square array of 16,384 spots it is necessary to make the area covered by the array as large as possible without causing the corner spots to fall off the barrier grid. A raster reference servo system was developed to hold the array in a fixed position regardless of power supply or deflection amplifier drifts. The servo is a sampled error system.

Several methods of measurement were used, showing that the low-

level digital-to-analog system developed adequately meets the requirements of the barrier grid tubes now in use.

#### IX. ACKNOWLEDGMENTS

Most of the ground work leading to a successful deflection system was done by T. S. Greenwood and H. Raag. The guidance of R. E. Staehler and R. W. Ketchledge is particularly appreciated. The raster reference owes its success to the tube developed by M. Chroney, H. Ericsson, and J. A. McCarthy.

#### APPENDIX A

*Deflection Amplifier Input Impedance [See Fig. 6(b)]*

$$Z = \frac{e_{in}}{i_{in}} = \frac{e_{in}}{\frac{e_{in} - e_0}{R_1}},$$

$$i = -\frac{e_0}{R_5} - \frac{e_0}{R_1},$$

$$e_0 = -\frac{R_1 Z_5}{R_1 + Z_5} i,$$

$$i = G_m E_{\theta k} = G_m \left( e_{in} \frac{R_3}{R_2 + R_3} - i R_4 \right),$$

$$i = \frac{G_m e_{in} R_3}{(1 + G_m R_4)(R_2 + R_3)},$$

$$e_0 = -\left( \frac{R_1 Z_5}{R_1 + Z_5} \right) \frac{G_m e_{in} R_3}{(1 + G_m R_4)(R_2 + R_3)},$$

$$Z = \frac{e_{in} R_1}{e_{in} + \left( \frac{R_1 Z_5}{R_1 + Z_5} \right) \left[ \frac{G_m e_{in} R_3}{(1 + G_m R_4)(R_2 + R_3)} \right]},$$

$$Z = \frac{R_1}{1 + \left( \frac{R_1 Z_5}{R_1 + Z_5} \right) \left( \frac{R_3}{R_2 + R_3} \right) \left( \frac{G_m}{1 + G_m R_4} \right)},$$

$$R_1 \approx 4 \times 10^3$$

$$Z_5 = 2500\Omega \text{ in parallel with } 72 \mu\text{mf.}$$

$$\frac{R_3}{R_2 + R_3} \approx 0.85 \quad G_m \approx 0.06,$$

$$R_4 = 6\Omega,$$

$$Z \approx 73\Omega \text{ at dc.}$$

## APPENDIX B

*Deflection Amplifier Output Impedance [See Fig. 7(a)]*

$$Z = \frac{e_{in}}{i_{in}} = \frac{e_{in}}{i + \frac{e_{in}}{Z_5}},$$

$$i = G_m E_{gk} = G_m \left[ e_{in} \left( \frac{Z_6}{R_1 + Z_6} \right) \left( \frac{R_3}{R_2 + R_3} \right) - iR_4 \right],$$

$$Z = \frac{1}{\frac{G_m \left( \frac{Z_6}{R_1 + Z_6} \right) \left( \frac{R_3}{R_2 + R_3} \right)}{1 + G_m R_4} + \frac{1}{Z_5}},$$

$$R_6 \approx 12 \times 10^3,$$

$$Z_0 \approx 34\Omega \text{ at dc.}$$

## REFERENCES

1. Greenwood, T. S., and Staehler, R. E., A High-Speed Barrier Grid Store, B.S.T.J., **37**, September 1958, p. 1195.
2. Hines, M. E., Chroney, M. and McCarthy, J. A., Digital Memory in Barrier Grid Storage Tubes, B.S.T.J., **34**, November 1955, p. 1241.
3. Hoover, C. W., Jr., Staehler, R. E. and Ketchledge, R. W., Fundamental Concepts in the Design of the Flying Spot Store, B.S.T.J., **37**, September 1958, p. 1161.
4. Joel, A. E., Jr., An Experimental Switching System Using New Electronic Techniques, B.S.T.J., **37**, September 1958, p. 1091.



# Verification of the Logic Structure of an Experimental Switching System on a Digital Computer

By DOLORES C. LEAGUS, C. Y. LEE and  
GEORGE H. MEALY

(Manuscript received September 9, 1958)

*The verification problem is concerned with the construction on a computer of a logical program which satisfies all the design specifications prescribed for an experimental switching system and with the process of putting calls through the computer simulation to evaluate the system's logical structure.*

## I. INTRODUCTION

The experimental switching system,<sup>1</sup> unlike its predecessors the electromechanical switching systems, is a universal machine in the sense that its actions are dictated by an internally stored program. In order to verify whether the system behaves according to the designers' intent, it is therefore necessary to check both the program and the circuitry. Since by far the larger portion of the logical complexity of the switching system resides in the program rather than in the hardware, it might be supposed that a corresponding proportion of effort would be required to check the program in the system laboratory and, further, that the program could not be checked until the system circuitry was functioning properly.

A strikingly similar problem arises in computer development: when a new computer is in final development, programs must be written and verified by the time the first model of the computer is ready for use. The solution to this problem is, when feasible, to use an existing computer together with a so-called interpretative program which simulates the actions of the new computer. In this type of simulation, internal processing can almost always be simulated exactly, but at a sacrifice of processing speed; terminal equipment of the computer usually cannot be simulated exactly.

From our present point of view, the experimental switching system is a computer, with its central control corresponding to the control and

arithmetic sections, the flying spot store and barrier grid store corresponding to internal storage and the flip-flop groups and miscellaneous flip-flops in central control corresponding to the various registers and triggers in the arithmetic and control sections of a more conventional computer.

The IBM 704 was used for verifying programs for the experimental switching system, and the 704 program which was constructed for this purpose will be described in the following section. In this work, 19 different call patterns, involving intraoffice calls, outgoing calls, partial dials, calls to busy lines, wrong numbers and various other conditions were processed. A complete record of the progress of the calls was kept on each of the call patterns, showing the exact conditions of pertinent registers and conditions of flip-flops in the experimental switching system at the completion of every network operation. The 704 program can be used to record the conditions of every bit in the system's storage at any time.

## II. THE COMPUTER PROGRAM

The functions of the computer program are to simulate the operations of the central control, the scanner and the network control of the experimental switching system; to carry out the switching system program orders stored in the flying spot store; and to give output indications of whether calls submitted to the system are successfully completed.

In the switching system, actions are completed in units of 5 milliseconds. Each 5-millisecond period is called a cycle. A cycle is also the time that the switching system takes to go once through its main stored-program loop. In the simulation program on the computer, two counters are provided: a cycle counter and an order counter. The cycle counter keeps a count of the switching system program cycles, thus serving as the clock of the computer program. The order counter advances once each time a system order is carried out, but is cleared in the beginning of each cycle. It therefore keeps a count of the number of system orders executed within a cycle.

In the switching system customer actions and actions of the central control, scanner and network all occur in parallel, whereas on the computer these actions must be serialized. In the computer program, the serial positions in time of these actions are all in reference to the contents of the cycle counter.

In order to simulate the actions of the experimental switching system, the computer program contains complete images of the flying spot store and the barrier grid store as well as images of associated flip-flop registers.

In addition to these images, the computer program also includes an input program, an order control program, a network control program, an output program, a frequency-count program for order usage and other auxiliary programs.

2.1 *The Input Program*

The inputs received by the computer program consist of simulated dial pulses representing calls from customers. The form in which the dial pulses are received is illustrated in Fig. 1. Let us suppose that the telephone number dialed is WH 2-1111 and that the first off-hook pulse occurs at time  $t_0$ . Then the sequence of times  $t_1, t_2, \dots, t_{38}$  represents the number dialed and  $t_t$  represents the time at which the call is terminated. If this call happens to be the only one in the system from time  $t_0$  to  $t_t$ , the computer then receives as its input the sequence  $t_0, t_1, \dots, t_t$  in that order. If there should be several calls present in the system simultaneously, the sequence of times of each call is then interlaced with the other sequences and ordered according to the actual time of occurrence, and the complete list is stored in the computer in that order.

This list of times is examined once every cycle, when the contents of the cycle counter is compared with the next time entry appearing in the list. If this entry is not the same as the contents of the counter, no change in line condition has occurred in that cycle. If the two numbers are the same, then a change in line condition has occurred. This change is recorded by the computer program and the computer program enters the network control program.

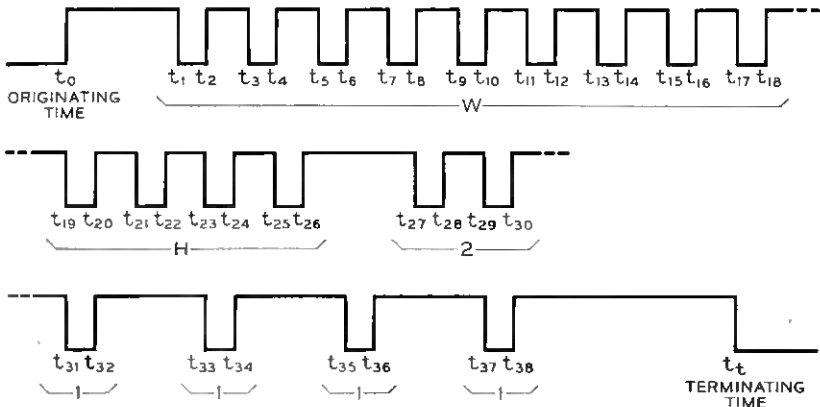


FIG. 1 — Form in which dial pulses are received..

## 2.2 *The Order Control Program*

The function of the order control program is to interpret and execute each of the 52 types of system program orders. At the heart of the order control program are some nine subroutines. Each system order is composed of five parts (A, B, C, D and E) and, according to the code for each part, a different set of subroutines is selected for the execution of the order by the computer program.

For example, the order 0,0,11,47,0 says that a customer line condition is to be matched against some spot in the barrier grid store. The address of the line is stored in the scanner register and the X part of the barrier grid store address is stored in the barrier grid register. The Y part of the barrier grid store address is the D code, or 47. If a mismatch occurs, the address of the next order to be executed is to be found in transfer register 1. If a match occurs, no transfer action is to be taken.

This order is carried out by the order control program in several steps. First, the order code is split into five subcodes, A, B, C, D and E. The subcodes A, B, C and E cause the order control program first to enter a subprogram which finds and stores the condition of the customer line in question, and then to enter another subprogram which finds and stores the condition of the spot in the barrier grid store in question. The two bits are then compared and no action is taken if a match occurs. If a mismatch occurs, a third subprogram is entered. The functions of this subprogram are, among other things, to set the return address, to set certain 704 addresses in preparation for the system program transfer, to check and see whether the transfer is to a new program order or for translation and, finally, to check the 704 console switches to see if transfer mode operation (Section 2.4) is desired.

## 2.3 *Network Control Program*

The function of the network control program is to simulate all the interactions between the network and central control circuitry. In the switching system, there are nine possible commands the common control circuitry may transmit to the network control, and the network can answer in one of two ways: "a command has been carried out partially," or "a command has been carried out completely and successfully." The network control program also sets and resets appropriate flip-flops, and checks and records conditions of all lines and trunks.

As an example, the command 0,20 says to release a distribution network connection from the A side of the distribution network; the A side distribution network trunk address is stored in the A side trunk selector

register. This command is carried out by the network control program in several steps. First, contents of the A side trunk selector register are gated to the A side trunk identifier register. The B side trunks are then scanned to see which one is connected to the A side trunk in question. The fact that both of these trunks are now made idle by the release command is then recorded. Finally, the network reports back to the central control that the command has been carried out completely and successfully.

#### 2.4 *The Output Program*

There are three modes of operation in the computer program, giving three types of outputs. The desired mode of operation can be selected manually on the 704 console. In the first or normal mode of operation, the machine gives an output only under one of the following two situations:

- i. The network had been requested to perform some action and has completed this action, or
- ii. Dialed digits are being outpulsed to a distant office.

Under the first situation the following information is printed out on the 704 printer: the time (in terms of 5-millisecond intervals) at which the network action is completed; the number of stored program orders that were executed in the particular 5-millisecond interval involved; the network action itself; the contents of various flip-flops and the contents of the originating registers, ringing register, network register and disconnecting registers.

In the second mode of operation (transfer mode I), in addition to the print-out under normal mode, a transfer record for the stored program is written on tape, which can then be put on a peripheral tape-to-print converter to give a printed transfer record. A transfer record consists of a count of the number of actual transfers made in the stored program, the transfer order executed, the return address for the transfer order, the address to which the transfer is made and the 5-millisecond interval in which the transfer has occurred. The return address in this case means the address to which the common control would have gone if the transfer had not been made.

A sample transfer record for one of the call patterns is shown in Table I. The first transfer order executed is 0,0,1,48,0, which says to read the bit at address  $X, Y$  of the barrier grid store, where  $X = 48$  and  $Y$  is to be found in the barrier grid register. The order itself is stored in address  $X = 2, Y = 15$  of the flying spot store, and the address transferred to is

TABLE I

Transfer Count	Return Address		Order Executed					Transfer to Address		5-Millisecond Interval Count
	X	Y	A	B	C	D	E	X	Y	
00001	03	15	0	0	001	048	0	18	15	00001
00002	21	15	0	0	001	050	0	26	49	
00003	31	49	2	0	010	028	0	10	28	
00004	14	28	0	2	000	026	0	08	30	
00005	15	30	0	0	004	004	0	22	40	
00006	03	15	0	0	001	048	0	18	15	00002
00007	21	15	0	0	001	050	0	26	49	
00008	31	49	2	0	010	028	0	10	28	
00009	14	28	0	2	000	026	0	08	30	
00010	16	30	0	0	004	006	0	22	40	
00011	03	15	0	0	001	048	0	18	15	00003
00012	21	15	0	0	001	050	0	26	49	
00013	31	49	2	0	010	028	0	10	28	
00014	14	28	0	2	000	026	0	08	30	
00015	15	30	0	0	004	004	0	22	40	
00016	03	15	0	0	001	048	0	18	15	00004
00017	21	15	0	0	001	050	0	26	49	
00018	31	49	2	0	010	028	0	10	28	
00019	14	28	0	2	000	026	0	08	30	
00020	18	30	0	0	004	008	0	22	40	
00021	03	15	0	0	001	048	0	18	15	00005
00022	21	15	0	0	001	050	0	26	49	
00023	31	49	2	0	010	028	0	10	28	
00024	14	28	0	2	000	026	0	08	30	
00025	13	30	1	0	002	002	0	28	05	
00026	30	05	1	0	000	008	0	07	03	
00027	10	03	2	0	020	054	0	20	54	
00028	25	54	0	0	001	048	0	26	54	
00029	29	54	0	0	001	050	0	22	40	
00030	03	15	0	0	001	048	0	18	15	
00031	21	15	0	0	001	050	0	26	49	
00032	31	49	2	0	010	028	0	10	28	
00033	14	28	0	2	000	026	0	08	30	

$X = 18$ ,  $Y = 15$  of the flying spot store. The next transfer order is encountered at address  $X = 20$ ,  $Y = 15$ , the order executed is 0,0,1,50,0 and the address transferred to is  $X = 26$ ,  $Y = 49$ , and so forth. The numbers at the right are the 5-millisecond intervals in which the transfers have occurred.

The third mode of operation (transfer mode II) is similar to the second except that, in addition to a transfer record on tape, the record is also printed immediately. The purpose of operating in this mode is to have immediate access to the transfer information.

### 2.5 *Frequency Count for Order Usage*

A program to record the frequency of usage of the stored program orders in any given period of time is available. Records were kept on two of the 19 call patterns and one of these is illustrated in Table II, in which three columns of data are shown. The first column is the stored-program order code, the second is an order usage count when the system is idle (i.e. there is no call in the system) and the third column shows an order usage count when there is a single call in the system. A comparison of columns 2 and 3 shows what orders are used and how often they are used because of the presence of the call in the system. From these records it appears that, of the 52 stored-program orders, about 60 per cent are used less than 1 per cent of the total time and about 20 per cent are used more than 88 per cent of the time.

### 2.6 *Other Auxiliary Programs*

The computer program includes about 75 error stops. These point out incorrect functioning of the system and possible computer error. The appearance of an illegal system program order or other malfunctioning of the system would lead the computer program to an error stop. The error stop code is readily identified and the error involved is found by consulting a list of possible errors prepared beforehand.

The computer program also includes several conversion programs, of which one converts the system orders from symbolic to binary and another converts the input dial pulses from decimal to binary.

## III. REMARKS AND CONCLUSIONS

The computer program attains a computer-to-real-time time-ratio of about 15 to 1 in the normal mode of operation and about 50 to 1 in transfer mode I. In other words, in the normal mode, the 704 takes about 75 milliseconds to go through the work involved in a 5-millisecond period in real time. To get a transfer record on tape, it would take the 704 about one quarter second to go through a 5-millisecond interval in real time.

This time ratio is achieved by taking advantage of the extra time normally inherent in the actual system. The experimental system as a whole is essentially a clocked system, in that the principal parts of the stored program are normally repeated once every 5 milliseconds, even though the work specified for each 5-millisecond interval is usually performed in less than 5 milliseconds. By making the computer program asynchronous — in the sense that each simulated 5-millisecond interval

TABLE II

Order Code			Usage, No Call	Usage, One Call
A	B	C		
0, 1	0, 1, 2	0	872	944
		1	1156	1161
		2	835	860
		3	0	0
		4	867	998
		5	0	0
		6	54	87
		7	0	2
		8	0	19
		9	0	5
		10	432	432
		11	0	344
		12	0	0
		13	1100	1160
		14	0	1
		15	0	0
		16	0	1
		17	0	1
18	0	1		
2	—	—	1031	1115
3	0	—	0	0
3	1	—	0	64
3	3	—	803	1423
4	—	—	3879	4357
5	—	—	632	647
6	—	—	90	115
7	0	—	550	5126
7	1	—	0	29
7	2	—	0	355
7	3	0	0	101
		1	393	404
		2	0	0
		3	0	0
		4	0	3
		5	0	11
		6	0	2
		7	27	46
		8	0	0
		9	0	0
		10	1156	1162
		11	1807	1858
		12	0	81
		13	0	4
		14	0	4
		15	0	0
		16	0	0
		17	0	0
		18	0	0
		19	0	2
		20	0	1
		21	0	2
		22	0	0

is only as long as the work requires it to be — a sharp reduction in time ratio is attained.

To save time in putting calls through the computer program, customer dialing time is speeded up by a factor of about six (i.e. actual dialing time is six times longer). Under this condition, the longest call pattern involves some 4,000 5-millisecond intervals and takes approximately 5 minutes of computer time to go through.

In writing the computer program, we are confronted with three basic problems: the computer-to-real-time time-ratio, the process of understanding the system requirements and disciplines and the process of finding those output parameters which will give a good reflection of the correctness of the performance of the actual system.

The computer-to-real-time time-ratio determines whether a simulation problem is practically and economically possible to run. The simulation of any complex structure such as a telephone system is hampered at the start by the lack of commercially available computers which are capable of carrying out several logical programs simultaneously. It means that the work performed by a telephone system must be serialized before it can be programmed on a computer and, as a result, the computer program will be run at a much slower pace.

We have purposely omitted memory requirements in this list of problems. With the kinds of tape and optical storage now available, the amount of memory needed ceases to be a true obstacle in practice; rather, a basic consideration is the time requirement. In other words, we may say (with some exaggeration) that, in practice, as much memory as any person should need can be obtained, but that there may not be sufficient time in his life for him to make use of this memory.

The problem of understanding the system requirements and disciplines is a basic one in systems design. At the root is the question of how to find a simple and flexible language in which the requirements and disciplines can be spelled out concisely, correctly and easily. The logical design or analysis problem is then one of mapping (other names: compiling, automatic coding, automatic programming) the specifications in the basic language into the language of logical circuitry or the language of a computer.

As a result of this work, the logical validity of the program for the experimental system was verified in advance of the time when the program could be written into the flying spot store and verified in its ultimate environment. Until the program was used in the system, it could not be said to have been completely verified, since certain timing relations peculiar to the circuitry in the system could interact with the pro-

gram in an unfavorable manner. On the other hand, had the system itself been used for the entire program verification, the amount of time required for system testing would probably have been greatly increased. In the case of a suspected error, it might be quite difficult to determine whether the error was due to difficulty with the circuitry or to some peculiarity of the program. The use of a computer for program verification therefore has two great advantages: over-all developmental time for the system is reduced and logical difficulties can be made almost independent of electrical difficulties.

#### REFERENCE

1. Joel, A. E., Jr., An Experimental Switching System Using New Electronic Techniques, B.S.T.J., **37**, September 1958, p. 1091.

# Nonuniformities in Laminated Transmission Lines

By GORDON RAISBECK

(Manuscript received April 4, 1958)

*The effect on transmission properties of certain nonuniformities in laminated transmission lines has been calculated by a perturbation method. Particular cases have been calculated, including the effect of varying radius of curvature in a cylindrical Clogston line, the effect of systematic variation in effective dielectric constant and the effect of random variation in layer thickness where the nonuniformities are known only through statistical properties. In one Clogston line where measurements of nonuniformity have been made the method predicts a transmission impairment in substantial agreement with observations.*

## I. INTRODUCTION

The remainder of this paper is divided into seven parts. Section II contains an outline of the notation used and then a discussion of a new formula for the losses in a parallel-plane laminated transmission line\* due to irregularities in the laminations. The section concludes with an outline of a procedure for calculating losses in a given line due to known irregularities.

Section III shows the derivation of the formula by the application of a perturbation procedure to a differential equation derived by Morgan.<sup>3†</sup> The procedure leads to an expansion of the attenuation in a

\* The fundamental notions about laminated conductors, often called "Clogston conductors"<sup>1</sup> or "Clogston lines"<sup>1</sup>, are given in a paper by Clogston.<sup>1</sup> Further details and embodiments are also shown in U. S. Patents 2,769,147 (A. M. Clogston and H. S. Black), 2,769,148 (A. M. Clogston), 2,769,149 (J. G. Kreer) and 2,769,150 (H. S. Black and S. P. Morgan). Experimental results were described in a report by Black, Mallinckrodt and Morgan.<sup>2</sup> The most thorough mathematical treatment published to date is an exhaustive and detailed analysis by Morgan.<sup>3</sup> Vaage<sup>4</sup> has reduced some of the results to terms more familiar to transmission engineers. King and Morgan<sup>5</sup> give a lucid retrospective glance over the whole subject, and present a series of charts and formulas which enable one easily to make quantitative estimates of transmission parameters of interest. This paper is probably the easiest place to start a study of laminated conductors, and provides more than enough background for reading the present paper.

† Ref. 3 is referred to hereafter simply as Morgan.

power series whose argument is the magnitude of the irregularities in the laminations and whose coefficients depend on the distribution of the irregularities. The expansion is carried as far as the first nonvanishing term.

Section IV compares the magnitude of allowable irregularities computed with the new formula to values computed by an exact method for the two extreme cases described by Morgan. The results correspond within five per cent.

Section V shows that the effect of finite lamination thickness can be correctly computed by considering the finite laminae as perturbations of a uniform medium. It is proved heuristically that the effects of non-uniformity and of finite lamination thickness are independent and additive.

Section VI applies the formula of Section III to random irregularities. It is shown that the formula is directly applicable when the irregularities are specified by the absolute value of their Fourier spectra (i.e., by their autocorrelation), and two special cases are worked out in detail.

Section VII applies the formula to the measured irregularities in an experimental cylindrical laminated line. The correspondence between predicted and measured losses is satisfactory, and demonstrates that the method described, despite drastic simplifying assumptions, gives results agreeing quantitatively with experiment.

Section VIII shows how to compute the effect of curvature of laminae in a coaxial Clogston line. The results are precisely those predicted by Morgan. They give independent support to his formulas, which are based on certain plausible physical assumptions and approximations.

## II. DESCRIPTION OF RESULTS

The notation used by Morgan will be adopted throughout. In particular, we shall deal repeatedly with thin laminae of a conductor and of an insulating dielectric, with physical properties identified as follows:

$$\begin{aligned}
 \text{conductor thickness} &= t_1, \\
 \text{conductor magnetic permeability} &= \mu_1, \\
 \text{conductor conductivity} &= g_1, \\
 \text{insulator thickness} &= t_2, \\
 \text{insulator dielectric permittivity} &= \epsilon_2, \\
 \text{insulator magnetic permeability} &= \mu_2.
 \end{aligned} \tag{1}$$

Sometimes the properties of all layers of one material will be assumed identical, but at other times, as shown by the context, we shall assume

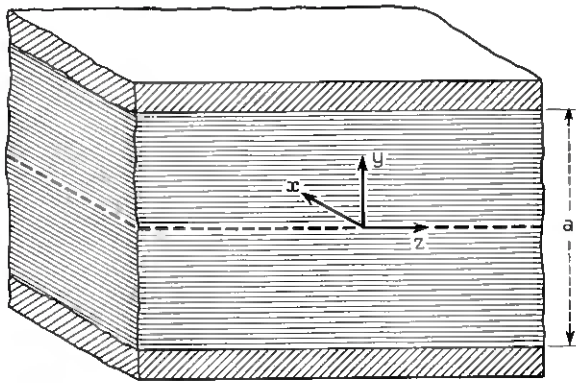


Fig. 1—A schematic section of a parallel-plane Clogston 2 laminated transmission line between two bounding surfaces, showing the orientation of a coordinate system.

that the properties vary from layer to layer about their nominal values. In general, we shall assume

$$\mu_1 = \mu_2 = \mu_0 \quad (2)$$

because this seems to be sufficiently general to include most cases of interest.

Consider a parallel-plane Clogston 2 transmission line bounded by infinite-impedance sheets at  $y = \pm \frac{1}{2}a$  (see Fig. 1). Near any given point the average electrical constants of the stack are\* (see Fig. 2)

$$\begin{aligned} \bar{\epsilon} &= \frac{\epsilon_2}{1 - \theta}, \\ \bar{\mu} &= \theta\mu_1 + (1 - \theta)\mu_2, \\ \bar{g} &= \theta g_1, \end{aligned} \quad (3)$$

where the subscript "1" refers to the conductor material, the subscript "2" to the dielectric material and

$$\theta = \frac{t_1}{t_1 + t_2} \quad (4)$$

is the fraction of the cross section of the line made up of the conducting material.

Assume that  $\bar{\epsilon}$ ,  $\bar{\mu}$  and  $\bar{g}$  are not quite constant, but vary about average values thus:

\* Morgan,<sup>3</sup> Equation 90.

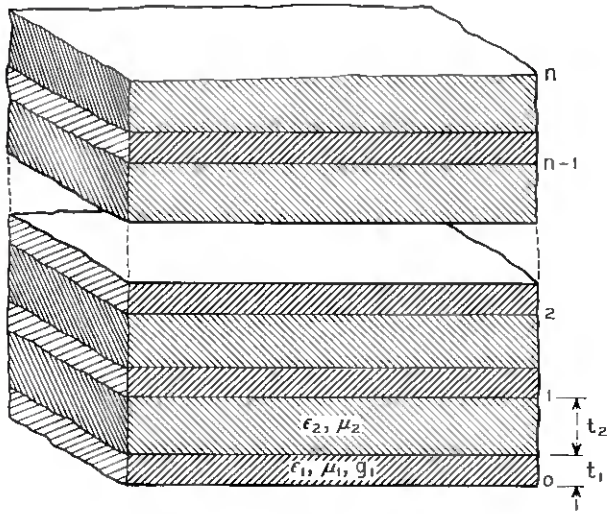


Fig. 2 — Detailed schematic section showing the individual layers in a laminated transmission line.

$$\begin{aligned}\bar{\epsilon} &= \bar{\epsilon}_0 + \Delta\bar{\epsilon}, \\ \bar{\mu} &= \bar{\mu}_0 + \Delta\bar{\mu}, \\ \bar{g} &= \bar{g}_0 + \Delta\bar{g},\end{aligned}\quad (5)$$

where the average values are characterized by a subscript "0", and  $\Delta\bar{\epsilon}$ ,  $\Delta\bar{\mu}$  and  $\Delta\bar{g}$  have average value zero.

Following Morgan, let

$$\xi = \frac{y}{a} + \frac{1}{2}. \quad (6)$$

This normalizes the thickness, so that in terms of  $\xi$  the line is bounded by the planes  $\xi = 0$ ,  $\xi = 1$ . Then let

$$w(\xi) = H_x(y), \quad (7)$$

the  $x$ -component of the magnetic field of a wave traveling down the line in the  $z$ -direction. Also let

$$\begin{aligned}\frac{\Delta\bar{\mu}}{\bar{\mu}_0} + \frac{\Delta\bar{\epsilon}}{\bar{\epsilon}_0} &= \frac{C}{\omega\bar{\mu}_0\bar{g}_0a^2} \varphi(y) \\ &= \frac{C}{\omega\bar{\mu}_0\bar{g}_0a^2} f(\xi).\end{aligned}\quad (8)$$

The new function  $f(\xi)$  is a dimensionless function which is a measure of the deviation of  $\bar{\mu}$  and  $\bar{\epsilon}$  from their average values  $\bar{\mu}_0$  and  $\bar{\epsilon}_0$ . The constant  $C$  is a dimensionless parameter. (It is convenient to assume that  $f(\xi)$  has fixed magnitude in some sense but a variable shape, and that all variation in the magnitude of the irregularities of the line is due to  $C$ . Actually, all that is specified is the product  $Cf(\xi)$ , which may be factored in any way you please.) It is shown by Morgan that

$$\frac{d^2 w}{d\xi^2} + [\Lambda - iCf(\xi)]w(\xi) = 0, \quad (9)$$

with the boundary conditions

$$w(0) = w(1) = 0, \quad (10)$$

and also that

$$\gamma = \alpha + j\beta = i\omega\sqrt{\bar{\mu}\bar{\epsilon}_0}(1 + \Lambda/i\omega\bar{\mu}_0\bar{g}_0a^2)^{1/2}, \quad (11)$$

or approximately

$$\begin{aligned} \alpha &= \operatorname{Re} \gamma = \operatorname{Re} \frac{\Lambda}{2\sqrt{\bar{\mu}_0/\bar{\epsilon}_0\bar{g}_0a^2}}, \\ \beta &= \operatorname{Im} \gamma = \omega\sqrt{\bar{\mu}_0\bar{\epsilon}_0} + \operatorname{Im} \frac{\Lambda}{2\sqrt{\bar{\mu}_0/\bar{\epsilon}_0\bar{g}_0a^2}}, \end{aligned} \quad (12)$$

where  $\Lambda$  is an eigenvalue of the differential equation. If the stack is perfectly uniform,  $\Delta\bar{\mu}$  and  $\Delta\bar{\epsilon}$  are zero, and the eigenvalues are

$$\Lambda = \pi^2, 4\pi^2, 9\pi^2, \dots \quad (13)$$

corresponding to the eigenfunctions

$$w = \sqrt{2} \sin \pi\xi, \sqrt{2} \sin 2\pi\xi, \sqrt{2} \sin 3\pi\xi, \dots \quad (14)$$

These eigenfunctions show that (as is well known from Morgan) the magnetic field strengths in the various modes in a uniform line vary sinusoidally across the stack, the variation going through one, two, three,  $\dots$  half sine waves and always vanishing at the surfaces.

Since  $C$  varies continuously, we expect the eigenvalues and eigenfunctions to vary continuously in a manner depending on  $f(\xi)$ . If  $C$  is small, i.e., if the irregularity of the stack is small, the eigenvalues can be expanded in a power series in  $C$ . The analysis is in Section III of this paper. The first three terms of the series for the lowest eigenvalue are

$$\Lambda_1 = \pi^2 + iCa_1 + C^2 \sum_{m=2}^{\infty} \frac{a_m^2}{\pi^2 m^2 - \pi^2} + O(C^3), \quad (15)$$

where

$$a_m = 2 \int_0^1 f(x) \sin \pi x \sin m\pi x \, dx; \quad (16)$$

that is, the coefficients  $a_m$  are the coefficients of the Fourier sine series for

$$f(x)\sqrt{2} \sin \pi x = \sum_1^{\infty} a_m \sqrt{2} \sin \pi m x. \quad (17)$$

From the above expression one can conclude that

$$\alpha = \alpha_0 \left( 1 + \frac{C^2}{\pi^2} \sum_2^{\infty} \frac{a_m^2}{\pi^2 m^2 - \pi^2} \right), \quad (18)$$

where  $\alpha_0$  is the attenuation which the line would have if it had no irregularities.

An alternative approach is derived from the theory of operators. The result is

$$\begin{aligned} \Delta_1 &= \pi^2 + iC \int_0^1 f(x)\sqrt{2} \sin \pi x \sqrt{2} \sin m\pi x \, dx \\ &+ C^2 \int_0^1 \int_0^1 k(x, y) f(x) \sqrt{2} \sin \pi x f(y) \sqrt{2} \sin \pi y \, dx \, dy + O(C^3), \end{aligned} \quad (19)$$

where  $k(x, y)$  is the reduced resolvent kernel:

$$\begin{aligned} k(x, y) &= \sum_{m=2}^{\infty} \frac{\sqrt{2} \sin m\pi x \sqrt{2} \sin m\pi y}{m^2 \pi^2 - \pi^2} \\ &= \frac{1}{\pi^2} [\sin \pi x \sin \pi y - 2\pi x \cos \pi x \sin \pi y \\ &\quad - 2\pi y \cos \pi y \sin \pi x + 2\pi \sin \pi x \cos \pi y], \quad x \leq y, \end{aligned} \quad (20)$$

$$k(y, x) = k(x, y).$$

In this particular case it is not hard to show that the results are identical.

For practical results, it is convenient to let

$$\frac{\Delta \bar{\epsilon}}{\bar{\epsilon}_0} + \frac{\Delta \bar{\mu}}{\bar{\mu}_0} = A\varphi(y) = Af(\xi) \quad (21)$$

and to assume

$$\int_0^1 f^2(\xi) \, d\xi = 1. \quad (22)$$

Note that

$$A = \left\langle \frac{\Delta\bar{\epsilon}}{\bar{\epsilon}_0} + \frac{\Delta\bar{\mu}}{\bar{\mu}_0} \right\rangle, \quad (23)$$

where the angular brackets denote the root mean square value. As a convenience, we make the definition

$$\Sigma = \sum_2^{\infty} \frac{a_m^2}{\pi^2 m^2 - \pi^2} = 2 \int_0^1 \int_0^1 k(x, y) f(x) f(y) \sin \pi x \sin \pi y \, dx \, dy, \quad (24)$$

where  $a_m$  and  $k$  are defined as above.

The expression for attenuation can be written

$$\alpha = \alpha_0 \left( 1 + \frac{f^2}{f_i^2} \right), \quad (25)$$

where

$$f_i = \frac{1}{2A\bar{\mu}_0\bar{g}_0\alpha^2\Sigma^{1/2}}. \quad (26)$$

In a line having finite laminations,

$$\alpha_0 = \alpha_{00} \left[ 1 + \frac{f^2}{(f_2')^2} \right] \quad (27)$$

(see Fig. 3), except for very low or very high frequencies, where

$$f_2' = \frac{\sqrt{3}}{2\mu_1 g_1 t_1 T_1}. \quad (28)$$

Heuristic reasoning and experimental evidence are given in a later section to show that the effects of finite laminations and of nonuniformity are additive, at least if both are small. Hence we can write

$$\begin{aligned} \alpha &= \alpha_{00} \left[ 1 + \frac{f^2}{f_i^2} + \frac{f^2}{(f_2')^2} \right] \\ &= \alpha_{00} \left[ 1 + \frac{f^2}{(f_2')^2} (1 + b^2) \right] \\ &= \alpha_{00} \left[ 1 + \frac{f^2}{(f_{i2})^2} \right], \end{aligned} \quad (29)$$

where

$$b = \frac{f_2'}{f_{i2}} \quad (30)$$

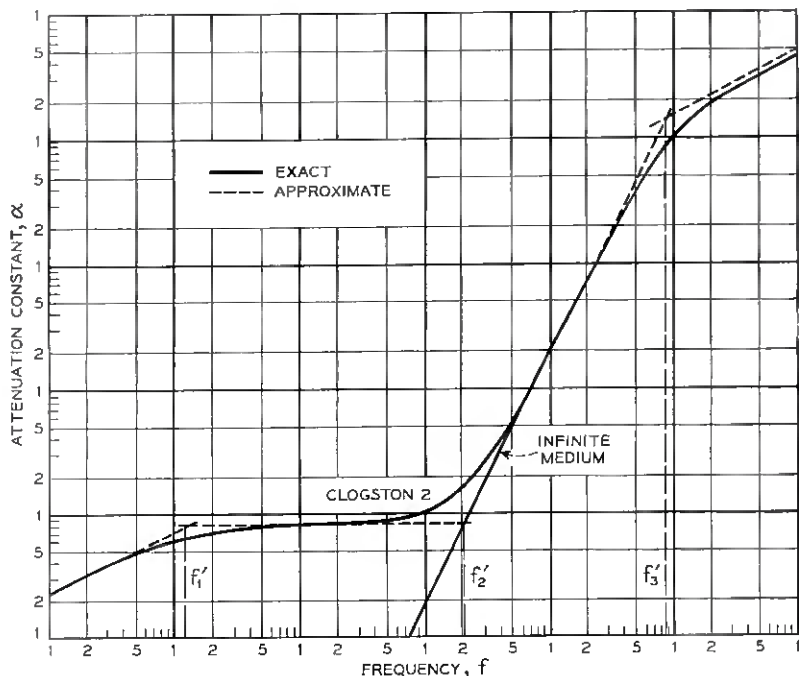


Fig. 3 — Attenuation in a plane Clogston 2 laminated transmission line, and in an infinite laminated medium, on a log-log scale as a function of frequency.

and  $\alpha_{00}$  is the low-frequency attenuation of the uniform line. The particular reason for this choice of variable is the simplification of various formulac. If we assume

$$\mu_1 = \mu_2 = \bar{\mu}, \quad (31)$$

as is ordinarily the case when no ferromagnetic materials are involved,

$$b = \frac{\sqrt{3}nA\sqrt{\Sigma}}{\theta}, \quad (32)$$

where  $n$  is the number of layers in the stack. This expression is simple, and separates the various parameters that enter into the problem:  $n$  and  $\theta$  depend only on the geometry of the line,  $A$  on the magnitude of the irregularities and  $\Sigma$  on the distribution of the irregularities. The whole effect of the irregularities can be summed up by saying that the effec-

tive bandwidth of the line is reduced by a factor

$$\frac{f_{i2}}{f_2'} = \frac{1}{\sqrt{1 + b^2}}. \quad (33)$$

It is clear that such quantities as conductivity, dielectric constant, dimensions and so on do not appear in the expression for  $b$ . Hence, although the cutoff frequency of the line is a complex function of all these quantities, the relative bandwidth of the line compared with that of a similar line having no irregularities depends only on  $n$ ,  $\theta$ , the magnitude of the irregularities  $A$  and the quantity  $\Sigma$  derived from the distribution of the irregularities.

If it is assumed that  $\mu_1 = \mu_2$ , then it is logical to assume that  $\Delta\bar{\mu} = 0$ . In this case

$$Af(\xi) = \frac{\Delta\epsilon}{\bar{\epsilon}_0}. \quad (34)$$

If it is further assumed\* that the local variations are due to variation in thickness  $t_1$  and  $t_2$ , it is easy to show from the formula for  $\bar{\epsilon}$  that

$$\frac{\Delta\bar{\epsilon}}{\bar{\epsilon}_0} = \theta \left( \frac{\Delta t_1}{t_1} - \frac{\Delta t_2}{t_2} \right), \quad (35)$$

where  $t_1$  and  $t_2$  are nominal values, and  $\Delta t_1$  and  $\Delta t_2$  are deviations of the actual from the nominal values, of the thicknesses of conductor material and dielectric material, and

$$\theta = \frac{t_1}{t_1 + t_2}. \quad (36)$$

As a practical matter, the computation of the loss of bandwidth due to irregularities can be carried out as follows. First, determine the fractional irregularities in the line

$$\frac{\Delta t_1}{t_1} \quad (37)$$

and

$$\frac{\Delta t_2}{t_2} \quad (38)$$

---

\* At present, it seems likely that the effect of irregularity in  $\epsilon_2$  will be small compared to the effect of thickness irregularities in practical cases.

as functions of  $\xi = y/a + 1/2$ . Then determine

$$A = \left\langle \frac{\Delta \bar{\epsilon}}{\bar{\epsilon}_0} \right\rangle \quad (39)$$

$$= \theta \left[ \int_0^1 \left( \frac{\Delta t_1}{t_1} - \frac{\Delta t_2}{t_2} \right)^2 d\xi \right]^{1/2}$$

and

$$f(\xi) = \frac{\theta}{A} \left( \frac{\Delta t_1}{t_1} - \frac{\Delta t_2}{t_2} \right). \quad (40)$$

Now,

$$\int_0^1 f^2(\xi) d\xi = 1 \quad (41)$$

and

$$A f(\xi) = \frac{\Delta \bar{\epsilon}}{\bar{\epsilon}_0}. \quad (42)$$

Then, using either the Fourier coefficients  $a_m$  (16) or the reduced solvent  $k$  (20), find the sum  $\Sigma$  defined in (24). Finally, form the quantity  $b$  (32). Then the reduction in bandwidth of the line compared to a similar line with no irregularities is given by (33).

The perturbation method can also be applied to finding the effect of finite lamination thickness. When applied to the above case, it gives Morgan's result

$$\gamma^2 = -\omega^2 \mu \bar{\epsilon} \left[ 1 + \frac{\pi^2}{i\omega \mu \bar{g} a^2} - \frac{i\omega \mu \bar{g} \theta^2 a^2}{12n^2} \right]. \quad (43)$$

When applied to a cylindrical line of outer radius  $b$  and inner radius zero, it gives, in agreement with Morgan's equation 486,

$$\gamma^2 = -\omega^2 \mu \bar{\epsilon} \left[ 1 + \frac{(3.8317)^2}{i\omega \mu \bar{g} b^2} - \frac{i\omega \mu \bar{g} \theta^2 b^2}{12n^2} \right]. \quad (44)$$

The only difference between (43) and (44) is that the first root  $\pi$  of

$$\sin x = 0 \quad (45)$$

is replaced by the first root 3.8317 of

$$J_1(x) = 0. \quad (46)$$

As a result, the low-frequency attenuation of a solid cylindrical Clogston

line of radius  $b$  is higher than that of a flat line of thickness  $b$  by a factor  $(3.8317/\pi)^2 = 1.4876$ , but the high-frequency attenuation is exactly the same! The crossover frequency  $f_{2i}$  is shifted up by a factor  $3.8317/\pi = 1.2197$ .

### III. EVALUATION OF ATTENUATION IN THE NONUNIFORM LINE

The expansion of  $\Lambda_1$ , and hence of  $\alpha$ , in terms of powers of  $C$  is accomplished as follows.† The governing equation is equation 532 of Morgan (Ref. 3, p. 131):

$$\frac{d^2 w}{d\xi^2} + [\Lambda - jCf(\xi)]w(\xi) = 0, \quad (47)$$

subject to the boundary conditions

$$w(0) = 0, \quad w(1) = 0. \quad (48)$$

Here  $\Lambda$  is the eigenvalue from which the propagation constant of the line can be derived by (11), and  $w(\xi)$  is the corresponding eigenfunction which tells, according to (7), how the amplitude of the transverse component of the magnetic field varies across the stack. Equation (47) can be considered a perturbation of the equation

$$\frac{d^2 w}{d\xi^2} + \Lambda w = 0, \quad (49)$$

subject to the same boundary conditions. Suppose this equation has as its eigenvalues

$$\Lambda_1, \Lambda_2, \dots, \quad (50)$$

and as its corresponding normalized eigenfunctions

$$w_1, w_2, \dots. \quad (51)$$

In fact,

$$\begin{aligned} \Lambda_n &= \pi^2 n^2, \\ w_n &= \sqrt{2} \sin \pi n \xi. \end{aligned} \quad (52)$$

Now suppose the perturbed equation

$$\frac{d^2 w^*}{d\xi^2} + [\Lambda^* - jCf(\xi)]w^* = 0, \quad (53)$$

† This method is given by Courant and Hilbert.<sup>6</sup> It was pointed out to the author by S. P. Morgan.

where  $f(\xi)$  is a given function of  $\xi$ , and  $C$  is a (small) parameter, has as its eigenvalues

$$\Lambda_1^*, \Lambda_2^*, \dots \quad (54)$$

and as corresponding eigenfunctions

$$w_1^*, w_2^*, \dots \quad (55)$$

Following Courant and Hilbert,<sup>6</sup> suppose there exists an expansion

$$\begin{aligned} w_n^* &= w_n + Cx_n + C^2y_n + \dots, \\ \Lambda_n^* &= \Lambda_n + C\mu_n + C^2\nu_n + \dots. \end{aligned} \quad (56)$$

Using the notation of Courant and Hilbert, let

$$\begin{aligned} d_{nl} &= \int_0^1 j f(\xi) w_n(\xi) w_l(\xi) d\xi, \\ a_{nn} &= 0, \\ a_{nl} &= \frac{d_{nl}}{\Lambda_n - \Lambda_l}, \quad n \neq l. \end{aligned} \quad (57)$$

Then, as shown in Courant and Hilbert, the series expansions to terms of the second degree are:

$$\begin{aligned} w_n^* &= w_n + C \sum_{j=1}^{\infty} \frac{d_{nj}}{\Lambda_n - \Lambda_j} w_j \\ &+ C^2 \left[ \sum_{j=1}^{\infty} \frac{w_j}{\Lambda_n - \Lambda_j} \left( \sum_{k=1}^{\infty} a_{nk} d_{kj} - \mu_n a_{nj} \right) - \frac{1}{2} w_n \sum_{k=1}^{\infty} a_{nk}^2 \right] \end{aligned} \quad (58)$$

$$\Lambda_n^* = \Lambda_n + C d_{nn} + C^2 \sum_{j=1}^{\infty} a_{nj} d_{jn} + \dots$$

By following the same method, further terms of the power series could be found.

An equivalent exposition in terms of linear operator is given by Kato.<sup>7</sup> He discusses the behavior of eigenvalues of the equation

$$(H_0 + kH^{(1)} - \lambda_k)\varphi = 0 \quad (59)$$

and shows that, formally,

$$\lambda_k = \lambda_0 + k(H^{(1)}\varphi_0, \varphi_0) + k^2[-(SH^{(1)}\varphi_0, H^{(1)}\varphi_0)] + O(k^3), \quad (60)$$

and a corresponding equation for  $\varphi_K$ . The relation of his notation to

ours is given below. Note that  $H_0$ ,  $H^{(1)}$  and  $S$  represent operators, not functions, and that  $(, )$  is a functional of the variables it surrounds.

$$\begin{aligned}
 \epsilon &\leftrightarrow -iC, \\
 \lambda_0 &\leftrightarrow \Lambda_1, \\
 \lambda_k &\leftrightarrow \Lambda_1^*, \\
 \varphi_0 &\leftrightarrow w_1, \\
 \varphi_k &\leftrightarrow w_1^*, \\
 H_0 u &= \frac{d^2 u}{dx^2}, \\
 H^{(1)} u &= f(x)u(x), \\
 (u, v) &= \int_0^1 u(x)v(x) dx, \\
 Su &= \int_0^1 k(x, y)u(y) dy,
 \end{aligned}
 \tag{61}$$

where  $k$  is the resolvent kernel

$$k(x, y) = \sum_2^\infty \frac{w_m(x)w_m(y)}{\Lambda_m - \Lambda_1}.
 \tag{62}$$

The resulting expression for  $\Lambda_1^*$  is

$$\begin{aligned}
 \Lambda_1^* &= \Lambda_1 + jC \int_0^1 f(x)w_1^2(x) dx \\
 &\quad + C^2 \int_0^1 \int_0^1 k(x, y)f(x)f(y)w_1(x)w_1(y) dx dy + O(C^3) \\
 &= \Lambda_1 + 2jC \int_0^1 f(x) \sin^2 \pi x dx \\
 &\quad + 2C^2 \int_0^1 \int_0^1 k(x, y)f(x)f(y) \sin \pi x \sin \pi y dx dy + O(C^3),
 \end{aligned}
 \tag{63}$$

as stated before.

The advantage of these expressions is that the function  $f(\xi)$  need not be specified beforehand. In fact, as we shall see later, it need not even be exactly specified. We shall presently apply these expressions to cases where  $f(\xi)$  is a random function with a specified spectrum.

## IV. NUMERICAL RESULTS — COMPARISON WITH MORGAN

As a preliminary to further numerical results, we can check the formulas just derived with exact numerical results derived in Morgan for certain special cases. For example, in Fig. 22 of Ref. 3 an irregularity is described for which

$$\begin{aligned} f(\xi) &= -1, & 0 \leq \xi \leq \frac{1}{2}, \\ f(\xi) &= +1, & \frac{1}{2} < \xi \leq 1. \end{aligned} \quad (64)$$

In the case of the lowest eigenvalue

$$\begin{aligned} a_m &= 0, & m \text{ odd} \\ &= 4 \int_0^{1/2} \sin \pi \xi \sin \pi m \xi d\xi & m \text{ even} \\ &= \frac{4m(-1)^{(m/2)+1}}{\pi(m^2 - 1)} & m \text{ even,} \\ \Sigma &= \sum_2^{\infty} \frac{16m^2}{\pi^4(m^2 - 1)^3} & (65) \\ &= 0.0329, \\ \alpha &= \alpha_0 \left[ 1 + \frac{C^2}{\pi^2} \Sigma \right] \\ &= \alpha_0 [1 + 0.00333C^2]. \end{aligned}$$

For the second eigenvalue

$$\alpha = \alpha_0 [4 - 0.0019C^2], \quad (66)$$

where  $\alpha_0$  is still the low frequency attenuation corresponding to the lowest eigenvalue. Fig. 4 shows a comparison of these curves with the curves published in Ref. 3, Fig. 22. The value of  $C$  which makes  $\alpha$  twice  $\alpha_0$  is

$$C = (0.00333)^{-1/2} = 17.3. \quad (67)$$

This compares well with Morgan's precise value 16.5. Similarly, if

$$Cf(\xi) = -C \cos 6\pi\xi, \quad (68)$$

as in Ref. 3, Fig. 30,

$$Cf(\xi) \sin \pi\xi = -\frac{C}{2} \sin 7\pi\xi + \frac{C}{2} \sin 5\pi\xi,$$

$$C^2\Sigma = \frac{C^2}{\pi^2} \left( \frac{1/4}{49-1} + \frac{1/4}{25-1} \right) = \frac{C^2}{64\pi^2}, \quad (69)$$

$$\alpha = \alpha_0 \left( 1 + \frac{C^2}{64\pi^4} \right).$$

On a graph, this is indistinguishable from the curve in Ref. 3, Fig. 30. The value of  $C$  for which the attenuation is doubled is

$$C = 8\pi^2 = 78.9, \quad (70)$$

the same as Morgan's result to three significant figures. These two results, representing both extremes in the computation reported in Morgan, are sufficiently close to give us a good deal of confidence in this method.

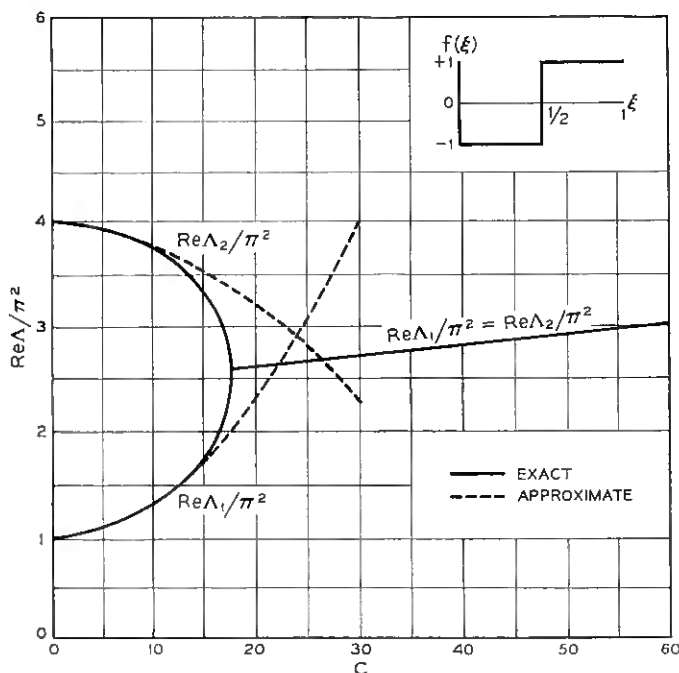


Fig. 4 — Eigenvalues for a nonuniform laminated stack whose average properties are constant except for a single symmetric step-discontinuity: approximate values computed from two terms of the perturbation-method power series compared with exact values derived by Morgan.

The following relation can be used to simplify numerical computation. If  $f(x)$  is expanded in a Fourier cosine series

$$f(x) = \frac{b_0}{2} + \sum_1^{\infty} b_m \cos m\pi x, \quad (71)$$

then

$$\begin{aligned} f(x) \sin \pi x &= \frac{b_0}{2} \sin \pi x + \sum_1^{\infty} b_m (\cos m\pi x \sin \pi x) \\ &= \frac{b_0}{2} \sin \pi x + \sum_1^{\infty} \frac{b_m}{2} [\sin (m+1)\pi x - \sin (m-1)\pi x] \\ &= \sum_0^{\infty} \frac{b_{m-1} - b_{m+1}}{2} \sin m\pi x \\ &= \sum_0^{\infty} a_m \sin m\pi x, \end{aligned} \quad (72)$$

where

$$a_m = \frac{b_{m-1} - b_{m+1}}{2}, \quad (73)$$

and we assume that  $b_{-1}$  (otherwise undefined) equals zero.

If  $b_{m-1}$  and  $b_{m+1}$  are random variables with Gaussian distribution about zero and rms values  $\langle b_{m-1} \rangle$  and  $\langle b_{m+1} \rangle$ , then  $a_m$  is also a random variable with Gaussian distribution about zero, and its rms value is

$$\langle a_m \rangle = \frac{1}{2} \sqrt{\langle b_{m-1} \rangle^2 + \langle b_{m+1} \rangle^2}. \quad (74)$$

## V. THE EFFECT OF FINITE LAMINATIONS

Following Morgan, equations 2 and 3 [but supposing that  $(g + j\omega\epsilon)$  is a function of  $y$ , as it is indeed if the medium has finite laminations], we arrive at the equation

$$\frac{1}{g + j\omega\epsilon} \frac{\partial^2 H_x}{\partial y^2} + \frac{\partial H_x}{\partial y} \frac{\partial}{\partial y} \left( \frac{1}{g + j\omega\epsilon} \right) - \left( j\omega\mu - \frac{\gamma^2}{g + j\omega\epsilon} \right) H_x = 0. \quad (75)$$

Now let

$$\begin{aligned} \tilde{f} &= \int_{-a/2}^{+a/2} (g + j\omega\epsilon) dy, \\ u &= \frac{1}{\tilde{f}} \int_{-a/2}^y (g + j\omega\epsilon) dy, \end{aligned} \quad (76)$$

$$H_x(y) = H(u).$$

Then we find

$$\frac{\partial^2 H}{\partial u^2} - \bar{f}^2 \left[ \frac{j\omega\mu}{g + j\omega\epsilon} - \frac{\gamma^2}{(g + j\omega\epsilon)^2} \right] H = 0, \tag{77}$$

subject to the boundary conditions

$$H(0) = 0, \quad H(1) = 0. \tag{78}$$

We can regard this as a perturbation of

$$\frac{\partial^2 H}{\partial u^2} + k^2 H = 0, \tag{79}$$

where

$$\begin{aligned} k^2 &= -\bar{f}^2 \int_0^1 \left[ \frac{j\omega\mu}{g + j\omega\epsilon} - \frac{\gamma^2}{(g + j\omega\epsilon)^2} \right] du \\ &= -\bar{f} \int_{-a/2}^{a/2} \left( j\omega\mu - \frac{\gamma^2}{g + j\omega\epsilon} \right) dy. \end{aligned} \tag{80}$$

To a very good degree of approximation,

$$\begin{aligned} \bar{f} &= a\theta g_1 = a\bar{g}, \\ k^2 &= -j\omega\mu\bar{g}a^2 + \frac{\gamma^2 a^2 \bar{g}}{j\omega\epsilon}. \end{aligned} \tag{81}$$

The equations for  $\bar{f}$  and  $k^2$  provide some insight into the source of the effective or average values  $\bar{\epsilon}$ ,  $\bar{g}$  and  $\bar{\mu}$ . Inasmuch as  $\epsilon$  and  $g$  always occur in the combination  $g + j\omega\epsilon$ , it is hard to see why two different "average" values arise. Now it is clear that  $\bar{\epsilon}$  is the harmonic mean value and  $\bar{g}$  the arithmetic mean value. Because of the overwhelmingly large ratio of  $g_1$  to  $j\omega\epsilon_2$ , the larger dominates the arithmetic mean and the smaller the harmonic mean. If we had assumed  $\mu_1$  and  $\mu_2$  different,  $\bar{\mu}$  would turn out to be the arithmetic mean, but, inasmuch as they are of the same general order of magnitude, both  $\mu_1$  and  $\mu_2$  appear in the resulting formula for  $\bar{\mu}$ .

The eigenvalues of the wave equation above are (Ref. 3, equation 537)

$$k^2 = n^2 \pi^2 \tag{82}$$

and the corresponding values of  $\gamma$  are

$$\gamma = j\omega\sqrt{\mu\bar{\epsilon}} \left[ 1 + \frac{n^2 \pi^2}{i\omega\mu\bar{g}a^2} \right]^{1/2} \tag{83}$$

in agreement with Morgan's equation 534.

In terms of the variable  $u$ , the function

$$-jCf(u) = -\bar{f}^2 \left[ \frac{j\omega\mu}{g + j\omega\epsilon} - \frac{\gamma^2}{(g + j\omega\epsilon)^2} \right] + j\omega\mu\bar{g}a^2 - \frac{\gamma^2 a^2 \bar{g}}{j\omega\bar{\epsilon}} \quad (84)$$

alternates periodically between two values. It is interesting to note, however, that the "electrical thickness" of a dielectric layer, i.e., its thickness in terms of  $u$ , is

$$\delta u = \frac{1}{\bar{f}} \int_{y_0}^{y_0+t_2} j\omega\epsilon_2 dy = \frac{j\omega\epsilon_2 t_2}{a\bar{g}}, \quad (85)$$

which is infinitesimal if  $\bar{g}$  has any reasonable value. Hence the function  $f(u)$  in question really has the appearance of a sequence of sharply spaced spikes, having

$$\begin{aligned} \text{spike width} &= \frac{j\omega\epsilon t_2}{a\bar{g}}, \\ \text{spike height} &= -a^2 \bar{g}^2 \left( \frac{t_2}{\epsilon} + \frac{\gamma^2}{\omega^2 \epsilon^2} \right), \end{aligned} \quad (86)$$

$$\text{spike spacing} = \frac{1}{n}.$$

Using the approximation

$$\gamma^2 = -\omega^2 \mu \epsilon$$

and defining spike strength  $S$  as the product of spike height and spike length, we find

$$\begin{aligned} S &= \frac{j\omega\epsilon t_2}{a\bar{g}} (-a^2 \bar{g}^2) \left( \frac{\mu}{\epsilon} - \frac{\omega^2 \mu \bar{\epsilon}}{\omega^2 \epsilon} \right) \\ &= \frac{j\omega\mu\bar{g}\theta a^2}{m}. \end{aligned} \quad (87)$$

Now it happens that the Fourier coefficients  $a_m$  can be evaluated explicitly in this case, and this procedure leads fairly easily to the results in Morgan's equations 455, 459 and 460. The computation succeeds only because  $f(u)$  is in this case a supremely simple function. When  $f(u)$  is not quite so regular, it is easier to return to the double integral formulation. The more general procedure will be carried out here for two reasons. First, it shows that the effects of local variations of layer thickness and dielectric constant are independent of the effect of finite lamination thickness; i.e., the two effects can be computed

separately and added. Second, it shows that the result is not restricted to flat lines, but is immediately applicable to other cases which can be set up as self-adjoint differential equations, including the cylindrical case.

The central idea is to observe that, when  $f(u)$  is a function consisting of a sequence of (nearly) equally spaced pulses of (nearly) equal amplitudes, then

$$\int_0^1 \int_0^1 f(u)f(v)k(u, v)w_1(u)w_1(v) du dv \tag{88}$$

$$\cong \int_0^1 \int_0^1 f(u)f(v) du dv \int_0^1 \int_0^1 k(u, v)w_1(u)w_1(v) du dv.$$

The expression on the left is a finite sum which approximates, by the two-dimensional analog of the trapezoid rule, the integral on the right. The remainder of the process consists in evaluating the difference between the two, i.e., the error in the approximation. It is not surprising that the result depends heavily on the special characteristics of the reduced resolvent kernel  $k(u, v)$ , which depend in turn on its relation to Green's function. Let

$$k(u, v)w_1(u)w_1(v) = h(u, v). \tag{89}$$

Then we need in particular:

$$\int_0^1 \int_0^1 h(u, v) du dv = 0, \tag{90}$$

$$\int_0^1 h(u, v) dv = 0, \tag{91}$$

$$\left. \frac{\partial h}{\partial u} \right|_{u=c+0} - \left. \frac{\partial h}{\partial u} \right|_{u=c-0} = w_1^2(v), \tag{92}$$

$$\int_0^1 w_1^2(v) dv = 1, \tag{93}$$

$$\begin{aligned} h(u, v) &= O(u^2) \\ &= O(v^2) \\ &= O(1 - u)^2 \\ &= O(1 - v)^2 \end{aligned} \tag{94}$$

in the neighborhood of the boundaries of the unit square.

First note that, because of the pulse character of  $f$ , the integral can

be transformed into a sum:

$$\iint C^2 f(u) f(v) h(u, v) du dv = \sum_i \sum_j S^2 h(u_i, v_j), \quad (95)$$

where

$$\begin{aligned} u_i &= u_0 + i/n, \\ v_j &= v_0 + j/n, \\ u_0 &= v_0. \end{aligned} \quad (96)$$

We can approximate each term of the sum by an integral thus by setting

$$\begin{aligned} h(u_i + x, v_j + y) &= h(u_i, v_j) + x \frac{\partial h}{\partial u} + y \frac{\partial h}{\partial v} \\ &+ \frac{x^2}{2} \frac{\partial^2 h}{\partial u^2} + xy \frac{\partial^2 h}{\partial u \partial v} + \frac{y^2}{2} \frac{\partial^2 h}{\partial v^2} + O(n^{-3}), \end{aligned} \quad (97)$$

$$|x| \leq \frac{1}{2n}, \quad |y| \leq \frac{1}{2n}.$$

Integrating directly, we get, for  $i \neq j$ :

$$\begin{aligned} \int_{-1/2n}^{1/2n} \int_{-1/2n}^{1/2n} h(u_i + x, v_j + y) dx dy \\ = n^{-2} h(u_i, v_j) + \frac{1}{24} n^{-4} \frac{\partial^2 h}{\partial u^2} + \frac{1}{24} n^{-4} \frac{\partial^2 h}{\partial v^2} + O(n^{-5}) \end{aligned} \quad (98)$$

and, for  $i = j$ :

$$\begin{aligned} \iint = n^{-2} h(u_j, v_j) - \frac{1}{12} n^{-3} \left( \frac{\partial h^-}{\partial u} - \frac{\partial h^+}{\partial u} \right) \\ - \frac{1}{12} n^{-3} \left( \frac{\partial h^-}{\partial v} + \frac{\partial h^+}{\partial v} \right) + O(n^{-4}). \end{aligned} \quad (99)$$

Now, in performing the indicated double summation, note that

$$\sum_{i=1}^{j-1} \frac{\partial^2 h}{\partial u^2} (u_i, v_j) = n \left( \frac{\partial h}{\partial u} \Big|_{u=v-0} - \frac{\partial h}{\partial u} \Big|_{u=0} \right) + O(1) \quad (100)$$

and, hence, using (92) and (93),

$$\begin{aligned} \left( \sum_{i=1}^{j-1} + \sum_{j+1}^n \right) \frac{\partial^2 h}{\partial u^2} (u_i, v_j) &= -nw^2(v_j) + O(1) \\ \sum_{i \neq j} \frac{\partial^2 h}{\partial u^2} &= -n^2 + O(n) \end{aligned} \quad (101)$$

and, similarly,

$$\sum_{i \neq j} \sum \frac{\partial^2 h}{\partial v^2} = -n^2 + O(n). \quad (102)$$

In the terms involving  $i = j$ , using (92) and (93) again, we find

$$\sum_{i=1}^n w^2(u_i) = -n + O(1). \quad (103)$$

Now, taking all terms and summing, we get

$$\begin{aligned} & \int_{u=u_0-1/2n}^{1+u_0-1/2n} \int_{v=v_0-1/2n}^{1+v_0-1/2n} h(u, v) \, du \, dv \\ &= n^{-2} \sum \sum h(u_i, v_j) + \frac{1}{24} n^{-4} [-2n^2 + O(n)] \\ & \quad - \frac{1}{12} n^{-3} [-2n + O(1)] \\ &= n^{-2} \sum \sum h(u_i, v_j) + \frac{n^{-2}}{12} + O(n^{-3}). \end{aligned} \quad (104)$$

But the integral, by direct integration using (91) and (94), is  $O(n^{-3})$ . Hence,

$$\begin{aligned} \sum \sum h(u_j, v_j) &= -\frac{1}{12} + O(n^{-1}), \\ \iint C^2 f(u) f(v) h(u, v) \, du \, dv &= S^2 \sum \sum h(u_i, v_j) \\ &= -\frac{S^2}{12} + O(n^{-1} S^2), \\ C^2 \Sigma &= \frac{\omega^2 \mu^2 \bar{g}^2 \theta^2 a^4}{12n^2} + O(n^{-3}), \\ \gamma^2 &= -\omega^2 \mu \bar{\epsilon} \left( 1 + \frac{\pi^2}{i\omega \mu \bar{g} a^2} - \frac{i\omega \mu \bar{g} \theta^2 a^2}{12n^2} \right). \end{aligned} \quad (106)$$

This is the same as Morgan's formula 455, except that, in his case, the number of layers is  $2n$  rather than  $n$ . In the appropriate frequency range, (including Morgan's "low" and "high", but not his "very low" and "very high" frequencies)

$$\begin{aligned} \alpha &= \frac{\pi^2}{2\sqrt{\mu/\bar{\epsilon}} \bar{g} a^2} + \frac{\omega^2 \mu^2 \bar{g} t_1^2}{24\sqrt{\mu/\bar{\epsilon}}}, \\ \beta &= \omega \sqrt{\bar{\mu}/\bar{\epsilon}}, \end{aligned} \quad (107)$$

as already found by Morgan (Ref. 3, equations 459 and 460). To simplify the arithmetic, it has been assumed that  $\mu_1 = \mu_2 = \bar{\mu}$ , and the computation has been restricted to the lowest-order mode. Generalization to remove these restrictions alters nothing.

By this time the reader, exhausted or bored according as he has or has not attempted to bridge the gaps in the above computation, may reasonably ask: why compute the effect of finite lamination thickness by such a laborious method when the matrix method of Morgan yields the same result so simply? The answer is that the matrix method fails\* if the layers are not identical, whereas the perturbation method does not. The exercise in this section was designed simply to show that when both methods apply, they agree.

Two important cases arise where the layers are not identical. The first is a cylindrical laminated line, where the radii of the layers gradually increases from center to outside layer. This case is discussed in Section VIII. The second is a laminated line in which the lamination are finite but not perfectly regular. In this case one would expect some contribution from irregularity and some from finite thickness, and may ask how they combine. From the nature of the computation for the uniform case, it is easy to guess that the contributions are independent and additive. We can replace the integral to be approximated by one including the effects of irregularity, which does not vanish identically, but the contribution due to finite granularity of the approximating sum remains unchanged. Alternatively, we can actually compute the effect of irregularities as a finite sum rather than an integral, taking one point corresponding to each layer. This was what was in fact done in the experimental case presented in Section VII. In this case, the sum computed can be compared term-by-term with the sum for the ideal case above, and the difference turns out to be precisely the finite analog of the integrals at the end of Section IV. The results can be presented in several forms, but the conclusion is always the same: that to a first order of approximation the contribution to the quantity  $\Sigma$  (24) due to finite layer thickness is independent of the contribution due to irregularities in the layers.

## VI. NUMERICAL RESULTS — RANDOM VARIATIONS

The expression for  $b$  derived in Sections II and III does not depend explicitly on  $f(\xi)$ , but only on the squares of the coefficients of its Fourier

---

\* But see Hayashi and U-O.<sup>8</sup> Here the matrix computation is carried out by an approximation method which appears to be valid if the radius of the innermost layer is not too small compared to the total thickness of the stack.

series, or on what is known to communications engineers and statisticians as its power spectrum. Consequently, the expression is especially adapted for use when  $f$  is a random function known only by its average power spectrum. The functions of this class have been used widely in discussions of electrical noise and other random processes, and their introduction into this problem should not come as a surprise.

Suppose that  $\bar{\epsilon}$  varies randomly from layer to layer, i.e., that

$$\bar{\epsilon} = \bar{\epsilon}_0 + u(\xi), \quad (108)$$

where  $u(\xi)$  is a random variable whose value in every layer is independent of its value in every other layer. Then  $f(\xi)$  is a random function having a flat spectrum, and can be represented as

$$f(\xi) = \sum_{m=1}^n b_m \cos m\pi\xi, \quad (109)$$

where

$$\langle b_m \rangle = k, \quad (110)$$

$k$  being a constant. (The angular brackets indicate, as before, rms values.)

Inasmuch as the number of layers is finite, it seems reasonable that the series should be terminated after a finite number of terms. Because of the strong convergence factor  $1/(m^2 - 1)$  the exact termination point is not very important. Inasmuch as  $f(\xi)$  has only  $n$  degrees of freedom, we have terminated the series after  $n$  terms. In the practical cases worked out, we used the formulation having a definite integral, which was integrated point by point, using one data-point per layer. This was precisely the number of measured data available (i.e., one conductor-to-conductor capacitance measurement through each insulating layer) so there was no choice about how many terms to use anyway.

The function  $f(\xi)$  was defined so that  $\langle f(\xi) \rangle$  is unity. It follows from Parseval's theorem that

$$\int_0^1 f^2(\xi) d\xi = 1 = \frac{1}{2} \sum_1^n b_m^2 = \frac{n}{2} k^2, \quad (111)$$

and hence that

$$k = \sqrt{\frac{2}{n}}. \quad (112)$$

It follows that

$$\begin{aligned}
 \langle a_m \rangle &= \frac{1}{2} \sqrt{\langle b_{m+1} \rangle^2 + \langle b_{m-1} \rangle^2} \\
 &= n^{-(1/2)}, \\
 \Sigma &= \sum_{m=2}^n \frac{1}{\pi^2 n (m^2 - 1)} \\
 &= \frac{3n^2 - n - 2}{(4n^3 + 4n^2)\pi^2} \\
 &\cong \frac{3}{4n\pi^2},
 \end{aligned} \tag{113}$$

and

$$\begin{aligned}
 b &= \frac{3\sqrt{n}}{2\pi\theta} \left\langle \frac{\Delta\bar{\epsilon}}{\bar{\epsilon}_0} \right\rangle \\
 &= \frac{3\sqrt{n}}{2\pi} \left\langle \frac{\Delta t_2}{t_2} - \frac{\Delta t_1}{t_1} \right\rangle.
 \end{aligned} \tag{114}$$

From this quantity  $b$  it is easy to compute the reduction in bandwidth  $(1 + b^2)^{-1/2}$ , as a function of  $n$  and the mean square fractional variations of  $t_1$  and  $t_2$ . The reduction in bandwidth is plotted as a function of the number of layers  $n$  for several values of

$$\left\langle \frac{\Delta t_2}{t_2} - \frac{\Delta t_1}{t_1} \right\rangle$$

in Fig. 5. Notice that, if the variations in  $t_1$  and  $t_2$  are independent,

$$\left\langle \frac{\Delta t_2}{t_2} - \frac{\Delta t_1}{t_1} \right\rangle = \left\langle \frac{\Delta t_2}{t_2} \right\rangle + \left\langle \frac{\Delta t_2}{t_1} \right\rangle. \tag{115}$$

However, if  $t_1$  and  $t_2$  are the thicknesses of layers successively formed about the same core, one can imagine that they would not be uncorrelated. In fact, it is plausible to believe that when one is too small, the other will be too large. In any case, however, the expression at the left can be no greater than twice the expression at the right.

As an alternative to controlling the effective dielectric constant of each layer independently, one might control the average dielectric constant of the incomplete stack, as it is built up layer by layer. In this case, one would expect the average dielectric constant to vary in a random manner about its nominal value. Suppose, for example, that the elastance per unit length of the stack is measured after each layer is added, that the next layer is added to bring the average dielectric

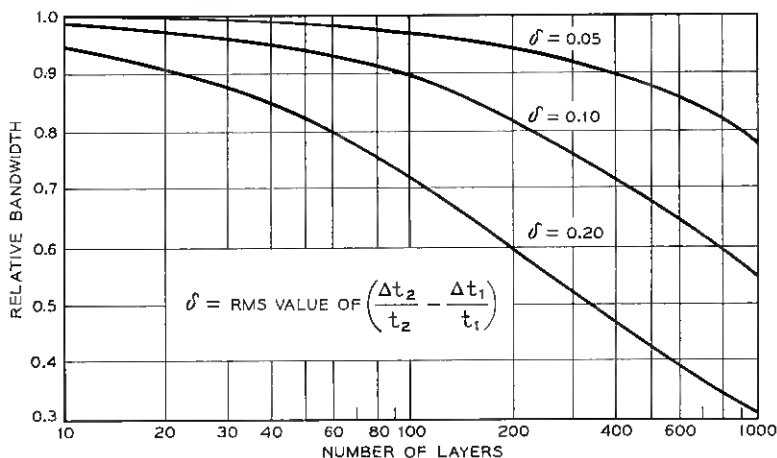


Fig. 5 — Bandwidth degradation in a laminated transmission line due to random irregularities of a certain type plotted as a function of number of laminae for several amounts of irregularity.

constant to its nominal value and that the error (i.e., the measure of the amount by which we fail to bring the average dielectric constant to its nominal value) varies randomly from layer to layer. Then, except for a multiplicative constant,

$$\begin{aligned}
 S(\xi) &= \int_0^\xi \frac{d\xi}{\bar{\epsilon}} \\
 &= \frac{\xi}{\bar{\epsilon}_0} + u(\xi),
 \end{aligned}
 \tag{116}$$

where  $S(\xi)$  is the elastance of a unit length measured from one side to the  $m$ th layer,  $m = n\xi$  and  $u(\xi)$  is a random function with a flat spectrum. Then

$$\begin{aligned}
 \frac{\Delta \bar{\epsilon}}{\bar{\epsilon}_0} &= \frac{\bar{\epsilon} - \bar{\epsilon}_0}{\bar{\epsilon}_0} \\
 &= -\bar{\epsilon} \frac{du}{d\xi} \\
 &\approx -\bar{\epsilon}_0 \frac{du}{d\xi}.
 \end{aligned}
 \tag{117}$$

Now  $f(\xi)$  is proportional to  $-(du/d\xi)$ , and hence has a spectrum whose

amplitude increases with frequency, i.e.,

$$\langle b_m \rangle = km. \quad (118)$$

Proceeding as before,

$$\begin{aligned} \int_0^1 f^2(\xi) d\xi &= \frac{1}{2} \sum_1^n b_m^2 \\ &= \frac{k^2}{2} \sum_1^n m^2 \\ &\cong \frac{k^2 n^3}{6}, \end{aligned} \quad (119)$$

or

$$k \cong \sqrt{\frac{6}{n^3}}. \quad (120)$$

Then

$$\begin{aligned} \langle a_m \rangle &= \frac{1}{2} \sqrt{\langle b_{m-1} \rangle^2 + \langle b_{m+1} \rangle^2} \\ &\cong m \sqrt{\frac{3}{n^3}} \end{aligned} \quad (121)$$

and

$$\begin{aligned} \Sigma &= \sum_{m=2}^n \frac{a_m^2}{\pi^2 m^2 - \pi^2} \\ &\cong \sum_{m=2}^n \frac{3m^2}{\pi^2 n^3 (m^2 - 1)} \\ &\cong \frac{3}{n^2 \pi^2}. \end{aligned} \quad (122)$$

Hence,

$$\begin{aligned} b &= \frac{3}{\pi \theta} \frac{\Delta \bar{\epsilon}}{\bar{\epsilon}_0} \\ &= \frac{3}{\pi} \left\langle \frac{\Delta t_2}{t_2} - \frac{\Delta t_1}{t_1} \right\rangle. \end{aligned} \quad (123)$$

Notice that, for the same rms deviations in  $t_1$  and  $t_2$ ,  $b$  is smaller by a factor  $2/\sqrt{n}$ . This is, of course, due to the fact that the variations in successive layers are no longer uncorrelated, but are adjusted to make the variations cancel over several layers. The variations of average

dielectric constant having long wavelength are reduced, and the only remaining variations left have short wavelength. However, in the expression for  $\Sigma$  the contribution of each component is weighted with the factor  $1/(m^2 - 1)$ , and hence the contribution of the components having short wavelengths is reduced. The over-all result is that the line is not degraded so much by this kind of variation. The relation in bandwidth for the same values of the parameters as were used in Fig. 5 is independent of  $n$ , and has the values 0.983, 0.995 and 0.999 for  $\delta = 0.20, 0.10$  and 0.05, respectively.

One might ask how the way in which one aims for the nominal dimensions can make a difference, if the errors in film thickness are the same in both cases. The fact can be made plausible by the following argument: in the first case a layer is laid in ignorance of what has gone before, while in the second case the layers that have gone before are studied and an attempt is made to compensate for past errors. As an example, one might examine the following: suppose one is making a ruler by marking off successive inches with a pair of dividers. First one might set the dividers and mark off, say, 36 nominally equal spaces. As an alternative, one might measure the result after each step, and adjust the dividers so that the measured distance plus the distance laid down for the new step should be as near as possible to an integral number of inches. There is no doubt that, even if the precision of each individual inch is the same in both cases, the latter process will make a ruler having a more uniform scale. This example is more than an illustration; it is a good analog of the two processes of laminated line construction which are described above.

This conclusion is of great practical importance. In dealing with layers with a thickness smaller than 0.001 inch, a variation of 0.05 in relative thickness corresponds to a thickness change of one wavelength of visible light. There is not much hope of producing laminated lines having hundreds of layers if this kind of precision must be maintained. On the other hand, the measurement of capacitance to a high degree of accuracy is quite reasonable, and a feedback mechanism to translate that measurement into an objective for the thickness of the next layer is quite conceivable. With this kind of servo control in the fabrication process, laminated lines having any number of layers could be constructed using layers no more regular than were those in the experiment described in Section VII, with degradation of bandwidth no more than 2 per cent. Thus, irregularities can be conquered by feedback, and the laminated line made of less-than-perfect materials can be rescued and brought back to the realm of the practical.

## VII. COMPARISON WITH EXPERIMENT

In 1951 an experimental 100-layer Clogston 2 cable was fabricated. A description of this cable and of measurements made on it has never been published, largely because measured transmission properties could not be reconciled quantitatively with the theory available at the time. The unresolved differences motivated the research which culminated in the results of the present paper. A laboratory report on the fabrication

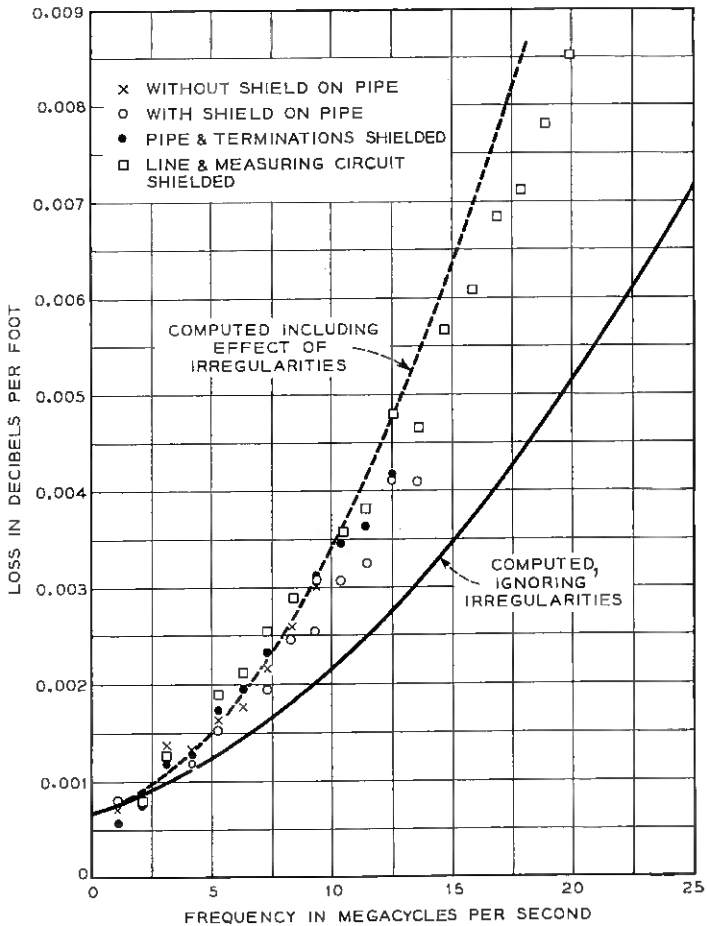


Fig. 6—Computed and measured losses in a 276-foot terminated laminated transmission line. The measurements were made with several different electrical shielding means to exclude certain possible spurious effects.

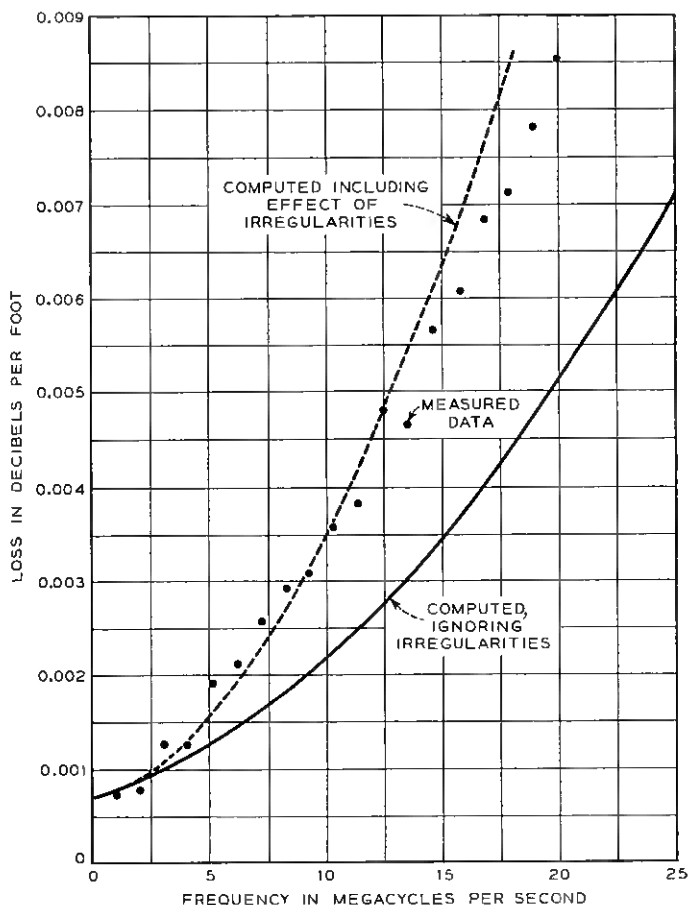


Fig. 7 — Computed and measured losses in a 276-foot terminated laminated transmission line. The line and the measurement circuit were completely shielded electrically, resulting in less scatter than in the previous figure.

and measurement of this cable is being published as a companion paper<sup>9</sup> to the present theoretical study.

The cable was a 276-foot laminated conductor assembled by hand around a  $\frac{7}{8}$ -inch conducting core. The laminations consisted of 100 concentric layers of 0.00025-inch aluminum foil separated by 99 polystyrene cylindrical insulators each 1.35 mils thick. After fabrication the cable was shielded by a wrap of 0.010-inch aluminum foil.

The Clogston 2 dominant mode was propagated. Measurements were

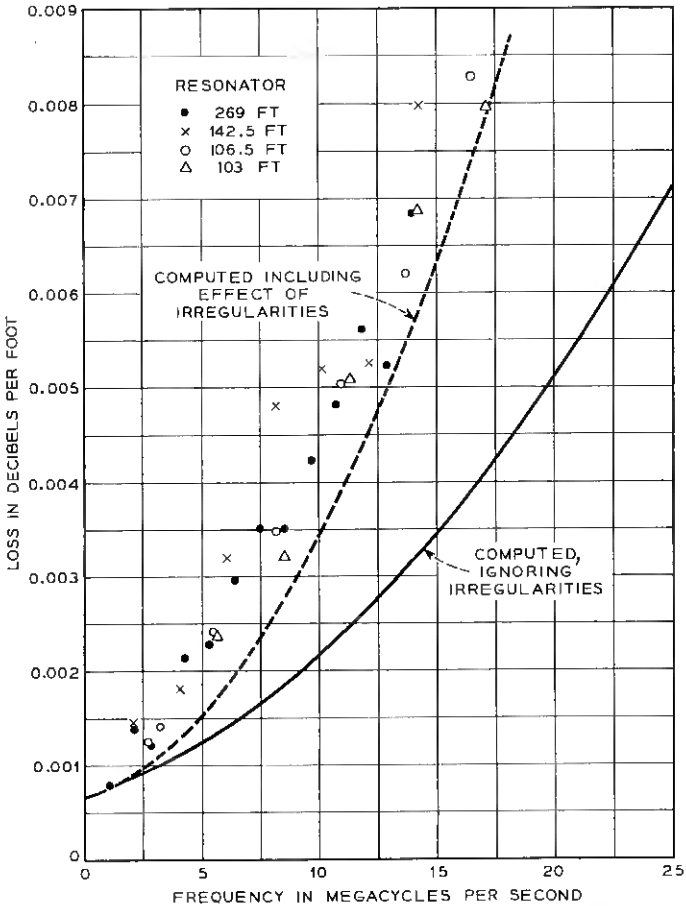


Fig. 8 — Computed and measured losses in several lengths of a laminated transmission line measured as a resonator.

made of the mode pattern and the attenuation as a function of frequency up to 25 mc. Measured attenuation was compared with attenuation computed for a uniform laminated line, and exceeded the theoretical values by a factor of two, as shown in Figs. 6, 7 and 8. At the time, the discrepancy was attributed to lack of uniformity in the laminae. However, no quantitative theory of the effect of irregularities was available and definite association of the discrepancy with this cause was not possible.

At the time the 100-layer Clogston line was tested, a wise decision

was made to measure the capacitance between consecutive layers of conductor. The thickness of the dielectric layer is easily derived by assuming that the capacitance is proportional to area and inversely proportional to thickness. Because of the fact that the conducting layers each consist of a single sheet of relatively firm metal, while the dielectric layers are built up of several thicknesses of relatively soft dielectric, it is reasonable to assume that the principal effect of irregularity of layer thickness can be traced to variation in dielectric thickness.

With the assumption that the principal effect of irregularity is due to variations in dielectric thickness, it is not difficult to show that

$$\frac{\bar{\epsilon}_m}{\bar{\epsilon}_0} = (1 - \theta) + \theta \frac{C_m}{C_{av}}, \quad (124)$$

where

$\bar{\epsilon}_m$  = the effective dielectric constant at layer  $m$ ,

$\bar{\epsilon}_0$  = the average dielectric constant,

$C_m$  = the capacitance per unit area across the layer  $m$ , (125)

$C_{av}$  = the average capacitance per unit area, averaged over all the dielectric layers.

The value  $C_m$  was derived from measurements of capacitance between adjacent conducting layers, which were measured separately for two different lengths of the completed cable. To simplify the computation, the small variation in area from layer to layer was ignored. The reduction in bandwidth  $b$  was determined by (32),

$$b = \frac{\sqrt{3nA}\sqrt{\Sigma}}{\theta}, \quad (126)$$

where

$$A^2\Sigma = \frac{\theta^2}{\pi^2 n^2 C_{av}^2} \left( \frac{1}{2} I_n^2 - \frac{2\pi}{n} I_n' I_n + 2\pi I_n'' \right), \quad (127)$$

$$I_n = \sum_1^n C_m \sin^2(\pi m/n),$$

$$I_n' = \sum_1^n m C_m \sin(\pi m/n) \cos(\pi m/n),$$

$$I_n'' = \sum_1^n C_m \sin(\pi m/n) \cos(\pi m/n) I_m.$$

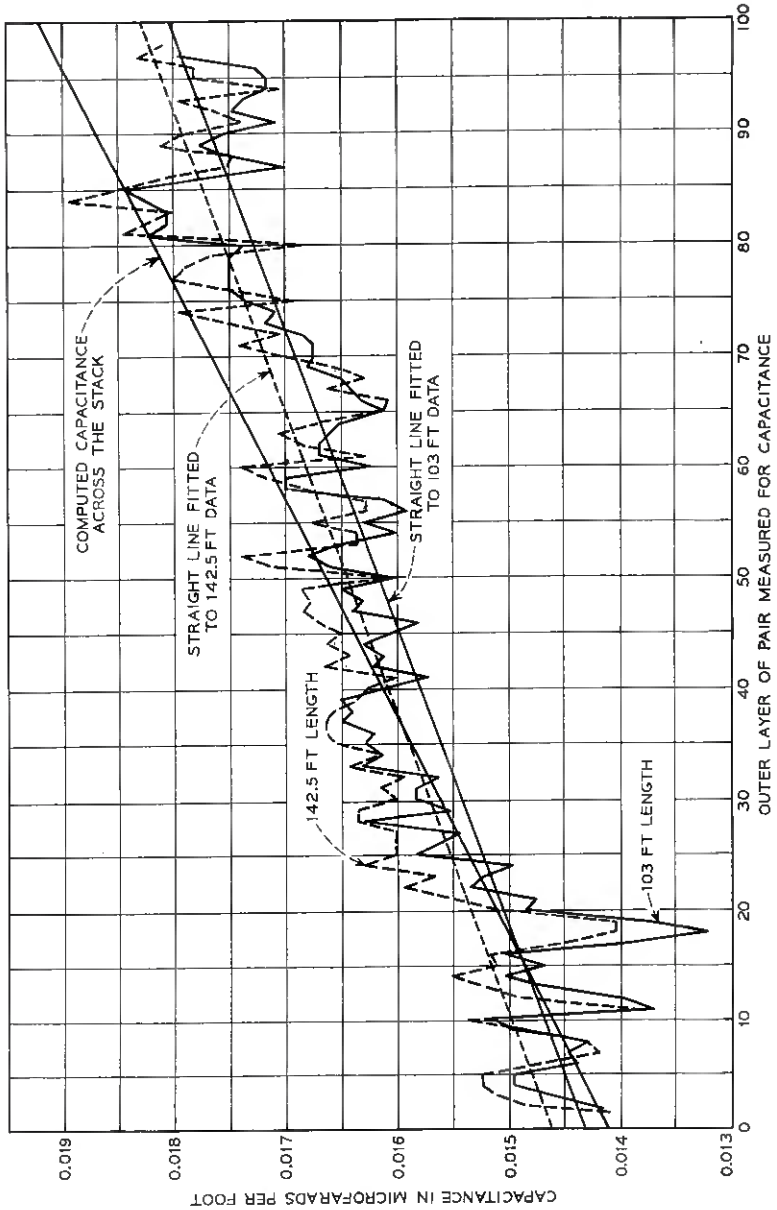


Fig. 9 — Measured capacitances between adjacent layers in two sections of a laminated transmission line.

This is the finite analog of the integral (24)

$$\begin{aligned}
 A^2\Sigma &= A^2 \int_0^1 \int_0^1 f(x)f(y)h(x, y) dx dy = \left| \frac{1}{\pi} \int_0^1 Af(x) \sin^2 \pi x dx \right|^2 \\
 &\quad - \frac{4}{\pi} \int_0^1 Af(x) \sin^2 \pi x dx \int_0^1 xAf(x) \sin \pi x \cos \pi x dx \quad (128) \\
 &\quad + \frac{4}{\pi} \int_0^1 Af(x) \sin \pi x \cos \pi x dx \int_0^x Af(y) \sin^2 \pi y dy,
 \end{aligned}$$

where  $h(x, y)$  is the function defined in (89). The reduction to iterated integrals made numerical computation much simpler. In actual computation,  $C_m$  was used rather than  $\Delta C_m = C_m - C_{av}$ , because the nature of the computation is such that addition of a constant to the values of  $\Delta C_m$  does not alter the result.

The computation was carried out for two sets of data, measured on two lengths of the original 100-layer Clogston cable. The data, shown in graphical form in Fig. 9, are in the form of measured values of capacitance between consecutive layers of conductor. Only 98 values were recorded in one set and 97 in the other, because the outer layers were apparently not rigid enough to give reproducible capacitance measurements. To simplify the computation, only 97 values were used (i.e.,  $n = 97$  was assumed). Inasmuch as the values near the surface would have been weighted with a factor  $\sin n\pi/100$ , the resulting error is likely to be small. In one case, where the capacitance measurement was indeterminate because of a short circuit, the mean of the two adjacent measurements was used to avoid introducing an apparent gross discontinuity.

The computation resulted in two different values of  $b$ :

$$b = 1.345 \text{ for a 145.5-foot length,}$$

$$b = 1.296 \text{ for a 103-foot length.}$$

The corresponding reductions in bandwidth are

$$\begin{aligned}
 \frac{f_{i2}}{f_2'} &= \frac{1}{\sqrt{1 + b^2}} = 0.597 \text{ for length 145.5 feet,} \\
 &= 0.611 \text{ for length 103 feet.} \quad (129)
 \end{aligned}$$

These differ by about 2 per cent. It would be misleading to assume, because of this agreement, that the result is accurate within 2 per cent: on the basis of these two results only, there is still a chance of one in 20

that a large sample of similar measurements might have a standard deviation as high as 50 per cent.<sup>10</sup>

The correction was applied to results computed earlier by Morgan, for a perfectly uniform line. The results are shown as dashed lines on the figures.\* It is clear that the correction accounts for substantially all of the difference between the measured data and the curve computed for a uniform line. The corrected curves predict an attenuation somewhat lower than that measured by resonance measurements and slightly higher than that measured by direct transmission measurements.

In comparing the new computed results with experiment, the following three facts must be borne in mind:

i. The theory of losses due to irregularities is not known to be accurate beyond a point where loss is about twice the low frequency loss (say 0.002 db/ft on the three figures). Hence, the calculated values are of doubtful validity in the upper three-quarters of each graph in Figs. 6, 7 and 8.

ii. Variations in conductor thickness have been assumed to be negligible.

iii. Longitudinal variations in the line have been ignored.

In view of the good correlation between measurement and theory, we can tentatively draw the following conclusions:

i. The theory of losses in Clogston 2 lines is consistent with the experiments. This also provides an experimental confirmation of the work of S. P. Morgan on which it was founded.

ii. We know enough about the effect of irregularities to predict in an intelligent and sufficiently accurate way the losses to be expected from manufacturing irregularities in Clogston 2 lines, provided we can make sufficiently accurate estimates of manufacturing tolerances.

#### VIII. CYLINDRICAL CLOGSTON LINES WITH LAYERS OF FINITE THICKNESS

Let us now apply the methods of Sections II, III, and V to a structure having finite laminations and cylindrical (rather than planar) symmetry. We shall study the properties of a Clogston 2 line which is completely filled with laminated layers; i.e., the radius of the inner core is zero.

The equation to be solved, with its boundary condition, is (from Ref.

---

\* Actually, Morgan's curves include a linear term accounting for dielectric loss. The curve computed for the uniform line is approximately  $\alpha = 0.00065[1 + (f/9.372)^2] + 0.000076f$ , where  $\alpha$  is in db/ft and  $f$  in mc. The dashed curve is  $\alpha = 0.00065[1 + (f/5.659)^2] + 0.000076f$ . Thus  $f_{i2}/f_2 = 5.659/9.372$ , corresponding to a value  $b = 1.32$  in (129).

3, equations 27, 28 and 29

$$\frac{d}{d\rho} \left[ \frac{1}{\rho(g + j\omega\epsilon)} \frac{d}{d\rho} [\rho H_\varphi] \right] + \left[ \frac{\gamma^2}{g + j\omega\epsilon} - j\omega\mu_0 \right] H_\varphi = 0, \quad (130)$$

$$H_\varphi(0) = H_\varphi(b) = 0,$$

where  $b$  is the radius of the outer sheath. The real interest in the equation is the determination of the eigenvalues  $\gamma$ .

In order to transform the equation to a self-adjoint equation with no first-order term, define a new independent variable  $u$  by

$$u^2 = \frac{2}{k} \int_0^\rho r(g + j\omega\epsilon) dr \quad (131)$$

and a new dependent variable,  $W$ , by

$$W = \frac{f}{\sqrt{u}} H_\varphi. \quad (132)$$

If we choose

$$k = 2 \int_0^b r(g + j\omega\epsilon) dr \cong \theta b^2 g, \quad (133)$$

then the boundary conditions on  $W$  are

$$W(0) = W(1) = 0 \quad (134)$$

and the equation is transformed to

$$\frac{d^2 W}{du^2} + \left\{ k^2 \frac{u^2}{\rho^2} \left[ \frac{\gamma^2}{(g + j\omega\epsilon)^2} - \frac{j\omega\mu_0}{g + j\omega\epsilon} \right] - \frac{3}{4u^2} \right\} W = 0. \quad (135)$$

This can be considered a perturbation of the equation

$$\frac{d^2 W}{du^2} + \left( \Lambda - \frac{3}{4u^2} \right) W = 0, \quad W(0) = W(1) = 0, \quad (136)$$

where  $\Lambda$  is the average value

$$\Lambda = k^2 \int_0^1 \frac{u^2}{\rho^2} \left[ \frac{\gamma^2}{(g + j\omega\epsilon)^2} - \frac{j\omega\mu_0}{g + j\omega\epsilon} \right] du. \quad (137)$$

Write

$$jCf(u) = \Lambda - k^2 \frac{u^2}{\rho^2} \left[ \frac{\gamma^2}{(g + j\omega\epsilon)^2} - \frac{j\omega\mu_0}{g + j\omega\epsilon} \right] \quad (138)$$

and the original equation becomes

$$\frac{d^2W}{du^2} - \frac{3}{4u^2}W + [\Lambda - jCf(u)]W = 0. \quad (139)$$

Having once obtained the quantities  $\Lambda_n$ ,  $n = 1, 2, \dots$ , we can get  $\gamma_n$  from the relation (137).

The eigenfunctions of the unperturbed equations are

$$w_n = \sqrt{2u} \frac{J_1(\sqrt{\lambda_n}u)}{J_1'(\sqrt{\lambda_n})} \quad (140)$$

and the eigenvalues are determined from

$$\begin{aligned} J_1(\sqrt{\lambda_n}) &= 0: \\ \sqrt{\lambda_1} &= 3.8317, \\ \sqrt{\lambda_2} &= 7.0156, \\ \sqrt{\lambda_n} &\cong n\pi + \frac{1}{4}. \end{aligned} \quad (141)$$

From the technique in Courant and Hilbert,<sup>6</sup> we can write a second-order approximation to the first eigenvalue (the one we desire) as follows:

$$\Lambda_1 = \lambda_1 + 2Ca_1 + C^2 \sum_2^{\infty} \frac{a_m^2}{\lambda_m - \lambda_1}, \quad (142)$$

where

$$a_n = 2 \int_0^1 uf(u) \frac{J_1(\sqrt{\lambda_1}u)}{J_1'(\sqrt{\lambda_1})} \frac{J_1(\sqrt{\lambda_n}u)}{J_1'(\sqrt{\lambda_n})} du. \quad (143)$$

Proceeding by either route used before, we find

$$\Sigma = 2 \int_0^1 \int_0^1 \sqrt{uv} f(u)f(v) \frac{J_1(\sqrt{\lambda_1}u)J_1(\sqrt{\lambda_1}v)}{[J_1(\sqrt{\lambda_1})]^2} k(u, v) du dv. \quad (144)$$

The actual value of  $k$  is not important for the present study, but is given here as a matter of record:

$$\begin{aligned} k(v, u) = k(u, v) &= \frac{\pi\sqrt{uv}}{2J_1'(l)} [uJ_1'(ul)J_1(l)Y_1(l) \\ &+ vJ_1'(lv)J_1(lu)Y_1(l) + J_1(lu)J_1(lv)Y_1'(l)] - \frac{\pi}{2} \sqrt{uv} J_1(lv)Y_1(lv) \\ &- \sqrt{uv} \frac{J_1(lu)J_1(lv)}{l^2[J_1'(l)]^2}, \quad u \leq v, \quad l = \sqrt{\lambda_1}. \end{aligned} \quad (145)$$

Now let us re-examine (138) in detail, bearing in mind (131) and (133).

The thickness of the  $n$ th conducting layer is determined in terms of  $u$  as follows:

$$\begin{aligned} u_0^2 - u_i^2 &= \frac{2}{k} \int_{\rho_i}^{\rho_0} r g \, dr \\ &= \frac{2}{k} g \frac{\rho_0^2 - \rho_i^2}{2} = \frac{1}{\theta b^2} (\rho_0^2 - \rho_i^2). \end{aligned} \quad (146)$$

If the layers are uniform,

$$\begin{aligned} \rho_i &= \frac{m - c}{n} b, \\ \rho_0 &= \frac{m - c + \theta}{n} b, \end{aligned} \quad (147)$$

where the constant  $c$  is unity if the center is a conducting rod of radius equal to a layer,  $\theta$  if the center is a dielectric rod of radius equal to a dielectric layer and intermediate otherwise. It is arithmetically convenient to choose a fractional value for  $c$ . Squaring and subtracting, we get

$$\rho_0^2 - \rho_i^2 = \frac{b^2}{n^2} (\theta)(2m - 2c + \theta). \quad (148)$$

The total through the first  $n$  layers is

$$\begin{aligned} u_{0,m}^2 &= \sum_{i=1}^m \frac{b^2 \theta}{n^2} \frac{1}{\theta b^2} (-2c + \theta + 2m) \\ &= \frac{1}{n^2} [(-2c + \theta)m + 2m(m + 1)] \\ &= \frac{m^2}{n^2} + \frac{m}{n^2} (\theta - 2c + 1). \end{aligned} \quad (149)$$

Choosing

$$c = \frac{\theta + 1}{2}, \quad (150)$$

we find

$$u_{0,m} = \frac{m}{n}. \quad (151)$$

This corresponds physically to putting one-half layer of metal, i.e., a wire of radius  $\theta b/2n$  at the center.

Under these conditions, the thickness of each metal layer is, in terms of  $u$ , precisely  $1/n$ .

The pulse strength is

$$\int f(u) du \quad (152)$$

integrated through one dielectric layer. Recalling (151) and (133), and assuming the unperturbed value of the propagation constant

$$\gamma^2 = -\omega^2 \mu \bar{\epsilon}, \quad (153)$$

we get, after some tedious calculation

$$S = j\omega\epsilon\theta b^2 g_1 \left[ \frac{\mu}{\epsilon} \left( \frac{\bar{\epsilon}}{\epsilon} - 1 \right) \right] \frac{1 - \theta}{n} [1 + O(m^{-2})]. \quad (154)$$

Recalling (3), we finally get

$$S = \frac{j\omega\mu\theta b^2 \bar{g}}{n} [1 + O(m^{-2})]. \quad (155)$$

Thus we see that the pulse strength is approximately the same as before [see (87)], but is slightly altered in the neighborhood of the center.

If we now evaluate the double sum, we find

$$\begin{aligned} \sum_i \sum_j S_i S_j h(u_i, v_j) &= \sum_i \sum_j S^2 (1 + \delta_i + \delta_j + \delta_i \delta_j) h_{ij} \\ &= S^2 \sum_i \sum_j h_{ij} + S^2 \sum_i \delta_i \sum_j h_{ij} \\ &\quad + S^2 \sum_j \delta_j \sum_i h_{ij} + S^2 \sum_i \sum_j \delta_i \delta_j h_{ij}, \end{aligned} \quad (156)$$

where

$$\frac{S_i}{S} - 1 = \delta_i = O(m^{-2}). \quad (157)$$

Now

$$\begin{aligned} \delta_i h_{ij} &= O(n^{-2}), \\ \sum_j h_{ij} &= 0 + O(n^{-1}), \\ \delta_i \delta_j h_{ij} &= O(n^{-4}), \end{aligned} \quad (158)$$

and hence

$$\sum_i \sum_j S_i S_j h(u_i, v_j) = S^2 \sum_i \sum_j h_{ij} + O(S^2 n^{-1}). \quad (159)$$

Therefore, to the order of precision attained in the plane case, the result

is the same. However, the unperturbed eigenvalues are not the numbers  $n^2\pi^2$ , but rather the squares of the roots of  $J_1(x) = 0$  (141). The first root, in particular, is 3.8317. The analogs of (106) and (107) for a cylinder of radius  $b$  are:

$$\begin{aligned}\gamma^2 &= -\omega^2\mu\epsilon\left[1 + \frac{(3.8317)^2}{j\omega\mu\bar{g}b^2} - \frac{j\omega\mu\bar{g}t_1^2b^2}{12n^2}\right], \\ \alpha &= \frac{(3.8317)^2}{2\sqrt{\bar{\mu}/\bar{\epsilon}}\bar{g}b^2} + \frac{\omega^2\mu^2\bar{g}t_1^2}{24\sqrt{\bar{\mu}/\bar{\epsilon}}}, \\ \beta &= \omega\sqrt{\bar{\mu}/\bar{\epsilon}}.\end{aligned}\tag{160}$$

The second of these is equivalent to Morgan's equation 486 (remembering that Morgan calls the number of layers in his cable  $2n$  rather than  $n$ ). In presenting this equation, Morgan emphasized that it depended on certain physical assumptions and approximations; in view of the present result, these assumptions and approximations seem amply justified. The principle adopted by Morgan of assuming the current distribution of an unperturbed mode in a system and computing losses consequent from such currents is often the easiest to use and sometimes the only known way to compute attenuation. It is highly gratifying to see an application in a case quite different from the ordinary where the result is confirmed by an alternative method. Our confidence in this method is thus increased.

A careful analysis of the method used in the present paper would probably show that the particular choice of physical configuration at the origin is immaterial. We can conclude, in agreement with Morgan's equations 484 and 485, that the result is valid also for a Clogston 2 line bounded inside with a finite cylinder, provided that appropriate eigenvalue of the unperturbed problem is used. As the ratio of inside to outside diameter increases towards unity, these eigenvalues rapidly approach the values  $n^2\pi^2$ , which are those of the plane configuration.

#### IX. ACKNOWLEDGMENTS

The help of S. P. Morgan, J. M. McKenna, H. P. Kramer, Mrs. R. A. King and the computing group in the Mathematical Research Department of Bell Telephone Laboratories is gratefully acknowledged.

#### REFERENCES

1. Clogston, A. M., Reduction of Skin Effect Losses by the Use of Laminated Conductors, *B.S.T.J.*, **30**, July 1951, p. 491.

2. Black, H. S., Mallinckrodt, C. O. and Morgan, S. P., Experimental Verifications of the Theory of Laminated Conductors, Proc. I.R.E., **40**, August 1952, p. 902.
3. Morgan, S. P., Mathematical Theory of Laminated Transmission Lines, B.S.T.J., **31**, September 1952, p. 883; November 1952, p. 1121.
4. Vaage, E. F., Transmission Properties of Laminated Clogston-Type Conductors, B.S.T.J., **32**, May 1953, p. 695.
5. King, Mrs. R. A. and Morgan, S. P., Transmission Formulas and Charts for Laminated Coaxial Cables, Proc. I.R.E., **42**, August 1954, p. 1250.
6. Courant, R. and Hilbert, D. *Methods of Mathematical Physics*, Interscience, New York, 1953, Vol. 1, Chs. 5 and 13.
7. Kato, T., On the Convergence of the Perturbation Method, J. Fac. Sci. Univ. Tokyo, **6**, March 31, 1951.
8. Hayashi, S. and U-O, Koji, The Attenuation Characteristics of the Coaxial Laminated Cable, Technical Report No. 40, The Engineering Research Institute, Kyoto Univ., Kyoto, Japan, December 1957.
9. King, Mrs. R. A., this issue, p. 517.
10. Kaplan, E. L., private communication.

# An Experimental Clogston 2 Transmission Line

By Mrs. R. A. KING

(Manuscript received May 6, 1958)

*With the aid of two special machines, a 276-foot laminated conductor was assembled by hand around a  $\frac{7}{8}$ -inch conducting core. The laminations consisted of 100 concentric layers of  $\frac{1}{4}$ -mil aluminum foil separated by 99 polystyrene cylindrical insulators, each 1.35 mils thick. After fabrication, the cable was shielded by a wrap of 10-mil aluminum foil.*

*The Clogston 2 dominant mode was propagated. Measurements were made of the mode pattern and the attenuation as a function of frequency up to 25 mc. Cavity-resonator and insertion-loss measurements were in approximate agreement. Measured attenuations exceeded the theoretical values for a uniform Clogston 2 line in the ratio of 2 to 1 for frequencies above 10 mc, but were in agreement with theoretical values for a line showing a systematic lack of uniformity of the laminae. The 276-foot cable was cut into shorter lengths. Measured attenuation-frequency characteristics were proportional to length of cable.*

*As a by-product, successful methods were evolved both for cutting and joining laminated conductors.*

## I. INTRODUCTION

Clogston<sup>1</sup> has discovered that it is possible to reduce skin effect losses in transmission lines by properly laminating the conductors and adjusting the velocity of transmission of the waves. During a period in late 1951 and early 1952, a transmission line completely filled with laminated material was constructed and its loss was measured in the frequency range from 1 to 25 mc. This structure is referred to as the Clogston 2 stack to distinguish it from the Clogston 1 described by Black, Malinckrodt and Morgan.<sup>2</sup> The measured loss was compared with the loss computed by Morgan for a uniform line and was found to match at low frequencies, but to rise to a value of twice the computed loss at 10 mc. The ratio of measured loss to computed loss was nearly 2 to 1 over the

remainder of the measured frequency range. The explanation of this difference awaited the work of Raisbeck<sup>3</sup> on the effect of lack of uniformity in a laminated line. The measured loss was then compared with the loss computed by Raisbeck and was found to match reasonably well in the frequency range where the computation is expected to be valid.

A description is given of the construction of the line and the technique used for measuring, with some emphasis on the way this line departs from the ideal.

## II. CONSTRUCTION OF THE LINE

One of the transmission lines described by Clogston, known as a Clogston 2 cable, is a line in which the space is entirely filled with insulated laminations. For a line of prescribed cross section and top operating frequency, there exists an optimum thickness of insulation which will minimize the loss for a prescribed thickness of metal.<sup>4</sup> It is believed that approximate equality of thickness of metal and insulation will usually be desirable in practice. However, when choosing dimensions for a manually constructed transmission line, practical considerations, based on materials conveniently available, dictated a dielectric layer approximately six times as thick as the conducting layer. Aluminum foil approximately 0.25 mil thick and polystyrene films 0.60 mil thick were chosen. Each dielectric layer was composed of two polystyrene films and a layer of adhesive. The base on which the layers were placed was an aluminum pipe with a  $\frac{7}{8}$ -inch outside diameter.

The foil laying machine shown in Fig. 1 was equipped with a series

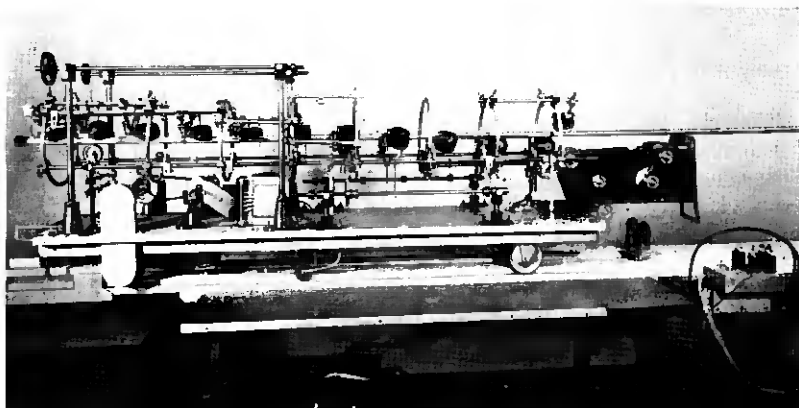


Fig. 1 — Foil laying machine.

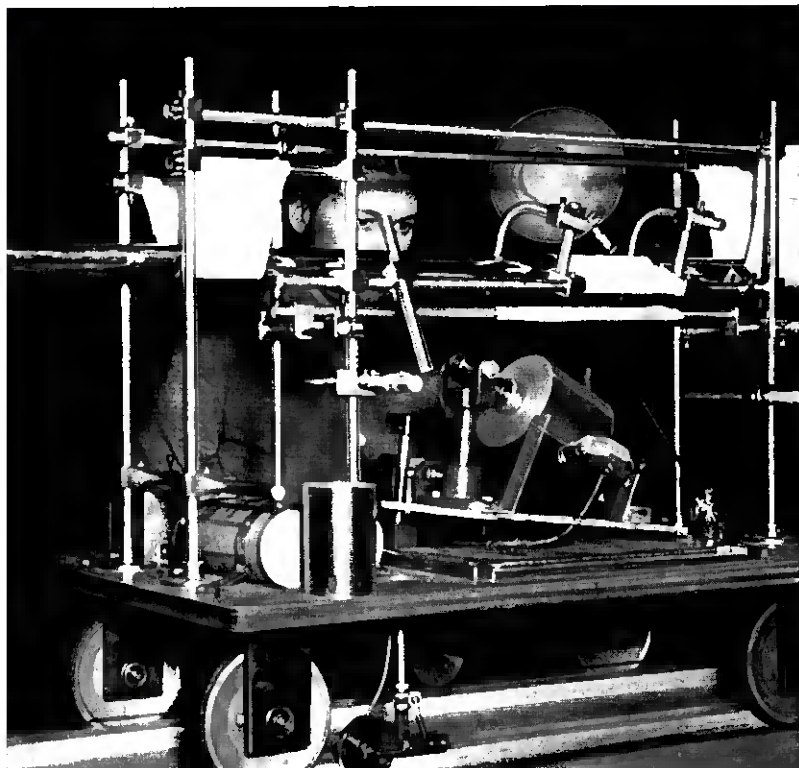


Fig. 2 — Insulating layer mechanism.

of metal rollers which reeled off the foil, put a coating of adhesive in a petroleum-ether solution on the inside surface of the foil and then laid the foil longitudinally along the under surface of the pipe, after which a series of rubber rollers progressively formed the foil around the pipe as the machine moved forward. For a short interval before it made initial contact with the pipe, the foil was exposed to a stream of heated air to hasten evaporation of the solvent from the adhesive. In putting the foil layers on longitudinally, the hope was to have a butt joint down the length of the pipe. Actually, this proved difficult and, consequently, the final result had few butt joints and more gaps than laps at the longitudinal seam.

The insulating polystyrene layers were wrapped spirally by a semi-automatic mechanism shown in Fig. 2, which rotated the pipe and synchronously moved a carriage along the deck which supported the pipe.

The feed mechanism for the polystyrene film was mounted on this carriage. To correct for imperfections in match between the rotation of the pipe and the carriage travel, the carriage was equipped with a manually controlled vernier for advancing or retarding its motion. An overlap in the spiral wrap very slightly in excess of 50 per cent was the goal aimed for, which would give an insulating layer of at least two thicknesses of polystyrene film everywhere. This was considered necessary in view of the imperfections in the film. The irregularities in the commercially available material, together with a cut-and-try method of controlling the winding pitch, led to overlaps that exceeded 50 per cent and often increased steadily until the film had to be cut and spliced and a new start made. The same adhesive used on the conducting layers was used for splicing the polystyrene films.

The adhesive coating on the inside surface of the aluminum foil was a 10 per cent solution of Vistac (polyisobutylene) in a petroleum ether solvent. The process of evaporating off the petroleum ether, which is normally rapid, was accelerated by blowing hot air over the coated surface just before it was wrapped and leaving a thin film of Vistac on the foil. This film was estimated to be 0.1 mil thick.

The composition of one full layer is shown in Fig. 3. Its thickness was estimated to be 1.6 mils. While every effort was made to keep the layers as uniform as possible, the foregoing explanation of the methods of applying the layers is sufficient to indicate that the resulting line was far from uniform. It was not known at the time of the experiment what effect nonuniformity would have.

### III. TERMINATING PROBLEM

The distribution of currents and voltages in the several conductors has been computed by Morgan<sup>5</sup> for a flat stack one meter wide.\* The current density  $J_2(y)$  at a distance  $y$  from the center of the stack is

$$J_2(y) = \frac{I_0\pi}{2b} \sin \frac{\pi y}{2b}, \quad (1)$$

where  $I_0$  is the total one-way current flowing in the line and  $2b$  is the total thickness of the stack of laminae. The voltage with reference to the inner surface is

$$V(y) = \frac{2b}{\pi} I_0 \sqrt{\mu/\epsilon} (1 + \sin \pi y/2b). \quad (2)$$

\* The equation for current distribution in a cylindrical medium is (305). In the present paper, the stack is assumed to be flat; i.e., the thickness of the stack is assumed small compared to its radius of curvature. Then the Bessel functions reduce to their asymptotic trigonometric forms.

The total voltage from inner to outer surface is

$$V_0 = \frac{4b}{\pi} I_0 \sqrt{\bar{\mu}/\bar{\epsilon}}. \quad (3)$$

In these formulas  $\bar{\mu}$  is the magnetic permeability of the materials in the stack (equal to the permeability of free space) and  $\bar{\epsilon}$  is the equivalent dielectric constant of the stack, as described by Morgan, and equals:

$$\bar{\epsilon} = \epsilon_2/(1 - \theta), \quad (4)$$

where  $\epsilon_2$  is the dielectric constant of the polystyrene dielectric layers and  $\theta$  is the proportion of the total stack thickness contributed by the thickness of the aluminum layers.

The current in the 50th foil is zero. Taking foils by pairs from 0 and 100 to 49 and 51, the ratio of potential difference to current was computed and found to be a constant value of 19.4 ohms. The line was assumed to be correctly terminated if 19.4 ohms were connected across each of these pairs. However, convenience dictated a different arrangement and an equivalent termination was worked out with a resistance of appropriate value from each conductor to its neighbors. The computed dc resistance values varied from 0.00475 to 0.00943 ohm. It was overlooked that these resistances apply to a stack one meter wide, and should, in general, be multiplied by the reciprocal of the stack width in meters. Therefore, the resistance values actually used departed from the matching resistances by a factor of approximately 1/11.5.

These resistance values are smaller than any physical resistors ordinarily supplied and some means of fabricating the wanted values was looked for. Tests on aluminum foil of the same thickness as was used for the metal laminations in the cable itself proved that this material, when wrapped over the edge of a strip of polystyrene so as to double back on itself, had the right order of magnitude of resistance. The final result is

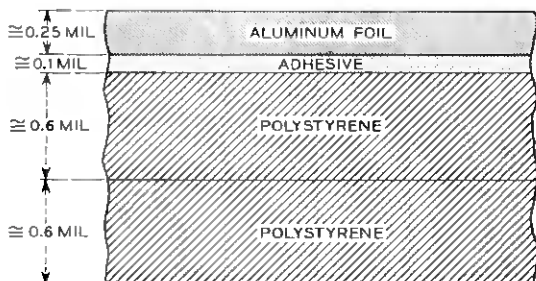


Fig. 3 — One composite layer of foil and insulation.

shown on Fig. 4. A suggestion from D. A. McLean that the points of contact between conducting layers and terminating resistors be arc-welded by discharging a capacitor across them succeeded in reducing the contact resistance to a negligible figure.

At the receiving end, the terminations were left as indicated above and a tab was connected to each junction to permit measurement of the voltages.

At the transmitting end, it was desired to launch a wave as near as possible to the principal mode of transmission. This was accomplished by sending currents through high-impedance padding resistors into each junction on the terminating network. These desired currents vary as the cosine of the distance from the junction to the 50th foil.

#### IV. LOSS MEASUREMENTS

With 276 feet of cable with a pileup of 100 composite layers having been built and terminated so that the previously determined resistance existed between each layer and its adjacent layers at both ends of the cable, the line was ready for loss measurement.

A signal generator was used to supply all the currents. A transformer with a stepdown ratio of about 3.75 to 1 was used to give a reasonably balanced output voltage. Suitable resistors were determined to connect conducting layers 0 through 49 to one side of the transformer secondary and 51 through 100 to the other side. With the proper distribution established, the ratio of voltage-to-ground to current at each junction was 4.85 ohms when foil 50 was taken as ground. This was one-fourth of the resistance needed between pairs. The termination resistors constituted one half of the conductance and the line the other half.

This value of 4.85 ohms had to be considered in fixing the ratio of the padding resistors. The resistors were chosen as a compromise between

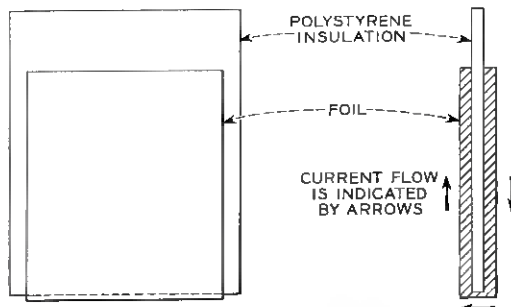


Fig. 4—Termination configuration.

various needs. A high value would have the undesirable result of increasing the dead loss of the pad. On the other hand, a low value would have shunted the termination resistors, which were not adjusted with this in mind and so would have increased the reflection factor. The inductance of the tabs making contact to the conducting layers was not thought to be negligible at high frequencies; the reactance was estimated to be as great as 10 ohms at 20 megacycles. Mutual inductance between tabs was not small either. The use of large resistors would have minimized the effect of inductance in the leads but would have made the capacitance across the resistors more serious.

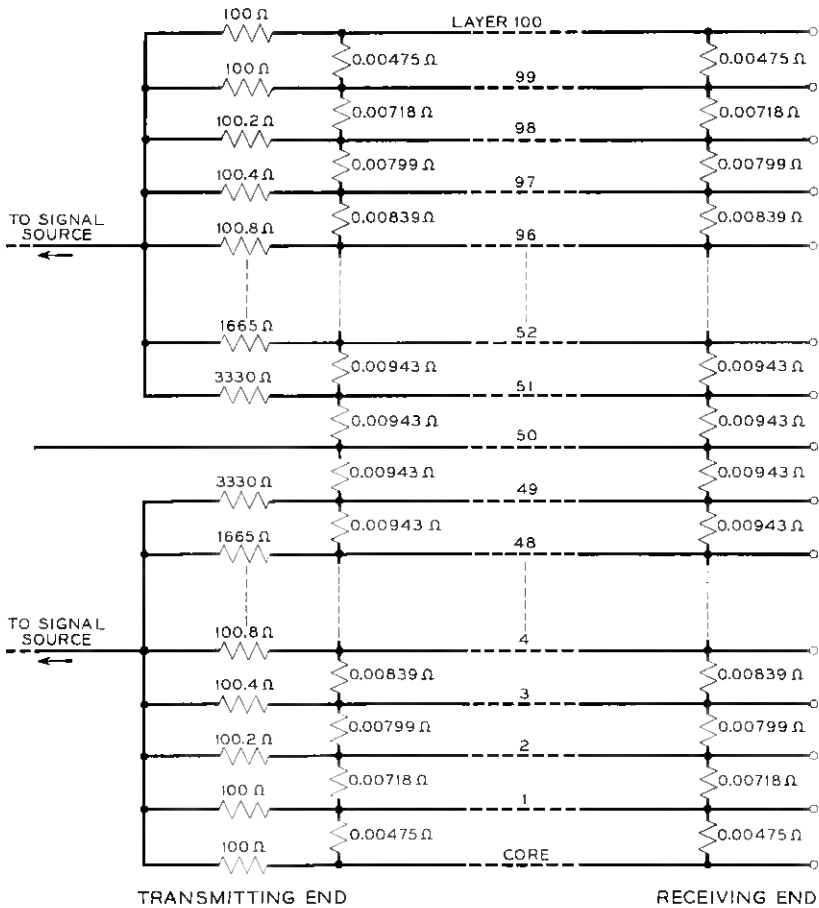


Fig. 5 — Terminating and padding resistor arrangement.

It was decided that 100 ohms would be a good compromise value to use for the resistors to the extreme conductors of the stack. The others were higher. By taking  $100 + 4.85$  ohms as the total resistance and by applying a cosine variation with distance in to the center of the stack, and then subtracting the constant 4.85 ohms, the values of the padding resistors were obtained. In order to insure that the values were as nearly correct as possible, the molded resistors used were pre-aged by the application of heat and were measured both before and after being connected.

The padding resistors at the sending end introduced a loss of 26.8 db between the transformer secondary and voltage across the transmission line. Fig. 5 shows the arrangement of the terminating and padding resistors at the sending and receiving ends of the line.

The measuring circuit for the terminated line is shown in Fig. 6. A wideband radio receiver feeding a vacuum tube voltmeter was used as a detector. A pad of resistors at the input of the receiver provided a 75-ohm impedance at all frequencies. Transmission loss to any of the

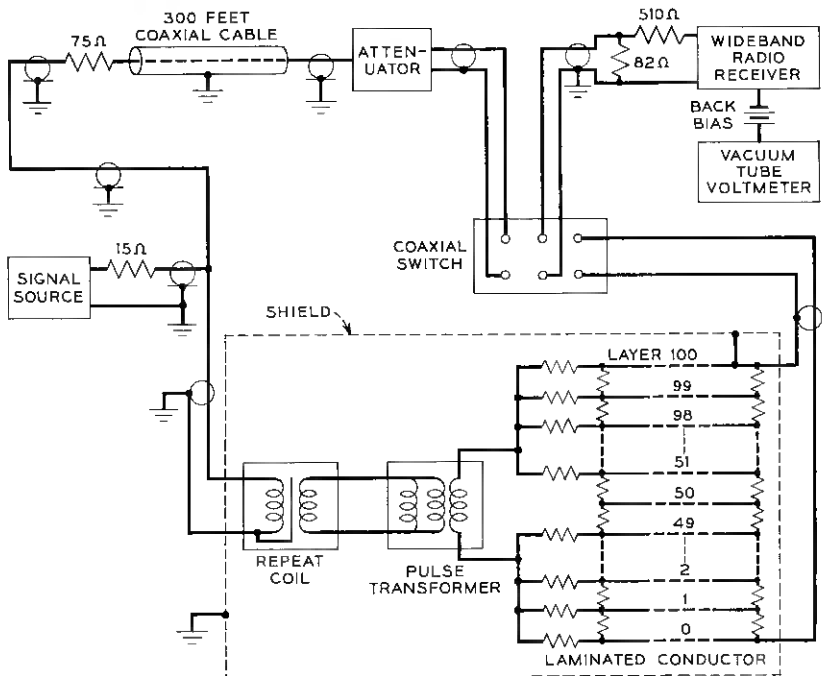


Fig. 6 — Measuring circuit for terminated line.

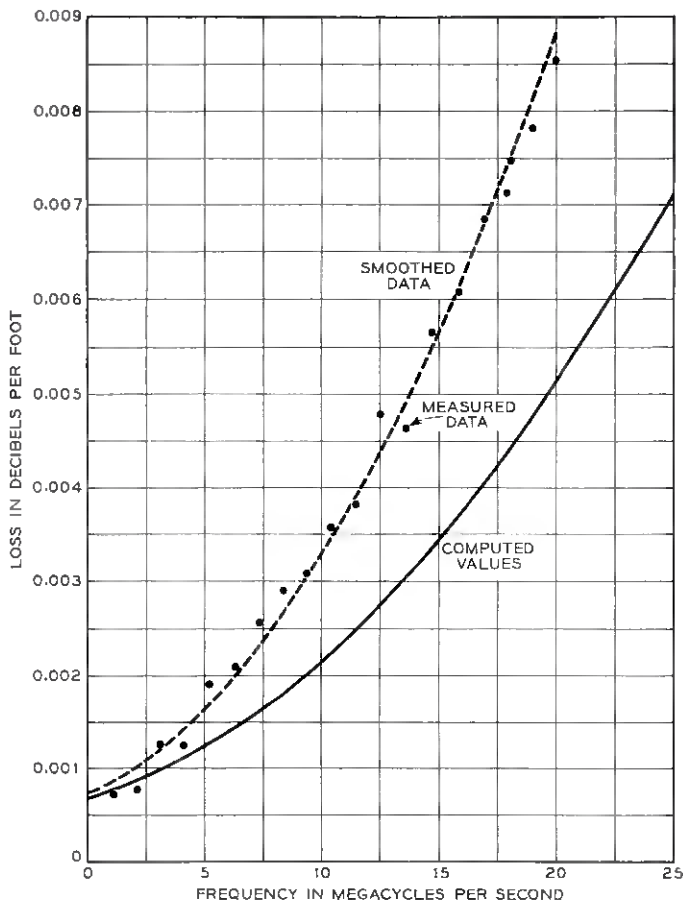


Fig. 7 — Loss measurements on 276-foot terminated laminated transmission line, with line and measuring circuit completely shielded.

available taps could be measured by comparison to the calibrated loss of a 300-foot length of solid-polyethylene dielectric coaxial cable. In order to obtain the net loss of the line, the calibration loss and the 26.8 db loss of the pads back-to-back were subtracted from the measured attenuations.

Before any measurement could be made over the frequency band desired, it was necessary to shield the pipe by adding a longitudinal strip of 10-mil aluminum wrapped as closely as possible. It was also necessary to shield the terminations. Before these shields were applied,

strong fields were set up in the space outside the system and large irregularities in loss occurred at frequencies for which the outside of the pipe was in resonance with free space waves.

The first data taken showed the mismatch introduced by the terminating resistors. A resume of the method used for finding the true loss from the measured values is given in the Appendix. Fig. 7 shows the loss data found for the completely shielded line. A theoretical loss curve found by S. P. Morgan is also shown. At the time when the experiment was conducted, the only computed curve available was that in which irregularities were ignored, and it is seen that the correspondence with experimental values is not satisfactory.

#### V. RESONANT CAVITY MEASUREMENT

The terminations were cut away and both ends of the pipe were faced off smoothly so that no shorts existed between adjacent layers at the cut ends. A check, using a micromanipulator and a pair of transistor points that made contact to each pair of adjacent layers in turn, revealed a number of shorts, some of which were removed by applying a small voltage across the layers.

The line, now 269 feet in length, was measured as a resonator by

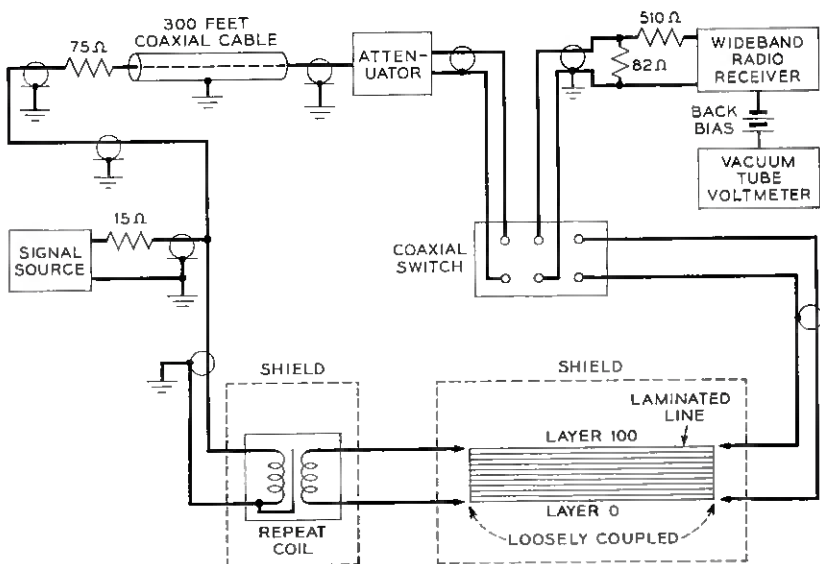


Fig. 8 — Circuit for measuring laminated line as a resonator.

loosely coupling a coaxial lead to each end of the line. The measuring circuit is shown in Fig. 8 and the connector permitting loose coupling is shown in Fig. 9.

Loss measurements were made on a 269-foot length of line with five known shorts, a 252-foot length with three shorts, a 142.5-foot length with three shorts and 106.5- and 103-foot lengths that were short-free. The loss data for the various lengths were consistent enough to lead to the conclusion that the presence of shorts in some of the lengths measured was not affecting the results enough to account for the spread between the measured and theoretical values of loss. In fact, the experiments indicate that, as a practical matter, shorts to this extent could be tolerated.

Fig. 10 shows the loss data for the pieces of cable measured. Fig. 11 shows a curve that is a composite of all the data taken compared with Morgan's values, which were computed assuming a dielectric constant,  $\epsilon_r = 2.56$  and a loss tangent,  $\tan \phi = 0.0015$ . The loss curves for an aluminum coaxial cable of the same dimensions with the same dielectric and with an air dielectric are included in Fig. 11.

#### VI. METHOD OF FINDING LOSS

The measurements of attenuation on the sections of laminated conductor gave a loss vs. frequency curve from which it was necessary to deduce the interaction loss.

The total transmission loss of a network is the sum of four factors:

- (a) image transfer constant,
- (b) reflection loss at the input,
- (c) reflection loss at the output,
- (d) interaction loss or gain.

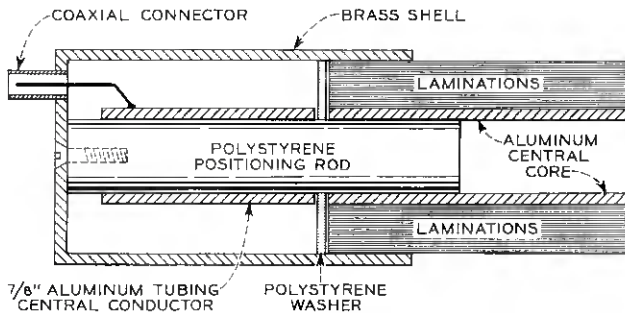


Fig. 9 — Cross section of the coupler used in measuring laminated line as a resonator.

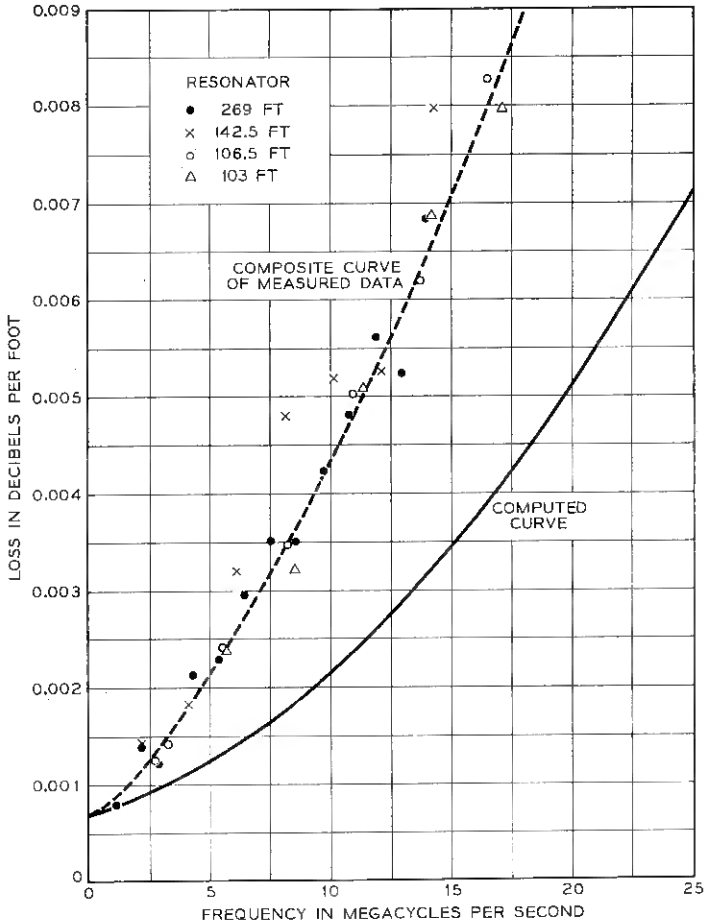


Fig. 10 — Loss measurements on various lengths of laminated transmission line measured as a resonator.

The first three terms will be positive losses but the fourth can be positive or negative. The interaction factor is expressed as

$$\frac{1}{1 - \rho_1 \rho_2 \epsilon^{-2\theta}} \quad \text{or} \quad \frac{1}{1 - \rho_1 \rho_2 \epsilon^{-2\alpha} \epsilon^{-2\beta j}}, \quad (5)$$

where  $\rho_1$  and  $\rho_2$  are the reflection coefficients at the sending and receiving ends of the line and  $\theta = \alpha + j\beta$  is the image transfer constant. With a high impedance at each end, both reflection coefficients have the same sign and the interaction phase angle is  $\beta = \pi f/f_0$ , where  $f_0$  is the fre-

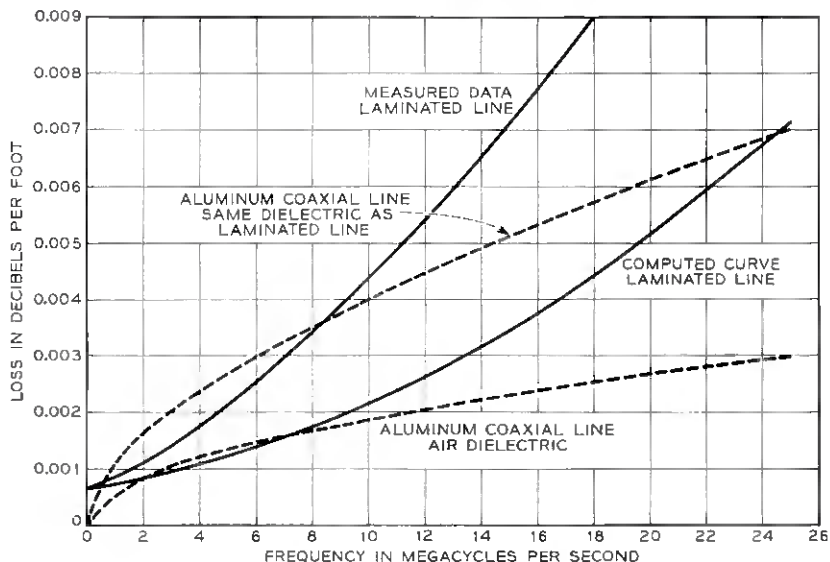


Fig. 11 — Measured and computed losses of a laminated transmission line compared with coaxial lines of the same dimensions.

quency of the first resonance or minimum loss point. When  $\beta$  is an integral multiple of  $\pi$ , ( $\beta = n\pi$ ), the interaction factor is

$$\frac{1}{1 - \rho_1 \rho_2 \epsilon^{-2\alpha}}, \quad (6)$$

and when  $\beta = m\pi/2$  and  $m$  is odd, the interaction factor becomes

$$\frac{1}{1 + \rho_1 \rho_2 \epsilon^{-2\alpha}}. \quad (7)$$

Calculations by J. O. Edson showed that  $\rho_1 = \rho_2 = 1$  to an accuracy better than 1 per cent and, for our purposes, can be ignored in the calculation of true loss. Then,  $\alpha$  can be computed from the measured attenuation, since

$$\frac{1 + \epsilon^{-2\alpha}}{1 - \epsilon^{-2\alpha}} = K, \quad (8)$$

where  $20 \log_{10} K$  is the spread between maximum and minimum loss points in decibels.

In the case under consideration,  $2\alpha$  is not independent of frequency and neither are the reflection losses, but the quantity  $K$  may still be ob-

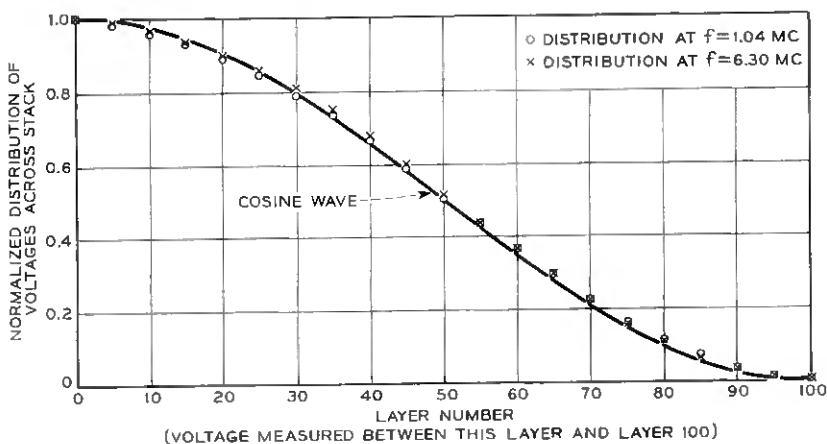


Fig. 12 — Distribution of voltages across 276-foot terminated Clogston 2 line at two minimum-loss points.

tained from a study of the measured loss. The procedure is to draw an envelope of the maximum loss points and an envelope of the minimum loss points and to interpret the spread between the two envelope curves as  $20 \log_{10} K$ .

#### VII. MEASUREMENTS ON DISTRIBUTION OF VOLTAGE

Two sets of distribution measurements were made, one on the 276-foot terminated line and one on the 103-foot unterminated length of line. On the 276-foot line, readings were made at two minimum loss points and the normalized distributions were plotted and compared to a cosine wave which is a fair approximation to the expected voltage distribution across the stack. The results are shown in Fig. 12. On a 103-foot length that was short-free, the same kind of measurements were made and compared to a cosine wave. This is shown in Fig. 13. The distributions under the two conditions varied considerably from each other and it was concluded that the terminated line, in spite of the mismatch, forced the principal mode, while the unterminated line distribution shows the presence of other modes. The loss measurements, however, do not show this marked variation although the terminated line loss is somewhat smaller than the loss taken on the line as a resonator.

#### VIII. VELOCITY OF PROPAGATION

For the different lengths of line measured, the phase velocities were found by using the measured lengths and the observed first resonances

of the standing waves. The velocities were of the order of 0.586 to 0.592 times the speed of light in free space. A check of these figures was made by using the formula

$$v = \frac{1}{\sqrt{\bar{\epsilon}\mu}}, \quad (9)$$

where  $\bar{\epsilon}$ , the effective dielectric constant, is given by

$$\bar{\epsilon} = \epsilon_2 \left( 1 + \frac{t_1}{t_2} \right) = \frac{\epsilon_2}{1 - \theta}, \quad (10)$$

where  $\epsilon_2$  is the dielectric constant of the insulating material and  $t_1$  and  $t_2$  are the thicknesses of the conducting and insulating layers. This resulted in a velocity equal to 0.574 times the speed of light. The experimental velocity is probably more accurate than the computed velocity, since the frequencies and lengths could be determined somewhat more accurately than the thicknesses of the layers. The agreement is very satisfactory and further supports the view that transmission follows Clogston's prediction.

#### IX. CAPACITANCE MEASUREMENTS

The loss-frequency curves show that the data on the terminated 276-foot line and the various unterminated lengths show a highly consistent increase in loss over that computed for a uniform line. This disparity between the measured and computed values was noted on the

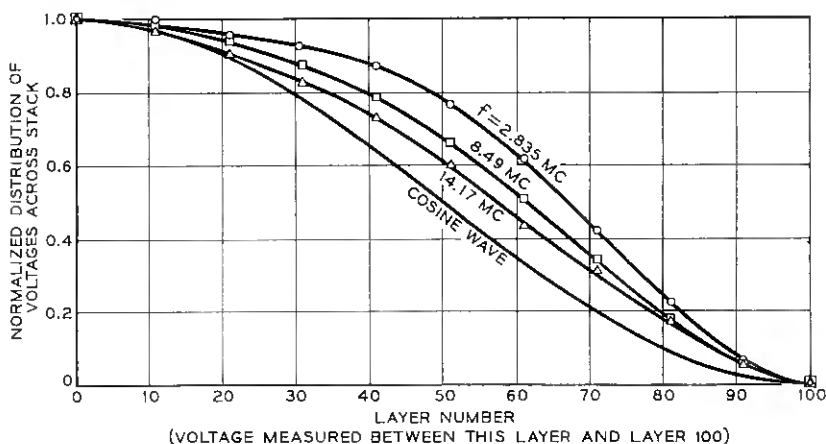


Fig. 13 — Distribution of voltages across unterminated 103-foot Clogston 2 line at three minimum-loss points.

first attenuation-frequency data, and each new set of measurements was made with the hope of finding the reason for and thereby reducing this spread. The increase in loss with frequency remained painfully persistent whether the data were taken on the whole line or on any of the sections into which it was later cut.

In addition to the check on the voltage distributions mentioned above, again using a micromanipulator and a pair of transistor points, the capacitance was measured between each layer and its neighbor, going from the inside to the outside of the stack in order to find a clue to the increase in loss. These capacitance measurements are shown in Fig. 9 of the accompanying paper<sup>3</sup> for the 103- and 142.5-foot lengths of unterminated line. When these capacitances were reduced to a unit area basis, they were found to correlate well with a computed value of 0.000426 microfarads per square inch of area for an assumed thickness of 1.35 mils of dielectric.

It will be noted that the two sets of measurements show similar fluctuations across the stack and at first these fluctuations were felt to be small enough not to be troublesome. However, Morgan,<sup>5</sup> considered the effects of nonuniformity in laminated lines and his work indicates that small systematic variations across the stack can cause substantial variations in transmission properties. Further work by Raisbeck on the analysis of these capacitance fluctuations is reported in the companion paper.<sup>3</sup>

## X. SPLICING EXPERIMENTS

Computations by J. G. Kreer and J. O. Edson indicated that a separation of 1 mil between two lengths of Clogston 2 line would give 0.3-db loss for the splice and the loss would increase to about 1.8 db when the separation exceeded the thickness of the stack though the inner pipes and the outer foils of the two sections are connected.

One further experiment was made on the Clogston 2 line. Two lengths of cable, one 142.5 feet long with two known shorts and the other a short-free 103-foot line were faced off as plane as possible, butted together and measured for loss. A second set of measurements was made with a 2-mil spacer at the butt joint.

Interpretation of the data shown in Fig. 14 is made difficult by the fact that reflections occur at the junction as well as at the two ends of the line. The reflections from the individual sections confuse the picture at high frequency. The low-frequency points should be fairly reliable. When the ends were butted together as tightly as possible, the indicated

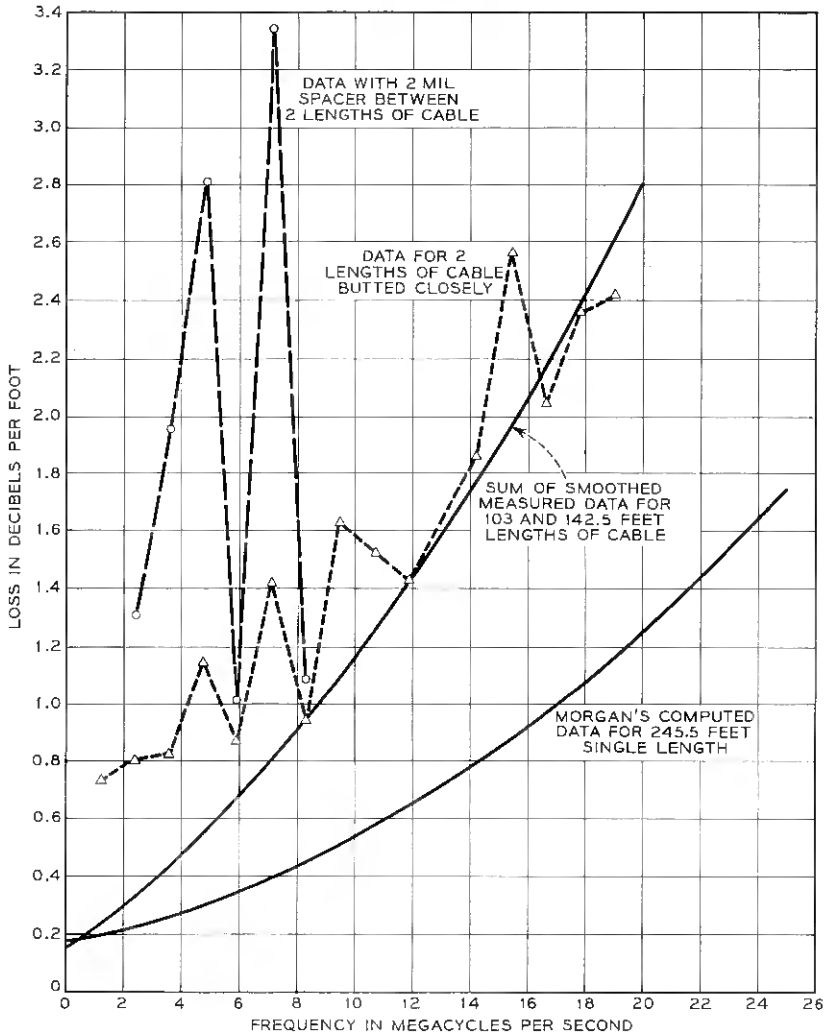


Fig. 14 — Loss measurements on two lengths of laminated conductor spliced together.

loss was about 0.5 db greater than the sum of the losses of the individual sections of line. At higher frequencies, the points are found to be on either side of the sum of the parts. This is not unreasonable, since the loss at the splice is of the nature of a reflection loss rather than a real dissipative transfer loss, and consequently this loss may be reduced by reflections in the individual sections of line. With a 2-mil spacer between

the ends of the two lines, the low-frequency loss of the splice appears to be about 1 db and the variations due to multiple reflections are more violent.

With a machine for cutting the faces plane within closer tolerances than was accomplished here, and with a jig that squeezed the two faces together as closely as possible, this method of splicing Clogston 2 cable appears feasible.

#### XI. ACKNOWLEDGMENT

The experiment described above was designed by J. O. Edson and J. G. Kreer and was carried out under the supervision of H. S. Black with considerable credit for mechanical ingenuity going to C. R. Meissner. In addition, many other members of Bell Telephone Laboratories contributed to various phases of this project.

#### APPENDIX

##### *Method Used to Figure Insertion Loss of a Network With a Mismatch*

Assume a network of unknown image impedance  $Z_0 = k$  ohms and unknown transfer constant  $\theta = \alpha + j\beta$  working between a 1-ohm source and a 1-ohm load.

Start by adding  $(k - 1)$  ohms in series with the source and call the total applied voltage  $e_0$ . Then the open circuit output voltage is  $e_0\epsilon^{-\theta}$  volts and the voltage at 1-ohm load is

$$e_{\text{out}} = \frac{e_0 \cdot 1}{k + 1} \epsilon^{-\theta}. \quad (11)$$

The output resistance can be built up to a match by adding to the 1-ohm load a resistance  $(k - 1)$  and a generator

$$e_2 = \frac{k - 1}{k + 1} e_0 \epsilon^{-\theta}. \quad (12)$$

The voltage across the input terminals is then

$$e_1 = \frac{e_0}{2} - \frac{1}{2} e_2 \epsilon^{-\theta} = \frac{e_0}{2} \left( 1 - \frac{k - 1}{k + 1} \epsilon^{-2\theta} \right). \quad (13)$$

The voltage across the total source resistance is

$$e_0 - \frac{e_0}{2} + \frac{e_0}{2} \left( \frac{k - 1}{k + 1} \right) \epsilon^{-2\theta}. \quad (14)$$

That across  $(k - 1)$  ohms is

$$\frac{k - 1}{k} e_0 \left( 1 + \frac{k - 1}{k + 1} \epsilon^{-2\theta} \right). \quad (15)$$

Associating this part with the excess resistor leaves a net source

$$e_0 \left[ 1 - \frac{k - 1}{2k} - \frac{(k - 1)^2}{2k(k + 1)} \epsilon^{-2\theta} \right]. \quad (16)$$

The net insertion transmission ratio is one-half the ratio of the net source voltage in series with 1 ohm to the output voltage delivered to 1 ohm. It is

$$\frac{1}{2} \left[ 1 - \frac{k - 1}{2k} - \frac{(k - 1)^2}{2k(k + 1)} \epsilon^{-2\theta} \right] \div \frac{\epsilon^{-\theta}}{k + 1}. \quad (17)$$

The ratio is

$$\begin{aligned} \frac{\epsilon^\theta}{2} \left[ 1 + k - \frac{(k^2 - 1)}{2k} - \frac{(k - 1)^2}{2k} \epsilon^{-2\theta} \right] \\ = \epsilon^\theta \left[ \frac{1 + k}{2} - \frac{(k^2 - 1)}{4k} - \frac{(k - 1)^2}{4k} \epsilon^{-2\theta} \right]. \end{aligned} \quad (18)$$

If  $\beta = 0$  in  $\theta = \alpha + j\beta$ , the ratio is

$$\begin{aligned} \epsilon^\alpha \left[ \frac{1 + k}{2} - \frac{k^2 - 1}{4k} - \frac{(k - 1)^2}{4k} \epsilon^{-2\alpha} \right] \\ = \epsilon^\alpha \left[ \frac{(k + 1)^2}{4k} - \frac{(k - 1)^2}{4k} \epsilon^{-2\alpha} \right]. \end{aligned} \quad (19)$$

If  $\beta = \pi/2$ ,  $2\beta = \pi$ , which changes sign of the second term in brackets. The insertion loss is minimum for  $\beta = 0$ . The insertion loss is maximum for  $\beta = \pi/2$ .

If  $\alpha$  is small,

$$\epsilon^{-2\alpha} \cong 1 - 2\alpha,$$

$$\text{minimum loss} \cong \alpha + 20 \log_{10} \left[ 1 + \frac{(k - 1)^2 2\alpha}{4k} \right], \quad (20)$$

$$\text{maximum loss} \cong \alpha + 20 \log_{10} \left[ \frac{k^2 + 1}{2k} - \frac{(k - 1)^2}{4k} 2\alpha \right].$$

The approximations may be made exact if the quantity  $2\alpha$  is interpreted as the difference between  $\epsilon^{-2\theta}$  and unity.

## REFERENCES

1. Clogston, A. M., Reduction of Skin Effect Losses by the Use of Laminated Conductors, B.S.T.J., **30**, July 1951, p. 491.
2. Black, H. S., Mallinckrodt, C. O. and Morgan, S. P., Experimental Verification of the Theory of Laminated Conductors, Proc. I.R.E., **40**, August 1952, p. 902.
3. Raisbeck, G., this issue, p. 477.
4. King, Mrs. R. A. and Morgan, S. P., Transmission Formulas and Charts for Laminated Coaxial Cables, Proc. I.R.E., **42**, August 1954, p. 1250.
5. Morgan, S. P., Mathematical Theory of Laminated Transmission Lines, B.S. T.J., **31**, September 1952, p. 883; November 1952, p. 1121.

# Fundamental Processes of the Short Arc

## With Applications to Contact Erosion and Percussion Welding

By J. L. SMITH and W. S. BOYLE

(Manuscript received June 17, 1958)

*The short arc develops an instability when certain critical conditions of power input to the arc are not satisfied. In this unstable condition the arc is momentarily extinguished, a molten filament of metal is drawn between the electrodes and this may permanently bridge the electrodes. Semi-empirical expressions have been derived which predict at what time in the life of an arc it becomes unstable.*

*These expressions give a simple explanation of some of the erosion characteristics of relay contacts. In addition, the analysis is useful in determining the optimum current waveform for percussion welding, where a stable arc is desirable.*

### I. INTRODUCTION

When charged electrodes are brought together, an electric arc is formed before they touch. For potentials below about 300 volts, the arc is both initiated and maintained by field emission currents. The initiation and sustaining mechanisms are quite well understood and have been treated in considerable detail in papers by L. H. Germer and his co-workers.

Recently Germer and Boyle<sup>1</sup> have presented experimental evidence that two distinct types of short arcs exist. One of them, called the cathode arc, obtains the predominant supply of ions necessary to maintain an arc by continuously exploding small points on the cathode surface. This type of arc does not weld the electrodes together and will not be treated in this paper. The second type of arc, which derives its ions from metal vaporized from the anode by electron bombardment, is appropriately called an anode arc. If sufficient energy is supplied to this arc, the electrodes will be welded together. We have obtained experimental information which clarifies the physical processes that give rise

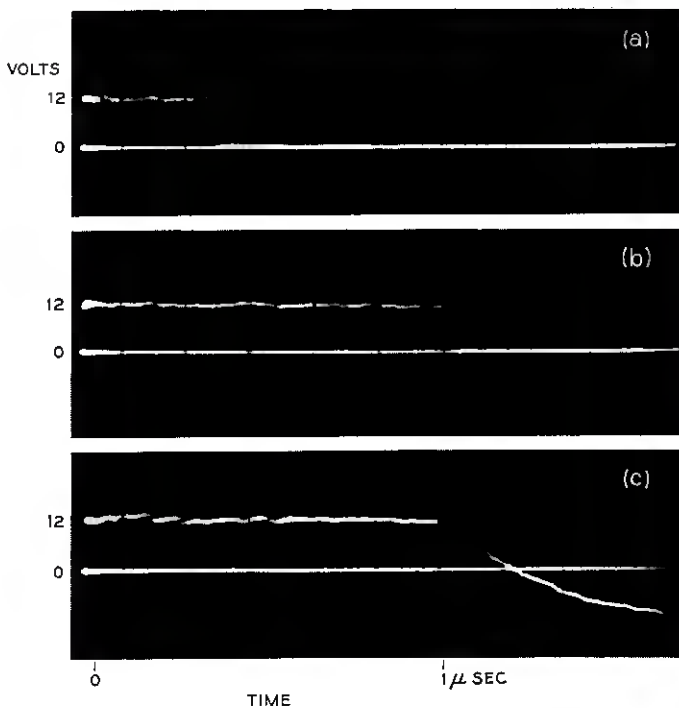


Fig. 1 — Oscilloscopic records of the potential across a constant-current arc: (a) electrodes welded at 0.35 microsecond, *before* complete discharge of the source of energy; (b) electrodes welded at 1 microsecond, just as the available energy was exhausted; (c) electrodes not welded.

to electrode welding and have developed a theory which enables one to predict under what conditions welding will take place. This information proves to be useful either for predicting the erosion of relay contacts in terms of the associated circuit parameters or, conversely, for designing the optimum circuit for percussion welding.

To illustrate what is meant by a weld in the present context, Fig. 1 shows three oscillograms of the potential across a pair of approaching gold electrodes as a function of time after the initiation of an arc. The electrodes were connected to 400 feet of RG58U transmission line charged to 200 volts. The transmission line supplied approximately 2 amperes of constant current to the arc for a duration of 1 microsecond. Each oscillogram shows a plateau voltage of approximately 12 volts, which is characteristic of a short arc between gold electrodes. The instant when closure (or welding) of the electrodes took place is indicated by a sudden change of potential reducing the voltage across the contacts to zero.

In the uppermost oscillogram, closure occurred before the transmission line was completely discharged; i.e., the electrodes were welded. In the middle oscillogram, a weld occurred at the instant the line was completely discharged. In the lower oscillogram, there was no weld, the contacts closing sometime after the line was completely discharged. Closures of the type illustrated by the upper and middle oscillograms predominate for anode arcs. Furthermore, if the power input to the arc is large and of short duration, such as a discharge of a transmission line or an  $LC$  circuit, the majority of the closures will take place at the end of the discharge period. This is shown quite clearly in Fig. 2, which was obtained by replotting the data from Fig. 7 of an earlier paper by Germer and Smith.<sup>2</sup> An explanation for this preference to weld just as the circuit is completely discharged will now be given.

## II. WELDING MECHANISM OF THE ANODE ARC

The initiation process for short arcs must differ from that of the usual breakdown process in air, since arcs can be initiated between electrodes with a potential difference considerably below the "minimum" sparking potential. To initiate this arc, an electric field is required of the order of  $10^7$  volts per cm, which has suggested a field emission process for obtaining the initial electrons. Kisiuk<sup>3</sup> has developed a model which shows that field emission currents can both initiate and maintain the short arc.

Because of the small electrode gap ( $\sim 1000 \text{ \AA}$ ), most of the initial electrons cross without collision, dissipating their energy on the anode surface. This raises a small spot on the anode surface to the boiling point.

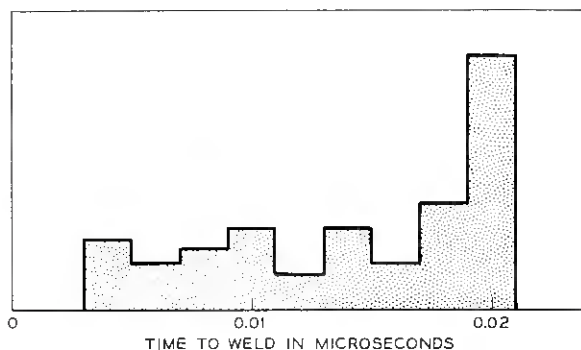


Fig. 2 — Statistical distribution of observed closure times at the discharge of an  $LC$  circuit having a discharge time of 0.02 microsecond ( $L = 0.10 \mu h$ ,  $C = 400 \mu f$ ).

creating a vapor that, when ionized, supplies the arc with ions. The ions form a space charge in front of the cathode. This produces a sufficiently large field to maintain by field emission the high current densities ( $>3 \times 10^7$  amps/cm<sup>2</sup>) necessary for the arc. Kisliuk has shown that this type of arc is very efficient in its use of ions to produce electrons and that more than 90 per cent of the current is carried by electrons. Since many of these electrons cross the gap without collision, a large portion of the total arc energy is dissipated on the anode by electron bombardment. Some of this energy is carried away by conduction, and the rest melts and vaporizes metal. During the arc, there is therefore a molten pool of metal on the anode.

The ionic space charge in front of the cathode increases the field at the cathode and lowers the field at the anode. A simple sketch of the potential distribution in the arc is shown by curve A in Fig. 3. With the low electrostatic field at the anode during the arc, the molten pool of metal remains intact — at least there are no large forces tending to pull it towards the cathode. When the arc is extinguished, there is a redistribution of the potential between the electrodes, with the potential attempting to approach that of curve B of Fig. 3. With this redistribution, there is an increase in the electric field at the anode, tending to pull a filament of the molten pool of metal across the gap, thus welding the electrodes.

When the power input to the arc is too low to vaporize sufficient metal to maintain the required number of ions, the arc will be extinguished. Boyle and Germer<sup>4</sup> have shown that the power needed to main-

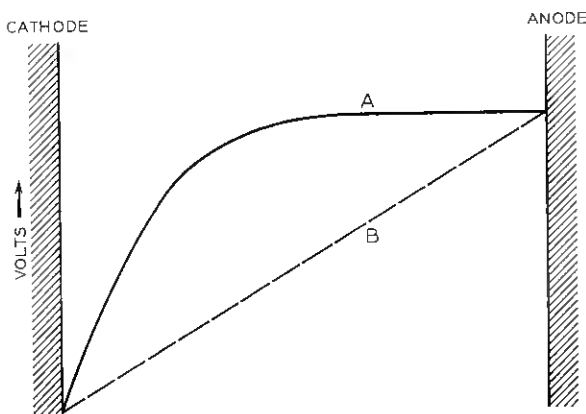


Fig. 3 — Potential distribution between electrodes: A — during arc; B — after end of arc.

tain the arc increases with the total energy which has been delivered to the arc. In a low-energy, high-power circuit, the arc will be extinguished when the supply of energy is completely exhausted. In higher-energy circuits the arc may be extinguished considerably before this point is reached and, because of the welding phenomenon, the remainder of the energy will be dissipated in the resistance of the circuit.

Fig. 4 is a photomicrograph of a single pit produced on the anode of a gold electrode by a discharge of a constant-current 3-ampere source for 0.3 microsecond. The shape of the pit is approximately that of a half hemisphere although the depth is usually less than that of the radius. Germer and Haworth<sup>5</sup> have shown that the diameter of the pit varies as the cube root of the energy.

Since the power lost in conduction increases with the diameter, one expects that, for a given power input, the arc will grow to some maximum diameter at which time the power available for evaporation of metal will be insufficient to produce the number of ions needed to maintain the arc. This is indeed the case, and Boyle and Germer have shown that the maximum pit diameter is quite sensitive to the input power.

The clearest demonstration of the nature of the welding process comes from a study of the welding characteristics of a constant-current circuit.

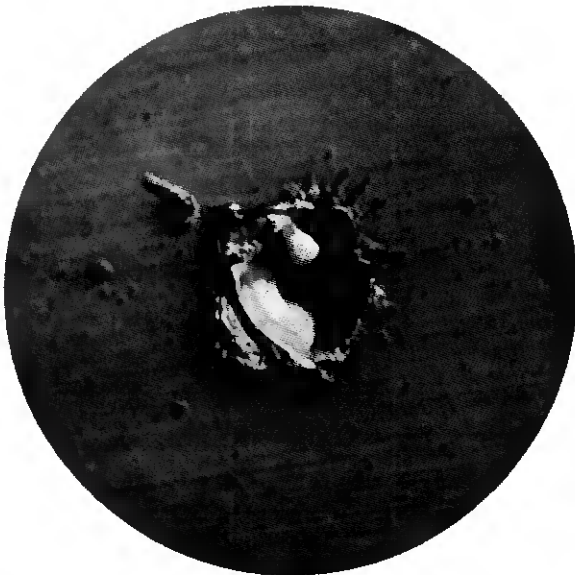


Fig. 4 — Pit made on the anode by a single arc of the anode type.

TABLE I — WELDING TIMES WITH SHORT CABLES

Trial	Time to Weld/Maximum Time of Cable Discharge, for Cable Length of		
	10 ft.	50 ft.	150 ft.
1	1.0	1.0	0.9
2	1.0	1.0	0.9
3	1.0	1.0	1.0
4	1.0	1.0	1.0
5	open	0.9	0.9
6	1.0	1.0	0.8
7	1.0	1.0	0.9
8	1.0	0.9	0.8
9	1.0	1.0	1.0
10	1.0	1.0	1.0

If various lengths of transmission line are discharged through a pair of electrodes in a short arc, it is found, as remarked earlier, that, for the short lengths of cable, there is a great tendency for the weld to occur at a time when the cable has just been completely discharged. In other words, the weld occurs under those conditions when the arc has just been terminated by the discharge of the circuit, in agreement with the idea that the gap is bridged when the field is redistributed.

By way of further illustration of the fact that, for short discharge times, the weld always occurs when the circuit is discharged, some data on welding times for polished palladium electrodes are presented in Table I. These data were obtained by discharging various short lengths of 50-ohm cable charged to 50 volts. Experimental details are given as a footnote in Ref. 1, p. 33.

From this it is quite clear that, even though 10 feet of cable provides enough energy to weld the electrodes, in many cases the arc lasted for the full period of the 150-foot cable, with the dissipation of 15 times as much energy.

With longer cables or in an  $RC$  circuit, the weld will occur before the arc has been terminated by the external circuit. Once again this is due to the fact that the arc goes out. In these cases, the extinction of the arc is due to an instability in the arc itself; i.e., the pit diameter grows too large to be maintained by the available power. To establish this point, we shall give the appropriate calculations for the times of extinction of an arc carrying a steady or exponentially decaying current. Then it will be shown that these times agree well with experimentally observed welding times.

To make the calculations we start with the empirical expression  $d = AE^{1/3}$ , where  $d$  is the diameter of the anode hot spot,  $E$  the total arc

energy and  $A$  a proportionality constant determined experimentally in Ref. 4 for gold electrodes. The conduction loss from the anode is  $P_c = 2 KdT_B$ , where  $K$  is the thermal conductivity of the electrodes (at a temperature approximately midway between the boiling temperature  $T_B$  and room temperature). The power input to the anode,  $P_i$ , is approximately,  $Iv$ , where  $I$  is the arc current and  $v$  is the arc voltage. (Actually,  $P_i$  is somewhat less than this, since some energy is delivered to the cathode.) Eliminating  $d$  from these two expressions and using  $P_i > P_c$  for our condition of stability, we obtain

$$I > GE^{1/3}, \quad (1)$$

with  $G = 2 KT_B A/v$ , which is a semi-empirical constant to be evaluated. The arc is extinguished when the condition of (1) is no longer satisfied.

In a constant-current circuit  $E = I\tau v$ , where  $\tau$  is the time to extinction of the arc, and is therefore given by

$$\tau = I^2/G^3v. \quad (2)$$

In an  $RC$  circuit with  $I = I_0 \exp(-t/RC)$  the criterion for stability is

$$I > G \left( \int_0^t Iv dt \right)^{1/3}$$

and the time to extinction  $\tau$  is a solution of the equation

$$\exp(3\tau/RC) - \exp(2\tau/RC) = (V_0 - v)^2/G^3R^3Cv, \quad (3)$$

where  $V_0$  is the initial potential difference across the capacitor  $C$ .

To demonstrate the validity of the above analysis, we shall consider separately below a series of experiments with long cables and with various  $RC$  circuits.

All of the measurements were made with a pair of gold electrodes mounted on a standard telephone relay. The welding time was measured visually on an oscilloscope (see Fig. 1) and each measurement presented in Tables II and III represents the average of some 50 observations. The precision of the average welding time  $\tau$  is not great — not because of any instrumental error, but because of slow variations of  $\tau$  over many operations, presumably because of uncontrolled changes in the surface condition of the electrodes.

In Table II, where the results of the experiments on long cables are summarized,  $V$  is the voltage on the cable;  $Z$  is the effective cable impedance, including the termination, which was chosen so that the cable was matched at the electrode end;  $\tau$  is the observed average welding

TABLE II — WELDING TIMES WITH LONG CABLES

$V$ , volts	$Z$ , ohms	$I$ , amp	$\tau$ , $\mu$ sec	$E$ , ergs	$I^2/\tau$ , amp <sup>2</sup> /sec
250	100	2.4	1.95	560	$2.9 \times 10^6$
200	100	1.9	1.29	290	$2.7 \times 10^6$
170	100	1.6	1.15	220	$2.2 \times 10^6$
140	100	1.3	0.80	120	$2.1 \times 10^6$
121	186	0.59	0.12	8.5	$2.9 \times 10^6$
100	100	0.88	0.25	27	$3.2 \times 10^6$

time; and  $E$  is the total arc energy  $Iv\tau$ , with  $v = 12$  volts appropriate for gold. The last column gives the quotient  $I^2/\tau$ , which, according to (2), should be constant. In all cases the discharge time of the cable was much longer than the average welding time.

The average of the  $I^2/\tau$  values is  $2.7 \times 10^6$ , and there is a maximum deviation of 23 per cent about this mean. It should be noted that the energy to weld over this same range varied by a factor of 64. From (2), we determine  $G = 61$ .

In Table III are given the results of welding experiments using an  $RC$  network in place of the transmission cable, and a capacitor potential of 170 volts. Results are given for various combinations of three values of  $R$  and four values of  $C$ . These data can be used to test (3) by plotting  $\exp(3\tau/RC) - \exp(2\tau/RC)$  against  $1/R^3C$ . Such a plot on logarithmic scales is given in Fig. 5. The line is drawn as the best fit of the points by a straight line of unit slope. Although the deviation of some of the points from the line is quite large, in no case is this an indication of more than 30 per cent error in the predicted value of  $\tau$ . The value of  $G$  obtained from the line is 41.

It is apparent that (2) and (3) agree well with the experimental re-

TABLE III — WELDING TIMES WITH AN  $RC$  NETWORK

$C$ , $\mu$ f	$R$ , ohms	$\tau$ , $\mu$ sec	$E$ , ergs
0.03	21	1.3	495
0.03	51	1.1	290
0.03	121	0.7	99
0.09	21	2.4	1230
0.09	51	2.6	742
0.09	121	1.1	171
0.3	21	4.7	2550
0.2	51	2.9	937
0.2	121	2.3	340
0.5	21	8.2	5120
0.5	51	3.3	1170
0.5	121	2.6	407

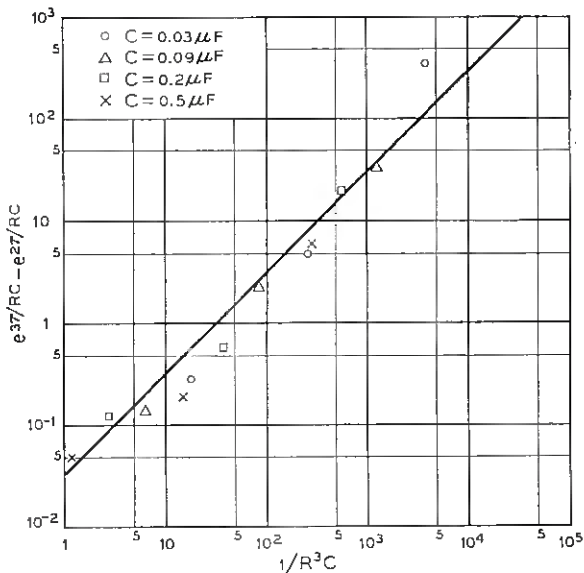


Fig. 5 — Plot of experimental values of welding time  $\tau$  for gold electrodes and various  $RC$  circuits, affording confirmation of (3) ( $V = 170$  volts,  $v = 12$  volts).

sults. It remains now to compare the values of the factor  $G$  obtained experimentally with its computed value,  $G = 2KT_B A/v$ .

From Ref. 4 we may obtain  $A = 0.05$  cm/joule<sup>1/3</sup> for gold. Combining this with  $K = 2.9$  watts/cm°C,  $T_B = 2600^\circ\text{C}$  and  $v = 12$  volts, we obtain  $G = 62$ . This is to be compared with  $G = 41$  obtained from arcs on the discharge of  $RC$  circuits, and with  $G = 61$  obtained from the experiments with long cables.

All the evidence supports the theory for the welding time which has just been presented. The agreement is better than one might expect, considering that all the experiments were performed with rough electrodes and that the theory does not take this into account. In addition, we have used the empirical expression  $d = AE^{1/3}$  for the arc diameter, and certainly this must hold only for short-duration arcs for which conduction losses are inappreciable.

### III. APPLICATIONS

#### 3.1 Contact Erosion

In early work on the erosion of relay contacts on closure, it was observed that the volume of metal transferred per unit of available arc

energy was constant. These experiments were carried out by discharging a small capacitor, which was connected to the contacts by short lead wires. When resistance was inserted between the contacts and the capacitor, the results were not so simple. Fig. 6 is a reproduction of a curve from Fig. 4 of Ref. 5, and shows clearly the effect of introducing the resistance in series with the capacitor. The previous explanation ascribed the reduction in erosion to a reduced circuit current. This is substantially correct; what we are concerned with here is deducing why the reduction in circuit current is of importance.

In a previous section it was shown that the contacts weld together at the end of the arc, the end being brought about by the power input becoming too low to maintain the necessary supply of ions. Once the weld occurs, the remainder of the source energy is dissipated in the resistance of the circuit and does not result in further damage to the electrodes.

The analysis given earlier for the time to weld in a constant current circuit, or an  $RC$  circuit, can be applied directly to the case of contact erosion if it is assumed that the erosion is proportional to the energy dissipated in the arc. For the short arc, the potential across the arc remains constant and the dissipated energy is simply  $E = Qv$ , where  $Q$  is the charge passed through the arc and  $v$  the arc voltage.

In an  $RC$  discharge the maximum energy which can be dissipated in the arc is  $E_0 = C(V_0 - v)v$ . The actual energy dissipated, because of

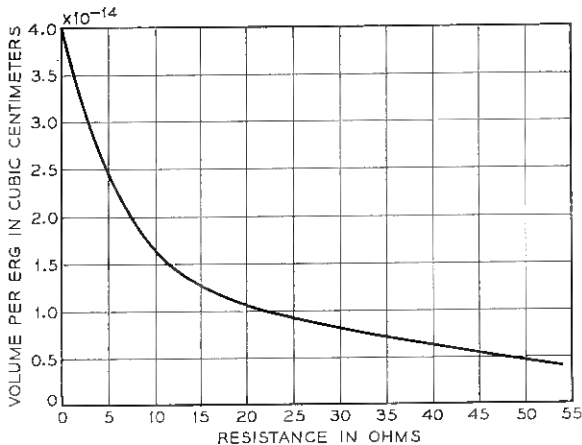


Fig. 6 — Metal transferred at the discharge of a capacitor, as a function of circuit resistance.

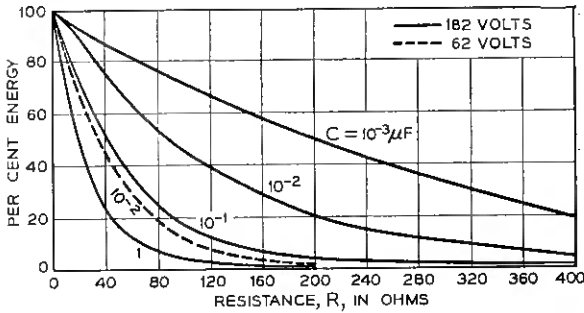


Fig. 7 — Arc energy  $E$  in various  $RC$  circuits, for gold electrodes.

early extinction, is only  $E = C(V_0 - v)v [1 - \exp(-\tau/RC)]$ . By eliminating  $\tau$  between this expression and (3) we obtain,

$$(E/E_0)/(1 - E/E_0)^3 = (V_0 - v)^2/G^3R^3Cv. \tag{4}$$

For the transmission line case, the corresponding formula is

$$E/E_0 = I^2/G^3Tv, \tag{5}$$

where  $T$  is the discharge time of the line. Curves calculated from (4) for gold are plotted in Fig. 7.

Recently Germer has published erosion measurements for silver electrodes that discharged either a capacitor through a resistor or a transmission line.<sup>6</sup> Some of these measurements (Fig. 6 of Ref. 7) are reproduced here as Fig. 8 and serve as further confirmation of the above theory. The plotted points represent measurements and the heavy line the predicted behavior from (4) and (5). The agreement is better than the theory warrants, since the theoretical curves depend quite strongly on some parameters, such as the thermal conductivity at high temperatures, which are not precisely known.

The most interesting region of the erosion curves is near 1 ampere, where the erosion decreases rapidly to zero. Such a region is common, and the magnitude of the current at which it occurs is known as the minimum arc current. The theory presented here predicts the erosion behavior in this region, and that the minimum arc current is not a fixed value but depends upon the energy already dissipated in the arc. In the next section on percussion welding it will be shown that, for large dissipated energies, the arc may fail at currents as large as several hundred amperes. The minimum arc current is a property of both the contact materials and also of the circuit parameters.

The strong impression of a constant minimum arc current in the past

is largely because the total energy which will be dissipated in the contacts is very strongly dependent on the circuit current.\* For instance, from (5) for a constant-current circuit, the energy dissipated at the contacts is  $E = (I/G)^2$ . This same relationship holds for an  $RC$  circuit if  $C$  and  $R$  are quite large, since this circuit then approaches a constant-current circuit. Now, for a particular relay contact application, there is a rather narrow range of energies which, if dissipated per operation, will be just tolerable. Energies greatly above this value will lead to too short a contact life, whereas energies greatly below this value will appear to give negligible contact erosion.

### 3.2 Percussion Welding

In percussion welding the surfaces to be joined are melted by an arc discharging a large capacitor, and they are then brought together before they have solidified. After contact, the molten zone solidifies and the weld is complete.<sup>7</sup>

In the previous sections of this paper we have discussed a welding phenomenon which takes place when the arc is extinguished. This weld is caused by molten metal bridging the gap and solidifying, creating a weld of small cross sectional area. One would expect this weld to be weak, and this has been verified by unpublished work of P. Kisliuk and J.

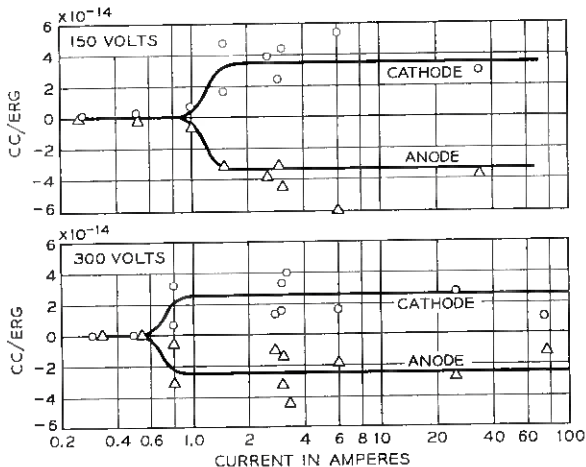


Fig. 8 — Calculated erosion per unit of available energy as a function of current (solid lines) and comparison with experimental values.

\* As pointed out earlier in this paper, all these considerations apply only to "clean" electrodes, where anode arcs predominate.

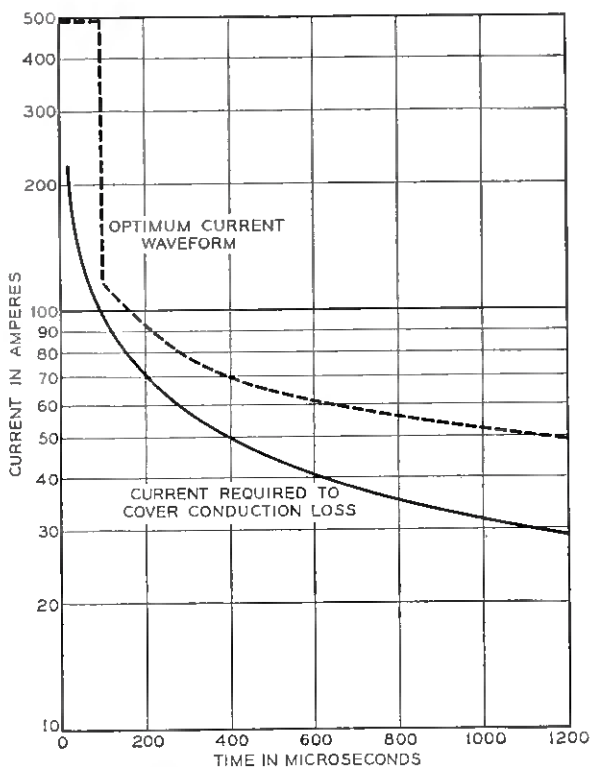


Fig. 9 — Calculated current required for percussion welding a 0.05 cm diameter copper wire to a copper plate.

Ammons. A much larger area and consequently stronger weld is obtained if the surfaces are held at the melting point until mechanical closure of the electrodes takes place. It is easy to show that the expected solidification time of the molten film is so short that this condition requires the arc to be maintained until the time of mechanical closure. It is required also that the arc power at all times exceed the rate of loss of energy by thermal conduction.

For calculating the conduction losses, the model is necessarily different from that used for the conduction-loss calculations made earlier. Let us consider the particular case of joining the end of a cylindrical wire to a flat surface. For welding, it is desirable to have the entire end of the wire held above the melting point, but in a short arc the surface will, in fact, be held more nearly at the boiling point. Radiation losses from the wire are negligible, so that, at least for a model of a right

circular cylinder opposed to a thick plate, we have one-dimensional heat flow. The power loss by thermal conduction is  $P_t = KT_B a/\pi kt$ , where  $K$  is the thermal conductivity,  $a$  is the area of the electrode,  $k$  is the diffusivity, and  $t$  is the time.

For the long-duration arcs ( $\sim 10^{-4}$  sec) with which we are concerned here, the power input is divided between the two electrodes. Assuming the division to be even, the power delivered by the arc to each electrode is  $Iv/2$ . The current needed to supply power equal to the conduction loss is then

$$I = 2KT_B a/\pi ktv. \quad (6)$$

Fig. 9 is a plot of  $I$  versus  $t$  from this equation, for a copper electrode of 0.05-cm diameter. For a satisfactory weld the current should exceed by only a small factor that needed to supply the energy lost by conduction for the entire time of the arc.

In Fig. 10 are shown oscilloscope traces of the currents for three test welds, with different values of the current waveform obtained in each case from an  $RC$  circuit in parallel with a simulated transmission line.

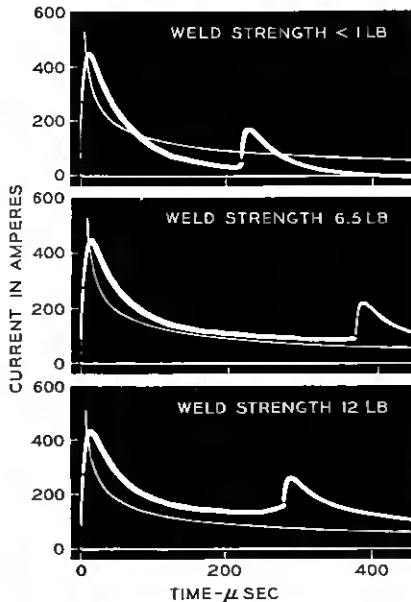


Fig. 10 — Oscilloscope traces of current for three experimental welds, with calculated values of the current required for a sound weld plotted upon each trace and strengths of the welds found in destructive tests.

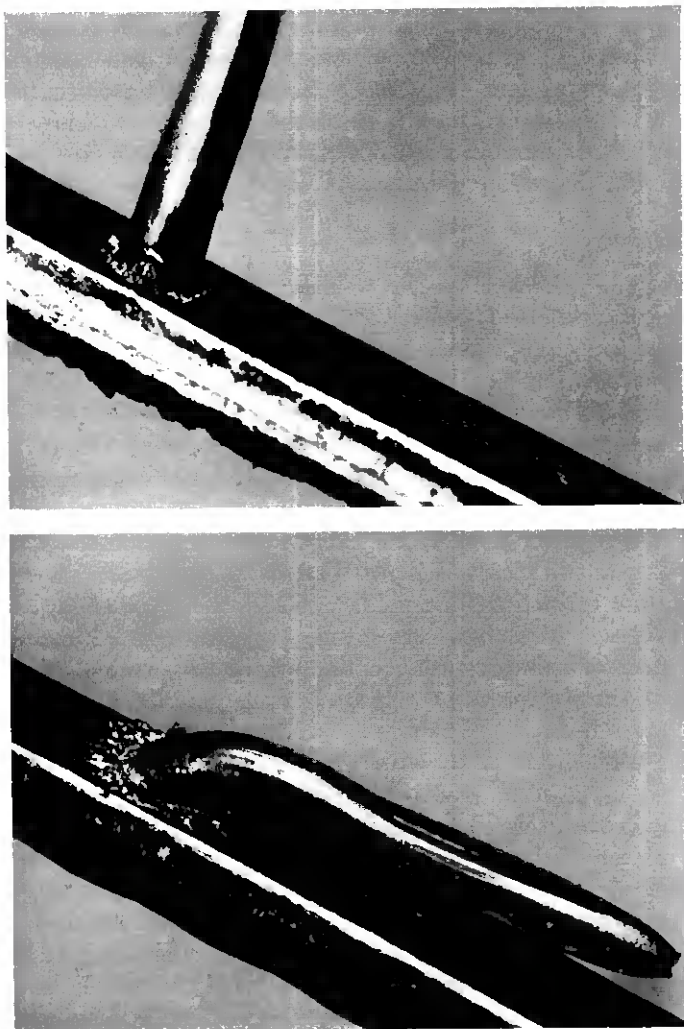


Fig. 11 — Photographs of sound welds, as made (top) and after a destructive test in which the wire broke (bottom).

The second peak on each trace is the sudden increase of current just as the contacts touch. Superposed on each trace is the calculated curve representing the current required to maintain the end of the wire at the boiling point. For each weld the breaking strength was measured by holding the large block fixed (Fig. 11) and pulling the wire with a force parallel to the surface of the block. The breaking strength of the wire

was approximately 12 pounds. From the experimental breaking strengths written down underneath the oscilloscope traces, it can be noted that the strength was that of the wire only in the case where the current was maintained for the entire time until the electrodes touched, and at values well above those which, from calculation, would maintain the end of the wire at the boiling point.

#### IV. CONCLUSION

A theory which explains the welding phenomenon associated with short arcs of the anode type has been presented, along with experimental evidence of the validity of the theory. The theory is based on the simple assumption that a molten pool of metal remains on the anode until the arc is extinguished. At the instant the arc is extinguished, the redistribution of the electric field creates a force at the anode, pulling the molten metal from the anode towards the cathode and bridging the gap.

Extinction of the arc is due to insufficient power being supplied from the external circuitry to overcome thermal conduction losses away from the growing anode pit. It is shown that excellent agreement exists between an arc extinction time predicated simply on the conduction loss basis and measured times at which bridging of the gap takes place.

The effect of this premature extinction of the arc and subsequent welding of the electrodes on the erosion characteristics has been predicted for both an *RC* circuit and a constant-current circuit, and excellent agreement has been obtained with Germer's published measurements.

For anode arcs, this effect determines the minimum arc current. The theory yields a minimum arc current for gold electrodes near 0.5 ampere, for circuits which are in common use in the telephone plant.

The theory has been used also to calculate the optimum current waveform for percussion welding, where it is of fundamental importance that the electrode be maintained molten immediately up until the time of mechanical closure. Welding experiments to test the theory have shown the quality of the weld to be in excellent agreement with predictions made from the current waveform.

#### REFERENCES

1. Germer, L. H. and Boyle, W. S., *J. Appl. Phys.*, **27**, 1956, p. 32.
2. Germer, L. H. and Smith, J. L., *J. Appl. Phys.*, **23**, 1952, p. 553.
3. Kisliuk, P., *J. Appl. Phys.*, **25**, 1954, p. 897.
4. Boyle, W. S. and Germer, L. H., *J. Appl. Phys.*, **26**, 1955, p. 571.
5. Germer, L. H. and Haworth, F. E., *J. Appl. Phys.*, **20**, 1949, p. 1085.
6. Germer, L. H., *J. Appl. Phys.*, **29**, 1958, p. 1067.
7. Quinlan, A. L., *B.S.T.J.*, **33**, 1954, p. 897.

# A Method of Computing Bivariate Normal Probabilities

## With an Application to Handling Errors in Testing and Measuring

By D. B. OWEN\* and J. M. WIESEN\*

(Manuscript received August 20, 1958)

*Charts and formulas are presented from which bivariate normal probabilities may be computed. Formulas involving the bivariate normal are given for the solution of a problem of handling errors in testing and measuring. These formulas include, in addition to previously published cases, two new cases. In one, the product is not necessarily centered relative to two-sided specification limits; in the other, one-sided specification limits are considered.*

### I. INTRODUCTION

Many manufactured products are 100 per cent tested with the idea of insuring that each unit of product meets the performance specifications. The general procedure is to set the test specification limits, which are the limits used for product unit acceptance, at or arbitrarily near the performance specification limits. These are established by engineering requirements and require a test-set accuracy and precision of a specified amount with respect to the performance specification limits or some nominal value. Eagle<sup>1</sup> and many others have studied the problem of locating test specification limits with respect to performance specification limits under various conditions of test-set precision when testing itself is subject to random error. He pointed out that, when random errors of testing exist, two types of errors or mistakes can occur which should be taken into account in setting test specification limits. The first error, called consumer's loss (CL), is defined as the probability that nonconforming product units will be accepted. The second error, called pro-

---

\* Sandia Corporation, Albuquerque, N. M.

ducer's loss (PL),\* is defined as the probability that conforming product units will be rejected.

The problem of locating test specification limits with respect to performance specification limits may be considered heuristically as in Fig. 1, where A and D are performance specification limits, and B and C are test specification limits. Consider a product unit which just fails to meet the lower performance specification limit and therefore is nonconforming and should not be accepted. The chance that a product unit of this value will be accepted by the test set is shown by the shaded area under the test-set-error distribution curve to the right of B, the lower test specification limit. This then is a part of the consumer's loss (CL), and the summation of similar considerations for all product units outside the performance specification limits constitutes the CL. Consider now a product unit with value at c, well within the performance specification limits, which should be accepted. The shaded area under the test-set-error distribution curve to the right of c, the upper test specification limit, shows that there is a 50 per cent chance of the test set rejecting a product unit of this value, and thus this is a part of the producer's loss (PL). The summation of similar considerations for all product units inside the performance specification limits constitutes PL. Different settings of the test specification limits, B and C, with respect to the performance specification limits, A and D, and/or different spreads (standard deviations) of the product and test-set distributions would lead to different producer's and consumer's losses.

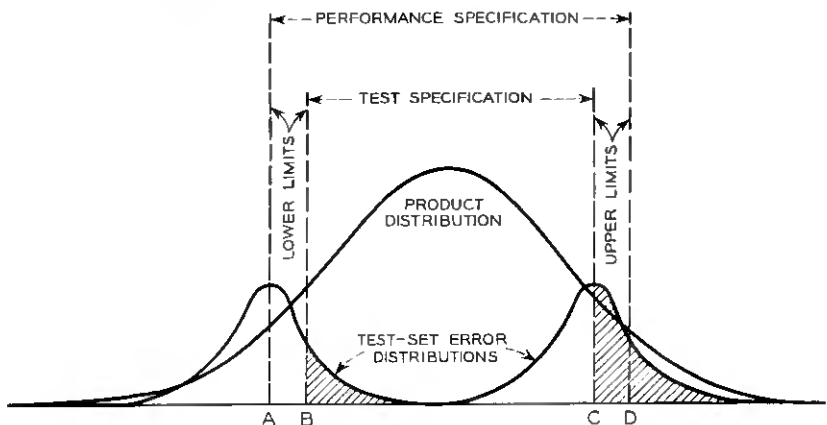


Fig. 1 — Diagram showing effect of test-set errors on test acceptance limits.

\* Consumer's loss and producer's loss are called consumer's risk and producer's risk by Grubbs and Coon<sup>2</sup> and others. The terminology used here is an effort to avoid confusion with present standard statistical quality control terminology.

Eagle presented graphs of PL and CL which assume that the product distribution and test-set-error distribution are both normal (Gaussian) and also that the mean of the product distribution is midway between the performance specification limits and also midway between the test specification limits. Thus, these two sets of limits are symmetrical with respect to the mean of the product distribution. He also presented formulas based on Pearson's tables<sup>3</sup> for computing PL and CL. Pearson's tables are now out of print and are not readily available to many who may wish to make these calculations. However, the National Bureau of Standards<sup>4</sup> plans to reissue Pearson's tables with some extensions.

Hayes<sup>5</sup> and Wiesen and Clark<sup>6</sup> have presented additional graphs of PL and CL for the same conditions as those considered by Eagle. In the present paper, the solution is given in formula form without the product distribution centering requirement. Also, one-sided test and performance specification limits are considered.

Grubbs and Coon<sup>2</sup> also considered the problem of setting the performance and test specification limits for a centered product distribution. They found the locations which minimized the sum CL plus PL, and also the locations which minimized total cost when the consumer's loss was subject to a given cost and the producer's loss subject to another cost. In this paper, formulas are given for the same cost assumptions, but for both one-sided and not necessarily centered two-sided performance and test specification limits.

Tingey and Merrill<sup>7</sup> considered the problem of minimizing the total cost when the cost to the consumer of accepting nonconforming product units varied with the degree of nonconformance. They presented a table of constants for constructing test specification limits under these circumstances. Formulas (20) and (21) are given below for computing the total cost under these assumptions.

Eagle<sup>1</sup> and Owen<sup>8,9</sup> showed that the bivariate normal distribution underlies the above problems. Consequently, a method for computing bivariate normal probabilities is first considered here. Although this method is discussed relative to the present problem, the method is perfectly general and can be used wherever bivariate normal probabilities are required.

## II. COMPUTATION OF BIVARIATE NORMAL PROBABILITIES FROM THE CHARTS

Let

$$M(h, k; \rho) = \frac{1}{2\pi\sqrt{1-\rho^2}} \int_h^\infty \int_k^\infty \exp\left[-\frac{1}{2}\left(\frac{x^2 - 2\rho xy + y^2}{1-\rho^2}\right)\right] dx dy. \quad (1)$$

$M(h, k; \rho)$  is the probability that a normal random variable  $X$  with

mean zero and variance one is greater than  $h$ , and another normal random variable  $Y$  with mean zero and variance one is greater than  $k$ , where  $\rho$  is the correlation between  $X$  and  $Y$ ; that is,  $\Pr(X > h, Y > k) = M(h, k; \rho)$ .

It is convenient also to have a functional notation for the univariate normal integral. To this end, define

$$G(h) = \frac{1}{\sqrt{2\pi}} \int_{-\infty}^h \exp\left(-\frac{x^2}{2}\right) dx.$$

Volumes of the bivariate normal over other rectangular regions may be expressed in terms of the  $M$ - and  $G$ -functions. In terms of standardized variables (zero means and unit variances),

$$\begin{aligned} \Pr(X < h, Y < k) &= M(-h, -k; \rho) \\ &= G(h) + G(k) + M(h, k; \rho) - 1, \end{aligned} \quad (2)$$

$$\begin{aligned} \Pr(X < h, Y > k) &= M(-h, k; -\rho) = G(-k) - M(h, k; \rho) \\ &= G(h) - M(-h, -k; \rho) \end{aligned} \quad (3)$$

$$\begin{aligned} \Pr(X > h, Y < k) &= M(h, -k; -\rho) = G(-h) - M(h, k; \rho) \\ &= G(k) - M(-h, -k; \rho). \end{aligned} \quad (4)$$

Ref. 8, which is an elaboration of Ref. 9, shows that

$$\begin{aligned} M(h, k; \rho) &= M\left(h, 0; \frac{(\rho h - k)(\text{sgn } h)}{\sqrt{h^2 - 2\rho hk + k^2}}\right) \\ &\quad + M\left(k, 0; \frac{(\rho k - h)(\text{sgn } k)}{\sqrt{h^2 - 2\rho hk + k^2}}\right) - \begin{cases} 0 \\ \frac{1}{2} \end{cases}, \end{aligned} \quad (5)$$

where the upper choice is made if  $hk > 0$  or if  $hk = 0$  but  $h + k \geq 0$ , and the lower choice is made otherwise; and  $\text{sgn } h = +1$  if  $h \geq 0$ , and  $\text{sgn } h = -1$  if  $h < 0$ . Note that  $\text{sgn } h$  as used in (5) is a multiplicative factor; i.e., it affects the sign of the quantity it operates on but not the absolute value of the quantity.

Equation (5) means that bivariate normal probabilities with any limits can be computed from a table of the bivariate normal probabilities where one of the limits is zero. Figs. 2 through 5 are graphs of these probabilities, i.e., of  $M(h, 0; \rho)$ . Figs. 4 and 5 can be obtained by rotating Figs. 2 and 3, respectively, 180 degrees and replacing  $h$  by  $-h$  and  $\rho$  by  $-\rho$ . However, to avoid confusion both figures are included. The following examples illustrate the use of these graphs.

*Example 1:* The following probabilities may be read from Figs. 2 through 5:

$$\begin{aligned}M(1, 0; 0.5) &= 0.127, \\M(1, 0; -0.5) &= 0.031, \\M(-1, 0; 0.5) &= 0.469, \\M(-1, 0; -0.5) &= 0.373.\end{aligned}$$

*Example 2:* Find  $M(1.96, 1; 0.56)$ .

*Solution:*

$$\begin{aligned}\sqrt{h^2 - 2\rho hk + k^2} &= \sqrt{2.6464} = 1.6268. \\M(1.96, 1; 0.56) &= M(1.96, 0; 0.060) + M(1, 0; -0.861) \\&= 0.014 + 0.002 \\&= 0.016.\end{aligned}$$

The value computed by more elaborate methods<sup>8,9</sup> is 0.016.

*Example 3:* Find  $M(0.4, 0.1; -0.5)$ .

*Solution:*

$$\begin{aligned}\sqrt{h^2 - 2\rho hk + k^2} &= \sqrt{21}. \\M(0.4, 0.1; -0.5) &= M(0.4, 0; -0.655) + M(0.1, 0; -0.982) \\&= 0.069 + 0.015 \\&= 0.084.\end{aligned}$$

The value read from Pearson's tables<sup>3</sup> is 0.0836.

*Example 4:* Find  $M(1, -2; 0.7)$ .

*Solution:*

$$\begin{aligned}\sqrt{h^2 - 2\rho hk + k^2} &= 2.793. \\M(1, -2; 0.7) &= M(1, 0; 0.967) + M(-2, 0; 0.859) - \frac{1}{2} \\&= 0.159 + 0.500 - 0.500 \\&= 0.159.\end{aligned}$$

The value computed from Pearson's tables<sup>3</sup> is 0.1587.

*Example 5:* Find  $M(1, -2; -0.5)$ .

*Solution:*

$$\begin{aligned}\sqrt{h^2 - 2\rho hk + k^2} &= 1.732. \\M(1, -2; -0.5) &= M(1, 0; 0.866) + M(-2, 0; 0) - \frac{1}{2} \\&= 0.157 + 0.489 - 0.500 \\&= 0.146.\end{aligned}$$

The value computed from Pearson's tables<sup>3</sup> is 0.1454.

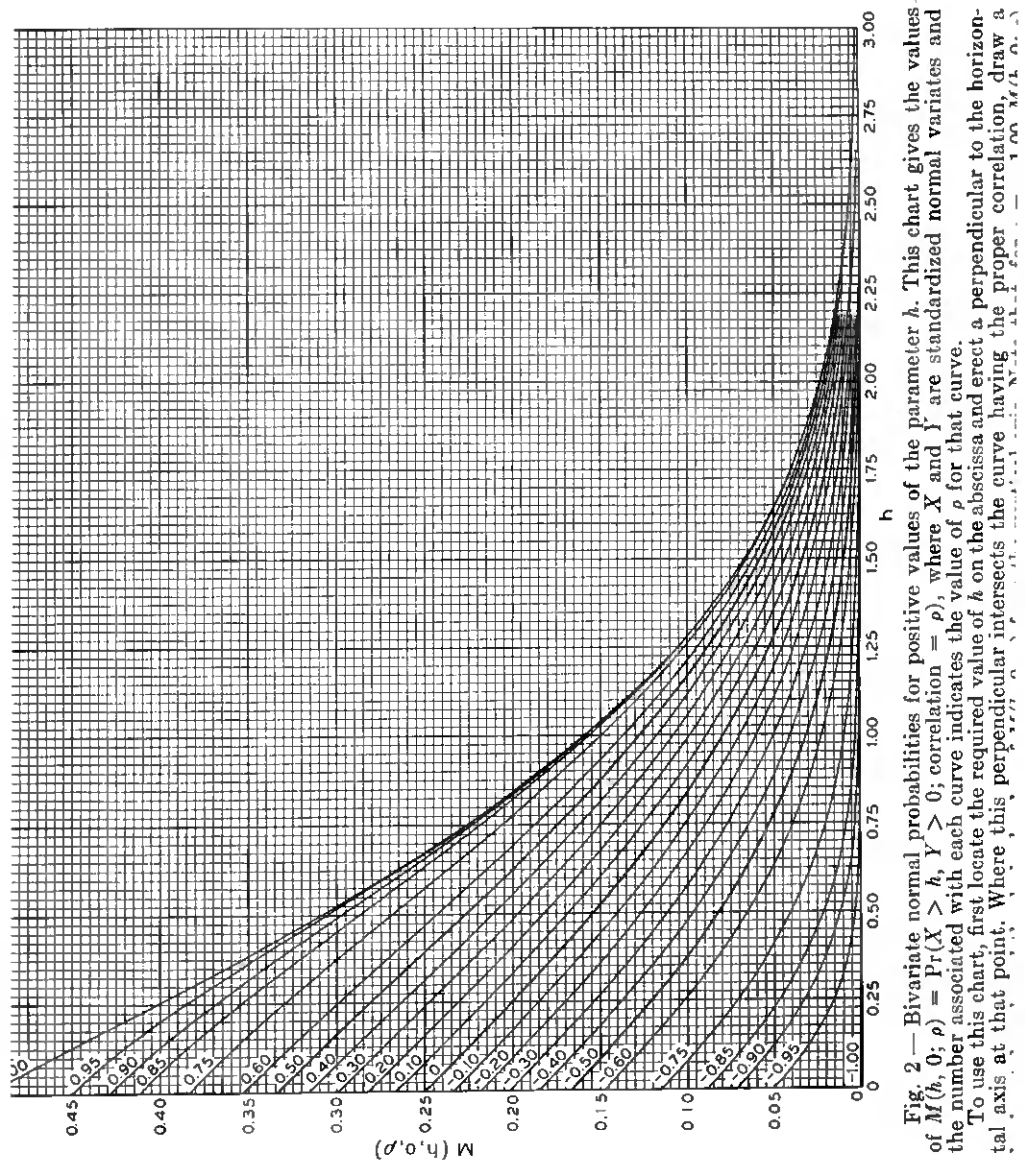


Fig. 2 — Bivariate normal probabilities for positive values of the parameter  $h$ . This chart gives the values of  $M(h, 0; \rho) = \Pr(X > h, Y > 0; \text{correlation} = \rho)$ , where  $X$  and  $Y$  are standardized normal variates and the number associated with each curve indicates the value of  $\rho$  for that curve. To use this chart, first locate the required value of  $h$  on the abscissa and erect a perpendicular to the horizontal axis at that point. Where this perpendicular intersects the curve having the proper correlation, draw a

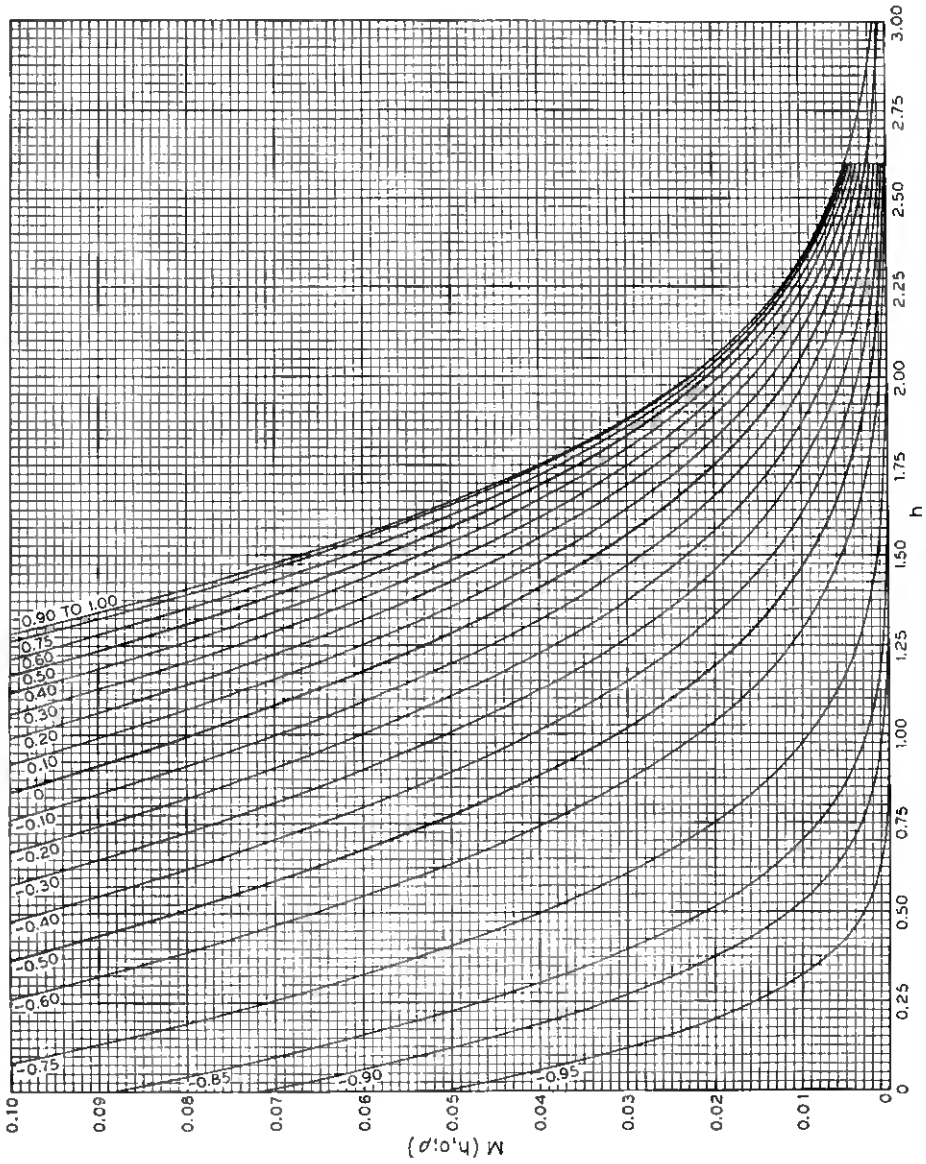


Fig. 3 — Bivariate normal probabilities for positive values of the parameter  $h$  and for values of  $M(h, 0; \rho)$  from 0 to 0.10.

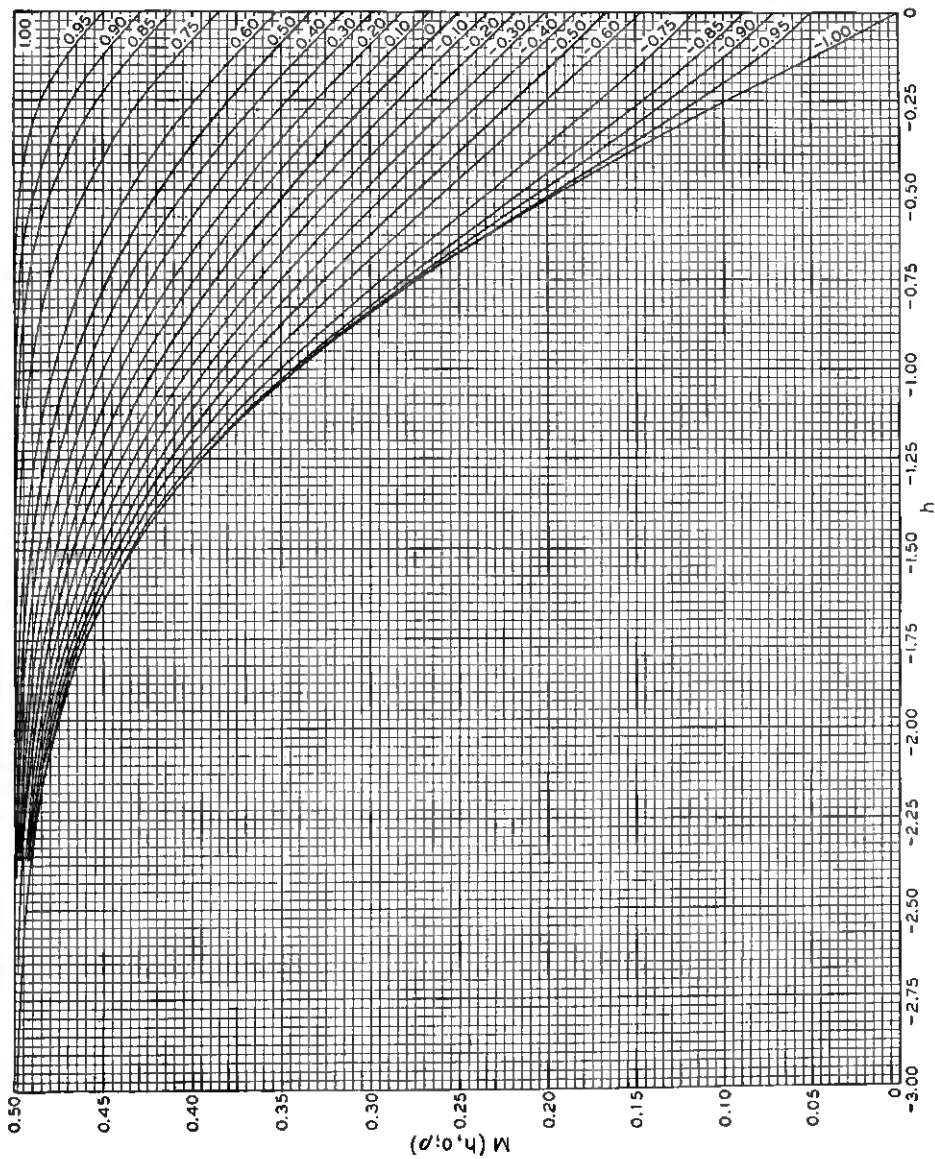


Fig. 4—Bivariate normal probabilities for negative values of the parameter  $h$ . Note that, for  $\rho = 1.00$ ,  $M(h, 0; 0) = 0.50$  for positive values of  $h$ . Values of  $M(h, 0; 0)$  between 0.40 and 0.50 were taken from Table 1.

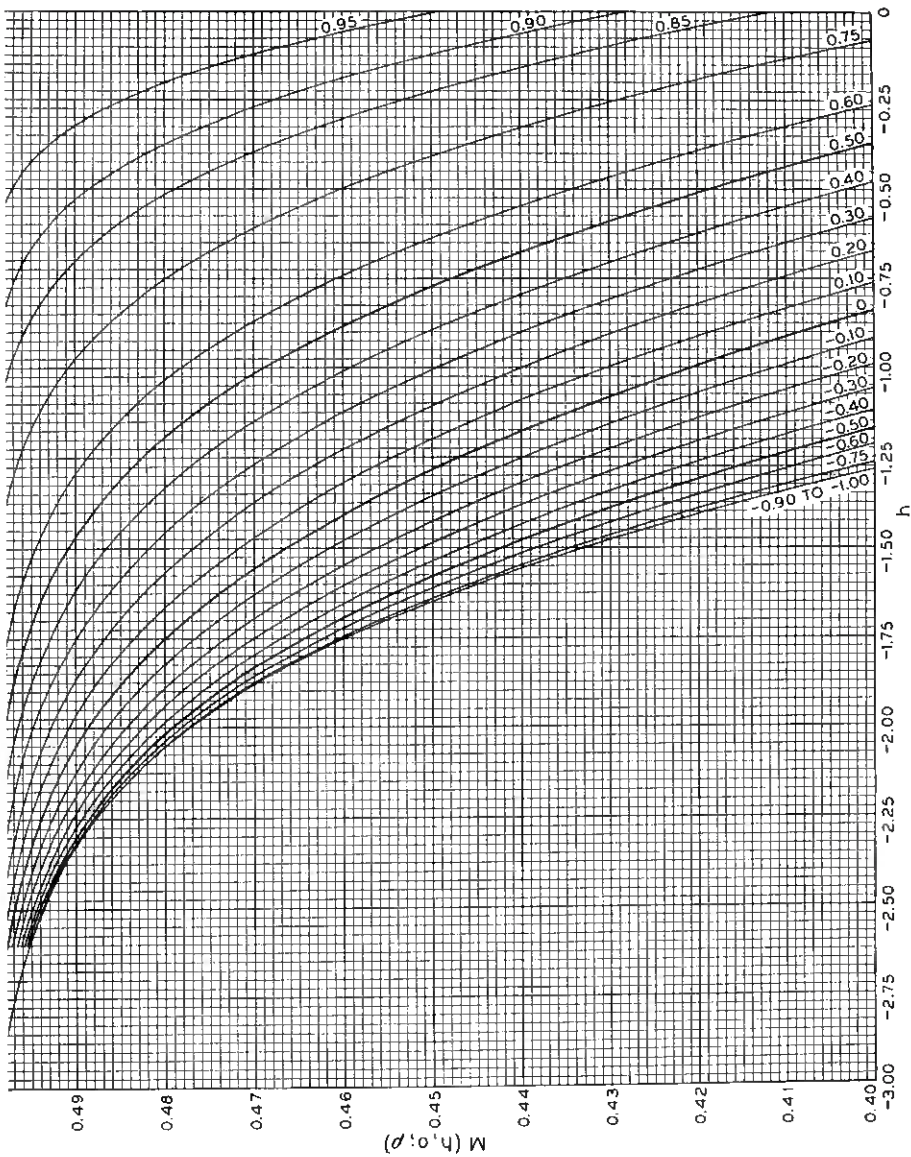


Fig. 5 — Bivariate normal probabilities for negative values of the parameter  $h$  and for values of  $M(h, 0; \rho)$  from 0.40 to 0.50.

## III. ERRORS IN TESTING AND MEASURING

Before giving the formulas for the problem of errors in testing and measuring, let the following quantities be defined.

Let  $P$  = a random variable (normally distributed with mean  $\mu$  and standard deviation  $\sigma_p$ ) which describes the true product values.

Let  $T$  = a random error of measurement (test-set error) normally distributed with mean  $\lambda$  and standard deviation  $\sigma_t$ .

The term  $\lambda$  is called the bias of the measuring instrument. In Refs. 1, 2, 5 and 6,  $\lambda$  was taken to be equal to zero. This is not necessary, as only a slight change in the definition of the test specification limits takes care of this. (See the definition of  $b_1$  and  $b_2$  below.) Of course, in most cases where  $\lambda$  is known, the test instrument would be recalibrated and the bias eliminated. There may be situations, however, where this would not be practical and it really is no problem to carry  $\lambda$  as an extra parameter. Also, in assessing the problem of an unknown bias, it is convenient to have the parameter  $\lambda$  available (see Example 8 below).

Let  $S$  = the observed measurement =  $P + T$ , so that, if  $T$  and  $P$  are taken to be independent,  $S$  is normal with mean  $\mu + \lambda$  and variance  $\sigma_s^2 = \sigma_p^2 + \sigma_t^2$ . Also,  $P$  and  $S$  are correlated, and it will be shown that the correlation is equal to  $\sigma_p/\sigma_s$ .

The expectation or mean of a random variable  $X$  is indicated symbolically by  $E(X)$ . The correlation between two variables  $X$  and  $Y$  is defined as

$$\frac{E[(X - \mu_x)(Y - \mu_y)]}{\sigma_x \sigma_y}$$

For  $P$  and  $S$ , then, the numerator of the correlation is

$$\begin{aligned} E[(P - \mu)(S - \mu - \lambda)] \\ &= E[(P - \mu)(P + T - \mu - \lambda)] \\ &= E[P^2 + PT - P\mu - P\lambda - \mu P - \mu T + \mu^2 + \mu\lambda]. \end{aligned}$$

Now,  $E(X^2) = \sigma_x^2 + \mu^2$ ;  $E(\text{constant}) = \text{constant}$ ;  $E(XY) = E(X)E(Y)$ , if  $X$  and  $Y$  are independent;  $E(X + Y) = E(X) + E(Y)$  and  $E(X) = \mu_x$ . The correlation between  $P$  and  $S$  is then

$$\rho_{ps} = \frac{\sigma_p^2 + \mu^2 + \mu\lambda - \mu^2 - \mu\lambda - \mu^2 - \mu\lambda + \mu^2 + \mu\lambda}{\sigma_p \sigma_s} = \frac{\sigma_p}{\sigma_s}$$

Let  $k_1$  and  $k_2$  be defined so that the performance specification limits are at  $\mu + k_1\sigma_p$  and  $\mu - k_2\sigma_p$ . For a lower performance specification limit only, take  $k_1 = \infty$ ; and for an upper performance specification

limit only, take  $k_2 = \infty$ . In Refs. 1, 2, 5 and 6, the  $k$ 's were taken to be equal which meant the product distribution was assumed to be centered with respect to the performance specification limits.

Let  $b_1$  and  $b_2$  be defined so that, when the test specification limits are placed at  $\mu + \lambda + k_1\sigma_p - b_1\sigma_t$  and at  $\mu + \lambda - k_2\sigma_p + b_2\sigma_t$ , either a desired consumer's loss or a desired producer's loss is not exceeded, or some combination of these losses is not exceeded.

In this paper,  $\mu$ ,  $\lambda$ ,  $\sigma_p$  and  $\sigma_t$  are assumed to be known. When any of them are unknown, experiments must be run to establish their values. In this connection, the reader may wish to read a paper by Grubbs,<sup>10</sup> which gives methods for estimating  $\sigma_p$  and  $\sigma_t$  when the variance of each observation is a linear function of  $\sigma_p^2$  and  $\sigma_t^2$ . Fig. 6 shows diagrammatically the relationship between  $\mu$ ,  $\lambda$ ,  $\sigma_p$ ,  $\sigma_t$ ,  $b_1$ ,  $b_2$ ,  $k_1$  and  $k_2$ .

- $\mu$  = MEAN OF PRODUCT DISTRIBUTION
- $\sigma_p$  = STANDARD DEVIATION OF PRODUCT DISTRIBUTION
- $\sigma_t$  = STANDARD DEVIATION OF TEST-SET ERROR DISTRIBUTION
- $\lambda$  = TEST-SET BIAS

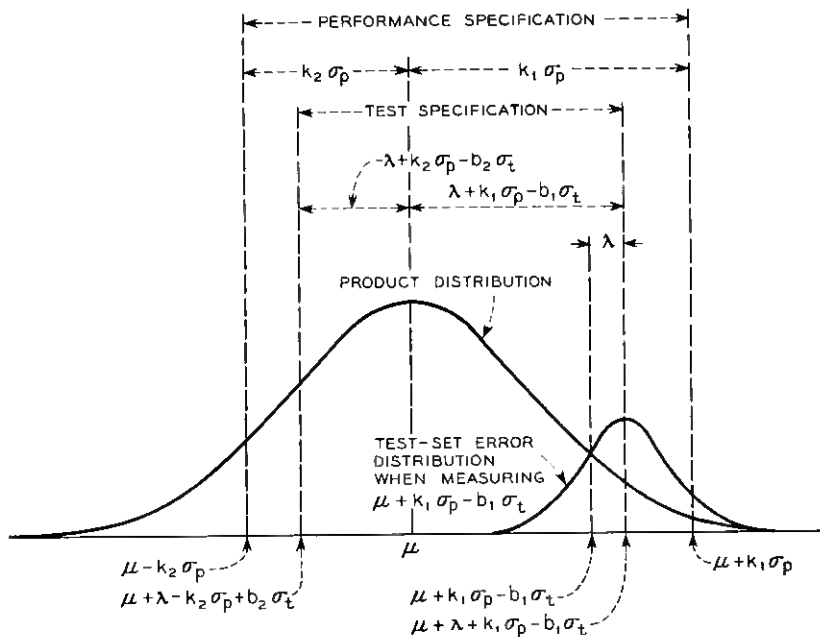


Fig. 6 — Diagram showing various constants defined for errors in the testing-and-measuring problem.

From the definition of consumer's loss (CL) it is clear that

$$\begin{aligned} \text{CL} = \Pr[P > \mu + k_1\sigma_p \text{ or } P < \mu - k_2\sigma_p \\ \text{and } \mu + \lambda - (k_2\sigma_p - b_2\sigma_t) < S < \mu + \lambda + (k_1\sigma_p - b_1\sigma_t)]. \end{aligned} \quad (6)$$

Since the correlation between  $P$  and  $S$  is given by

$$\rho_{ps} = \rho = \sigma_p/\sigma_s = \sigma_p/\sqrt{\sigma_p^2 + \sigma_t^2},$$

and  $P$  and  $S$  are assumed to be bivariate normal, the above probability can be expressed in terms of the  $M$ -function. The first step, as with the univariate normal, is to standardize the variables, i.e., subtract the mean and divide by the standard deviation. In order to save space and give compact formulas, additional notation is introduced. Let

$$q_1 = \frac{k_1\sigma_p - b_1\sigma_t}{\sqrt{\sigma_p^2 + \sigma_t^2}} \quad \text{and} \quad q_2 = \frac{k_2\sigma_p - b_2\sigma_t}{\sqrt{\sigma_p^2 + \sigma_t^2}}.$$

Then,

$$\begin{aligned} \text{CL} = \Pr\left(\frac{P - \mu}{\sigma_p} > k_1 \quad \text{or} \quad \frac{P - \mu}{\sigma_p} < -k_2 \right. \\ \left. \text{and } -q_2 < \frac{S - \mu - \lambda}{\sigma_s} < q_1\right) \\ = \Pr\left(\frac{P - \mu}{\sigma_p} > k_1 \quad \text{and} \quad \frac{S - \mu - \lambda}{\sigma_s} > -q_2\right) \\ - \Pr\left(\frac{P - \mu}{\sigma_p} > k_1 \quad \text{and} \quad \frac{S - \mu - \lambda}{\sigma_s} > q_1\right) \\ + \Pr\left(\frac{P - \mu}{\sigma_p} < -k_2 \quad \text{and} \quad \frac{S - \mu - \lambda}{\sigma_s} > -q_2\right) \\ - \Pr\left(\frac{P - \mu}{\sigma_p} < -k_2 \quad \text{and} \quad \frac{S - \mu - \lambda}{\sigma_s} > q_1\right). \end{aligned}$$

Now (2), (3) and (5) are used to reduce CL to its most easily used form:

$$\begin{aligned} \text{CL} = M(k_1, -q_2; \rho) - M(k_1, q_1; \rho) \\ - M(k_2, q_2; \rho) + M(k_2, -q_1; \rho). \end{aligned} \quad (7)$$

The producer's loss (PL) is given by

$$\begin{aligned} \text{PL} = \Pr[\mu - k_2\sigma_p < P < \mu + k_1\sigma_p \quad \text{and} \\ S < \mu + \lambda - (k_2\sigma_p - b_2\sigma_t) \quad \text{or} \quad S > \mu + \lambda + (k_1\sigma_p - b_1\sigma_t)]. \end{aligned} \quad (8)$$

If the same procedure as that with consumer's loss is followed, it can be shown that (8) reduces to

$$PL = CL + G(k_1) + G(k_2) - G(q_1) - G(q_2). \tag{9}$$

For one-sided specification limits the above formulas reduce to:

*For an upper limit only:*

$$CL = \Pr(P > \mu + k_1\sigma_p \text{ and } S < \mu + \lambda + k_1\sigma_p - b_1\sigma_t);$$

hence

$$CL = G(-k_1) - M(k_1, q_1; \rho) \tag{10}$$

and

$$PL = \Pr(P < \mu + k_1\sigma_p \text{ and } S > \mu + \lambda + k_1\sigma_p - b_1\sigma_t);$$

and hence,

$$PL = G(-q_1) - M(k_1, q_1; \rho). \tag{11}$$

*For a lower limit only:*

$$CL = \Pr(P < \mu - k_2\sigma_p \text{ and } S > \mu + \lambda - k_2\sigma_p + b_2\sigma_t);$$

hence

$$CL = G(-k_2) - M(k_2, q_2; \rho) \tag{12}$$

and

$$PL = \Pr(P > \mu - k_2\sigma_p \text{ and } S < \mu + \lambda - k_2\sigma_p + b_2\sigma_t);$$

hence

$$PL = G(-q_2) - M(k_2, q_2; \rho). \tag{13}$$

The following examples illustrate the use of (7) through (13).

*Example 6:* Suppose the performance specification limits are at  $\mu + 2\sigma_p$  and at  $\mu - 3\sigma_p$ . Suppose also that the test specification limits have been set at  $\mu + \lambda + 2\sigma_p$  and at  $\mu + \lambda - 3\sigma_p + \sigma_t$ . If  $\sigma_t/\sigma_p = 0.5$ , determine the producer's and consumer's losses of this procedure. Since the bias is known in this example and has been allowed for in setting the test specification limits,  $\lambda$  does not appear in the calculations of PL and CL. (See example 8 for the case where  $\lambda$  is not known.)

*Solution:* Here,  $k_1 = 2$ ,  $k_2 = 3$ ,  $b_1 = 0$ , and  $b_2 = 1$ . Then,

$$q_1 = \frac{k_1\sigma_p - b_1\sigma_t}{\sqrt{\sigma_p^2 + \sigma_t^2}} = \frac{2 - 0}{\sqrt{1.25}} = 1.789,$$

$$q_2 = \frac{k_2\sigma_p - b_2\sigma_t}{\sqrt{\sigma_p^2 + \sigma_t^2}} = \frac{3 - 0.5}{\sqrt{1.25}} = 2.236$$

and

$$\rho = \frac{\sigma_p}{\sqrt{\sigma_p^2 + \sigma_t^2}} = \frac{1}{\sqrt{1.25}} = 0.894.$$

From (7),

$$\begin{aligned} \text{CL} = & M(2, -2.236; 0.894) - M(2, 1.789; 0.894) \\ & - M(3, 2.236; 0.894) + M(3, -1.789; 0.894). \end{aligned}$$

Application of (5) results in

$$\begin{aligned} \text{CL} = & M(2, 0; 0.976) + M(-2.236, 0; 0.970) - 0.5 - M(2, 0; 0) \\ & - M(1.789, 0; -0.447) - M(3, 0; 0.316) - M(2.236, 0; -0.707) \\ & + M(3, 0; 0.958) + M(-1.789, 0; 0.985) - 0.5 \\ = & 0.023 + 0.500 - 0.500 - 0.017 - 0.004 - 0.000 \\ & - 0.000 + 0.000 + 0.500 - 0.500 \\ = & 0.008. \end{aligned}$$

From (7),

$$\begin{aligned} \text{PL} = & 0.008 + G(2) + G(3) - G(1.789) - G(2.236) \\ = & 0.008 + 0.977 + 0.999 - 0.963 - 0.987 = 0.034. \end{aligned}$$

*Example 7:* The circumference of a product has a mean value of 28.5 inches with a standard deviation of 0.5 inch. Only circumferences less than 29 inches are acceptable. The device for measuring the circumference is known to be biased so that on the average it measures 0.1 inch too small with a standard deviation of 0.2 inch. If the upper test specification limit is set at 29 inches, and there is no lower limit, what are the producer's and consumer's losses?

*Solution:* Here,  $\mu = 28.5$ ,  $\sigma_p = 0.5$ ,  $\lambda = -0.1$  and  $\sigma_t = 0.2$ . Hence, for the performance specification limits,

$$\mu + k_1\sigma_p = 29,$$

or

$$28.5 + k_1(0.5) = 29.$$

Solving this equation results in  $k_1 = 1$ . For the test specification limits,

$$\mu + \lambda + k_1\sigma_p - b_1\sigma_t = 29,$$

or

$$28.5 - 0.1 + 1(0.5) - b_1(0.2) = 29.$$

Solving this equation results in  $b_1 = -0.5$ . Hence

$$q_1 = \frac{k_1\sigma_p - b_1\sigma_t}{\sqrt{\sigma_p^2 + \sigma_t^2}} = \frac{0.5 + 0.01}{\sqrt{0.29}} = 1.114,$$

and

$$\rho = \frac{\sigma_p}{\sqrt{\sigma_p^2 + \sigma_t^2}} = \frac{0.5}{\sqrt{0.29}} = 0.928.$$

From (10),

$$\begin{aligned} \text{CL} &= G(-1) - M(1, 1.114; 0.928) \\ &= 0.159 - M(1, 0; -0.447) - M(1.114, 0; 0.083) \\ &= 0.159 - 0.036 - 0.073 = 0.050. \end{aligned}$$

From (11),

$$\text{PL} = G(-1.114) - M(1, 1.114; 0.928) = 0.133 - 0.109 = 0.024.$$

Thus, for the measuring device considered here, the consumer's loss is 0.050 and the producer's loss is 0.024.

*Example 8:* If the bias  $\lambda$  is assumed to be zero when it is actually positive, the effect is to accept more products in the lower tail of the product distribution and to reject more in the upper tail. The effect on CL and PL is the same as if  $k_1\sigma_p$  had been decreased by  $\lambda$  and  $k_2\sigma_p$  increased by  $\lambda$ , i.e., as if both test specification limits had been decreased by the quantity  $\lambda$ .

As an example, the performance specification limits for a product are at  $\mu + k_1\sigma_p = 90$  and  $\mu - k_2\sigma_p = 80$ . Also,  $\mu = 85$ ,  $\sigma_t = 1$  and  $\sigma_p = 2$ . Then  $k_1 = k_2 = 2.5$ , and Table I of Grubbs and Coon<sup>2</sup> can be used to find  $b_1 = b_2$  so that the consumer and the producer accept equal losses. The table gives  $b_1 = b_2 = -0.5902$  and results in a consumer's loss and producer's loss each equal to 0.0061 or a total loss of 0.0122. Now suppose that the tester is biased one unit high, i.e.,  $\lambda = 1$ . What effect does this have on the producer's loss and the consumer's loss?

*Solution:* The test limits were set at

$$\mu + k_1\sigma_p - b_1\sigma_t = 90.5902$$

and

$$\mu - k_2\sigma_p + b_2\sigma_t = 79.4098,$$

whereas, if the bias had been taken into account, they should have been set at

$$\mu + \lambda + k_1\sigma_p - b_1\sigma_t = 91.5902$$

and

$$\mu + \lambda - k_2\sigma_p + b_2\sigma_t = 80.4098$$

to maintain the equality of PL and CL. To find the effect of this error, it is only necessary to decrease  $k_1\sigma_p$  by  $\lambda$ ; i.e., redefine  $k_1$  so that  $k_1\sigma_p = 5 - \lambda = 4$  and hence take  $k_1 = 2$ , and redefine  $k_2$  so that  $k_2\sigma_p = 5 + \lambda = 6$  and hence take  $k_2 = 3$ . Now the formulas for CL and PL [(7) and (9)] are used with the following parameters:

$$\begin{aligned} k_1 &= 2, & k_2 &= 3, \\ b_1 &= -0.5902, & b_2 &= -0.5902, \\ \sigma_p &= 2, & \sigma_t &= 1. \end{aligned}$$

$$\begin{aligned} \text{CL} &= M(2, -2.947; 0.894) - M(2, 2.053; 0.894) - M(3, 2.947; 0.894) \\ &\quad + M(3, -2.053; 0.894) \\ &= M(2, 0; 0.982) + M(-2.947, 0; 0.962) - 0.500 - M(2, 0; -0.281) \\ &\quad - M(2.053, 0; -0.180) - M(3, 0; -0.193) - M(2.947, 0; -0.267) \\ &\quad + M(3, 0; 0.962) + M(-2.053, 0; 0.982) - 0.500 \\ &= 0.023 + 0.500 - 0.500 - 0.006 - 0.007 - 0.000 - 0.000 + 0.001 \\ &\quad + 0.500 - 0.500 \\ &= 0.011. \end{aligned}$$

$$\begin{aligned} \text{PL} &= 0.011 + G(2) + G(3) - G(2.053) - G(2.947) \\ &= 0.011 + 0.977 + 0.999 - 0.980 - 0.998 = 0.009. \end{aligned}$$

Hence, because of the bias in the test set, the consumer's loss is increased from 0.006 to 0.011, and the producer's loss is increased from 0.006 to

0.009. If the same test specification limits are used over a period of time, it would probably be worthwhile to compute the consumer's loss and producer's loss for a whole range of biases. These could be plotted on a graph showing the assumed bias on the abscissa and the producer's or consumer's loss on the ordinate.

#### IV. SPECIAL CRITERIA FOR DETERMINING SPECIFICATION LIMITS

Following Grubbs and Coon,<sup>2</sup> if the condition is that the producer and consumer accept the same or equal losses in rejecting a conforming product unit and in accepting a nonconforming product unit, the solution is obtained by setting  $CL = PL$  in (9) for two-sided test and performance specification limits, or setting  $CL = PL$  in (10) and (11) or (12) and (13) for one-sided test and performance specification limits. This results in  $q_1 = k_1$  and  $q_2 = k_2$  or

$$b_1 = \frac{k_1\sigma_p - k_1\sqrt{\sigma_p^2 + \sigma_t^2}}{\sigma_t} \quad (14)$$

and

$$b_2 = \frac{k_2\sigma_p - k_2\sqrt{\sigma_p^2 + \sigma_t^2}}{\sigma_t} \quad (15)$$

Equations (14) and (15) may be solved for  $b_1$  and  $b_2$ , respectively; or, if  $r$  is set equal to  $\sigma_p/\sigma_t$ , the value of  $b$  satisfying (14) and (15) may be read from Table I (p.16) of Ref. 2. The values for consumer's loss and producer's loss, however, will have to be calculated from (7), (9), (10), (11), (12) and (13).

Another criterion discussed by Grubbs and Coon is to assume that the sum of the consumer's and producer's losses is to be a minimum. Then the  $b$ 's for two-sided test specification limits are obtained by solving the equations

$$G\left(\frac{-k_2 - \rho q_1}{\sqrt{1 - \rho^2}}\right) + G\left(\frac{-k_1 + \rho q_1}{\sqrt{1 - \rho^2}}\right) = \frac{1}{2}$$

and

$$G\left(\frac{-k_1 - \rho q_2}{\sqrt{1 - \rho^2}}\right) + G\left(\frac{-k_2 + \rho q_2}{\sqrt{1 - \rho^2}}\right) = \frac{1}{2}.$$

Again following Grubbs and Coon, if  $k_1 \geq 1.5$ ,  $k_2 \geq 1.5$ ,  $\sigma_p \geq \sigma_t$  and the  $b$ 's are negative or small positive, then the first integral in each of the above equations is nearly zero, so that approximate solutions to the

above equations are  $k_1 \cong \rho q_1$  and  $k_2 \cong \rho q_2$ , or

$$b_1 \cong -\frac{k_1 \sigma_t}{\sigma_p} \quad (16)$$

and

$$b_2 \cong -\frac{k_2 \sigma_t}{\sigma_p}. \quad (17)$$

The  $b$  values can be read from Table II (p. 16) of Ref. 2, but the consumer's and producer's losses have to be computed from the formulas given in this paper. Equations (16) and (17) for the  $b$ 's are exact for one-sided test specification limits.

Let  $C_{cl}$  be the cost of accepting a nonconforming product unit, and  $C_{pl}$  be the cost of rejecting a conforming product unit. Then the values for  $b_1$  and  $b_2$  that minimize the total cost are those that satisfy the equations

$$G\left(\frac{-k_2 - \rho q_1}{\sqrt{1 - \rho^2}}\right) + G\left(\frac{-k_1 + \rho q_1}{\sqrt{1 - \rho^2}}\right) = \frac{C_{pl}}{C_{cl} + C_{pl}},$$

and

$$G\left(\frac{-k_1 - \rho q_2}{\sqrt{1 - \rho^2}}\right) + G\left(\frac{-k_2 + \rho q_2}{\sqrt{1 - \rho^2}}\right) = \frac{C_{pl}}{C_{cl} + C_{pl}}.$$

Again, if  $k_1 \geq 1.5$ ,  $k_2 \geq 1.5$ ,  $\sigma_p \geq \sigma_t$  and the  $b$ 's are negative or small positive, then the first integral in each of the above equations is nearly zero and the  $b$ 's may be obtained approximately from the equations

$$G\left(\frac{-k_1 \sigma_t - b_1 \sigma_p}{\sqrt{\sigma_p^2 + \sigma_t^2}}\right) \cong \frac{C_{pl}}{C_{cl} + C_{pl}} \quad (18)$$

and

$$G\left(\frac{-k_2 \sigma_t - b_2 \sigma_p}{\sqrt{\sigma_p^2 + \sigma_t^2}}\right) \cong \frac{C_{pl}}{C_{cl} + C_{pl}}. \quad (19)$$

In this case the  $b$ 's may be obtained approximately (for two-sided test specification limits) by setting the limit of the integral to that deviate of a univariate normal which corresponds to the fraction

$$\frac{C_{pl}}{C_{cl} + C_{pl}}.$$

Tingey and Merrill<sup>7</sup> also consider this problem, and they allow the cost of accepting a nonconforming item to be different for the two tails of the product distribution. They give a short table of values of  $b_1$  and  $b_2$  (their Table II) under these conditions. Note that the subscripts 1 and 2 must be interchanged to enter their table with the formulas given here.

For a one-sided test specification limit the  $b$  is obtained exactly by (18) and (19). The corresponding producer's and consumer's losses may then be calculated from (10), (11), (12) and (13) given in this paper.

As mentioned in the introduction, Tingey and Merrill<sup>7</sup> consider the case where the producer's loss is constant but the consumer's loss varies with the degree of nonconformance. They give a table of values of  $b_1$  and  $b_2$  which will minimize the total cost under these conditions. Note that they use the subscript 1 for the lower tail of the product distribution and 2 for the upper tail, while the reverse has been used here. Hence, if the formulas in this paper are being used, interchange  $b_1$  with  $b_2$  and  $k_1$  with  $k_2$  when entering Tingey and Merrill's table. They do not give values for the total loss, but their formula for the total loss may be reduced to a computing form as follows:

Let  $C_{cl}^u$  = cost to the consumer of accepting a nonconforming product unit from the upper tail only of the product distribution. Then, if the cost to the consumer varies with the degree of nonconformance, this is defined mathematically to be

$$C_{cl}^u = \frac{P - \mu - k_1\sigma_p}{\sigma_p} C^u,$$

where  $C^u$  is the unit cost associated with the acceptance of nonconforming product in the upper tail of the product distribution. Then, in the notation used here, Tingey and Merrill's formula can be reduced to

$$\begin{aligned} \frac{C_{cl}^u}{C^u} &= -k_1M(k_1, -q_2; \rho) + k_1M(k_1, q_1; \rho) \\ &+ \frac{\rho}{\sqrt{2\pi}} \exp(-\frac{1}{2}q_2^2)G\left(\frac{-k_1 - \rho q_2}{\sqrt{1 - \rho^2}}\right) \\ &- \frac{\rho}{\sqrt{2\pi}} \exp(-\frac{1}{2}q_1^2)G\left(\frac{-k_1 + \rho q_1}{\sqrt{1 - \rho^2}}\right) \\ &- \frac{1}{\sqrt{2\pi}} \exp(-\frac{1}{2}k_1^2)G\left(\frac{-q_1 + \rho k_1}{\sqrt{1 - \rho^2}}\right) \\ &+ \frac{1}{\sqrt{2\pi}} \exp(-\frac{1}{2}k_1^2)G\left(\frac{q_2 + \rho k_1}{\sqrt{1 - \rho^2}}\right). \end{aligned} \quad (20)$$

Hence, with the aid of Figs. 2, 3, 4 and 5 and a table of the univariate normal distribution function and its derivative, it is possible to compute  $C_{cl}^u$ . A similar formula for the consumer's cost for the lower tail of the product distribution may be obtained by interchanging  $k_1$  with  $k_2$  and interchanging  $q_1$  with  $q_2$ .

If the cost per product unit to the producer of rejecting conforming

product is constant, the total cost to the producer may be found by multiplying the PL obtained from (9) [where the CL in (9) is computed from (7)] by the per product unit cost. Then the total cost to both producer and consumer is obtained by adding (a) the consumer's cost for the upper tail of the product distribution, (b) the consumer's cost for the lower tail of the product distribution and (c) the producer's cost. It is this total cost which is minimized by the values of  $b_1$  and  $b_2$  found in Tingey and Merrill's Table I.

Consider now the case where the producer's cost of rejecting a conforming product unit is proportional to the degree of nonconformance, but only the upper tail of the product distribution is to be considered. The consumer's cost can be obtained by putting  $q_2$  equal to infinity in (20). The result is

$$\begin{aligned} \frac{C_{cl}^u}{C^u} = & -k_1 G(-k_1) + k_1 M(k_1, q_1; \rho) \\ & - \frac{\rho}{\sqrt{2\pi}} \exp\left(-\frac{1}{2}q_1^2\right) G\left(\frac{-k_1 + \rho q_1}{\sqrt{1 - \rho^2}}\right) \\ & + \frac{1}{\sqrt{2\pi}} \exp\left(-\frac{1}{2}k_1^2\right) G\left(\frac{q_1 - \rho k_1}{\sqrt{1 - \rho^2}}\right). \end{aligned} \quad (21)$$

As before, a similar formula holds if a lower tail only is considered and may be obtained by replacing  $k_1$  with  $k_2$  and  $q_1$  with  $q_2$ .

#### REFERENCES

1. Eagle, A. R., A Method for Handling Errors in Testing and Measuring, *Ind. Qual. Cont.*, **10**, March 1954, p. 10.
2. Grubbs, F. E. and Coon, H. J., On Setting Test Limits Relative to Specification Limits, *Ind. Qual. Cont.*, **10**, March 1954, p. 15.
3. Pearson, K., *Tables for Statisticians and Biometricians*, Part II, Cambridge Univ. Press, Cambridge, Eng., 1931.
4. *Tables of the Bivariate Normal Distribution Function and Related Functions*, National Bureau of Standards, to be published.
5. Hayes, J. L., The Determination of Allowable Instrumentation Error, Tech. Note No. 63-8, Naval Ordnance Lab., Corona, Calif., April 1955.
6. Wiesen, J. M. and Clark, C. R., Determining Allowable Test Set Errors, Tech. Memorandum 201-54-51, Sandia Corp., Albuquerque, N. M., September 1, 1954.
7. Tingey, F. H. and Merrill, J. A., *Minimum Risk Specifications Limits*, Research and Development Report No. IDO-16396, Phillips Petroleum Co., Atomic Energy Division, July 1957. (Available from Office of Technical Services, Department of Commerce, Washington 25, D. C.)
8. Owen, D. B., *The Bivariate Normal Probability Distribution*, Research Report No. SC-3831(TR), Sandia Corp., Albuquerque, N. M., March 1957. (Available from Office of Technical Services, Department of Commerce, Washington 25, D. C.)
9. Owen, D. B., Tables for Computing Bivariate Normal Probabilities, *Ann. Math. Stat.*, **27**, December 1956, p. 1075.
10. Grubbs, F. E., On Estimating Precision of Measuring Instruments and Product Variability, *J. Amer. Stat. Assn.*, **43**, June 1948, p. 243.

# The Anelasticity of Natural and Synthetic Quartz at Low Temperatures\*

By J. C. KING

(Manuscript received September 4, 1958)

*Certain imperfections in alpha-quartz are found to introduce anelastic absorption at low temperatures in crystal resonators. For a shear wave of 5 mc, absorption peaks are observed at approximately 20° and 50°K in unirradiated samples. X-irradiation effects a lowering of the amplitude of the 50°K absorption, while a new absorption is introduced at 100°K.*

*The results of acoustic absorption measurements on a number of selected samples of synthetic quartz resonators suggest that, whereas the 50°K absorption is attributable to excess oxygen, the 100°K defect involves aluminum which is present substitutionally in the crystal structure.*

*X-irradiation-induced lowering of the resonant frequency of crystal resonators is clearly the result of a lowering of the elastic modulus associated with the 100°K anelastic absorption.*

## I. INTRODUCTION

Measurements of the internal friction in crystals have revealed mechanical relaxation processes which can be attributed to crystal defects. Bordoni<sup>1</sup> first observed a mechanical relaxation of this kind in a number of metals at low temperatures. The amplitude of the absorption was found to be enhanced by cold work and reduced by annealing. Subsequent measurements of the loss in lead by Bömmel<sup>2</sup> and in copper by Niblett and Wilks<sup>3</sup> served to confirm Bordoni's findings and further to associate the relaxation with the movement of dislocations under the action of an applied shearing stress.

Recently, a study of the low-temperature anelasticity in quartz by Bömmel, Mason and Warner<sup>4</sup> disclosed two structural relaxation proc-

\* This work has been supported in part by U. S. Army Signal Corps Contract DA-36-039 sc-64586. This article will be a chapter in *Defect Structure of Quartz and Glassy Silica*, to be published in 1959 by John Wiley & Sons, New York.

esses. For a frequency of vibration of 5 mc, one relaxation absorption appears at about 20°K and probably derives from dislocations, while the other, occurring at 50°K, is apparently due to a deformation of the lattice network.

The purpose of the present investigation is two-fold: (a) to probe the nature of the deformation defects in quartz through a study of the dependence of the 50°K absorption on selected natural and synthetic samples, and (b) to determine the relationship between the behavior of quartz crystal resonators at room temperature and the anelastic effects arising from crystal imperfections. In these studies, samples of quartz are subjected to x-irradiation and electrolytic purification. A brief paper describing the dependence of the 50°K absorption in synthetic quartz upon seed plate orientation and the effect of x-irradiation on the amplitude of the 50°K absorption has been published.<sup>5</sup>

## II. EXPERIMENTAL PROCEDURE

The experimental technique adopted in this study involves the fabrication of high- $Q$  rotated Y-cut resonators<sup>6</sup> from the quartz to be examined. The  $Q^{-1}$  of the crystal unit at resonance is calculated from its equivalent electrical characteristics as determined in a transmission circuit test set. A block diagram of the essential components of the measuring circuit is shown in Fig. 1. The resonant frequency of the crystal unit at minimum impedance\* is the frequency of the variable oscillator (frequency synthesizer) adjusted to obtain a peak reading at the detector. For this condition, the equivalent resistance of the crystal unit,  $R_1$ , is the value of a resistor which, when substituted for the crystal, gives the same detector reading.

Since the  $Q$  for natural quartz thickness shear vibrators can be made as high as several million, it is assumed that  $Q^{-1}$  for such resonators is a measure of the internal friction of the quartz itself, i.e., it is independent of the mounting structure. Variations in the frequency-determining

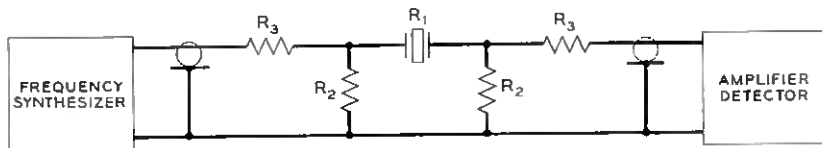


Fig. 1 — Transmission circuit test set used to measure resonator characteristics of quartz.

\* Except for large values of  $Q^{-1}$ , the frequency at minimum impedance may be taken to equal the frequency at series resonance.

elastic modulus of quartz due to anelastic processes are reflected as variations in the resonant frequency of vibration.

The crystal and resistance network shown in Fig. 1 are located in a holder assembly (see Fig. 2) which is suspended in a dewar containing liquid helium. The glass envelope surrounding the mounted crystal resonator is filled with helium gas to a pressure of 1 mm Hg at room temperature before it is sealed off. The amount of damping due to this background gas is negligibly small, and the gas provides a thermal lock between the crystal and a copper oven in which the resonator is placed. To maintain the crystal at the helium-bath temperature, a small amount of helium gas is transferred into the sample holder. For operation above 4.2°K, the pressure within the sample holder is reduced to less than  $5 \times 10^{-6}$  mm Hg and a current is passed through the oven winding. For each incremental increase in heater current, the oven will equilibrate at some higher temperature. The equivalent crystal resistance and frequency at resonance is recorded for increasing temperature.

The thermometry below 4.2°K employs the saturated vapor pressure of helium. Between 4.2°K and 30°K a carbon-composition type resistor is used and, above 30°K, a copper-constantan thermocouple. The frequency of the crystal unit is used to indicate whether the quartz sample is at temperature equilibrium with its surroundings. This technique is quite sensitive, because of the large temperature coefficient of frequency above 15°K for the type of crystals investigated.

### III. SOME THEORETICAL CONSIDERATIONS

In a non-ideal solid, stress and strain are not uniquely related. This can be demonstrated by observing that, although the stress required to cause an instantaneous strain in a solid is a linear function of the resulting strain, the continued application of stress will cause an additional reversible component of strain to develop. This gradual relaxation of strain for a constant stress can be characterized by a relaxation time. Alternately, if the solid is subjected to a constant strain, the initial stress becomes relaxed to a certain degree. Hence, the mathematical expression for the mechanical behavior of a solid must include the rates of change of stress and strain.

When a solid is made to vibrate at some frequency,  $f$ , it can be shown<sup>7</sup> that a relaxation process will cause the stress to be out of phase with the strain by an angle  $\delta$  and that

$$\tan \delta = \Delta \frac{\omega\tau}{1 + (\omega\tau)^2}, \quad (1)$$

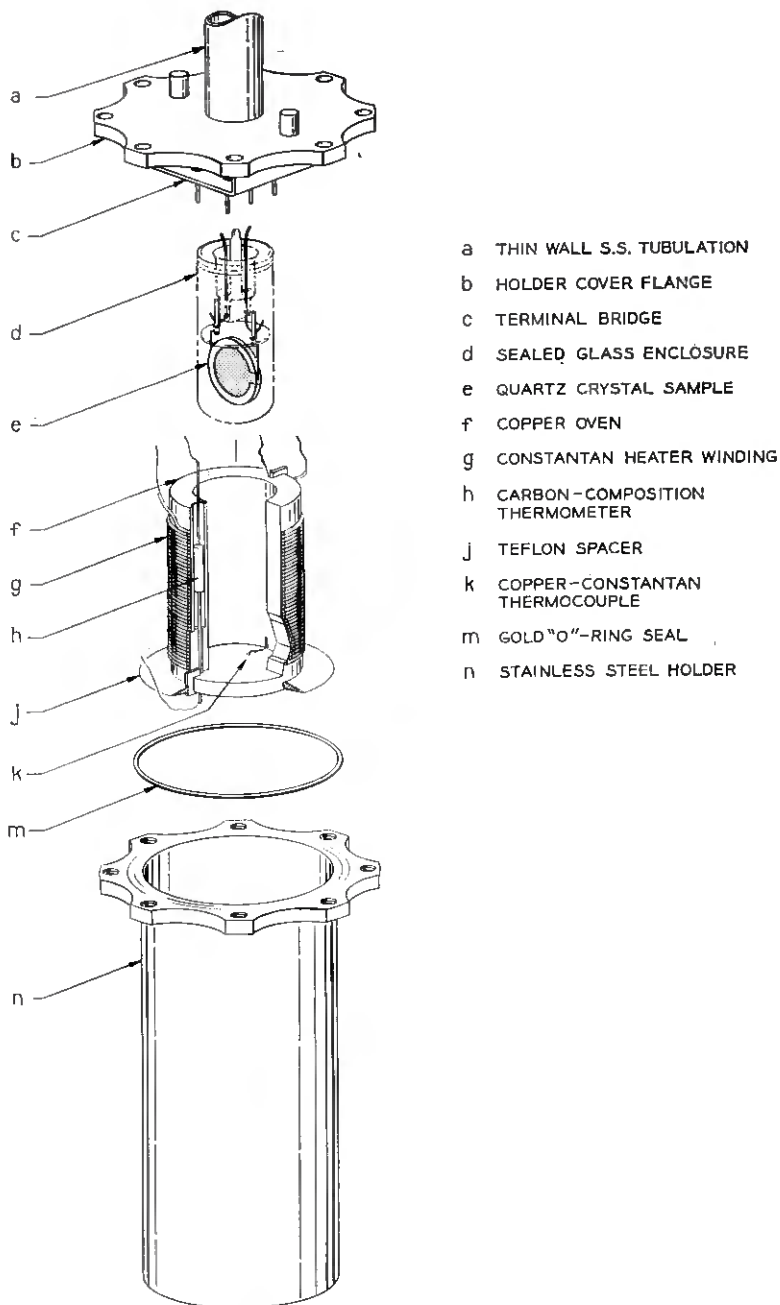


Fig. 2 — Crystal holder assembly used for measurement of internal friction of quartz at low temperatures.

where  $\omega = 2\pi f$ ,  $\tau$  is the relaxation time for the relaxation process, and  $\Delta$ , the relaxation strength, is a measure of the relative change due to complete relaxation in the frequency-determining elastic modulus.  $\tan \delta$  is a measure of the absorption of energy and is equivalent to  $Q^{-1}$ . A plot of  $\tan \delta$  vs.  $\omega$  describes a curve with an absorption maximum equal to  $\Delta/2$  when  $\omega = 1/\tau$ , or

$$Q_{\max}^{-1} = \Delta/2. \quad (2)$$

On either side of the peak,  $\tan \delta$  becomes vanishingly small for  $\omega \ll \tau$  and  $\omega \gg \tau$ . This means that, if the frequency of vibration is either much greater or much less than the jump frequency for the relaxation process given by  $1/\tau$ , the strain is essentially in phase with the stress. However, when the angular frequency of vibration is equal to  $1/\tau$ , the phase angle is a maximum, resulting in an absorption peak.

The relationship between relaxation time and temperature is provided by the distribution of energy levels. Most often this distribution is an Arrhenius type such that

$$\tau = \tau_0 e^{E/RT}, \quad (3)$$

where  $\tau_0$  is a constant,  $E$  is the activation energy for the relaxation and  $R$  is the gas constant. The absorption curve plotted as a function of temperature for a simple relaxation process, i.e., involving a single activation energy, is given in Fig. 3.

The effect which structural relaxation has upon the frequency-deter-

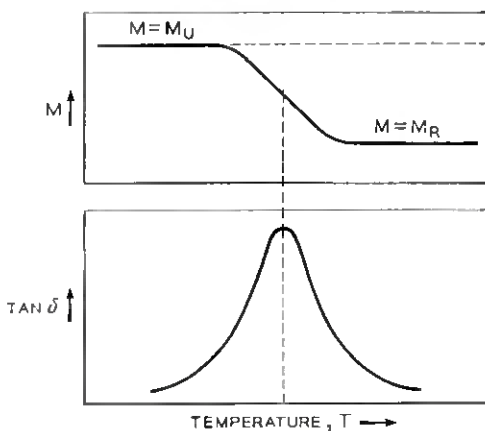


Fig. 3 — Variation of internal friction and real modulus with temperature for simple relaxation process.

mining elastic modulus  $M$  is given by

$$M = M_U - \frac{M_U - M_R}{1 + (\omega\tau)^2}, \quad (4)$$

where  $M = M_U$  when  $\omega \gg \tau$ , and  $M = M_R$  when  $\omega \ll \tau$ . Thus, when the frequency of vibration is much greater than the relaxation time, there occurs no delayed elastic response in the medium. The modulus for this condition is therefore unrelaxed and denoted by  $M_U$ . However, when  $\omega \ll \tau$  there is sufficient time between reversals in the direction of the stress for the delayed elastic response to be effective. The result of complete relaxation causes the modulus to be lowered to  $M_R$ .

The change in the modulus with temperature is also given in Fig. 3. It will be observed that the inflection temperature in the curve of  $M$  vs.  $T$  is the same as that corresponding with  $\tan \delta_{\max}$ . The mechanical behavior of a solid at temperatures below a given relaxation absorption peak is, therefore, unaltered by anelastic effects attending the relaxation process.

The terms in (3) can be rearranged in the following manner:

$$\frac{M_U - M}{M_R} = \frac{M_U - M_R}{M_R} / 1 + (\omega\tau)^2. \quad (5)$$

The expression  $(M_U - M_R)/M_R$ , giving the relative change in the modulus due to complete relaxation, has been previously denoted as the relaxation strength  $\Delta$ .

According to the above analysis, if a relaxation process is induced by some means in a solid, then the elastic modulus at temperatures where  $\omega$  is greater than  $\tau$  will be lowered. On the other hand, if a defect which introduces a structural relaxation is eliminated, then the elastic modulus for the solid will be increased at temperatures where  $\omega$  is greater than  $\tau$ .

#### IV. ANELASTIC ABSORPTION IN QUARTZ

There are at least three basic types of crystal defects which can contribute to the anelasticity of quartz:

- (a) impurity ions, which can break away from attracting centers and diffuse from one equivalent interstitial site to another within the crystal;
- (b) a deformation of the normal crystal network, allowing for the oscillation of segments of the crystal lattice between positions of equal potential energy and
- (c) rows of atoms comprising dislocation lines, which move in the crystal glide planes.

The indicated motions for the above defects are thermally activated

and, therefore, at a given temperature the structural elements involved surmount an energy barrier, whose height is given by  $E$  in (3), with a jump frequency,  $1/\tau$ , characteristic of the process. If, by subjecting quartz to a stress, there results an energy bias of the potential wells between which the defect element moves, then the defect population density in the position of lowest energy will preferentially increase. Thus, there occurs a delayed elastic response.

We will limit this report to an examination of the anelasticity of quartz arising from the deformation-type defects.

AT-cut\* overtone crystal units have been fabricated using electrical grade Brazilian quartz and various samples of synthetic quartz. In view of the dependence of a number of the physical properties of synthetic quartz upon the direction of crystal growth, the synthetic crystal units will be classified according to the particular seed surface on which the quartz is grown. Thus, resonators obtained from growth on a z-minor rhombohedron are termed z-face or z-minor samples. Samples taken from growth on a basal cut or from the Z-growth region on a Y-bar seed crystal are denoted as Z-growth sample resonators.

In Fig. 4 the internal friction at 5 mc in natural and synthetic quartz at low temperatures is shown by the curves of  $Q^{-1}$  vs.  $T$  for representative crystal units. In these samples two absorption peaks are immediately evident, one in the neighborhood of 20°K and the other at 50°K. In the case of natural quartz these absorptions have been attributed to structural relaxations. The relaxation frequencies for the two mechanisms are reported<sup>4</sup> to be

$$\tau_{20^\circ\text{K}} = 7.7 \times 10^{-10} e^{155/RT} \quad (6)$$

and

$$\tau_{50^\circ\text{K}} = 10^{-13} e^{1300/RT}. \quad (7)$$

An examination of the magnitudes of  $\tau_0$  and  $E$  for the two absorptions suggests that the 20°K relaxation mechanism involves the motion of dislocations and that the 50°K relaxation process is probably due to a deformation of the crystal lattice.

As may be observed in Fig. 4, the synthetic samples representative of both z-face and Z-growth material exhibit an extremely large absorption at 50°K.<sup>5</sup> (Henceforth, the same two samples of synthetic quartz will be used for all reported resonator measurements unless specified otherwise.) In comparison with natural quartz, it is common to find the 50°K absorption peak in z-face and Z-growth quartz almost three and two

\* A Y-cut plate rotated about the X-axis by an angle  $\theta = +35^\circ 15'$ .

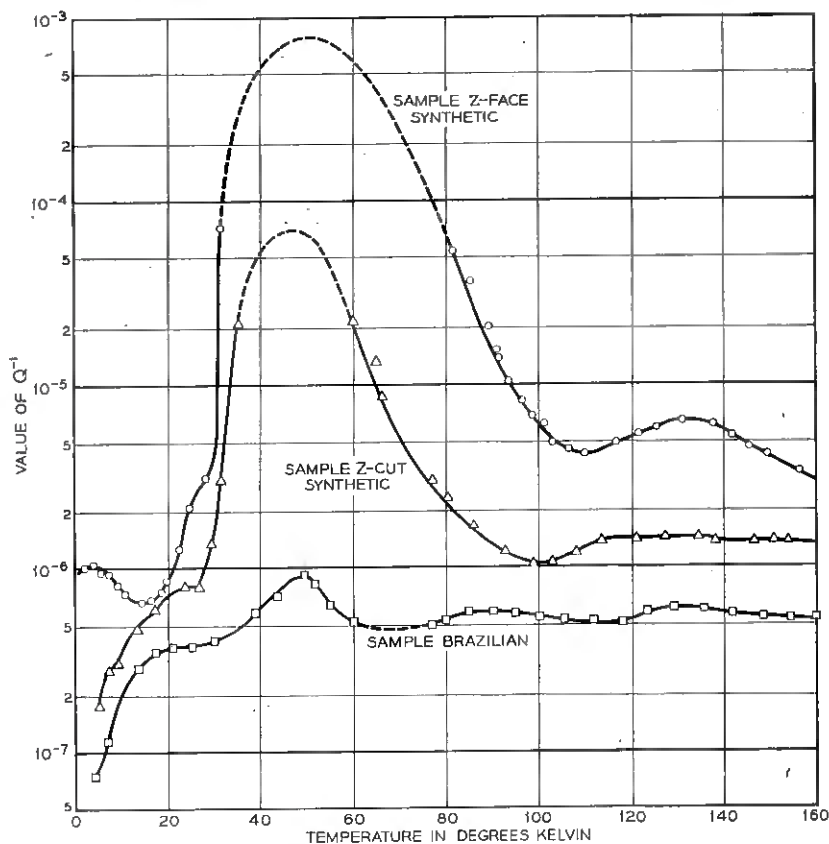


Fig. 4 — Internal friction at 5 mc for thickness shear vibration (AT-cut) in natural quartz and two representative samples of z-face and Z-growth synthetic quartz at low temperatures.

decades higher respectively. It is apparent that the concentration of crystal defects responsible for the 50°K peak is (a) commonly greater in synthetic quartz and (b) dependent upon the crystallographic orientation of the seed plate. It must be noted that other growth conditions besides seed orientation can affect the 50°K defect concentration.

Assuming that the 50°K relaxation process derives from some impurity or combination of impurities, a spectrochemical analysis of the z-face and Z-growth samples should reveal large differences in the impurity concentration between the two materials. In Table I may be seen the emission analysis\* of two quartz samples taken from the same mother

\* Analysis made by the Spectrographic Services and Research at the Naval Gun Factory Laboratory, Washington, D. C.

TABLE I—CONCENTRATION OF IMPURITIES IN PPM

Impurities	z-face	Z-growth
Al	30	10
Fe	10	10
Mg	0.3	0.3
Na	3	3
Cu	0.1	<0.1
Li	1	0.3
Ni	10	<10

crystals from which the z-face and Z-growth specimens (Fig. 4) were obtained.

The obvious similarity of the synthetic samples regarding the concentration of impurities, together with their vastly different 50°K absorption presents a rather strong argument against associating the 50°K defect with impurities in quartz. The spectrographic analysis, of course, does not rule out the possibility that the 50°K defect might involve an excess or deficiency of oxygen. A defect structure involving the former will be considered in Section V.

Significant differences between natural and some synthetic quartz crystals have also been noted in the AT-cut frequency-temperature characteristics.<sup>8,9,10,11</sup> The variation of frequency with temperature between -60° and 100°C for a series of crystal units fabricated from the Z-growth quartz is shown in Fig. 5. From the AT-cut family of curves two identifiable characteristics may be determined by graphical analysis. One is the angle of rotation,  $\theta_0$ , for which the frequency excursion over the temperature range is a minimum and the other is the inflection temperature,  $T_i$ , of the  $f$ - $T$  curve for a crystal cut at  $\theta = \theta_0$ . For natural and Z-growth quartz  $\theta_0$  and  $T_i$  are nearly the same and given by  $35^\circ 20' \pm 1'$  and  $30^\circ \text{C} \pm 2^\circ \text{C}$  respectively. Departures from the above characteristics occur in z-face quartz, where  $\theta_0$  is found to be some four minutes larger and  $T_i$  is shifted to 40°C. In all samples of quartz examined there is a unique concurrence of shifts in the frequency-temperature characteristics with amplitude of the 50°K relaxation absorption.

The resonant frequency of a rotated Y-cut crystal is given by:

$$f = \frac{1}{2t} \sqrt{\frac{c_{66}'}{\rho}}. \quad (8)$$

In this expression,  $t$  is the resonator thickness,  $\rho$  is the density of quartz and  $c_{66}'$ , the effective elastic constant, is

$$c_{66}' = c_{66} \cos^2 \theta + c_{44} \sin^2 \theta - c_{14} \sin 2\theta, \quad (9)$$

where  $c_{ij}$  are the elastic constants.

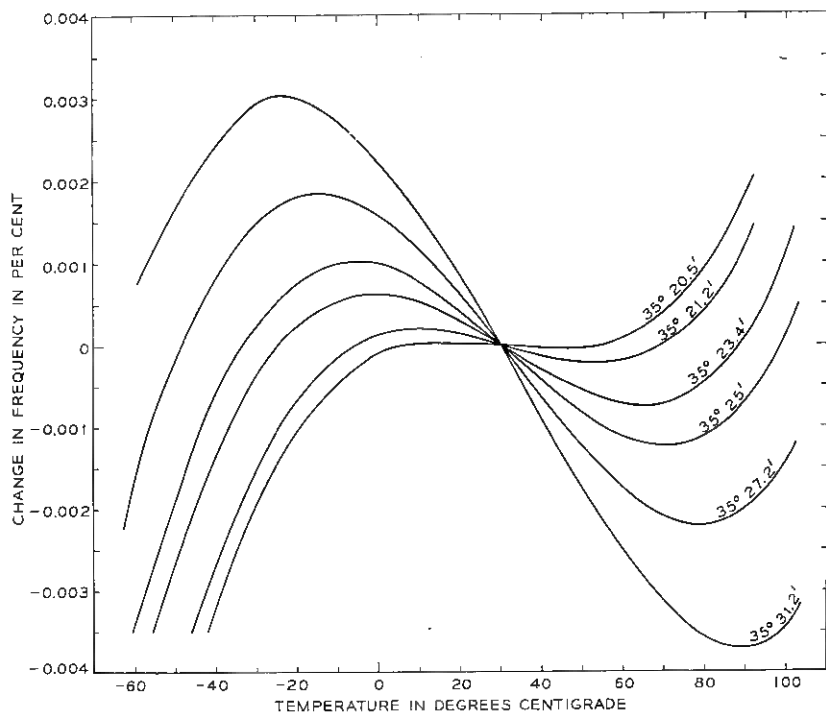


Fig. 5 — Frequency vs. temperature curves between  $-60^{\circ}$  and  $100^{\circ}\text{C}$  for a group of AT-cut resonators fabricated from the Z-growth synthetic crystal.

From (8) the change in frequency attending a small variation in  $c_{66}'$  is found to be

$$df = \frac{f}{2} \frac{dc_{66}'}{c_{66}'} \quad (10)$$

It was pointed out in the previous section that a relaxation process will cause a lowering of the elastic modulus, for a given frequency of vibration, at temperatures above the relaxation absorption. If  $dc_{66}'$  in (10) is taken as the change in the elastic modulus due to complete relaxation, then

$$\frac{\Delta f}{f} = \frac{\Delta}{2}, \quad (11)$$

or

$$\frac{df}{f} = Q_{\max}^{-1}. \quad (12)$$

Thus, the relative change in  $f$  attributable to the complete relaxation of a simple relaxation process, is just equal to the maximum value of the associated absorption.

Neglecting the normal variations of frequency with temperature, the effect described above should alone account for a difference of frequency of approximately 1,000 ppm between otherwise identical natural and z-face quartz AT-cut resonators above 50°K. It is suggested that the observed variations in the  $f$ - $T$  characteristics between natural and synthetic AT-cut resonators arise from a change of one or more of the elastic constants comprising  $c_{66}'$ , attending the relaxation of the 50°K defect.

The dielectric loss in quartz at low temperatures has been reported by Volger, et al.<sup>12</sup> The loss in natural quartz and samples of z-face and Z-growth quartz at 32 kc is described in Fig. 6. A number of the dielectric loss peaks in quartz have been associated<sup>12</sup> with the relaxation of specific crystal defects. The activation energy and relaxation time  $\tau_0$  for the dielectric loss which appears at 38°K in Fig. 6 are reported to be 1,270 cal/gm mole and  $2 \times 10^{-13}$  sec. These values compare closely with those for the 50°K mechanical relaxation. Furthermore, the relative position of the dielectric  $\tan \delta$  values for the z-face and Z-growth specimens is in general agreement with the mechanical absorption at 50°K for similar samples. It appears definite, therefore, that the 50°K defect gives rise to an orientational electric polarization.

Volger, et al. have suggested that the 38°K dielectric absorption is caused by what is referred to as a B-center type defect, namely  $^{2A}B$ . A two-dimensional schematic representation of the  $^{2A}B$  defect, along with others which will be of interest in Section V, is shown in Fig. 7.\* The association of the  $^{2A}B$  defect with the 38°K dielectric absorption peak in synthetic quartz is based primarily on an observed higher concentration of Al in the synthetic material. In view of the emission analysis given in Table I and the measured mechanical absorption in comparable synthetic samples, the above interpretation is subject to some doubt.

#### V. EFFECT OF X-IRRADIATION

A number of samples of natural and synthetic AT-cut crystal units have been irradiated with 50-kv X-rays from a tungsten target tube op-

\* In a recent communication Dr. Stevels now contends that  $\frac{Al}{H}P$  defects are responsible for the 38°K dielectric absorption rather than  $^{2A}B$  defects. The  $\frac{Al}{H}P$  defect is similar to  $\frac{Al}{Na}P$  shown in Fig. 7(c), except that  $Na^+$  is replaced by  $H^+$ .

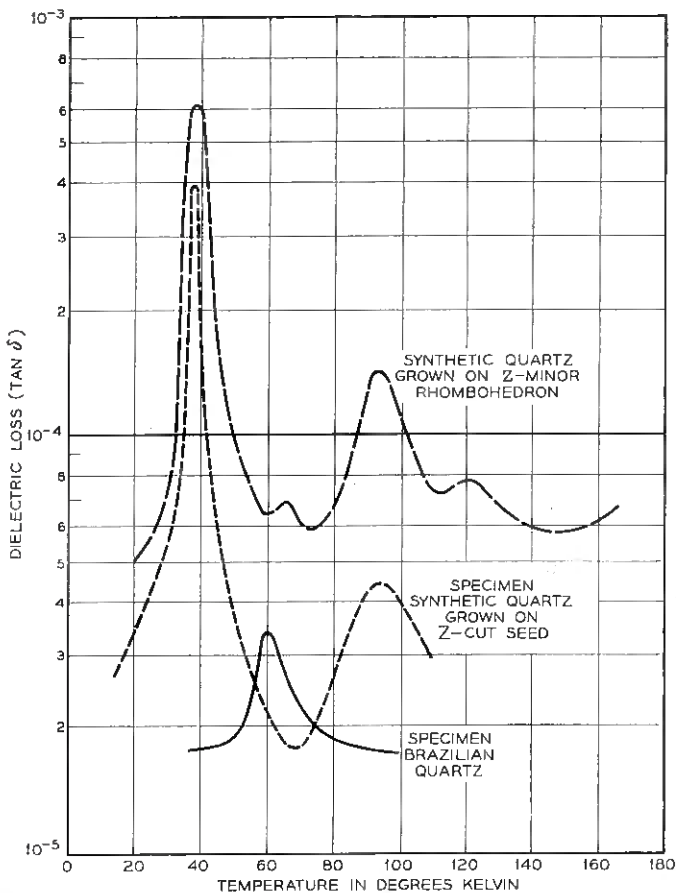


Fig. 6 — Low-temperature dielectric absorption at 32 kc in natural quartz and two samples of synthetic quartz.

erating at 48 ma. The exposure in all cases amounts to approximately  $10^6$  r. Two effects of considerable interest are observed: (a) in all samples, the  $50^\circ\text{K}$  defect is virtually eliminated and (b) an absorption at  $100^\circ\text{K}$  is induced in samples which color with irradiation. The effect listed under (a) will be considered first.

An example of the profound change in the concentration of  $50^\circ\text{K}$  defect with x-irradiation is shown in Fig. 8. Here the curves of  $Q^{-1}$  and  $\Delta f/f$  before and after x-irradiation are given for the Z-growth sample ( $\Delta f$  is equal to  $f - f_T$ , where  $f$  is the frequency of the crystal unit at room temperature and  $f_T$  is its frequency at temperature  $T$ ). Before irradiation,

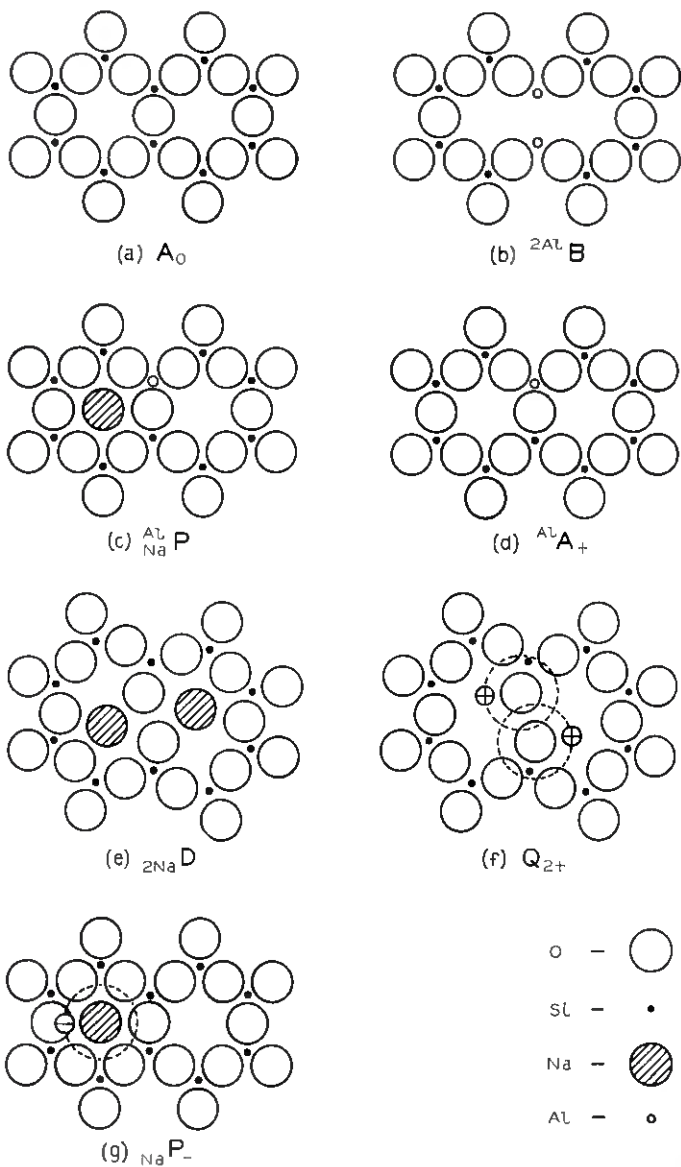


Fig. 7 — Two-dimensional schematic representation of some defects believed to occur in alpha-quartz.

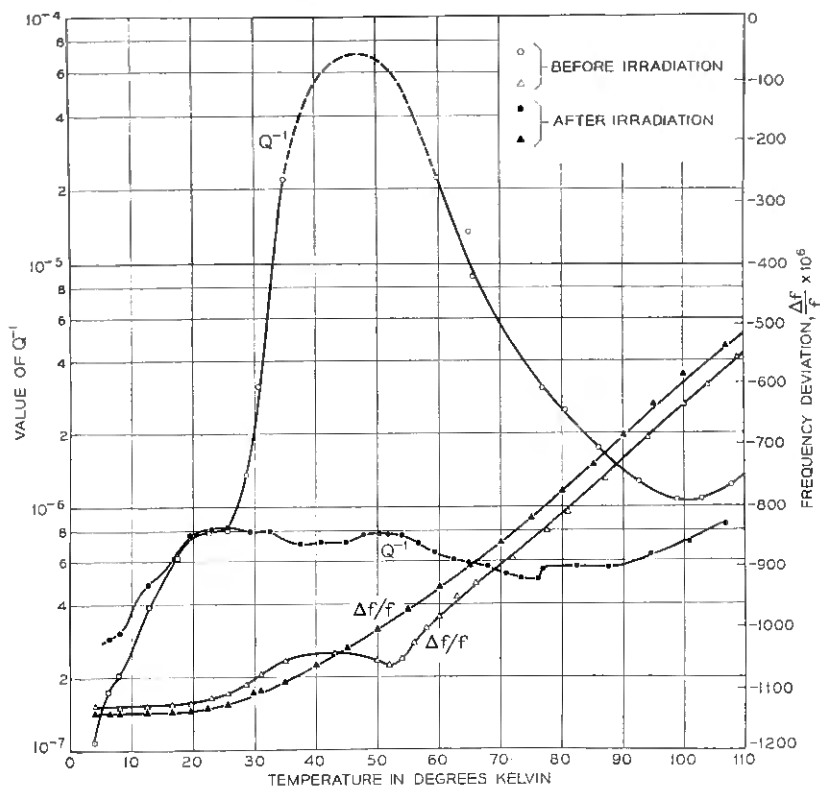


Fig. 8 — Internal friction and frequency deviation at low temperatures for 5-mc thickness shear vibration in Z-growth synthetic quartz before and after x-irradiation.

the change in frequency of the crystal above approximately 30°K is determined not only by the temperature dependence of the parameters at the right in (8) but also by:

$$\frac{df}{f} = \frac{Q_{\max}^{-1}}{1 + (\omega\tau)^2} \quad (13)$$

Here,  $Q_{\max}^{-1}$  and  $\tau$  relate to the 50°K relaxation process. Since the 50°K defects are all but eliminated with x-irradiation, the  $\Delta f/f$  vs.  $T$  curve after irradiation in Fig. 8 describes the change of frequency with temperature, exclusive of any change in  $c_{66}'$  due to stress relaxation. Therefore, a difference curve of  $\Delta f/f$ , before and after irradiation, should resemble the curve of  $M$  vs.  $T$  shown in Fig. 4. Such a curve is plotted in Fig. 9 for the Z-growth specimen, with relative frequency change con-

verted to read per cent change in  $c_{66}'$ . The dotted curve is derived from (5), with  $\tau$  given by (6) and  $\Delta$ , the change in  $c_{66}'$  due to complete relaxation, taken to be the difference between points A and B in Fig. 9. (The value of  $\Delta$ , computed in this manner, can be used to approximate  $Q_{\max}^{-1}$ , provided the relaxation process is one involving at most a very narrow distribution of activation energies.) A correction of the frequency measurements to read in terms of frequency at resonance rather than at minimum impedance would cause the calculated change in  $c_{66}'$  to coincide more nearly with the theoretical curve. The difference curve below 35°K, contrary to expectations, does not fall on the zero reference line. This can be interpreted to signify that the 50°K defect not only contributes to the crystal's anelasticity but also alters bonds in the crystal structure sufficiently to cause a change in the unrelaxed  $c_{66}'$  and in  $dc_{66}'/dt$ .

If, as suggested in Section IV, shifts in the  $f$ - $T$  characteristics of AT-cut resonators can be traced to the 50°K defect, then it must follow that x-irradiation will cause synthetic quartz to acquire the  $f$ - $T$  behavior of natural quartz. In Fig. 10 the  $f$ - $T$  curves for the z-face specimen before and after irradiation are shown between  $-60^\circ$  and  $100^\circ\text{C}$ . It is observed that the curve after irradiation assumes nearly the same form as that for a natural specimen having the same angle  $\theta$ .

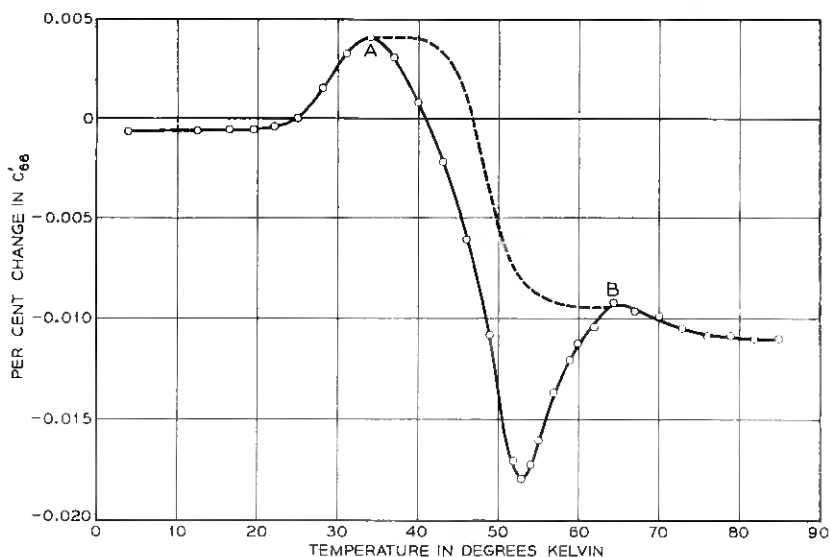


Fig. 9 — Variation of  $c_{66}'$  with temperature for 5-mc thickness shear vibration in unirradiated Z-growth resonator relative to  $c_{66}'$  after x-irradiation; dotted line describes the theoretical curve for a simple relaxation process.

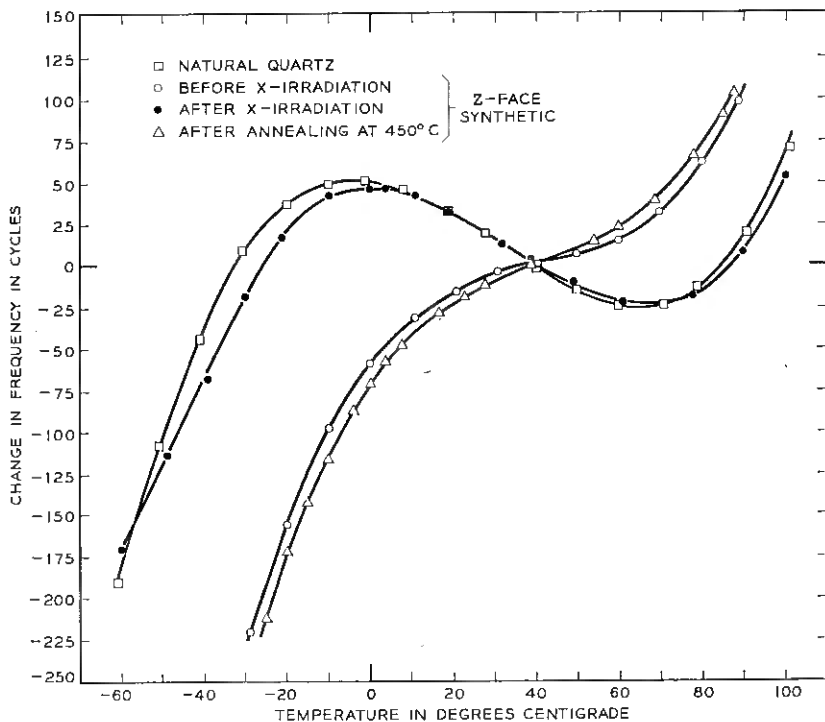


Fig. 10 — Frequency vs. temperature curves between  $-60^{\circ}$  and  $100^{\circ}\text{C}$  for 5-me AT-cut z-face synthetic resonator before and after x-irradiation and after annealing.

Annealing of x-irradiated synthetic resonators at  $500^{\circ}\text{C}$  for several minutes causes the return of the  $50^{\circ}\text{K}$  absorption to the same amplitude it had prior to irradiation. Therefore, annealing should also cause the  $f$ - $T$  characteristics of the x-irradiated z-face sample to return to the form it had before irradiation. By referring to Fig. 8, this can be observed to occur. Chi<sup>13</sup> has examined the effects of x-irradiation on the AT-cut  $f$ - $T$  characteristics of various samples of synthetic quartz.

The effective elimination by X-rays of the anelasticity associated with the  $50^{\circ}\text{K}$  defect requires that the underlying defect be readily altered by ionizing irradiation. The  $2^{\text{A}}\text{B}$  defect, however, represents a particularly stable configuration. This consideration, together with a lack of correlation between Al content and the  $50^{\circ}\text{K}$  absorption, does not favor designating the B-center as the responsible defect. A discriminative study of defect centers likely to occur in quartz and which are better

able to account for phenomena associated with the 50°K absorption, suggests considering the  $Q_{2+}$  defect [Fig. 7(f)].

A Q-center is simply a site at which an excess oxygen atom enters the lattice structure and forms a nonbridging oxygen defect. In the  $Q_{2+}$  defect, only one orbital electron from each of the nonbridging oxygen atoms is paired with an electron from the nearest silicon atom. If an ionizing radiation is sufficiently energetic to remove a paired electron from one of the nonbridging oxygen atoms, then the oxygen atom is effectively removed from the center. The remaining nonbridging oxygen atom may then cross-link with the silicon atom formerly associated with the freed oxygen and thereby reduce the center to the normal structure represented by  $A_0$  in Fig. 7(a). Thus, by a process not unlike x-irradiation, induced cross-linking occurring between polymer chains, Q-centers in quartz may be transformed to  $A_0$ -centers.

The inclusion of an extra oxygen atom in the crystal lattice will cause a corporate distortion of bond angles in the vicinity of the defect, as suggested by the disposition of the atoms about the center in Fig. 7(f). It is certain that other structure-sensitive properties of quartz will therefore be influenced by the presence of Q-centers. Berman<sup>14</sup> has shown that the low-temperature thermal conductivity of quartz is quite sensitive to the degree of crystal perfection. If it is assumed that, in the region immediately surrounding Q-centers, the crystal lattice is somewhat similar to the close-range misorientation within the silica tetrahedra of fused quartz, then it follows that the low-temperature thermal conductivity of quartz will be decreased by an amount dependent upon the Q-center concentration. Measurements of the thermal conductivity of a sample of natural and Z-growth quartz by Berman\* are given in Fig. 11. It is observed that the thermal conductivity of a Z-growth specimen is very little like that of a single crystal since the conductivity peak is depressed by more than a decade and shifted toward higher temperatures. This alteration of the conductivity peak is characteristic of an increase in thermal resistance caused by phonon-defect interaction. Indeed, the conductivity of Z-growth quartz approaches that of neutron irradiated quartz.

In line with the suggestion that Q-centers contribute to the low-temperature thermal resistance in quartz, it is of considerable interest to examine the effect of X-rays on the thermal conductivity of a synthetic sample. With the exception of Q-centers, it is unlikely that the defects in quartz could be modified by X-rays so as to effect an increase in ther-

\* R. Berman has kindly communicated the results of his measurements on synthetic specimens provided by the author.

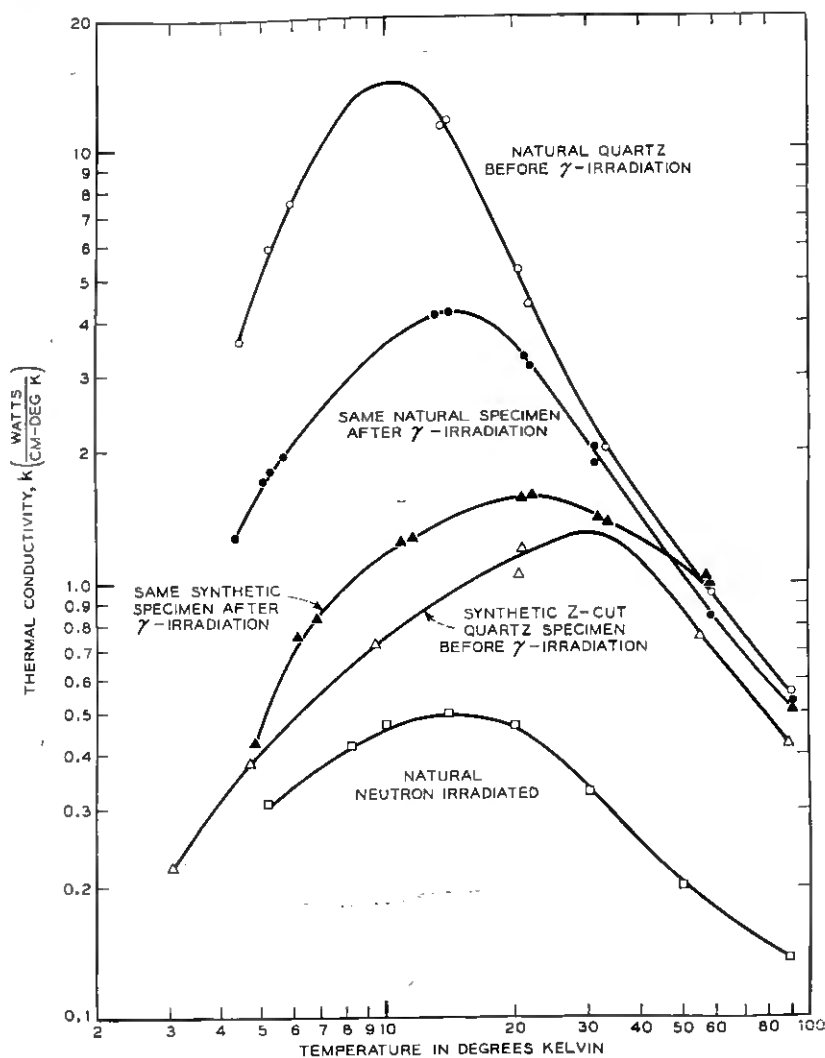


Fig. 11 — Low-temperature thermal conductivity of natural and synthetic quartz before and after gamma irradiation (neutron-irradiated natural sample is included for comparison).

mal conductivity. Hence, it is not surprising to find that, whereas irradiation causes an impairment of the conductivity of natural quartz (see Fig. 11), the conductivity of the irradiated synthetic specimen increases. It is reasonable to expect that  $\gamma$ -modified imperfections contributing to the increase of thermal resistance in natural quartz are probably also present in the Z-growth sample. In spite of such defects, however, the

thermal conductivity of the synthetic specimen is improved with irradiation.

The observed low-temperature conductivity in natural and synthetic quartz before and after  $\gamma$ -irradiation is thus found to be in general agreement with speculations based upon the Q-center model.

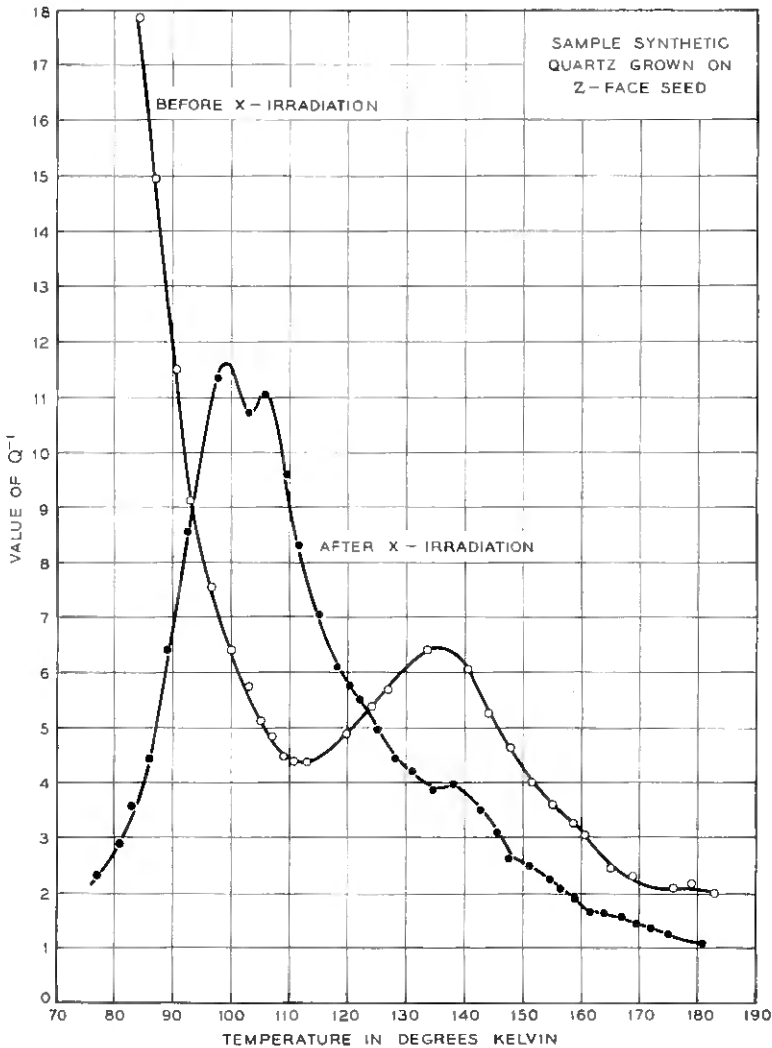


Fig. 12 — Internal friction vs. temperature for AT-cut z-face synthetic sample operating at 5 mc before and after x-irradiation. Note the radiation-induced absorption centered about 100°K.

Let us turn now to effect (b) above, which concerns the X-ray induced internal friction, appearing at 100°K.

In the course of examining the anelasticity of x-irradiated z-face quartz, a well-defined absorption peak centered about 100°K was observed. The curves of  $Q^{-1}$  vs.  $T$  for the z-face sample before and after x-irradiation are shown over the temperature range of interest in Fig. 12. The 100°K absorption is obviously nonexistent in the unirradiated sample, emerging only as the result of x-irradiation. (The precipitous increase in absorption below 100°K in the sample prior to irradiation is simply the high-temperature tail of the 50°K absorption.) The induced internal friction may be characterized as consisting primarily of two absorption peaks of nearly equal amplitude in the neighborhood of 100°K.

Operation of the z-face sample at its third, fifth and ninth overtone frequencies show the absorption peak to be displaced to higher temperatures with increase in frequency, indicative of a relaxation process. A plot of  $\log \omega$  as a function of  $1/T_{\max}$ , where  $T_{\max}$  is the temperature at which the lower temperature component of the 100°K absorption occurs for a given frequency of vibration, is given in Fig. 13. Over this somewhat narrow frequency range a straight line can be drawn through the plotted points. The slope of the line, according to (3), is proportional to the ac-

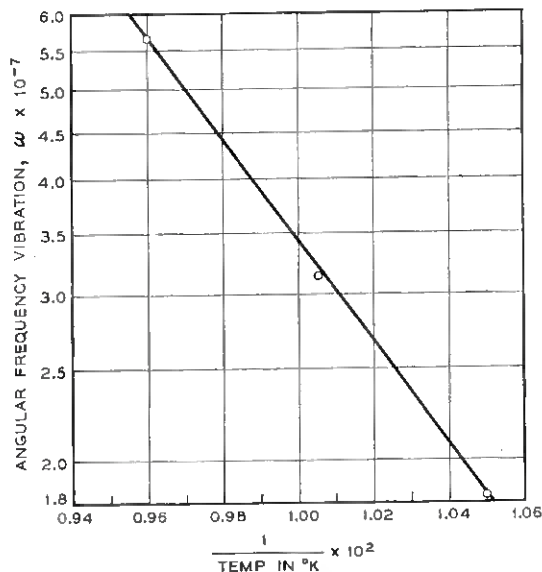


Fig. 13—Frequency of vibration plotted as a function of temperature at which maximum occurs in irradiation-induced absorption.

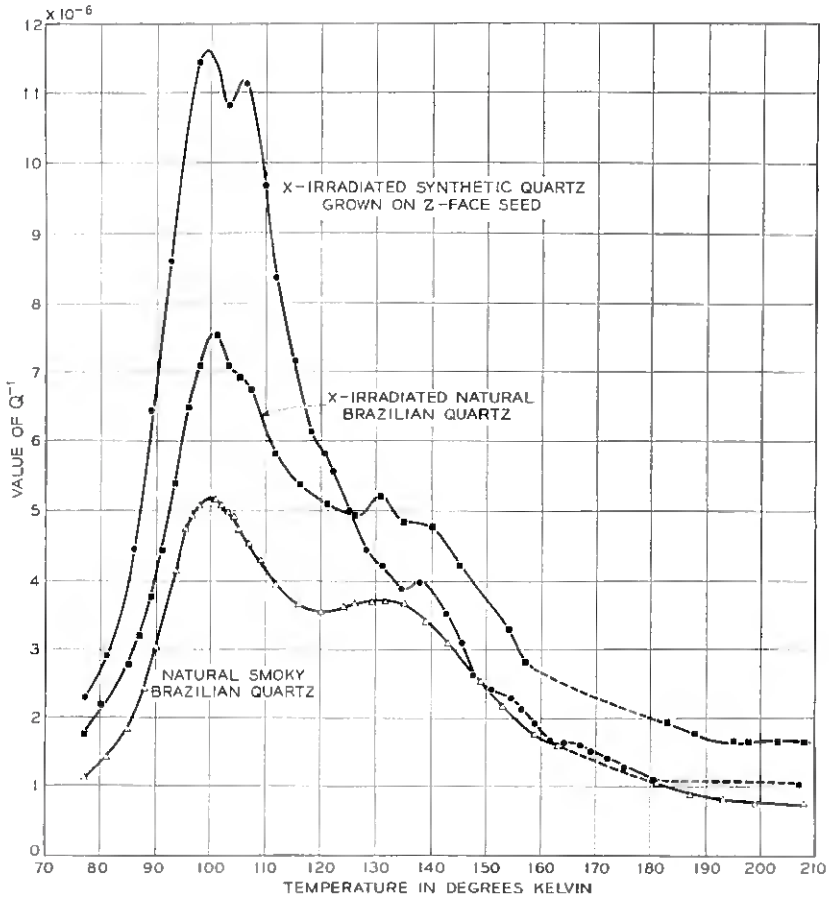


Fig. 14 — Comparison of x-irradiation-induced relaxation absorption in z-face synthetic and natural quartz resonators. Bottom curve is absorption in natural smoky Brazilian quartz.

tivation energy for the relaxation process. For some relaxation frequency,  $1/\tau$ , (3) then yields the value of  $\tau_0$ . Accordingly,  $E$  and  $\tau_0$  for the lower temperature component of the 100°K absorption are calculated to be 2,450 cal/gm mole and  $1.6 \times 10^{-13}$  sec respectively.

At first thought, it might appear that the 100°K defect is simply the 50°K defect modified by the ionizing radiation, since the 100°K absorption "grows" at the expense of the 50°K absorption in the z-face sample. In order to test this proposition, a natural quartz sample having a small 50°K absorption was x-irradiated. The resulting  $Q^{-1}$  vs.  $T$  curve for the

irradiated natural specimen, together with that for the z-face sample, is shown in Fig. 14. Although the absorptions at 50°K in these two crystal units prior to irradiation differ by some three decades, in the region of 100°K after irradiation they still agree to within an order of magnitude. This fact tends to refute any suggested relationship between the 50° and 100°K defects.

Crystal units fabricated from natural smoky Brazilian quartz also exhibit essentially the same absorption characteristics through 100°K (see bottom curve in Fig. 14), as induced by x-irradiation of clear quartz.

A visual examination of the three specimens used in Fig. 14 revealed their color density to be roughly proportional to the height of the 100°K absorption. Furthermore, the 100°K absorption is removed by annealing in much the same manner that the induced smoky color is eliminated. These observations naturally suggest that the so-called A-band optical absorption and the 100°K mechanical absorption in quartz derive from a common crystal defect. This argument is strengthened by measurement of the absorption in a sample of Z-growth quartz. (It is known<sup>16</sup> that Z-growth quartz shows only a very slight tendency to darken with irradiation.) In Fig. 15 it is quite clear that an absorption at 100°K is just barely detectable above background in an irradiated Z-growth specimen.

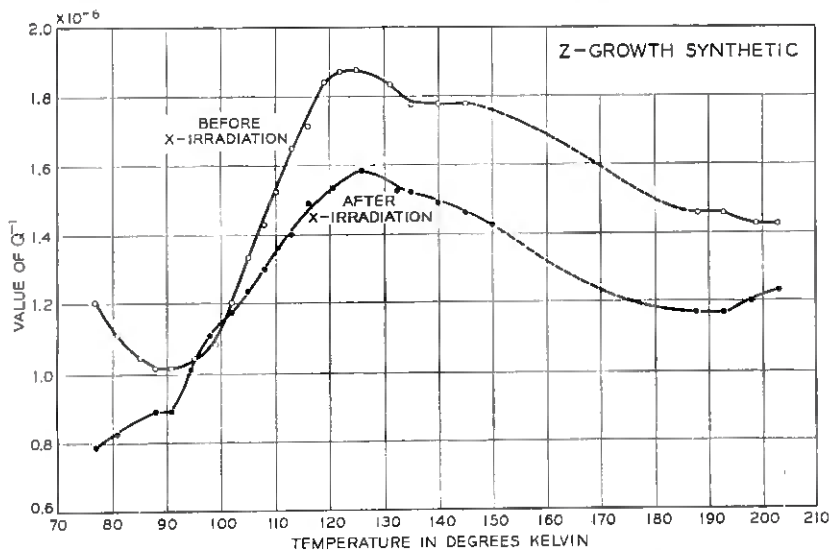


Fig. 15 — Internal friction vs. temperature for AT-cut Z-growth synthetic sample operating at 5 mc before and after x-irradiation.

The resonant frequency of natural AT-cut samples is found to be lowered by some 20 ppm as a result of the x-irradiation. This effect is explicable in terms of a reduction of the elastic modulus through the mechanical relaxation of the 100°K defect. The increase in modulus attending the elimination of the comparatively large 50°K defect in synthetic quartz precludes observing the above effect in most irradiated z-face and Z-growth samples.

Fondel<sup>16</sup> noted that the average resonant frequency of BT-cut\* resonators is lowered by 200 ppm after they are subjected to x-irradiation. The change in frequency appears to be proportional to the density of the induced smoky color. It was proposed<sup>16</sup> that the X-rays cause a change in the basic properties of the quartz. It can now be stated that this change involves the introduction of 100°K defects.

On the basis of the average frequency change for the BT-cut it is anticipated that  $Q_{\max}^{-1}$  for the 100°K absorption in the average BT-cut will be in the vicinity of  $10^{-4}$ . In Fig. 16 are shown the variations of the internal friction and resonant frequency of a natural BT-cut crystal unit down to the temperature of liquid nitrogen. This particular sample is not representative of the average natural quartz specimen since the induced frequency lowering amounts to only 47 ppm, nevertheless

i. the onset of the frequency change coincides with the absorption at 100°K and

ii. the sum of  $df/f$ , computed according to (12), for the two absorption peaks comprising the 100°K absorption is roughly equivalent to the observed frequency shift.

Upon substitution of the values of  $\theta$  equal to 35° 15' and -49° for the AT and BT-cut respectively into (9), the expressions for  $c_{66}'$  are

$$c_{66}'(\text{AT}) = 0.333 c_{44} + 0.666 c_{66} - 0.943 c_{14}, \quad (14)$$

$$c_{66}'(\text{BT}) = 0.570 c_{44} + 0.428 c_{66} + 0.990 c_{14}. \quad (15)$$

Since the term containing  $c_{14}$  is negative for the AT-cut, the value of  $c_{66}'(\text{AT})$  would in fact be increased if a mechanical relaxation affected only  $c_{14}$ . Instead,  $c_{66}'(\text{AT})$  is lowered approximately  $\frac{1}{10}$  as much as  $c_{66}'(\text{BT})$  by x-irradiation. The 100°K defect must, therefore, lower not only  $c_{14}$  but also one, or perhaps both, of the other elastic constants. Bottom<sup>17</sup> has measured the frequency constant of AT-cut, BT-cut and Y-cut crystals before and after irradiation. Through the use of these three orientations, Bottom has estimated that changes of -0.07 per cent,

\* A Y-cut plate rotated about the X-axis by an angle  $\theta = -49^\circ$ .

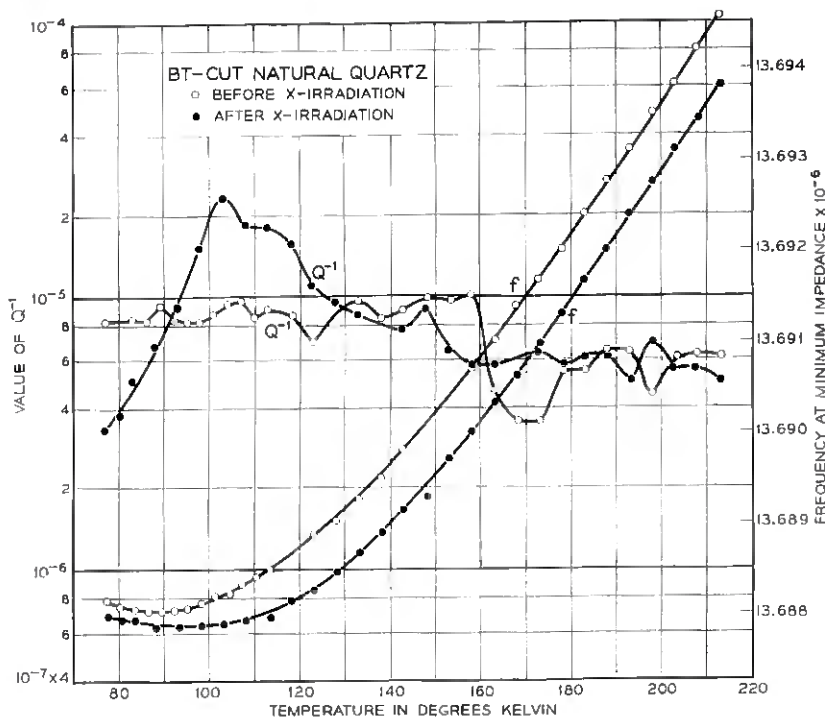


Fig. 16 — Internal friction and frequency of vibration at low temperatures for BT-cut natural quartz resonator before and after x-irradiation.

—0.03 per cent and —0.02 per cent occur in  $c_{14}$ ,  $c_{44}$  and  $c_{66}$  respectively as a result of x-irradiation.

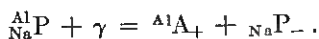
#### VI. DEFECT UNDERLYING THE 100°K ABSORPTION

In the preceding section evidence is presented which demonstrates the close relationship between a deformation-type structural relaxation and color centers. It is well established that the ability of a crystal to darken with x-irradiation is the necessary and sufficient condition for the appearance of a unique relaxation absorption. Henceforth, it will be assumed that the optical and associated mechanical absorption derive from the same crystal imperfection.

A number of investigations have been undertaken to define the nature of the A-band defect. Brown and Thomas<sup>15</sup> found that Z-growth colored much less readily when exposed to X-rays than did natural quartz. Later, Mitchell and Paige<sup>18</sup> showed that the A-band was probably associated

with some impurity, which Ditchburn, et al.<sup>19</sup> tentatively identified as substitutional aluminum. Griffiths, Owen and Ward<sup>20</sup> discovered a spin resonance absorption in quartz which also appears to originate from a defect center consisting of substitutional aluminum. More recently, Mitchell and Paige<sup>21</sup> have described some experimental work which indicates that the magnetic effect and the A-band can be traced to the same defect.

A defect model, adjusted to account for the observed paramagnetic resonance absorption in smoky quartz, has been described by O'Brien and Pryce.<sup>22</sup> In it, an Al atom acquires a co-ordination number of four by accepting an extra electron, becoming Al<sup>-</sup>. The Al<sup>-</sup> may then enter the crystal structure at a Si lattice site. In order to maintain electro-neutrality, a monovalent cation such as Na<sup>+</sup>, Li<sup>+</sup> or H<sup>+</sup> must be in close association with the Al<sup>-</sup>. It is proposed<sup>22</sup> that the effect of an ionizing irradiation on this center is to remove an orbital electron, most often from one of the oxygen atoms adjacent to the Al<sup>-</sup>. The cation is then no longer bound to the defect center and hence diffuses away, becoming an electron trap. A two-dimensional schematic representation of this defect, before irradiation, is shown in Fig. 7(c). It is denoted as  $\overset{\text{Al}}{\text{Na}}\text{P}$ . The probable interaction between this defect and an ionizing radiation is given by



The  $\overset{\text{Al}}{\text{A}}_+$  defect, Fig. 7(d), is quite similar to the A<sub>0</sub> structure except that an Al<sup>-</sup> resides at a Si site and the defect contains an unpaired electron. As the cation migrates from the A-center, it probably picks up an electron and becomes a  $\text{NaP}_-$  defect, Fig. 7(g). The  $\overset{\text{Al}}{\text{A}}_+$  defect is considered to be responsible for both the magnetic and optical effects.

The observed correlation between A-band and 100°K absorption simply means that x-irradiation of a defect in quartz produces other defects which provide the mechanisms for both optical and mechanical effects. The original defect is doubtless  $\overset{\text{Al}}{\text{Na}}\text{P}$  and, on the basis of the above-cited investigations, the color center can be traced to the  $\overset{\text{Al}}{\text{A}}_+$  defect.

The problem remaining is to determine whether it is the  $\overset{\text{Al}}{\text{A}}_+$  or the  $\text{NaP}_-$  defect which is responsible for the mechanical relaxation. An interesting approach to the solution of this problem involves the removal of mobile impurity ions from quartz. When a sample of quartz is placed in an electric field, directed along the Z-axis and heated to approximately 500°C, a deposit is observed to collect at the cathode surface.<sup>23</sup> The main constituent of the deposit on a sample of natural quartz has been identified as Na.<sup>23</sup> It is apparent, therefore, that impurity ions, which are

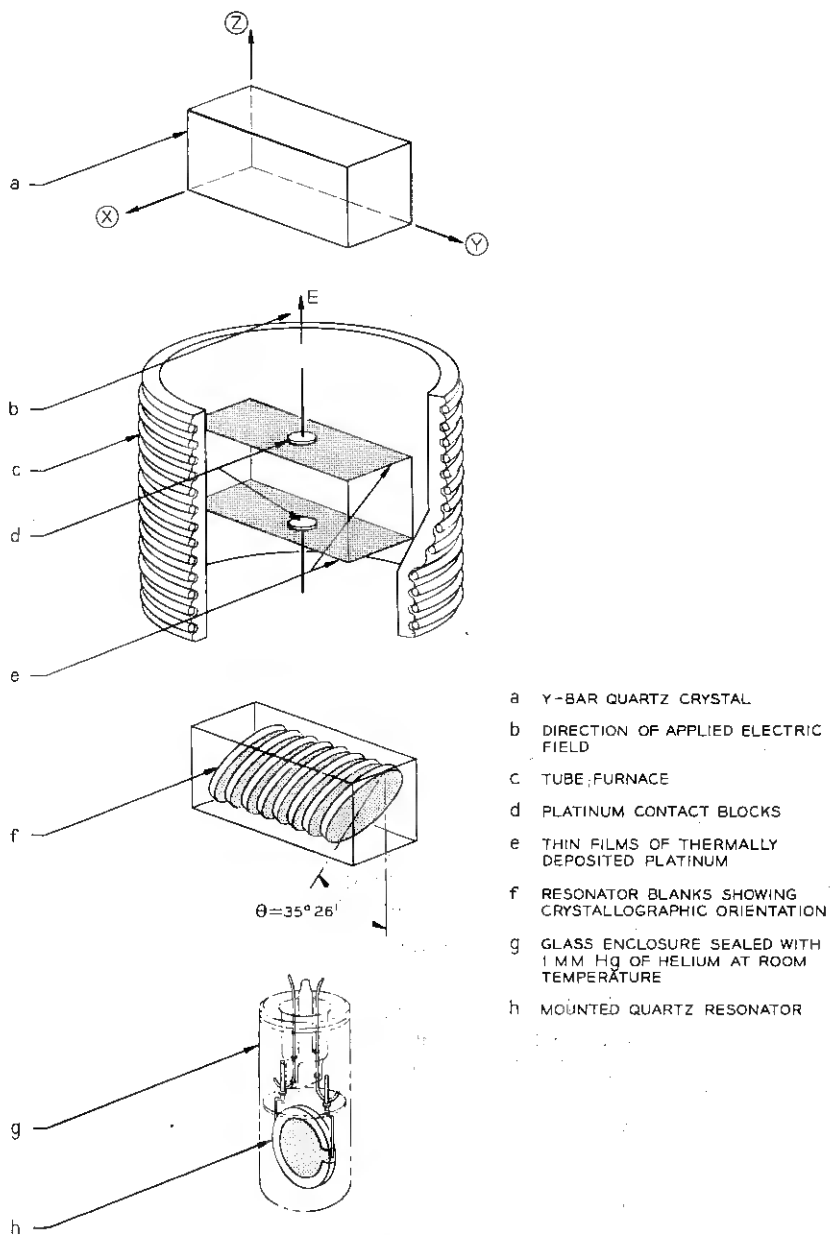


Fig. 17 — Process steps for the preparation of thermoelectrically treated quartz resonators.

known to have a high mobility along the optic axis, can be effectively swept from quartz.

Consider the effect of electrolytic purification on the  ${}_{\text{Na}}^{\text{Al}}\text{P}$  defect. In view of the foregoing, it is reasonable to expect  $\text{Na}^+$  to be stripped from P-centers and collected at the cathode surface. As a result, the  ${}_{\text{Na}}^{\text{Al}}\text{P}$  defects are reduced to  ${}^{\text{Al}}\text{A}_-$  which, except for an excess electron, closely resembles the structure of the irradiation-induced  ${}^{\text{Al}}\text{A}_+$  defect. The incidence of  ${}_{\text{Na}}\text{P}_-$  defects in the swept quartz should be quite rare. There are, therefore, two alternatives:

i. If the  $100^\circ\text{K}$  absorption is due to  ${}^{\text{Al}}\text{A}_+$  rather than  ${}_{\text{Na}}\text{P}_-$  defects, an absorption similar to the one at  $100^\circ\text{K}$  should be observed in thermoelectrically treated quartz, or

ii. If an absorption akin to the  $100^\circ\text{K}$  absorption cannot be generated by sweeping the material, the  $100^\circ\text{K}$  absorption probably involves the  ${}_{\text{Na}}\text{P}_-$  defect.

A number of test resonators were fabricated from a natural quartz crystal. Half the units were untreated and used for control purposes, while the rest were thermoelectrically treated. The process steps involved in the preparation of the treated crystal units are shown in Fig. 17. A plot of the mechanical loss at 5 mc in a representative treated sample, before and after x-irradiation, is compared in Fig. 18 with an untreated x-irradiated sample. It is obvious immediately that the absorption centered about  $85^\circ\text{K}$  in the swept quartz is strikingly similar to the  $100^\circ\text{K}$  absorption. Both have roughly the same amplitude and are characterized by two absorption peaks. Measurements at other frequencies demonstrate that the absorption at  $85^\circ\text{K}$  is due to a relaxation process with a  $\tau_0$  of the same order of magnitude as that for the  $100^\circ\text{K}$  relaxation process and an activation energy of approximately 2,000 cal/gm mole. The necessary conditions for the first alternative given above are satisfied; therefore, it is concluded that the *irradiation-induced defect underlying the relaxation process whose absorption peak occurs at  $100^\circ\text{K}$  for a frequency of 5 mc is the  ${}^{\text{Al}}\text{A}_+$  defect.* Conversely, the above observations and analysis can be effectively used to argue the propriety of relating the A-band absorption to  ${}^{\text{Al}}\text{A}_+$ .

The lower activation energy for the thermoelectrically induced relaxation is perhaps attributable to the excess negative charge carried by the  ${}^{\text{Al}}\text{A}_-$  defect. The  ${}^{\text{Al}}\text{A}_-$  defects in treated quartz could presumably be easily converted to  ${}^{\text{Al}}\text{A}_+$  defects by x-irradiation. However, A-band absorption cannot be induced in swept quartz\* and, significantly, neither

\* It appears that V. E. Bottom (Final Report, U. S. Army Signal Corps Contract DA-36-039 sc-66, 30 June 1953) first reported this effect.

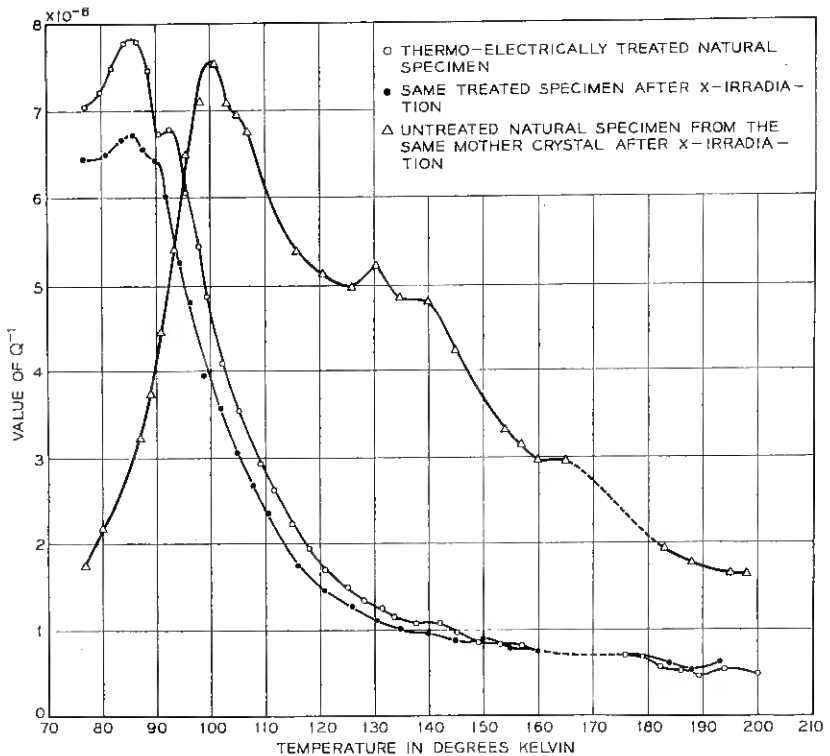


Fig. 18 — Comparison of relaxation absorption in sample of thermo-electrically treated natural quartz and x-irradiation-induced absorption in natural quartz.

can the 100°K absorption (see the curve for x-irradiated treated quartz in Fig. 18.) It is conceivable that removing  $\text{Na}^+$  in treated quartz effectively eliminates electron traps in the material. Consequently, electrons ionized off  $^{11}\text{A}_-$  defects by x-irradiation will readily diffuse back to these centers and thus negate the irradiation effect.

## VII. CONCLUSIONS

The concentration of deformation defects underlying the relaxation absorption, which occurs at 50°K for a frequency of 5 mc, has been found to be several decades higher in synthetic quartz than in the natural material. The characteristic lowering of the elastic modulus in the region of stress relaxation is observed as a decrease in the resonant frequency

of AT-cut resonators at temperatures above 50°K. It is apparent that the 50°K defect also alters the  $f$ - $T$  characteristics of the AT-cut.

The singular lack of correlation between concentration of impurities in quartz and the amplitude of the mechanical absorption at 50°K argues against proposing that the responsible lattice deformation derives from some specific impurity. This observation, together with the fact that x-irradiation effectively eliminates the 50°K absorption, suggests that the deformation defect consists of excess oxygen, forming nonbridging oxygen defects.

It has been demonstrated that x-irradiation induces a 100°K relaxation absorption at 5 mc in quartz which darkens with irradiation. The 100°K absorption is not found in clear quartz. Although a lowering of the frequency of crystal resonators which have been subjected to x-irradiation has been previously observed, it is now possible to attribute the change to a decrease of the elastic modulus caused by the relaxation of the 100°K defect. Since the amplitude of the 100°K absorption is proportional to the color density of the irradiated sample, the defect responsible for this relaxation could conceivably be either  ${}^A_1A_+$  or  ${}_{Na}P_-$ . Measurements of the mechanical absorption in electrolytically purified sample resonators clearly favor selecting  ${}^A_1A_+$  as the responsible defect.

#### VIII. ACKNOWLEDGMENTS

The author wishes to thank R. A. Sykes and M. D. Fagen for their counsel and support during the course of these investigations, and to acknowledge the valuable assistance given by Miss Margaret Simon in carrying out the resonator measurements.

#### REFERENCES

1. Bordoni, P. G., *J. Acoust. Soc. Amer.*, **23**, 1954, p. 495.
2. Bömmel, H. E., *Phys. Rev.*, **98**, 1955, p. 1136.
3. Niblett, D. H. and Wilks, J., *Phil. Mag.*, **2**, 1957, p. 1427.
4. Bömmel, H. E., Mason, W. P. and Warner, A. W., *Phys. Rev.*, **102**, 1956, p. 64.
5. King, J. C., *Phys. Rev.*, **109**, 1958, p. 1552.
6. Warner, A. W., *Proc. I.R.E.*, **40**, 1952, p. 1030.
7. Zener, C., *Anelasticity of Metals*, Univ. of Chicago Press, Chicago, 1948.
8. Chi, A. R., Hammond, D. L. and Gerber, E. A., *Proc. I.R.E.*, **43**, 1955, p. 1137.
9. Bechmann, R., *Proc. I.R.E.*, **44**, 1956, p. 1600.
10. Brown, C. S. and Thomas, L. A., *Proc. A.I.E.E.*, **104C**, 1956, p. 174.
11. King, J. C., U. S. Army Signal Corps Contract DA-36-039 sc-64586, Third Interim Report, April 1956; Fifth Interim Report, September 1956.
12. Volger, J., Stevels, J. M. and van Amerongen, C., *Philips Res. Rep.*, **10**, 1955, p. 260.
13. Chi, A. R., *Phys. Rev.*, **107**, 1957, p. 1524.
14. Berman, R., *Adv. in Phys.*, **2**, 1953, p. 103.
15. Brown, C. S. and Thomas, *Nature*, **169**, 1952, p. 39; Arnold, G., *Proc. 10th Ann. Freq. Cont. Symp.*, Asbury Park, N. J., 1956.

16. Frondel, C., *Am. Mineral.*, **30**, 1945, p. 432.
17. Bottom, V. E., *Phys. Rev.*, **71**, 1947, p. 476.
18. Mitchell, E. W. J. and Paige, E. G. S., *Proc. Phys. Soc.*, **B67**, 1954, p. 262.
19. Ditchburn, R. W., Mitchell, E. W. J., Paige, E. G. S., Custers, J. F., Dyer, H. B., and Clark, C. C., *Defects in Crystalline Solids — Report of Bristol Conference*, Physical Society, London, 1954.
20. Griffiths, J. H. E., Owen, J. and Ward, J. M., *Defects in Crystalline Solids — Report of Bristol Conference*, Physical Society, London, 1954.
21. Mitchell, E. W. J. and Paige, E. G. S., *Phil. Mag.*, **46**, 1955, p. 1353.
22. O'Brien, M. C. M. and Pryce, M. H. L., *Defects in Crystalline Solids — Report of Bristol Conference*, Physical Society, London, 1954.
23. King, J. C., U. S. Army Signal Corps Contract DA-36-039 sc-64586, Ninth Interim Report, August 1957.

# Recent Monographs of Bell System Technical Papers Not Published in This Journal\*

ABRAHAMS, S. C. and GELLER, S.

**Refinement of the Structure of a Grossularite Garnet**, Monograph 3120.

ANDERSON, P. W.

**Coherent Excited States in the Theory of Superconductivity**, Monograph 3090.

BALLHAUSEN, C. J. and LIEHR, A. D.

**Intensities in Inorganic Complexes — II. Tetrahedral Complexes**, Monograph 3121.

BARNES, M. W., see Basseches, H.

BASSECHES, H. and BARNES, M. W.

**Gassing of Liquid Dielectrics Under Electrical Stress**, Monograph 3122.

BEACH, A. L. and GULDNER, W. G.

**Application of Vacuum Fusion to Gas-Metal Studies**, Monograph 3123.

BEMSKI, G.

**Recombination in Semiconductors**, Monograph 3124.

BOZORTH, R. M. and WALSH, D. E.

**Ferromagnetic Moment of  $\text{CoMnO}_3$** , Monograph 3125.

---

\* Copies of these monographs may be obtained on request to the Publication Department, Bell Telephone Laboratories, Inc., 463 West Street, New York 14 N.Y. The numbers of the monographs should be given in all requests

DAVID, E. E., JR.

**Artificial Auditory Recognition in Telephony**, Monograph 3141.

FLANAGAN, J. L.

**Some Properties of the Glottal Sound Source**, Monograph 3126.

FRISCH, H. L.

**The Time Lag in Diffusion**, Monograph 3127.

GELLER, S., see Abrahams, S. C.

GELLER, S., see Gilleo, M. A.

GILLES, M. A. and GELLER, S.

**Magnetic and Crystallographic Properties of Substituted Yttrium-Iron Garnet**, Monograph 3092.

GULDNER, W. G., see Beach, A. L.

HOBSTETTER, J. N., see Pfann, W. G.

INDIG, G. S., see Pfann, W. G.

IWERSEN, J. E., see Nelson, J. T.

JAYCOX, E. K.

**Quantitative Spectrochemical Methods of Broad Applicability**, Monograph 3128.

KEYWELL, F., see Nelson, J. T.

LEE, C. Y.

**Some Properties of Nonbinary Error-Correcting Codes**, Monograph 3129.

LIEHR, A. D., see Ballhausen, C. J.

MCCALL, D. W. and SLICHTER, W. P.

**Diffusion in Ethylene Polymers, III**, Monograph 3140.

MILLER, R. C., see Smits, F. M.

MOLL, J. L.

**Theory for Voltage-Current Characteristic of p-n Junctions**, Monograph 3130.

MOLL, J. L., see Thomas, D. E.

NELSON, J. T. and IWERSEN, J. E.

**Measurement of Internal Temperature Rise of Transistors, Monograph 3131.**

NELSON, J. T., IWERSEN, J. E. and KEYWELL, F.

**A Five-Watt Ten-Megacycle Transistor, Monograph 3132.**

PFANN, W. G., HOBSTETTER, J. N. and INDIG, G. S.

**Preventing Conductivity Fluctuations During Growth of a Semiconducting Crystal, Monograph 3142.**

POOLE, K. M. and TIEN, P. K.

**A Ferromagnetic Resonance Frequency Converter, Monograph 3134.**

SLICHTER, W. P., see McCall, D. W.

SMITS, F. M.

**Formation of Junction Structures by Solid-State Diffusion, Monograph 3136.**

SMITS, F. M. and MILLER, R. C.

**Rate Limitation for Impurity Diffusion in Semiconductors, Monograph 3119.**

THOMAS, D. E. and MOLL, J. L.

**Junction Transistor Short-Circuit Current Gain and Phase Determination, Monograph 3137.**

TIEN, P. K., see Poole, K. M.

UHLIR, A., JR.

**Potential of Semiconductor Diodes in High-Frequency Communications, Monograph 3138.**

WALKER, L. R.

**Resonant Modes of Ferromagnetic Spheroids, Monograph 3139.**

WALSH, D. E., see Bozorth, R. M.

## Contributors to This Issue

CYRUS F. AULT, B.E. in E.E., 1950, University of Southern California; M.S., 1955, Stevens Institute of Technology; Bell Telephone Laboratories, 1955—. Mr. Ault is a member of the group working on the development of the barrier grid store for electronic switching. Member I.R.E.

WILLARD S. BOYLE, B.S., 1947, M.S., 1948 and Ph.D., 1950, McGill University; Royal Military College (Kingston, Ont.), 1951-53; Bell Telephone Laboratories, 1953—. He was first engaged in studies of electrical discharge phenomena in low voltage contacts. Since 1956 he has concentrated on research in optical and magnetic effects in solids in the infra-red and at very low temperatures. Member American Physical Society.

KENNETH BULLINGTON, B.S., 1936, University of New Mexico; M.S., 1937, Massachusetts Institute of Technology; Bell Telephone Laboratories, 1937—. Mr. Bullington first worked on systems engineering on wire transmission circuits. Since 1942 he has been concerned with transmission engineering on radio systems, particularly over-the-horizon radio propagation. He took part in engineering planning on the DEW and White Alice projects. He is now in charge of a group concerned with systems engineering problems related to TASI and submarine cable systems. In 1956 he received the Morris Liebmann Memorial Prize and the Franklin Institute's Stuart Ballantine Metal for contributions in tropospheric transmission and its application to practical communications systems. Fellow I.R.E.; member Phi Kappa Phi, Sigma Tau, Kappa Mu Epsilon.

R. W. DEGRASSE, B.S., 1951, California Institute of Technology; M.S., 1954 and Ph.D., 1958, Stanford University; California Institute of Technology Jet Propulsion Laboratory, 1951-1953; Stanford Electronics Laboratory, 1953-1957; Bell Telephone Laboratories, 1957—. At the Jet Propulsion Laboratory Mr. DeGrasse was engaged in missile radar development, and at Stanford Electronics Laboratory he did research work on microwave frequency memory devices, low-noise travel-

ing-wave tubes and traveling-wave frequency converters. Since joining Bell Laboratories he has been engaged in development work on solid state masers. Member I.R.E., Sigma Xi.

G. V. DEVERALL, B.S., 1948, Purdue University; M.S., 1951, University of Chicago; Ph.D., 1954, Purdue University; Bell Telephone Laboratories, 1957—. He has been engaged in optical and photographic studies with application to electronic switching. Member American Physical Society, Optical Society of America, Sigma Xi.

JOHN M. FRASER, B.E.E., 1945, Polytechnic Institute of Brooklyn; Bell Telephone Laboratories, 1934—. He first worked on problems of transmission systems performance and the design of equipment for simulating transmission systems in the laboratory. During World War II he was concerned with design and evaluation of military communications systems. He took part in systems engineering of the transatlantic telephone cable and at present is engaged in systems engineering on TASI. Senior member I.R.E.; member Sigma Xi, Tau Beta Pi, Eta Kappa Nu.

L. E. GALLAHER, B.S., 1951 and M.S., 1956, Case Institute of Technology; Bell Telephone Laboratories, 1955—. He has been engaged in development work on a beam-positioning servo system for the flying spot store. Member Sigma Xi, Tau Beta Pi, Eta Kappa Nu.

GEORGE HAUGK, B.S., in E.E., 1952, Newark College of Engineering; New York University; Western Electric Company, 1947-48; Bell Telephone Laboratories, 1952—. After completing the Communications Development Training Program course, Mr. Haugk worked on design of circuits for electronic switching systems for three years. Since then he has headed a group responsible for field trial and testing of electronic switching. Member I.R.E.

DONALD R. HERRIOTT, University of Richmond; Duke University; Bausch and Lomb, 1949-56; Bell Telephone Laboratories, 1956—. Mr. Herriott has been engaged in research in visual transmission systems. Member Optical Society of America.

C. W. HOOVER, JR., B.E. in M.E., 1946; M.S., 1951 and Ph.D. in physics, 1954, Yale University; B.S. in E.E., 1947, M.I.T.; Bell Telephone Laboratories, 1954—. Mr. Hoover has been engaged in design

of memory systems for use in electronic switching systems. He held the Yale University Sterling Fellowship and the National Research Council-Radio Corporation of America Fellowship in electronics. Member American Physical Society, Tau Beta Pi, Sigma Xi.

JAMES C. KING, B.A., 1949, Amherst College; M.S., 1951 and Ph.D., 1953, Yale University; Bell Telephone Laboratories, 1953—. He has been engaged primarily in the study of defects which occur in natural and synthetic quartz. This has led to investigations of the anelasticity of quartz at low temperatures and the effects of ionizing radiation. Member American Physical Society, Phi Beta Kappa, Sigma Xi.

RUTH A. KING, B.A., 1941, Brooklyn College; New York Telephone Co., 1927-29; Bell Telephone Laboratories, 1929—. Mrs. King joined the Bell System as a telephone operator and two years later transferred to the drafting department. In 1937 she turned to mathematical problems in circuit research. During the war years she took part in the development of pulse transmission systems and later worked on research studies of transmission lines and on repeaters for the transatlantic cable. Mrs. King is presently engaged in work on television transmission. Member I.R.E., Pi Mu Epsilon.

DOLORES C. LEAGUS, A.B., 1951, Wilkes College; M.A., 1953, Bucknell University; Bell Telephone Laboratories, 1953—. Miss Leagus is engaged in computer programming for mathematical research projects.

C. Y. LEE, B.E.E., 1947, Cornell University; M.S.E.E., 1949 and Ph.D., 1954, University of Washington; John McMullen Regional Scholar at Cornell, 1944-47; instructor, electrical engineering, University of Washington, 1948-51; Bell Telephone Laboratories, 1952—. Mr. Lee has been engaged in mathematical research in switching systems development. He was a visiting member of the Institute for Advanced Study in the School of Mathematics during the academic year 1957-58. Member Sigma Xi, Eta Kappa Nu.

GEORGE H. MEALY, A.B., 1951, Harvard College; Bell Telephone Laboratories, 1951—. After completing the C.D.T.P. course, Mr. Mealy was engaged in military work for a year. He then turned to work as a consultant in switching theory and programming research. He later headed mathematical studies in the switching training group and is now a consultant in logical design and computer programming. Mr.

Mealy teaches a course in switching theory and computer design at Columbia University. Member I.R.E., Association for Computing Machinery, Association for Symbolic Logic, Society for Industrial and Applied Mathematics.

D. B. OWEN, B.S., 1945, M.S., 1946 and Ph.D., 1951, University of Washington; associate and acting instructor, University of Washington, 1946-52; assistant professor and research associate, Purdue University, 1952-54; Sandia Corporation, 1954—. A member of the systems analysis department and supervisor of the statistical research division of the Sandia Corp., he specializes in research on statistical procedures and consultation on statistical problems. Member Institute of Mathematical Statistics, American Statistical Association, American Mathematical Society, Phi Beta Kappa, Sigma Xi.

MERTON B. PURVIS, B.S., 1944 and M.S., 1949, Iowa State College; Ph.D., 1954, Pennsylvania State University; Bell Telephone Laboratories, 1955—. He has been engaged in mechanical development work on an electronic switching system central office. This has included studies of problems in optics, photography, heat transfer and air conditioning. Associate member American Society of Mechanical Engineers; member Sigma Xi, Pi Tau Sigma.

GORDON RAISBECK, B.A., 1944, Stanford University; Ph.D., 1949, Massachusetts Institute of Technology; Bell Telephone Laboratories, 1949—. Mr. Raisbeck's early work at Bell Laboratories was in research in acoustics and underwater sound. From 1950 to 1953 he concentrated in research in transistor circuits and then took his present post in charge of a group engaged in research on transmission lines and pulse transmission systems. Throughout his Laboratories career, Mr. Raisbeck has done additional work on information theory. He was a Rhodes Scholar at Oxford University in 1947. Senior member I.R.E.; member American Mathematical Society, Mathematical Association of America, American Management Association, Sigma Xi.

E. O. SCHULZ-DUBOIS, Dipl. phys., 1950, and Dr. phil. nat., 1954, Johann Wolfgang Goethe University (Germany); Purdue University, 1954-55; Raytheon Manufacturing Co., 1956-57; Bell Telephone Laboratories, 1957—. At Purdue Mr. Schulz-DuBois was engaged in solid state research, particularly on paramagnetic resonance in irradiated semiconductors. At Raytheon he was concerned with the development

of ferrite materials and devices. After joining Bell Laboratories he worked for a short time on low-frequency ferrite isolators. His present work is with paramagnetic materials and slow-wave structures for application to solid state maser devices.

H. E. D. SCOVIL, B.A., 1948 and M.A., 1949, University of British Columbia; Ph.D., 1951, Oxford University; Nuffield research fellow, Oxford, 1951-52; assistant professor, University of British Columbia, 1952-55; Bell Telephone Laboratories, 1955—. Mr. Scovil has taken part in investigations of low temperature properties of magnetic materials and ferromagnetic materials at high microwave power levels. He has recently concentrated on development of solid state masers.

JAMES L. SMITH, B.S.E.E., 1956, Newark College of Engineering; Bell Telephone Laboratories, 1941—. Mr. Smith first worked on problems concerned with relay contact erosion. More recently he has been engaged in development work on solid state switching networks. His present work is on the twistor memory device. Member Tau Beta Pi.

JOHN M. WIESEN, B.S., 1949 and M.S., 1951, Iowa State College; graduate assistant, Iowa State College, 1949-51; Sandia Corporation, 1951—. A member of the reliability department and supervisor of the statistics and evaluation division of the Sandia Corp., he is involved in the application of statistical methods to atomic weapon reliability. Member American Society for Quality Control, Institute of Mathematical Statistics, American Statistical Association.